

JOINT EUROPEAN SUMMER SCHOOL  
ON  
FUEL CELL AND HYDROGEN TECHNOLOGY

A PRIMER ON HYDROGEN AND FUEL CELL TECHNOLOGY

TUTORIAL ON DEFLAGRATIONS AND  
DETONATIONS

Dr A.E. Dahoe

University of Ulster, United Kingdom

### Question 3.a

Figure 1 shows a picture of an enclosure containing a fuel-cell stack. The stack is operated by continuous stream of hydrogen and air. There is a concern that the continuous hydrogen stream may leak into the enclosure to form a combustible mixture. The dimensions of the enclosure are 0.7m by 0.8m by 1m. And the concern is that 5 to 15 grams of hydrogen might mix with the air contained by the enclosure.

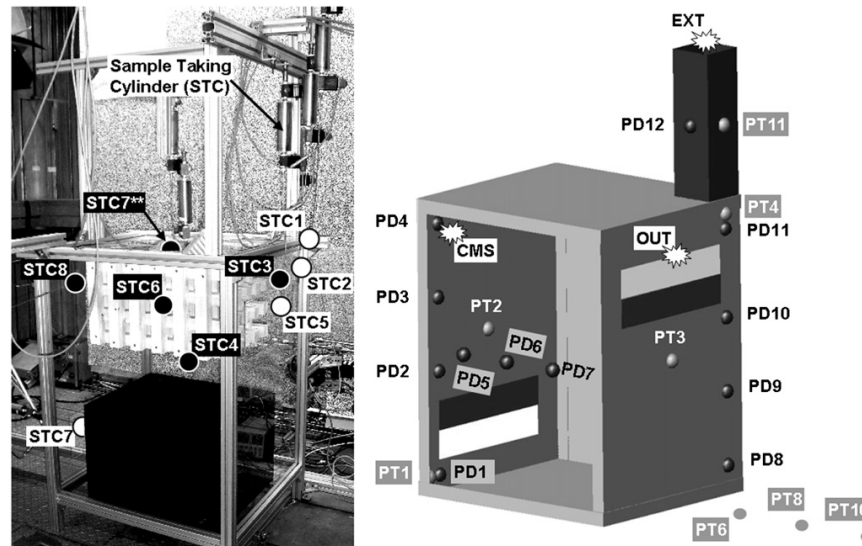


Figure 1: Enclosure containing a fuel-cell stack.

From: Friedrich A., Vesper A., Stern G., and Kotchourko N. Hyper experiments on catastrophic hydrogen releases inside a fuel cell enclosure. International Journal of Hydrogen Energy, 36:2678-2687, 2011.

## Question 3.a

### THE QUESTION

When 5 to 15 grams of hydrogen would mix with the air in the enclosure would like to know which amounts would cause the combustion to remain in the deflagration or pose a detonation risk. Apply your knowledge of flammability and detonation limits to calculate the amount of hydrogen below which combustion can only occur in the deflagration mode, and, beyond which detonation may occur.

---

- Flammability limits hydrogen-air mixtures at 298.15 K and 1 bar: 4 vol% - 75 vol% H<sub>2</sub> in air.
- Detonation limits hydrogen-air mixtures at 298.15 K and 1 bar: 18 vol% - 59 vol% H<sub>2</sub> in air.

Volume of the enclosure is  $V=0.56\text{ m}^3$ ; so it contains  $0.56\text{ m}^3$  air.

Volume occupied by hydrogen can be computed from the ideal gas law:  $pV_{\text{H}_2} = n_{\text{H}_2}RT$ .

Hydrogen concentration:

$m_{\text{H}_2}$ [ $10^{-3}$ g]	5	5.5	6	6.5	7	7.5	8	8.5	9	9.5	10	10.5	11	11.5	12	12.5	13	13.5	14	14.5	15
$n_{\text{H}_2}$ [moles]	2.5	2.75	3.0	3.25	3.5	3.75	4.0	4.25	4.5	4.75	5.0	5.25	5.5	5.75	6.0	6.25	6.5	6.75	7.0	7.25	7.5
$V_{\text{H}_2}$ [ $10^{-3}$ m <sup>3</sup> ]	62.0	68.2	74.4	80.6	86.8	93.0	99.2	105.3	111.5	117.7	123.9	130.1	136.3	142.5	148.7	154.9	161.1	167.3	173.5	179.7	185.9
$V_{\text{H}_2}/V$ [%]	11.1	12.2	13.3	14.4	15.5	16.6	17.7	18.8	19.9	21.0	22.1	23.2	24.3	25.5	26.6	27.7	28.8	29.9	31.0	32.1	33.2

$$\text{LDL} = 18\% = V_{\text{H}_2}/V \implies V_{\text{H}_2} = 0.1008\text{m}^3 \implies m_{\text{H}_2} = 8.13\text{g}$$

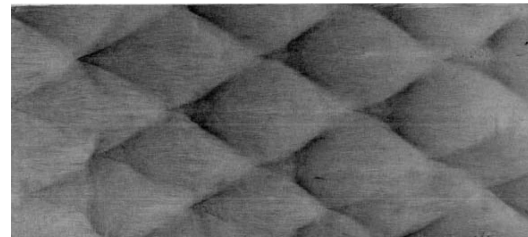
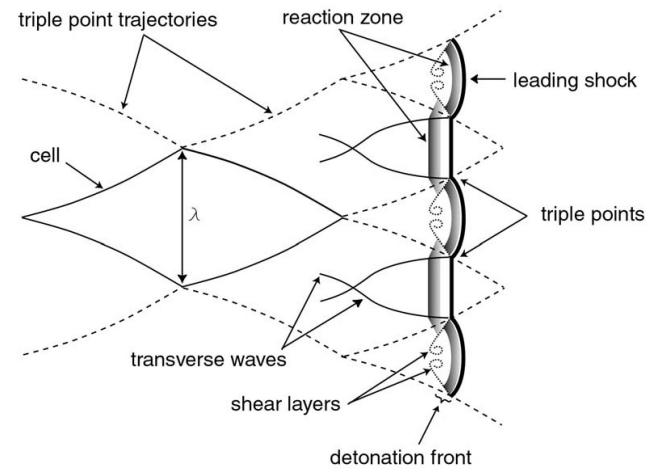
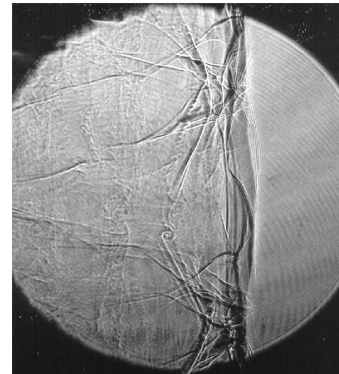
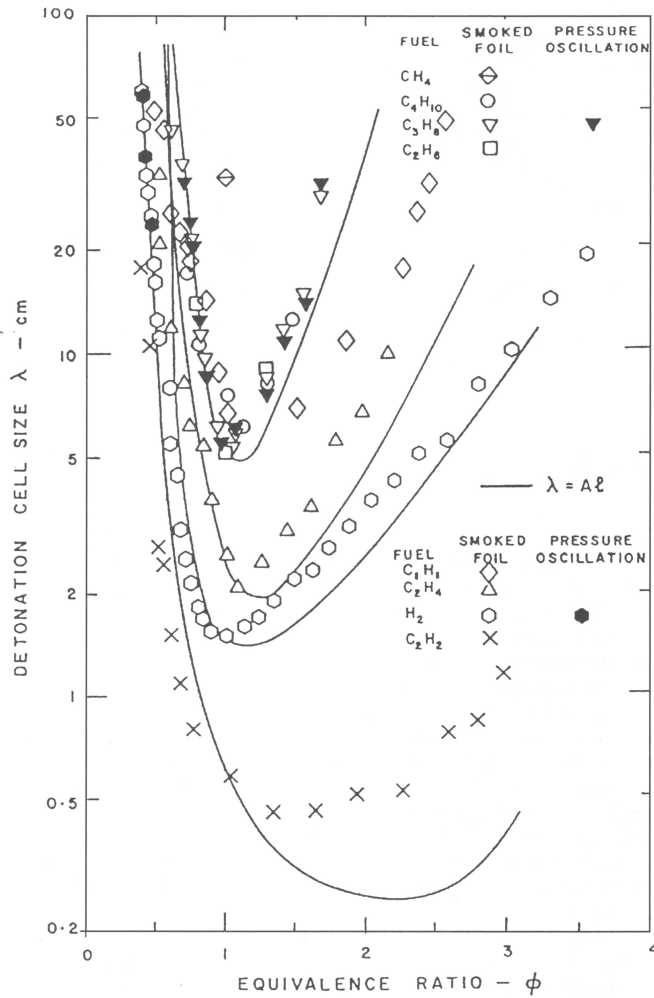
**Question 3.a**

## FLAMMABILITY LIMITS; CONFINED AND UNCONFINED DETONATION LIMITS OF HYDROGEN AND OTHER FUELS

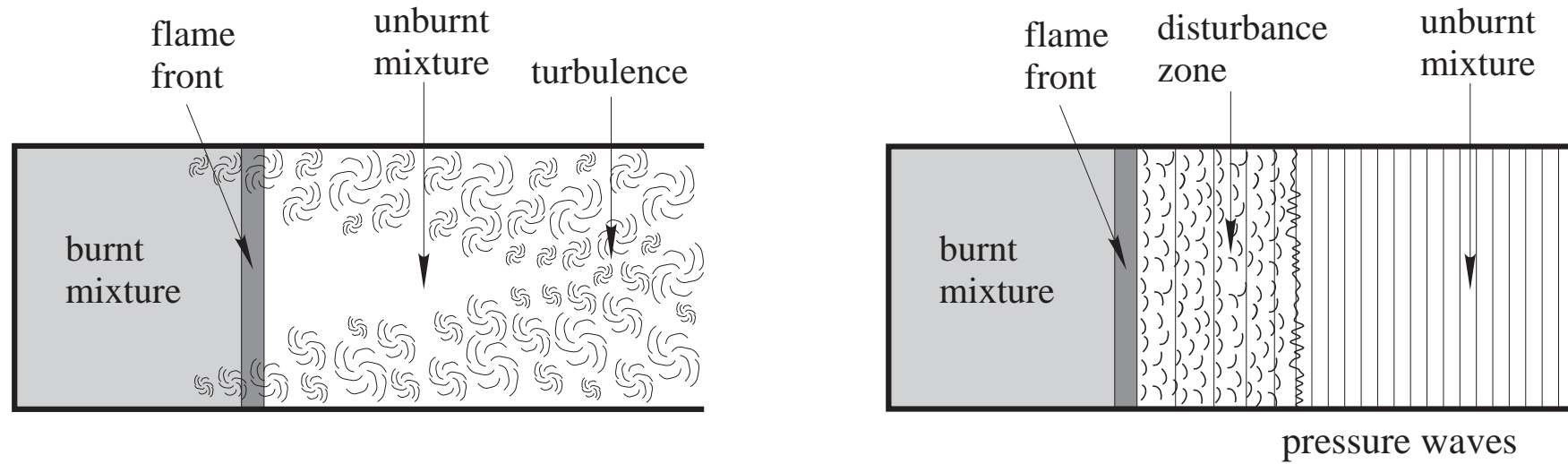
Detonation limits (vol%) of confined and unconfined mixtures and flammability limits (vol%) in oxygen and air (after Grossel (2002) [1], Kuo (2005) [2], and Nettleton (1987) [3]).

Fuel	Confined detonation limit		Confined detonation limit		Unconfined detonation limit		Unconfined detonation limit		Flammability limit		Flammability limit	
	O <sub>2</sub>		air		O <sub>2</sub>		air		O <sub>2</sub>		air	
	lower	upper	lower	upper	lower	upper	lower	upper	lower	upper	lower	upper
H <sub>2</sub>	15.0	90.0	18.3	58.9					4.0	95.0	4.0	75.0
CH <sub>4</sub>			5.7	14							5.3	15
C <sub>2</sub> H <sub>6</sub>	3.60	46.4	2.87	12.20	11.0	39.0	4.0	9.2	3.0	66.0	3.0	12.4
C <sub>3</sub> H <sub>8</sub>	2.50	42.5	2.57	7.37	7.0	31.0	3.0	7.0			2.1	9.5
nC <sub>4</sub> H <sub>10</sub>	2.05	38.0	1.98	6.18			2.5	5.2			1.8	8.4
nC <sub>8</sub> H <sub>18</sub>	1.55	17.3	1.45	2.85							0.95	
C <sub>2</sub> H <sub>4</sub>	4.10	60.0	3.32	14.70	9.2	51.0			2.9	80.0	2.7	36.0
C <sub>3</sub> H <sub>6</sub>	2.50	50.0	3.55	10.40	6.7	37.0	3.5	8.5	2.1	53.0	2.4	11.0
C <sub>2</sub> H <sub>2</sub>	2.90	88.8	4.20	50.0	6.7	68.0			2.5	80.0		
CH <sub>3</sub> OH	9.50	64.5									6.7	36.0
C <sub>2</sub> H <sub>5</sub> OH			5.1	9.8							3.3	19.0
C <sub>2</sub> H <sub>5</sub> OC <sub>2</sub> H <sub>5</sub>	2.6	>40	2.8	4.5	14.7	29.0			2.0	82.0	1.9	36.0
gasoline			1.1	3.3							1.4	7.6
CO	38.0	90.0							15.5	93.3		
NH <sub>3</sub>	25.4	75.0							13.5	79		
C <sub>6</sub> H <sub>6</sub>	1.55	36.0	1.60	5.55							1.3	7.9
xylene	1.05	26.5									1.1	6.4
CH <sub>3</sub> COCH <sub>3</sub>	3.3	40.0									2.6	13.0

Detonation cell size  $\lambda$ ; sustained detonation possible when geometry  $> 7\lambda$ ; ( $7\lambda$ -rule)



## Run-up distance for deflagration-to-detonation-transition



From: Dahoe A.E. Lecture Notes on Explosions. Delft University of Technology. 1997.

## Question 3.b

### THE QUESTION

What is the Rankine-Hugoniot diagram? Describe the features of this diagram i.e. derive expressions for Hugoniot curve, the Rayleigh lines, the detonation and deflagration branches and the Chapman-Jouget points. Using the Rankine-Hugoniot diagram point out the differences between deflagrations and detonations, and, explain why detonations are more dangerous than deflagrations.

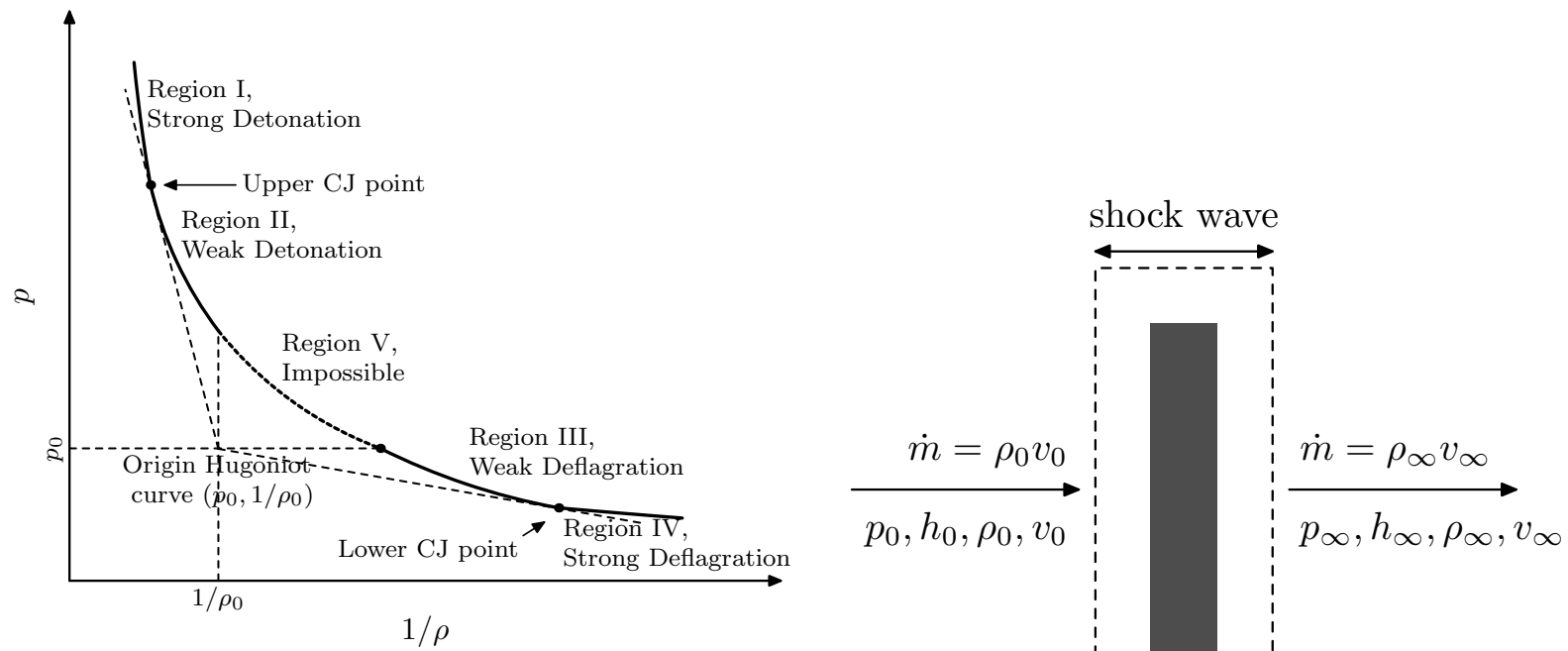


Figure 3: Left: Hugoniot-diagram. Right: Change of properties across a combustion wave.

### Question 3.b

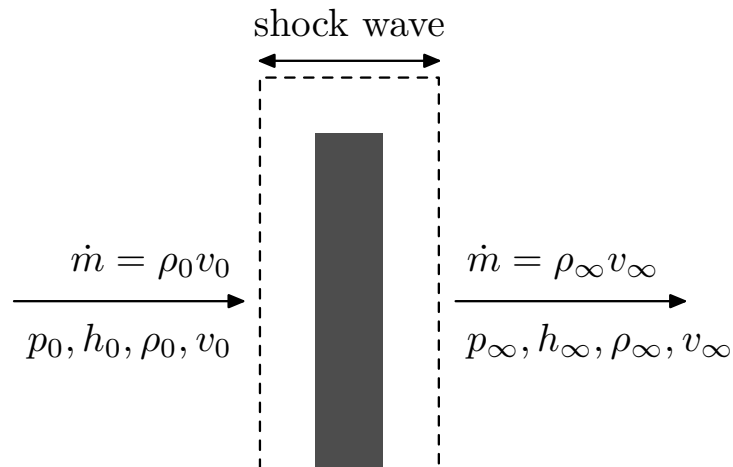


Figure 4: Change of properties across a shock wave.

The Hugoniot relations are:

$$\rho_0 v_0 = \rho_\infty v_\infty \equiv \dot{m} \quad (1)$$

$$p_0 + \rho_0 v_0^2 = p_\infty + \rho_\infty v_\infty^2 \quad (2)$$

$$\rho_0 v_0 h_0 + \rho_0 \frac{v_0^3}{2} = \rho_\infty v_\infty h_\infty + \rho_\infty \frac{v_\infty^3}{2} \quad (3)$$

- Relationships exist between the variables on the two sides of a shock wave. These are known as the Hugoniot relations.
- The Hugoniot relations establish the connection between eight quantities: four variables on the left (low pressure) side of the shock wave ( $p_0, h_0, \rho_0, v_0$ ) and four variables on the right (high pressure) side ( $p_\infty, h_\infty, \rho_\infty, v_\infty$ ).
- These variables are the solution to the inviscid conservation equations for mass, momentum, and energy for waves in a steady, constant area flow.
- There are three Hugoniot relations connecting eight quantities (four on either side of the shock wave).

## THE RANKINE-HUGONIOT RELATION

## Question 3.b

Equations (1) to (3) may be combined into the **Rankine-Hugoniot relation**

$$\frac{\gamma - 1}{\gamma} \left( \frac{p_\infty}{\rho_\infty} - \frac{p_0}{\rho_0} \right) - \frac{p_\infty - p_0}{2} \left( \frac{1}{\rho_\infty} + \frac{1}{\rho_0} \right) = -(h_\infty - h_1) \quad (4)$$

**The difference between a detonation and the shock in an inert gas is in the form of  $h_\infty$ .** In a shock the chemical composition remains unchanged, whereas in a detonation the chemical composition changes so that energy is released. Chemical equilibrium is attained after the gas passes through the wave.

- A plot of  $p_\infty$  versus  $1/\rho_\infty$  for a given value of  $(p_0, 1/\rho_0)$  and the heat release  $-(h_\infty - h_1)$  is called the Hugoniot curve.
- The Hugoniot curve is the locus of all possible solutions of equations (1) to (3), or equivalently, equation (4).
- The point  $(p_0, 1/\rho_0)$  is called the origin of the Hugoniot plot.
- There are two Chapman-Jouget points. They arise from drawing tangents to the Hugoniot curve through the origin of the Hugoniot plot  $(p_0, 1/\rho_0)$ .

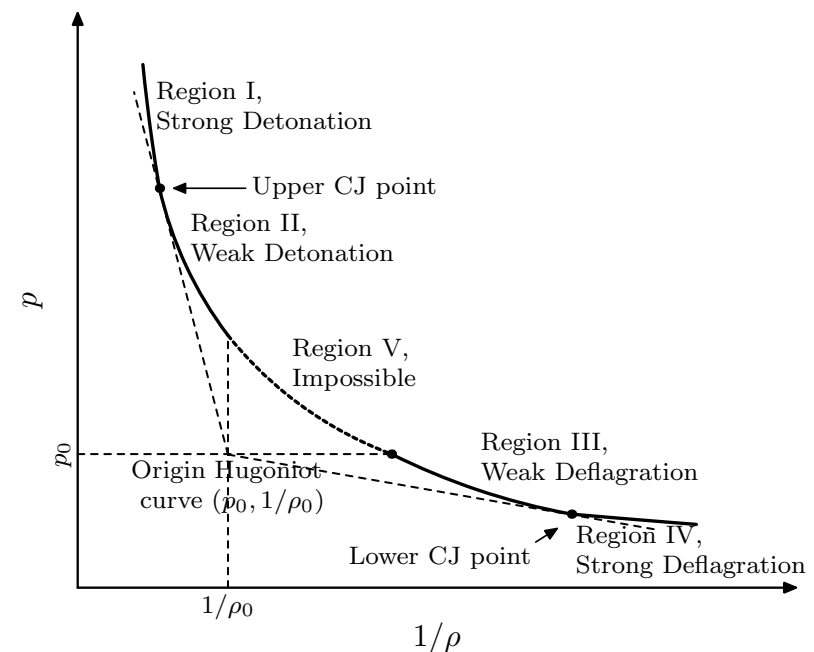


Figure 5: The Hugoniot-diagram.

## THE RAYLEIGH-LINE RELATION

## Question 3.b

Equations (1) and (2) may be combined into the **Rayleigh-line relation**

$$\rho_0^2 v_0^2 = \frac{p_\infty - p_0}{1/\rho_0 - 1/\rho_\infty} \equiv \dot{m}^2 \quad (5)$$

The Rayleigh-line relation is a criterion to identify regimes within the Hugoniot curve where deflagration and detonation are possible.

- Region I, strong detonation regime.
- Region II, weak detonation regime.
- Region III, weak deflagration regime.
- Region IV, strong deflagration regime.
- In region V, it is seen that  $1/\rho_0 - 1/\rho_\infty < 0$  and in  $p_0 - p_\infty > 0$ . The Rayleigh-line relation implies imaginary values for  $v_0$  (i.e. impossible for deflagration or detonation to exist).

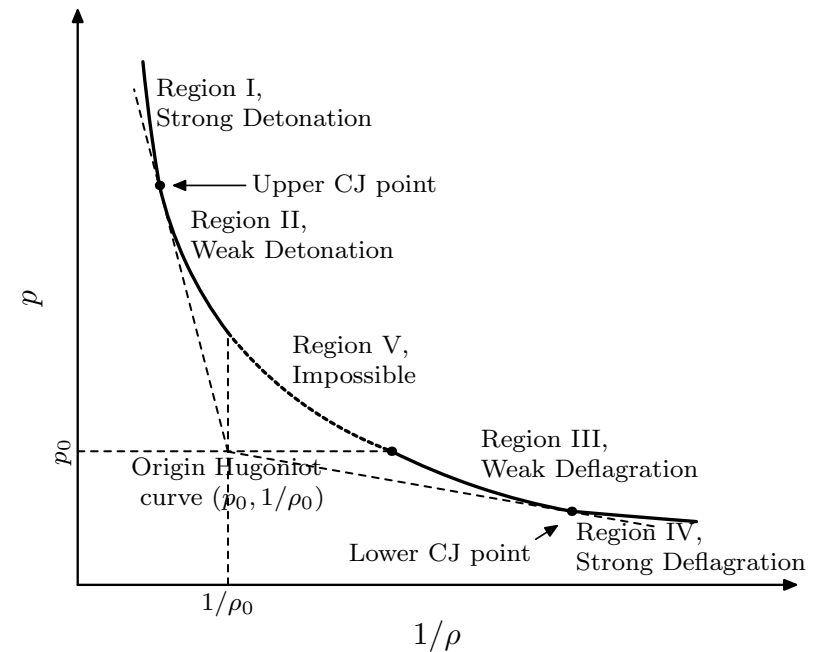


Figure 6: The Hugoniot-diagram.

## DEFLAGRATION AND DETONATION WAVES

## Question 3.b

### Deflagrations are subsonic combustion waves:

- Typical deflagrations propagate at speeds on the order of  $1\text{-}100\text{ m s}^{-1}$ .
- Across a deflagration, the pressure decreases while the volume increases:  $p_\infty < p_0$  and  $1/\rho_\infty > 1/\rho_0$ .
- For deflagrations, the structure of the wave, and, turbulent and diffusive processes, determine the propagation speed.

### Detonations are supersonic combustion waves:

- Typical detonation waves propagate at a velocity in the order of  $2000\text{ m s}^{-1}$ .
- Across a detonation, the pressure increases while the volume decreases:  $p_\infty > p_0$  and  $1/\rho_\infty < 1/\rho_0$ .
- For detonations in stoichiometric hydrogen and hydrocarbon fuel-air mixtures:  $p_\infty/p_0 = 15 - 20$ . For detonations, gas dynamic considerations are sufficient to determine the solution. Chapman (1899) [4] and Jouguet (1905) [5] proposed that detonations travel at one particular velocity, which is the minimum velocity for all the solutions on the detonation branch (the Chapman-Jouget velocity).
- Zeldovich (1940) [6], von Neumann (1943) [7] and Döring (1943) [8] postulated independently that a detonation is a combustion wave being sustained by a shock wave.

## THE CHAPMAN-JOUGET POINTS

## Question 3.b

Differentiate the Rankine-Hugoniot relation (4) with respect to  $\rho_\infty$  to obtain:

$$\frac{1}{\rho_\infty} \left( \frac{\gamma}{\gamma-1} \right) \frac{dp_\infty}{d(1/\rho_\infty)} + \left( \frac{\gamma}{\gamma-1} \right) p_\infty - \frac{1}{2}(p_\infty - p_0) - \frac{1}{2} \frac{dp_\infty}{d(1/\rho_\infty)} \left( \frac{1}{\rho_\infty} + \frac{1}{\rho_0} \right) = 0 \quad (6)$$

and hence:

$$\frac{dp_\infty}{d(1/\rho_\infty)} = \frac{(p_\infty - p_0) - \left( \frac{2\gamma}{\gamma-1} \right) p_\infty}{\left( \frac{2\gamma}{\gamma-1} \right) \frac{1}{\rho_\infty} - \left( \frac{1}{\rho_\infty} + \frac{1}{\rho_0} \right)} \quad (7)$$

The slopes at the Chapman-Jouget points are:

$$\left. \frac{dp_\infty}{d(1/\rho_\infty)} \right|_{\text{CJ}} = \frac{p_\infty - p_0}{(1/\rho_\infty) - (1/\rho_0)} \quad (8)$$

From (7) and (8):

$$\frac{p_\infty - p_0}{(1/\rho_\infty) - (1/\rho_0)} = -\gamma \rho_\infty p_\infty - p_0 \quad (9)$$

The Rayleigh-line is tangent to the Hugoniot curve at the Chapman-Jouget points. From (9) and the Rayleigh-line relation (5):

$$v_\infty^2 = \frac{\gamma p_\infty}{(\rho_\infty)} = c_\infty^2 \quad \text{or} \quad |v_\infty| = c_\infty \quad (10)$$

Equation (10) implies that the Mach number behind the shock wave is unity ( $\text{Ma}_\infty = 1$ ) at the Chapman-Jouget points.

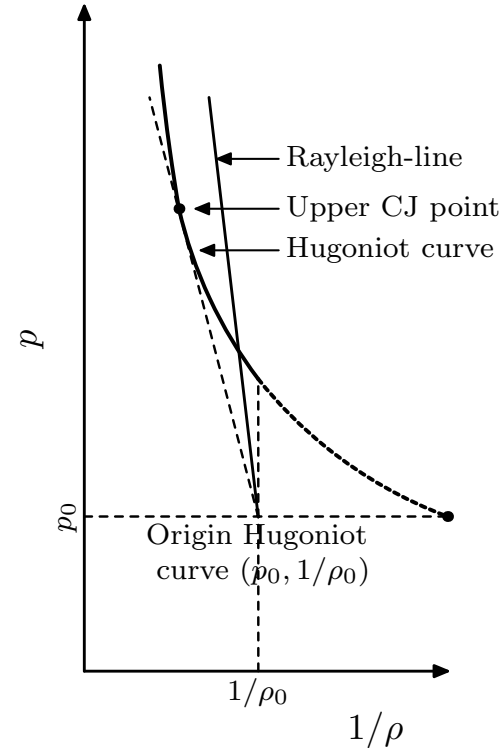


Figure 7: The upper Chapman-Jouget point and the tangency condition between the Rayleigh-line and the Hugoniot curve.

### Question 3.b

Experimentally observed conditions of pressure ( $p_\infty$ ), temperature ( $T_\infty$ ), and velocity ( $v_\infty$ ) at the upper Chapman-Jouget point. Initial conditions  $p_0 = 1$  bar and  $T_0 = 291$  K. After: Hirschfelder, Curtiss & Bird (1967) [9].

Explosive mixture	pressure $p_\infty$ (bar)	temperature $T_\infty$ (K)	velocity $v_\infty$ (m s <sup>-1</sup> )
(2 H <sub>2</sub> + O <sub>2</sub> )	18.1	3583	2819
(2 H <sub>2</sub> + O <sub>2</sub> ) + 5 O <sub>2</sub>	14.1	2620	1700
(2 H <sub>2</sub> + O <sub>2</sub> ) + 5 N <sub>2</sub>	14.4	2685	1822
(2 H <sub>2</sub> + O <sub>2</sub> ) + 4 H <sub>2</sub>	16.0	2976	3527
(2 H <sub>2</sub> + O <sub>2</sub> ) + 5 He	16.3	3097	3160
(2 H <sub>2</sub> + O <sub>2</sub> ) + 5 Ar	16.3	3097	1700

## ITERATIVE PROCEDURE FOR CALCULATING UPPER CHAPMAN-JOUGET CONDITIONS

### Question 3.b

A procedure for estimating the Chapman-Jouget velocity from the thermodynamic properties of the unreacted mixture may be derived as follows. The sonic velocity behind a detonation wave is:

$$c_{\infty} = \sqrt{\left[ \frac{\partial p_{\infty}}{\partial \rho_{\infty}} \right]_s} \quad (11)$$

Because  $u_{\infty} = c_{\infty}$  at the upper Chapman-Jouget point, the condition of mass conservation (1) across the shock wave and equation (11) lead to:

$$u_0 = \frac{1}{\rho_0} c_{\infty} \rho_{\infty} = \frac{1}{\rho_0} \sqrt{\rho_{\infty}^2 \left[ \frac{\partial p_{\infty}}{\partial \rho_{\infty}} \right]_s} = \frac{1}{\rho_0} \sqrt{- \left[ \frac{\partial p_{\infty}}{\partial (1/\rho_{\infty})} \right]_s} \quad (12)$$

Differentiation of the isentropic relation for the burned gas,

$$p_{\infty} \left( \frac{1}{\rho_{\infty}} \right)^{\gamma_{\infty}} = \text{constant} \quad \Rightarrow \quad - \left[ \frac{\partial p_{\infty}}{\partial (1/\rho_{\infty})} \right]_s = \frac{\gamma_{\infty} p_{\infty}}{1/\rho_{\infty}} \quad (13)$$

and substitution into equation (12) gives

$$\boxed{u_0 = p_{\infty} \frac{1/\rho_0}{1/\rho_{\infty}} \sqrt{\gamma_{\infty} p_{\infty} \frac{1}{\rho_{\infty}}} = \frac{\rho_{\infty}}{\rho_0} \sqrt{\gamma_{\infty} R_{\infty} T_{\infty}}} \quad \text{or} \quad \boxed{\rho_0^2 u_0^2 = \gamma_{\infty} p_{\infty} \rho_{\infty}} \quad (14)$$

after application of the ideal gas law.

## ITERATIVE PROCEDURE FOR CALCULATING UPPER CHAPMAN-JOUGET CONDITIONS

## Question 3.b

Derive an equivalent Rankine-Hugoniot relation by combining Kirckhoff's law with the ideal gas law,

$$\frac{p}{\rho} = \frac{\gamma - 1}{\gamma} \sum_{i=1}^N Y_i \left[ h_{f_i}^{\circ} + \int_{T^{\circ}}^T C_{P_i}(T) dT \right] \implies h = h^{\circ} + \left( \frac{\gamma}{\gamma - 1} \right) \frac{p}{\rho} \quad (15)$$

and substituting this into the conventional Rankine-Hugoniot relation (4):

$$h_{\infty} - h_0 = \frac{1}{2}(p_{\infty} - p_0) \left( \frac{1}{\rho_{\infty}} + \frac{1}{\rho_0} \right) \quad (16)$$

Because  $h = e + (p/\rho)$ ,

$$h_{\infty} - h_0 = (e_{\infty} - e_0)(p_{\infty} - p_0) \left( \frac{p_{\infty}}{\rho_{\infty}} + \frac{p_0}{\rho_0} \right) \quad (17)$$

so that (16) becomes

$$e_{\infty} - e_0 = \frac{1}{2}(p_{\infty} - p_0) \left( \frac{1}{\rho_{\infty}} + \frac{1}{\rho_0} \right) - \left( \frac{p_{\infty}}{\rho_{\infty}} + \frac{p_0}{\rho_0} \right) \quad (18)$$

$$\boxed{e_{\infty} - e_0 = \frac{1}{2}(p_{\infty} - p_0) \left( \frac{1}{\rho_0} - \frac{1}{\rho_{\infty}} \right)} \quad (19)$$

## ITERATIVE PROCEDURE FOR CALCULATING UPPER CHAPMAN-JOUGET CONDITIONS

Question 3.b

Substitute equation (14) into the Rayleigh-line relation (5):

$$\frac{1}{\rho_{\infty}} + \frac{1}{\rho_0} = -\frac{p_{\infty} - p_0}{\gamma_{\infty} p_{\infty} \rho_{\infty}} \quad (20)$$

and combine this result with equation (19) to obtain

$$e_{\infty} - e_0 = \frac{p_{\infty}^2 - p_0^2}{\gamma_{\infty} p_{\infty} \rho_{\infty}} \quad (21)$$

Multiply equation (20) by  $(p_{\infty} + p_0)$  to have

$$(p_{\infty} - p_0) \left( \frac{1}{\rho_{\infty}} + \frac{1}{\rho_0} \right) = \frac{(p_{\infty}^2 - p_0^2)}{\gamma_{\infty} p_{\infty} \rho_{\infty}} \quad (22)$$

**Equations (19), (21) and (22) form the design basis of an iterative procedure to determine the Chapman-Jouget velocity from the thermodynamic properties of the unreacted mixture.**

For a detonation wave  $p_{\infty} \gg p_0$  so that equations (21) and (22) may be rewritten into an approximate Rankine-Hugoniot relation (23) and an approximate Rayleigh-line relation (24):

$$e_{\infty} - e_0 \approx \frac{p_{\infty}^2 - p_0^2}{\gamma_{\infty} p_{\infty} \rho_{\infty}} = \frac{R_{\infty} T_{\infty}}{2\gamma_{\infty}} \quad (23)$$

$$\left( \frac{\rho_{\infty}}{\rho_0} \right)^2 \left( 1 + \frac{1}{\gamma_{\infty}} - \frac{R_0 T_0}{R_{\infty} T_{\infty}} \right) \left( \frac{\rho_{\infty}}{\rho_0} \right) - \frac{R_0 T_0}{R_{\infty} T_{\infty}} = 0 \quad (24)$$

## ITERATIVE PROCEDURE FOR CALCULATING UPPER CHAPMAN-JOUGET CONDITIONS

### Question 3.b

The iterative procedure to determine the Chapman-Jouget velocity from the thermodynamic properties of the unreacted mixture is as follows.

1. Assume  $p_\infty$ .
2. Assume  $T_\infty$ .
3. Calculate the equilibrium composition based on  $p_\infty$  and  $T_\infty$ .
4. From the equilibrium composition, determine  $\gamma_\infty$ ,  $R_\infty$  and  $e_\infty$ .
5. Verify whether  $\gamma_\infty$ ,  $R_\infty$  and  $e_\infty$  at the assumed temperature  $T_\infty$  satisfies the approximate Rankine-Hugoniot relation (23).
  - If equation (23) is satisfied, proceed to step 6.
  - If not, then reassume a new  $p_\infty$  and return to step 2.
6. Solve the approximate Rayleigh-line relation (24) for  $\rho_\infty/\rho_0$ .
7. Find  $p_\infty$  from the equation of state, e.g. the ideal gas law
$$p_\infty = \left(\frac{\rho_\infty}{\rho_0}\right) \left(\frac{R_\infty T_\infty}{R_0 T_0}\right) p_0 \quad (25)$$
  - If the calculated  $p_\infty$  equals the assumed  $p_\infty$ , the iteration sequence has completed. Proceed to step 8.
  - If not, then return to step 1 and assume a new  $p_\infty$ .
8. Calculate the Chapman-Jouget velocity,  $v_\infty$ , from equation (14).

# THE ZELDOVICH-VON NEUMANN-DÖRING THEORY OF DETONATION

## Question 3.b

The simplest model of the structure of a detonation wave (the ZND structure) consists of a shock wave coupled to a reaction zone. Zeldovich (1940), von Neumann (1943) and Döring (1943) were the first who postulated this view.

- The shock wave compresses and heats up the gas, which reacts after an induction period.
- The reaction triggers a volumetric expansion of the gas, which drives the shock wave.

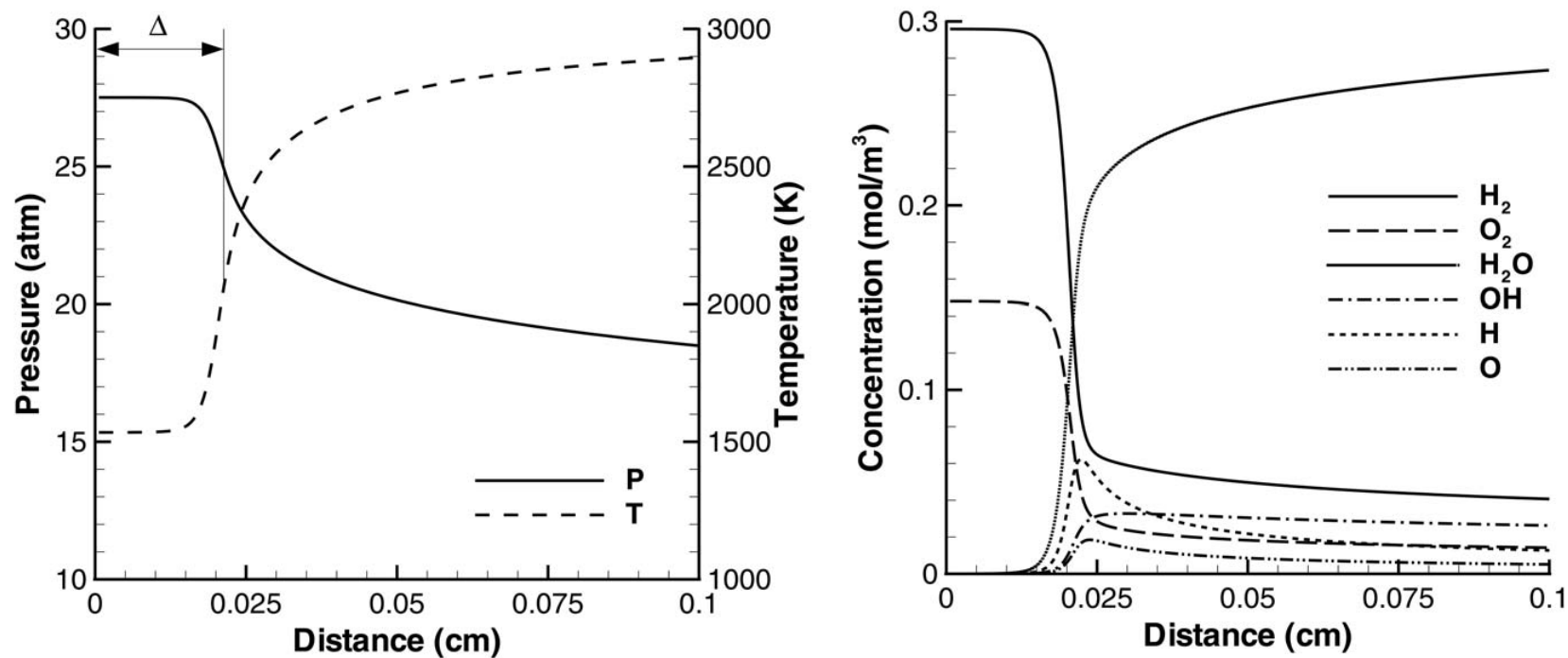


Figure 8: ZND profile of a detonation wave in stoichiometric hydrogen-air mixture ignited at 1 bar and 300 K.  $\Delta$  denotes the induction zone length.

## MULTI-DIMENSIONAL WAVE STRUCTURE

### Question 3.b

Detonation waves have a multidimensional structure.

- They consist of a leading shock waves, triple points, and transverse waves.
- The wave structure has a cellular pattern.
- The structure of a detonation wave is correlated with the induction length.
- The cellular structure left behind on sooted foils is a record of the triple point trajectory.
- Empirical correlations exist between cell width and induction length.

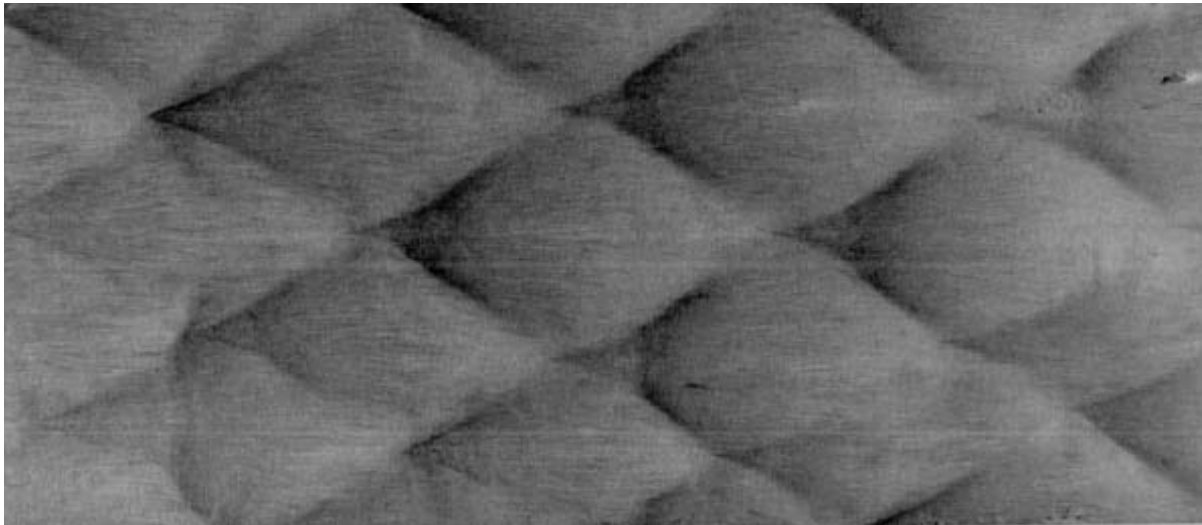


Figure 9: Cellular structure imprinted on a sooted foil record by the detonation of a  $2\text{H}_2 + \text{O}_2 + 17\text{Ar}$  mixture, ignited at 20 kPa and 295 K. After Austin (2003) [10].

# MULTI-DIMENSIONAL WAVE STRUCTURE

## Question 3.b

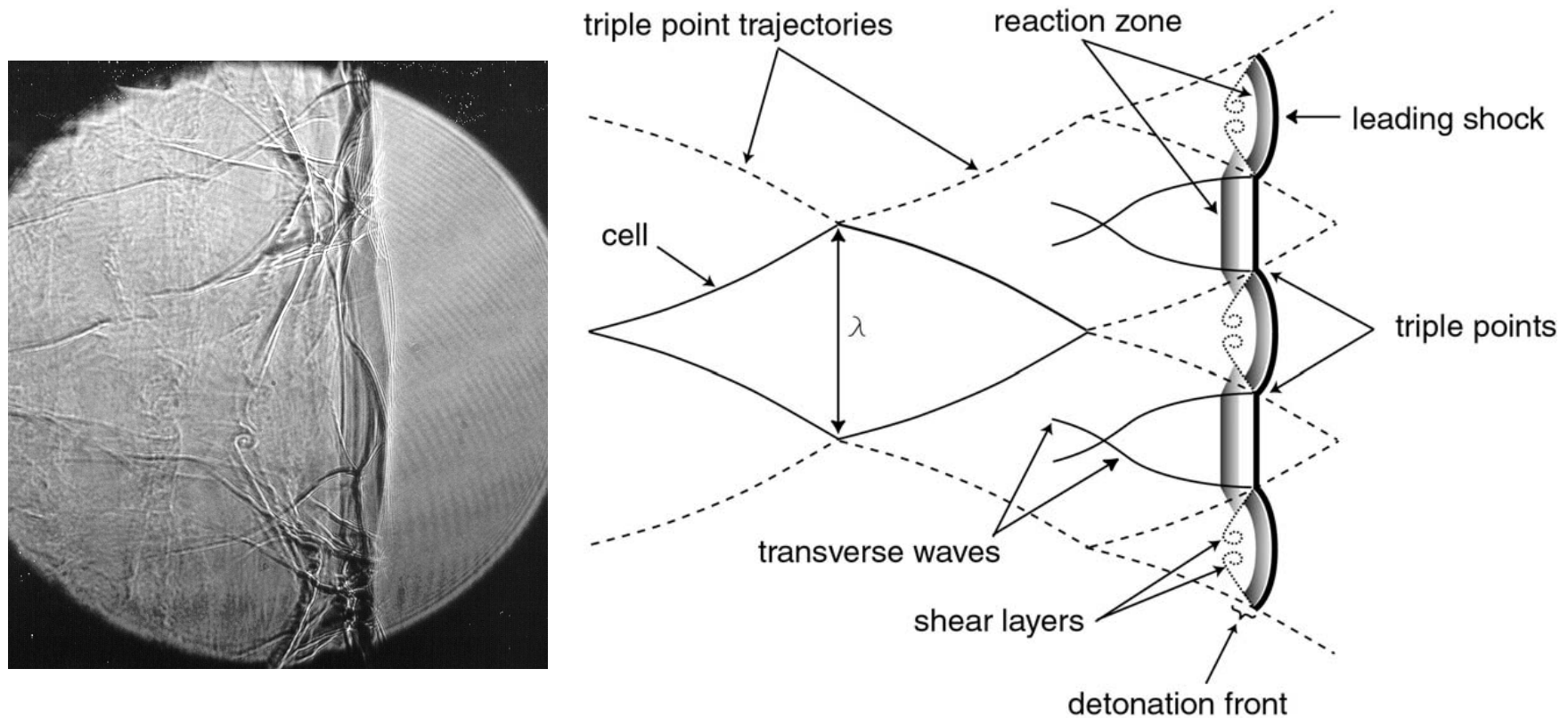


Figure 10: Left: Structure of a detonation wave in a  $2\text{H}_2 + \text{O}_2 + 20\text{Ar}$  mixture at 20 kPa and 295 K (after Akbar (1997) [11]). Right: Formation of the cellular structure on a sooted foil record by a detonation wave (after Winterberger & Shepherd (2004)).

## MULTI-DIMENSIONAL WAVE STRUCTURE

## Question 3.b

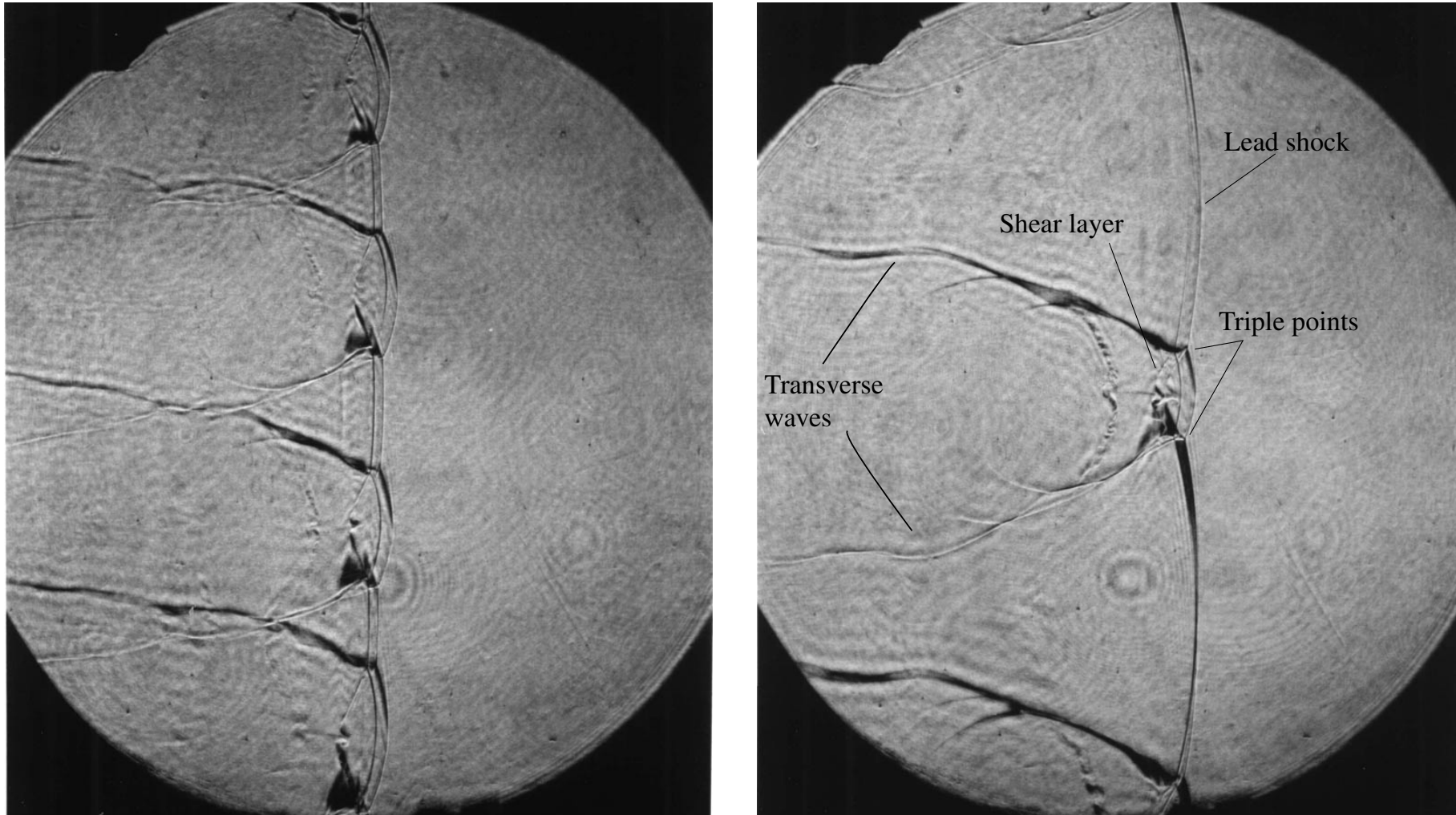


Figure 11: Schlieren images of (left) a  $2\text{H}_2\text{-O}_2\text{-12Ar}$  detonation,  $p_0=20$  kPa, and (right) a  $2\text{H}_2\text{-O}_2\text{-17Ar}$  detonation,  $p_0=20$  kPa (after Austin (2003) [10]).

# MULTI-DIMENSIONAL WAVE STRUCTURE

## Question 3.b

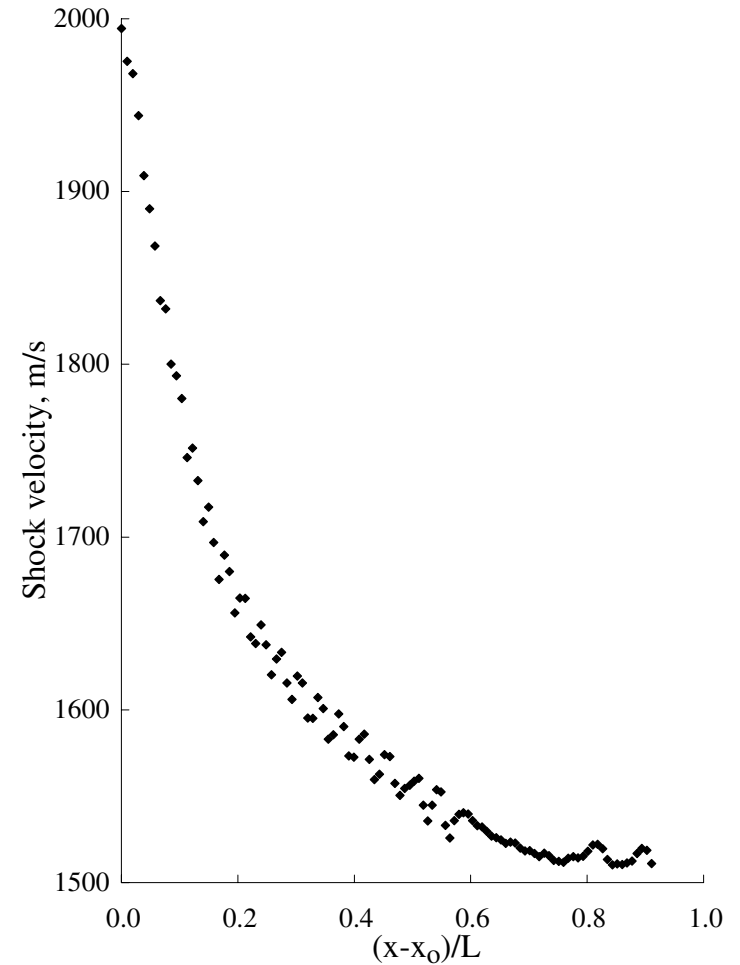
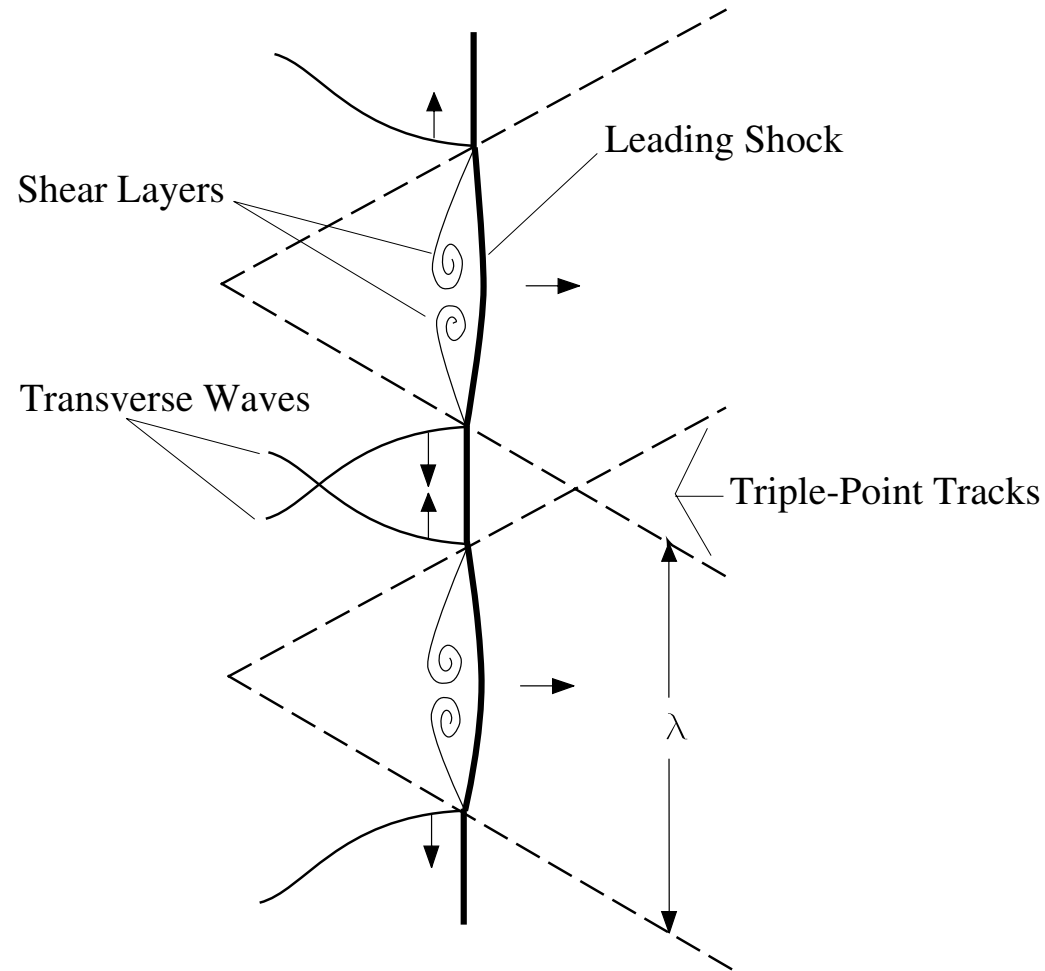


Figure 12: Morphology of a multi-dimensional detonation front propagating from left to right. After: Austin (2003) [10], Eckett(2000) [12], and Pintgen, Eckett, Austin & Shepherd (2003) [13].

## MULTI-DIMENSIONAL WAVE STRUCTURE

## Question 3.b

Morphology of a multi-dimensional detonation front:

- Triple points exist at the junction of the leading shock front and a transverse wave.
- The pattern observed on soot foils is a history of the triple point tracks in the propagating detonation front. Urtiew and Oppenheim (1966) [14] have shown that the tracks are closely related with the triple points on the detonation front.
- The precise physical mechanism by which the tracks are made in the soot layer is still unclear!
- The width of cells that appear on the foil are a measure of the spacing of the transverse waves in the detonation front. This global length scale, referred to as the detonation cell width,  $\lambda$ , can not in general be calculated a priori but may be related to the induction zone length,  $\Delta$ , by a constant of proportionality  $A$ . More specifically,

$$\lambda = A \Delta \quad (26)$$

- The constant  $A$  depends on the fuel-oxidiser-inert type (Westbrook (1982) [15]) and also varies with the equivalence ratio (Shepherd (1986) [16, 17]).
- The induction zone length can be empirically related to dynamic parameters such as the critical initiation energy (Lee (1984) [18]).

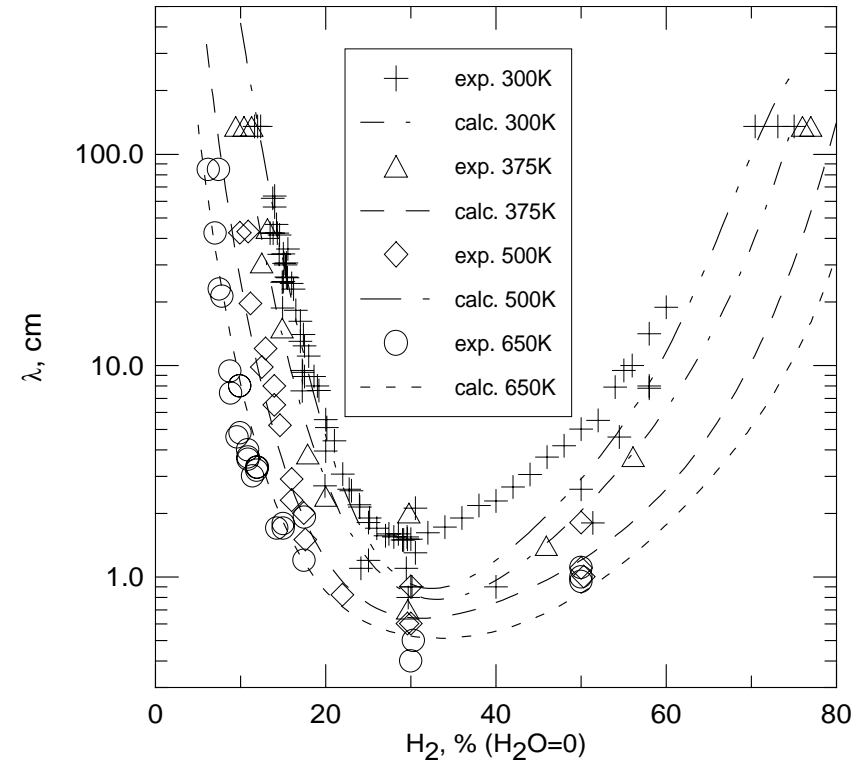
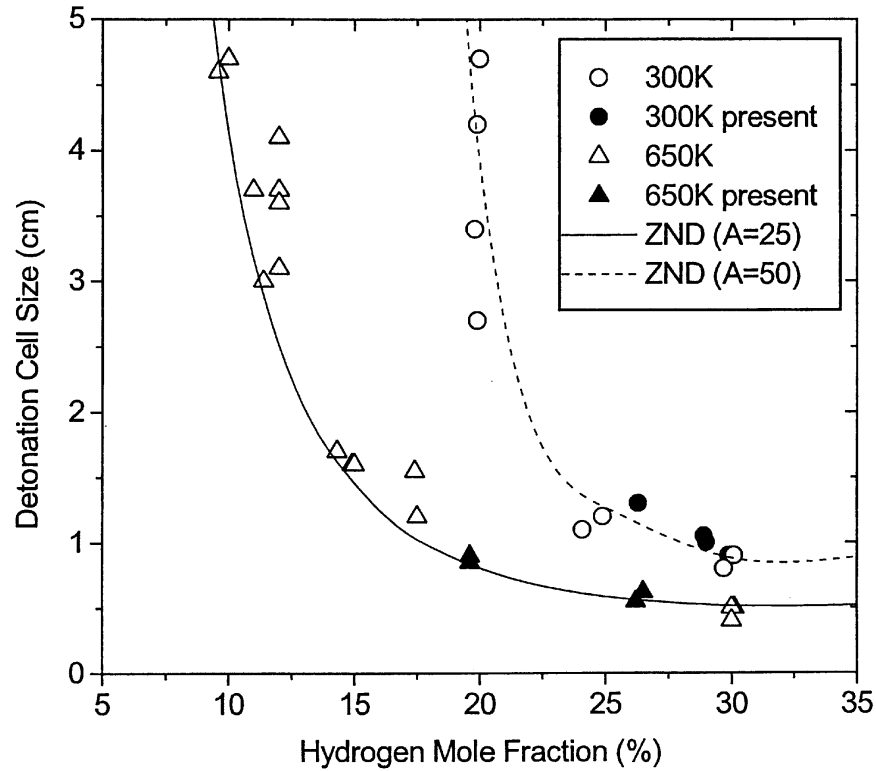


Figure 13: Detonation cell-size for hydrogen-air mixtures at different initial temperatures (after Breitung *et al.*(2000) [19]) and Ciccarelli (2002) [20]).

# DETONATION INITIATION ENERGY

## Question 3.b

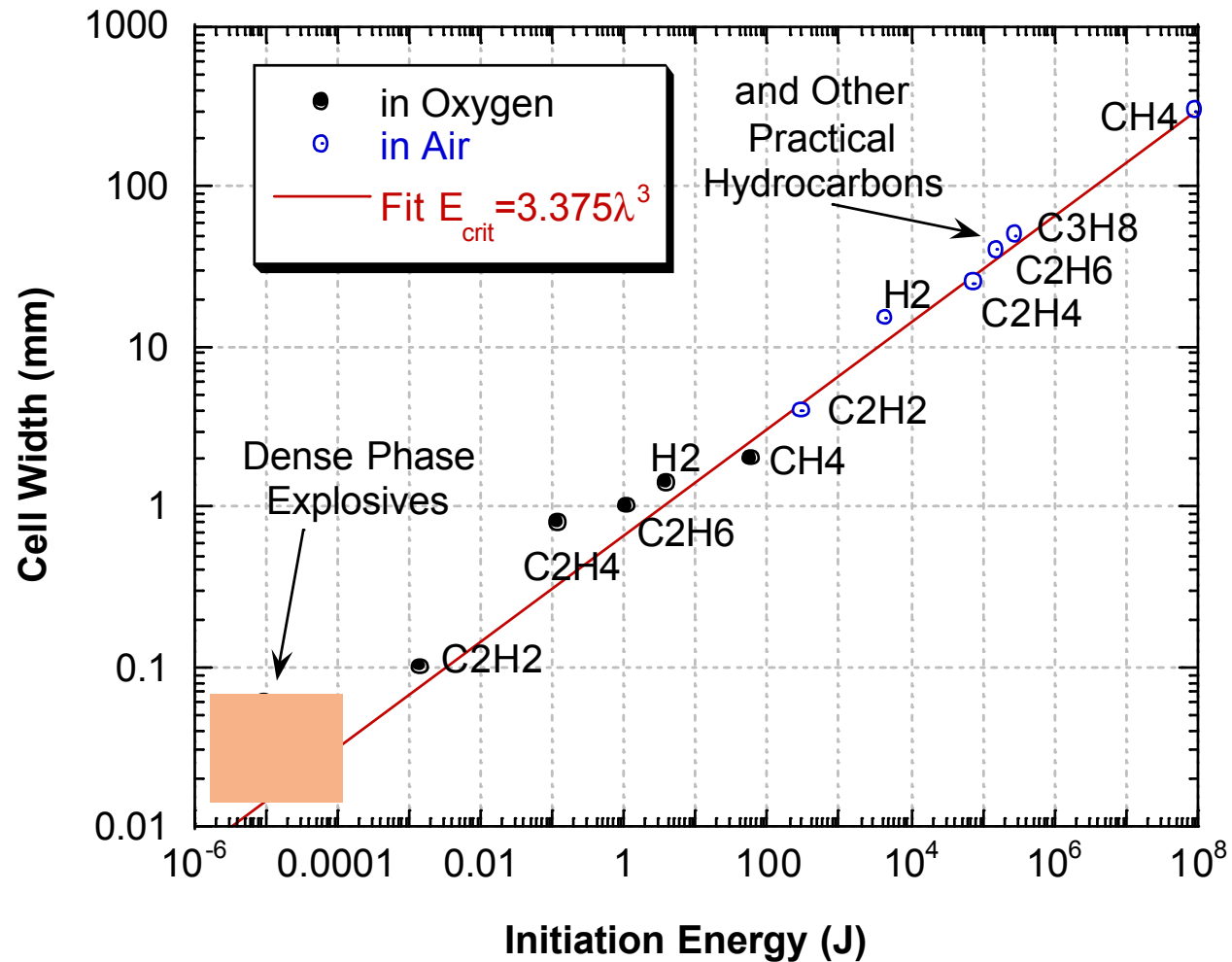


Figure 14: Detonation cell-size of different fuels (after Schauer *et al.* [21]).

## Question 3.g



Figure 16: Hemispherical balloon mock-up (10m radius) containing a 29.7 vol% hydrogen-air mixture.

From: Pfürtner H. and Schneider H. Ballonversuche zur Untersuchung der Deflagration von Wasserstoff Luft Gemischen (Abschlussbericht). PNP-Sicherheitssofortprogramm: Prozessgasfreisetzung - Explosion in der Gasfabrik und Auswirkungen von Druckwellen auf das Containment. ICT Internal Report, Fraunhofer Institut für Chemische Technologie, Pfinztal, Germany, 1983.

### Question 3.g



Figure 16: Hemispherical balloon mock-up (10m radius) containing a 29.7 vol% hydrogen-air mixture.

From: Pfürtner H. and Schneider H. Ballonversuche zur Untersuchung der Deflagration von Wasserstoff Luft Gemischen (Abschlussbericht). PNP-Sicherheitssofortprogramm: Prozessgasfreisetzung - Explosion in der Gasfabrik und Auswirkungen von Druckwellen auf das Containment. ICT Internal Report, Fraunhofer Institut für Chemische Technologie, Pfinztal, Germany, 1983.

## Question 3.g

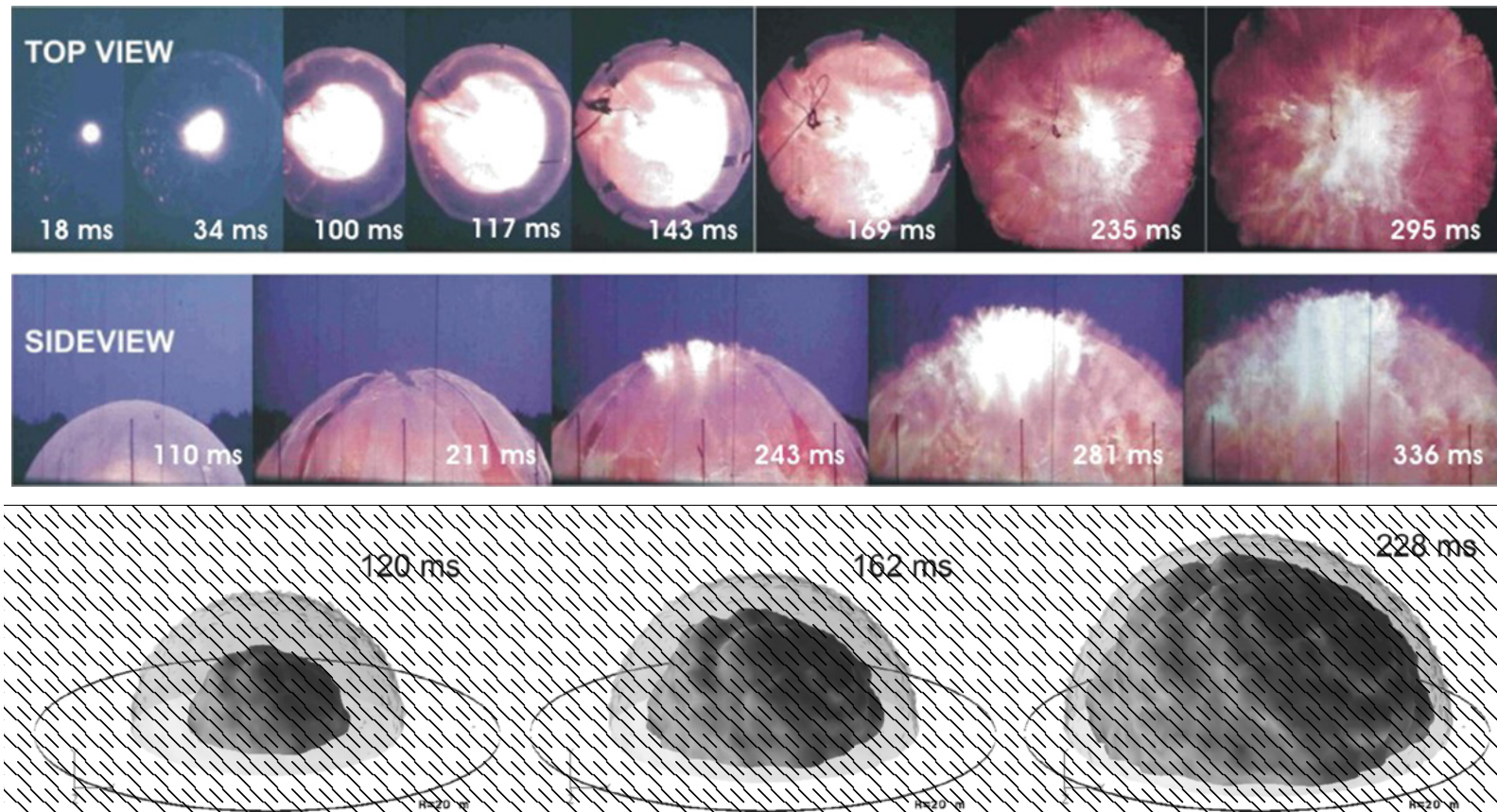


Figure 17: Snapshots of the propagating flame during an explosion of the 10m radius hemisphere filled with a 29.7 vol% hydrogen-air mixture.

From: Molkov V., Makarov D., and Schneider H. LES modelling of an unconfined large-scale hydrogen-air deflagration. *Journal of Physics D: Applied Physics*, 39:4366-4376, 2006.

## Question 3.g

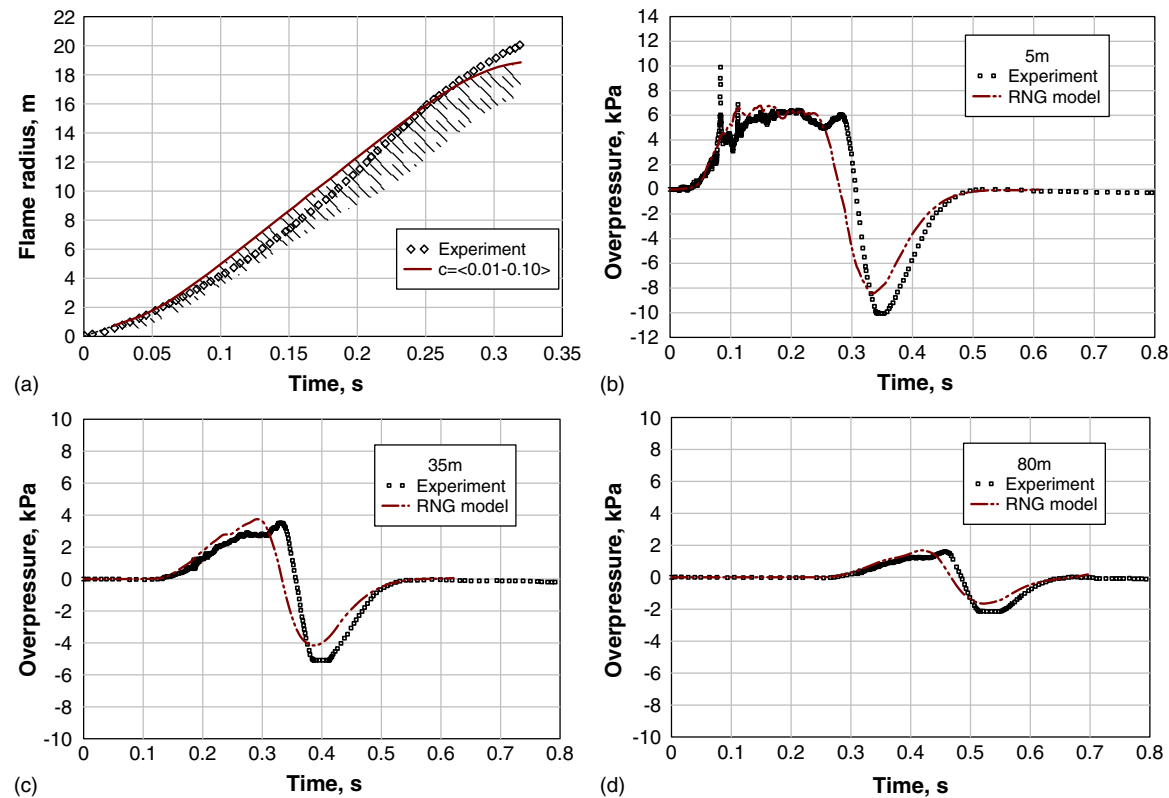


Figure 18: (a) Flame radius. (b) Over-pressure at 5 m from centre of explosion. (c) Over-pressure at 35 m from centre of explosion. (d) Over-pressure at 80 m from centre of explosion.

From: Molkov V., Makarov D., and Schneider H. LES modelling of an unconfined large-scale hydrogen-air deflagration. *Journal of Physics D: Applied Physics*, 39:4366-4376, 2006.

## Question 3.g

### THE QUESTION

For unconfined spherical deflagrations, [Dorofeev S.B. A flame speed correlation for unconfined gaseous explosions. Process Safety Progress, 26(2):140-149, 2007] provides a correlation of the form

$$S_f = C S_{uL}^{4/3} \chi^{-1/3} R_f^{1/3} \quad (27)$$

for the flame speed. Refer to [Dorofeev S.B. A flame speed correlation for unconfined gaseous explosions. Process Safety Progress, 26(2):140-149, 2007] for the meaning of the symbols in this expression. Use the data in Figure 18.a to determine the value of  $C$  and  $\chi$  in equation (27).

---

Since  $S_f$  is the time derivative of  $R_f$ , equation (27) can be rewritten as:

$$\frac{dR_f}{dt} = C S_{uL}^{4/3} \chi^{-1/3} R_f^{1/3} \quad (28)$$

which may be integrated to give:

$$\int_0^{R_f} \frac{dR_f}{R_f^{1/3}} = \int_0^t C S_{uL}^{4/3} \chi^{-1/3} dt \quad \Longleftrightarrow \quad \frac{3}{2} R_f^{2/3} \Big|_0^{R_f} = C S_{uL}^{4/3} \chi^{-1/3} t \Big|_0^t \quad (29)$$

$$\Rightarrow R_f = \left(\frac{2}{3}\right)^{3/2} C^{3/2} S_{uL}^2 \chi^{-1/2} t^{3/2} = \beta S_{uL}^2 t^{3/2} \quad \text{with} \quad \beta = \left(\frac{2}{3}\right)^{3/2} C^{3/2} \chi^{-1/2} \quad (30)$$

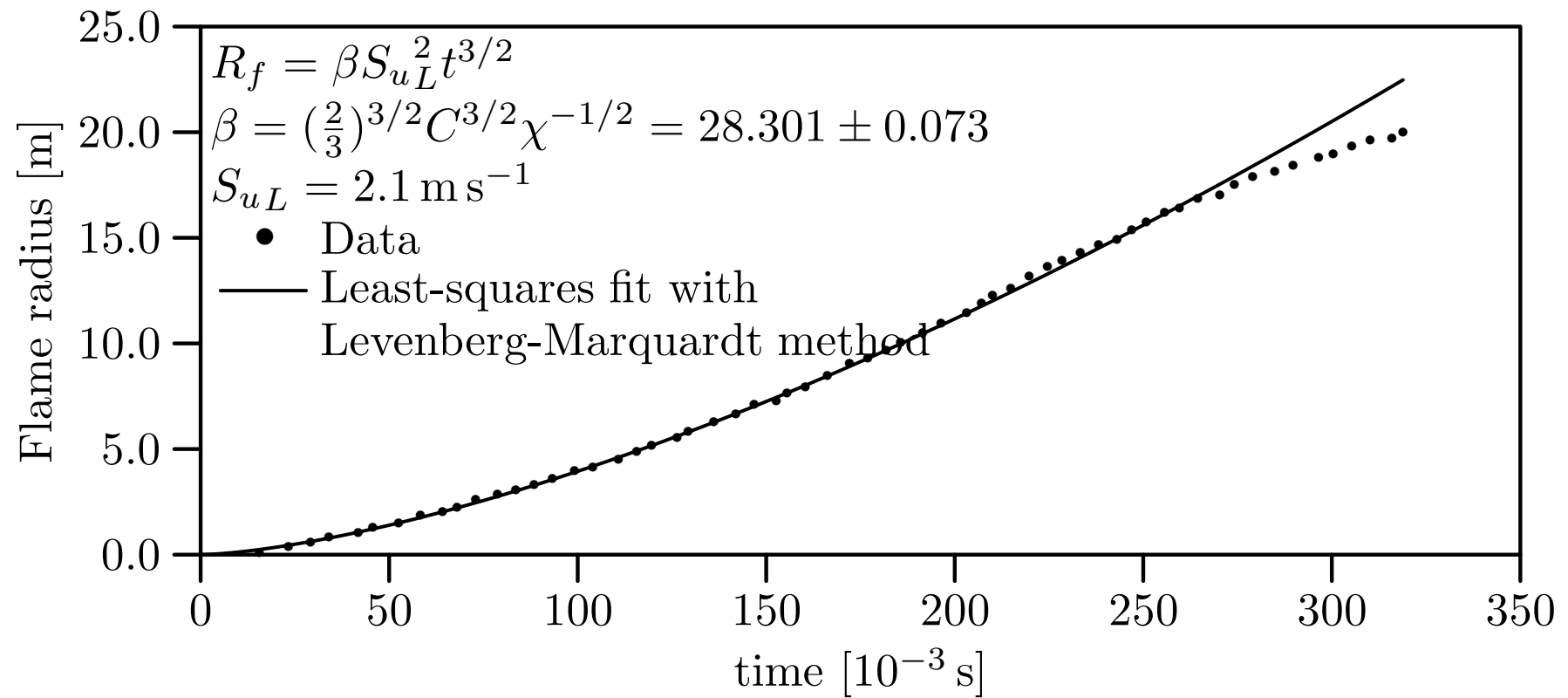
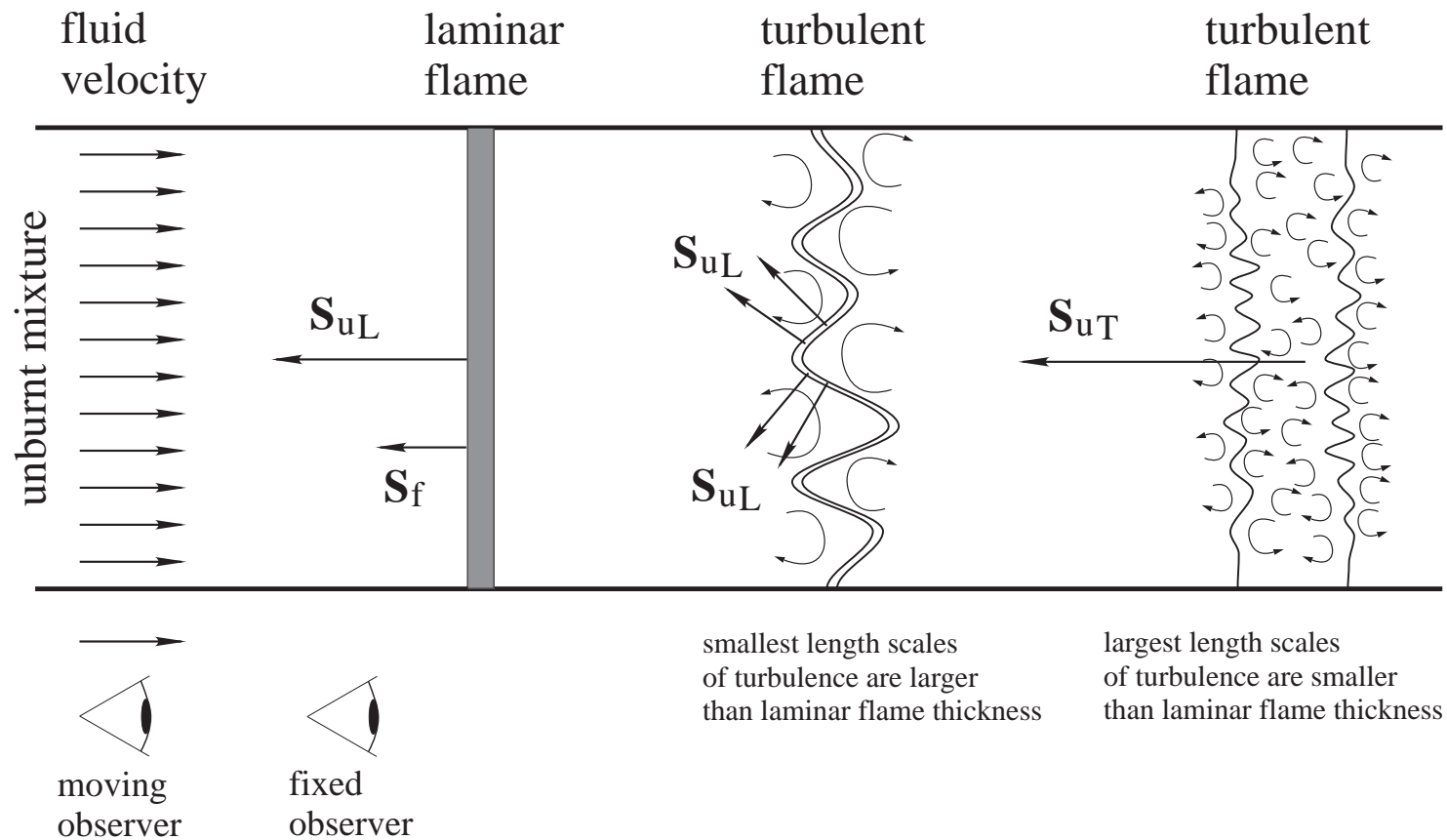


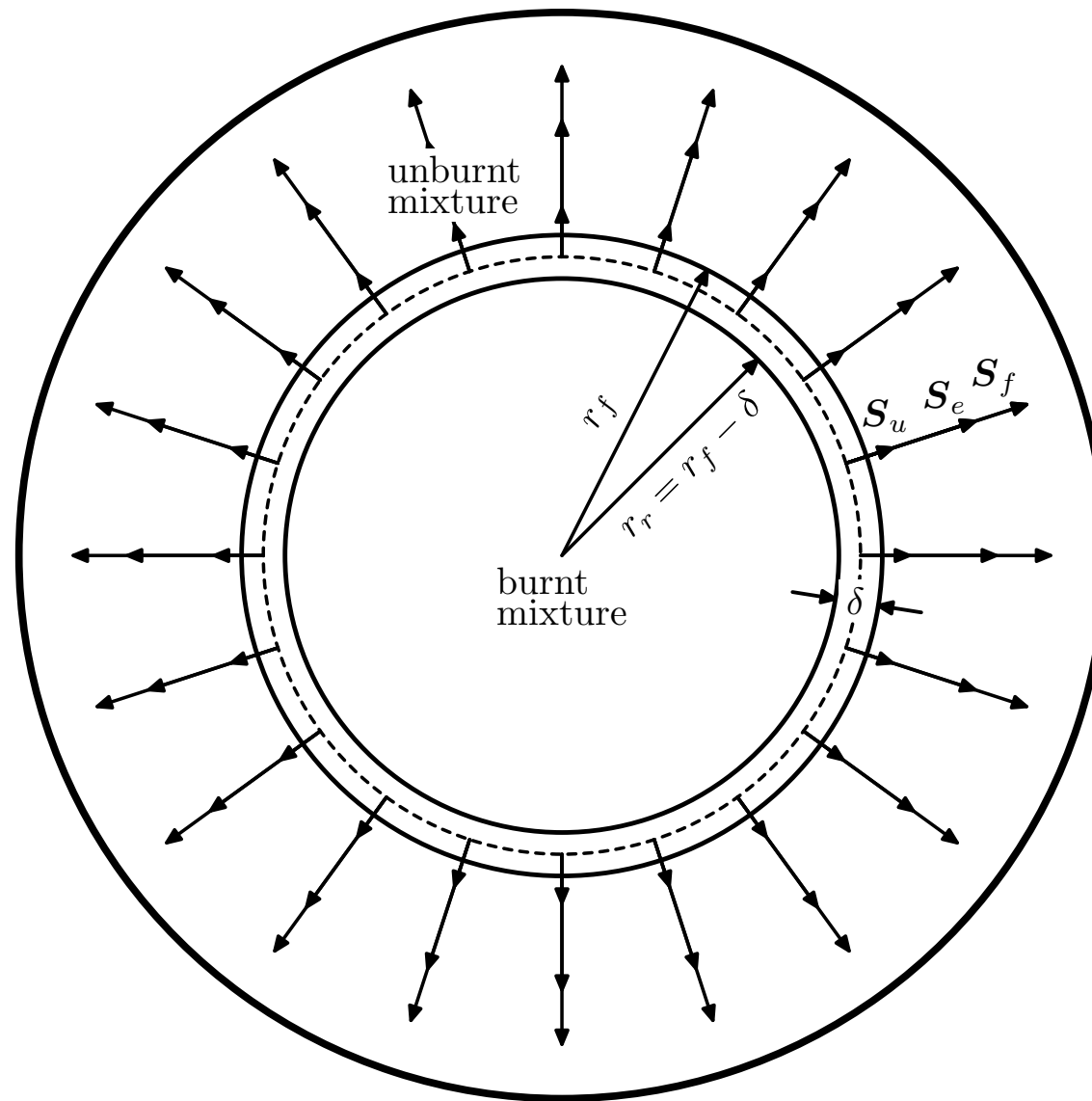
Figure 19: Flame radius as a function of time.

## Difference between flame speed and burning velocity



From: Dahoe A.E. Lecture Notes on Explosions. Delft University of Technology. 1997.

# Difference between flame speed and burning velocity



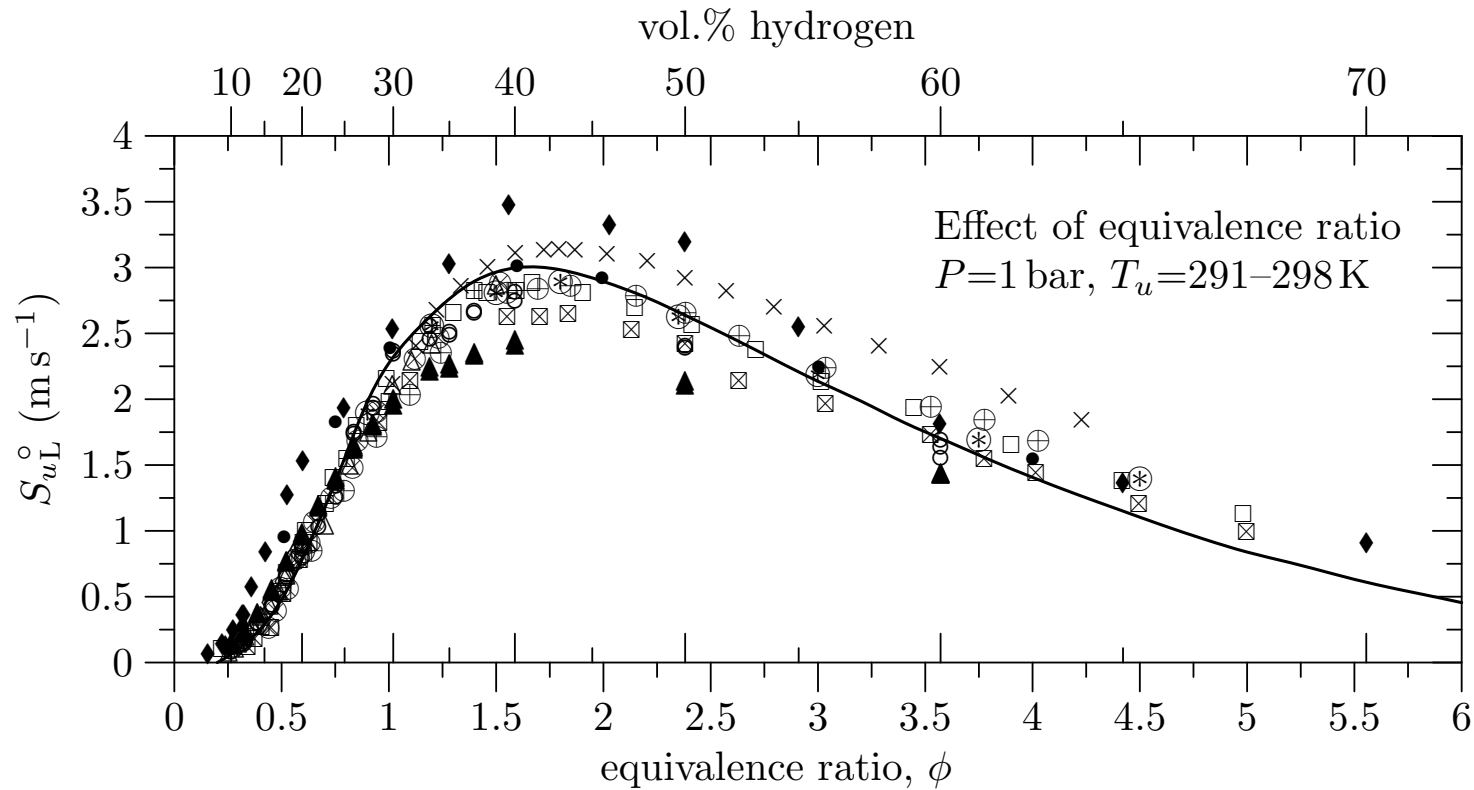


Figure 25: The laminar burning velocity of hydrogen-air mixtures as a function of equivalence ratio at  $T_0=293.15-298.15$  K and  $P_0=1$  bar.

From: Dahoe A.E. Laminar burning velocities of hydrogen-air mixtures from closed vessel gas explosions. *Journal of Loss Prevention in the Process Industries*, 18:152-166, 2005.

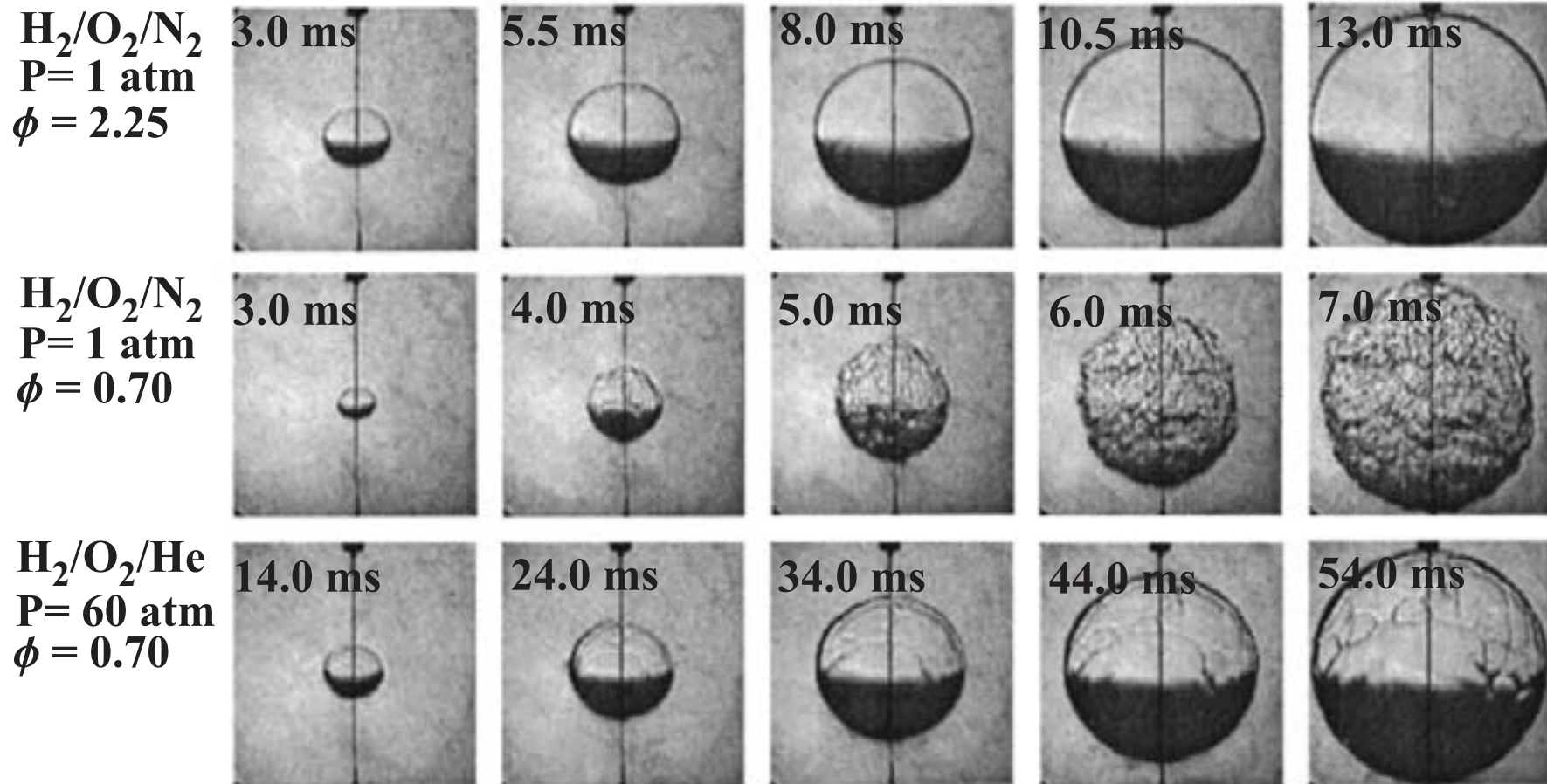


Figure 23: Flame morphology of propagating hydrogen-air flames.

From: Tse S.D., Zhu D.L., and Law C.K. Morphology and burning rates of expanding spherical flames in H<sub>2</sub>/O<sub>2</sub>/inert mixtures up to 60 atmospheres. In Proceedings of the Twenty-Eighth Symposium (International) on Combustion, pages 1793-1800, Pittsburgh, 2000. The Combustion Institute.

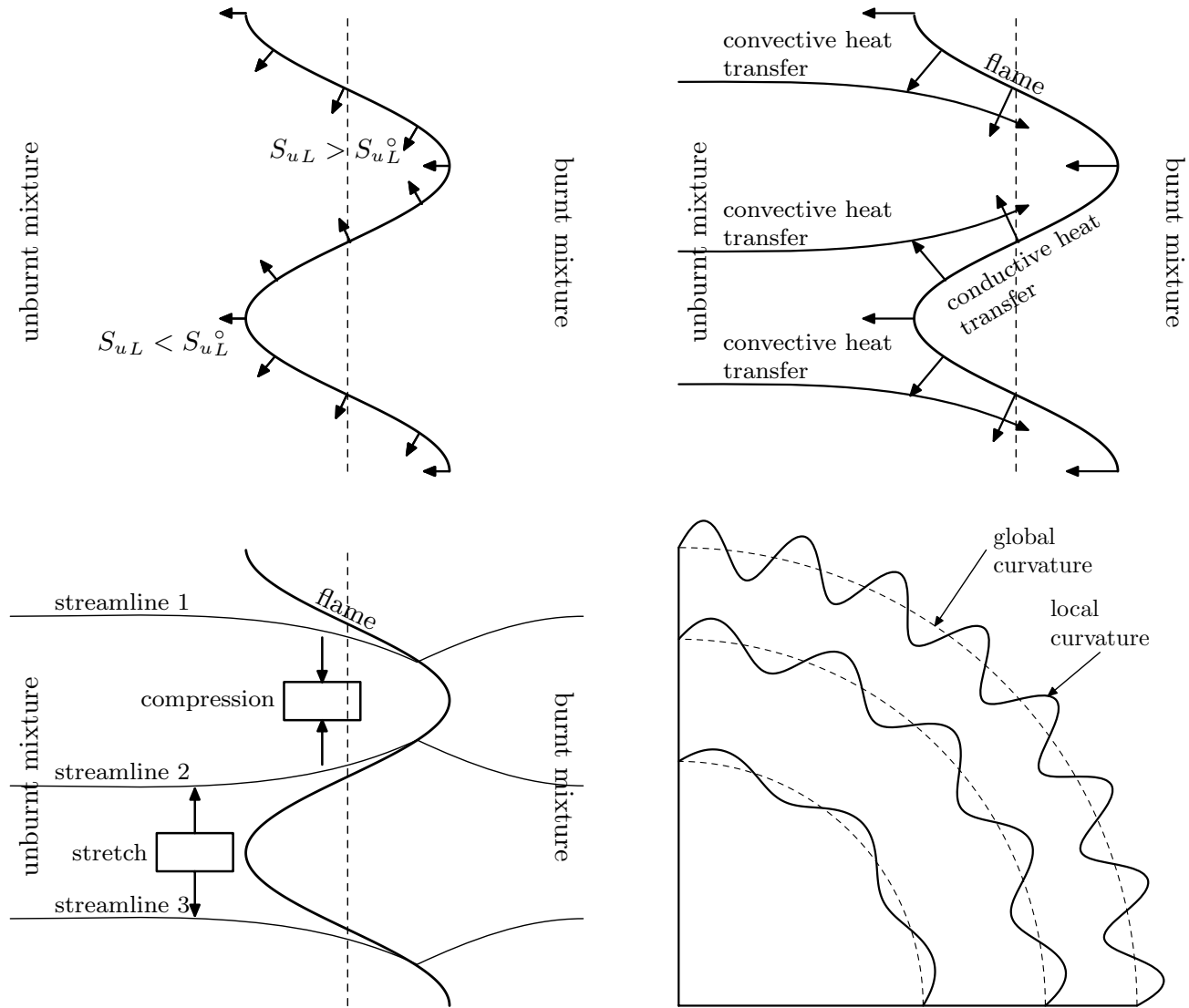


Figure 29: Effect of flame stretch and flame curvature on the laminar burning velocity.

Stretch rate of a surface element in a strained fluid:

$$\dot{s} = \frac{1}{A} \frac{dA}{dt} \quad (31)$$

Universal expression which relates the stretch rate of a flame surface element to the velocity field,  $\mathbf{v}$ , of a non-uniform flow-field:

$$\dot{s} = \underbrace{-\mathbf{nn}:\nabla\mathbf{v} + \nabla\cdot\mathbf{v}}_{\dot{s}_s} + \underbrace{S_{uL}^\circ\nabla\cdot\mathbf{n}}_{\dot{s}_c} \quad (32)$$

When a planar laminar flame with a thickness  $\delta_L^\circ$  is distorted into a bulge of size  $\Lambda$ , the local laminar burning velocity at each point can be related to the local stretch rate as

$$\frac{S_{uL}^\circ - S_{uL}}{S_{uL}^\circ} = \frac{\mathcal{L}}{S_{uL}^\circ} \left( \frac{1}{A} \frac{dA}{dt} \right) + \mathcal{O}(\epsilon^2) \quad (33)$$

where  $\epsilon = \delta_L^\circ/\Lambda$ . When  $\Lambda \gg \delta_L^\circ$ ,  $\epsilon$  is a small number so that:

$$S_{uL}^\circ - S_{uL} = \mathcal{L} \left( \frac{1}{A} \frac{dA}{dt} \right) + \mathcal{O}(\epsilon^2) \quad (34)$$

$$= \mathcal{L}\dot{s} + \mathcal{O}(\epsilon^2) \quad (35)$$

Express  $\mathcal{L}\dot{s}$  as a linear combination of quantities that account for the separate effects of the strain rate, flame curvature, pressure, etc., each having its own Markstein length:

$$\mathcal{L}\dot{s} \equiv \mathcal{L}_s\dot{s}_s + \mathcal{L}_c\dot{s}_c + \dots \quad (36)$$

$$\implies S_{uL}^\circ - S_{uL} = (\mathcal{L}_s\dot{s}_s + \mathcal{L}_c\dot{s}_c + \dots) + \mathcal{O}(\epsilon^2) \quad (37)$$

Combine equations (32), (35) and (37):

$$S_{uL} = \mathcal{L}_s [\mathbf{nn}:\nabla\mathbf{v} - \nabla \cdot \mathbf{v}] + [1 - \mathcal{L}_c\nabla \cdot \mathbf{n}] S_{uL}^\circ \quad (38)$$

$$= \mathcal{L}_s [\mathbf{nn}:\nabla\mathbf{v} - \nabla \cdot \mathbf{v}] + \left[ 1 + \frac{\mathcal{L}_c}{\kappa_1 + \kappa_2} \right] S_{uL}^\circ \quad (39)$$

$$= \mathcal{L}_s [\mathbf{nn}:\nabla\mathbf{v} - \nabla \cdot \mathbf{v}] + \left[ 1 + \frac{\mathcal{L}_c}{\mathcal{R}} \right] S_{uL}^\circ \quad (40)$$

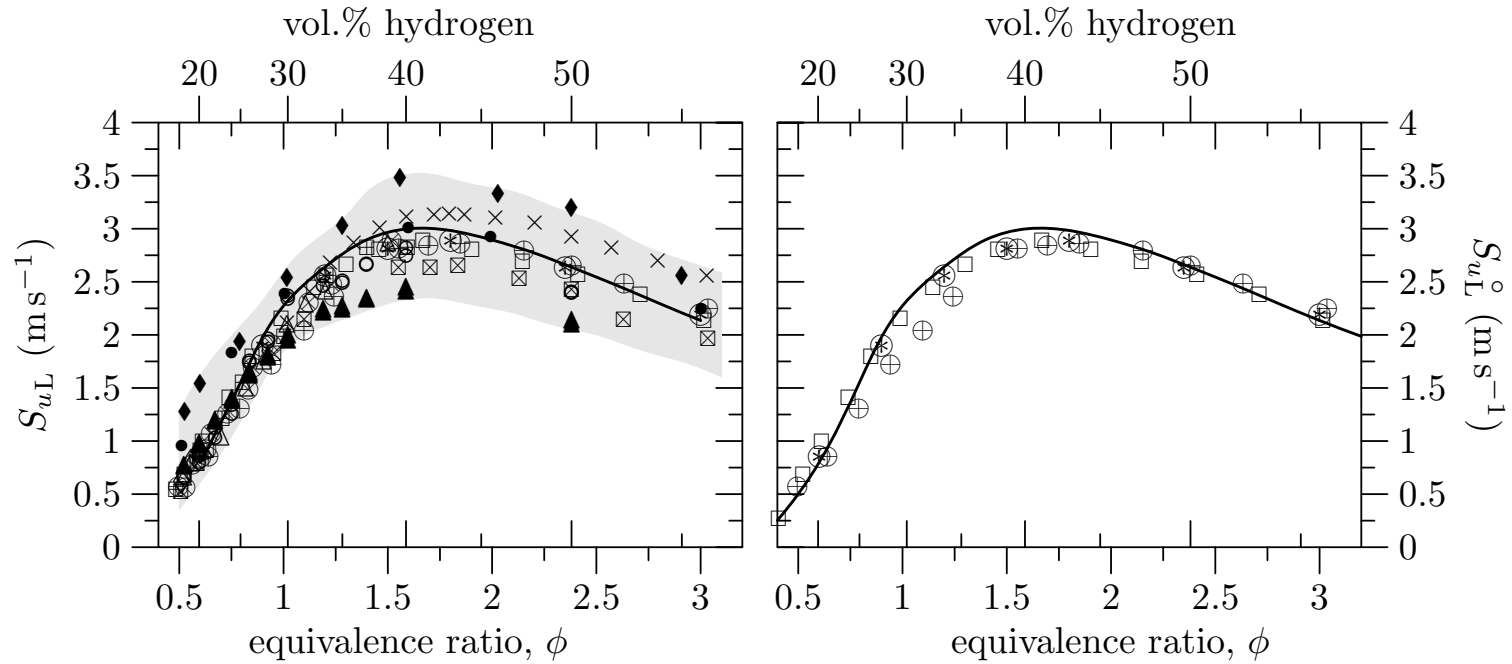


Figure 25: The unstretched laminar burning velocity of hydrogen-air mixtures as a function of equivalence ratio at  $T_0=293.15\text{--}298.15\text{ K}$  and  $P_0=1\text{ bar}$ .

From: Dahoe A.E. Laminar burning velocities of hydrogen-air mixtures from closed vessel gas explosions. *Journal of Loss Prevention in the Process Industries*, 18:152-166, 2005.

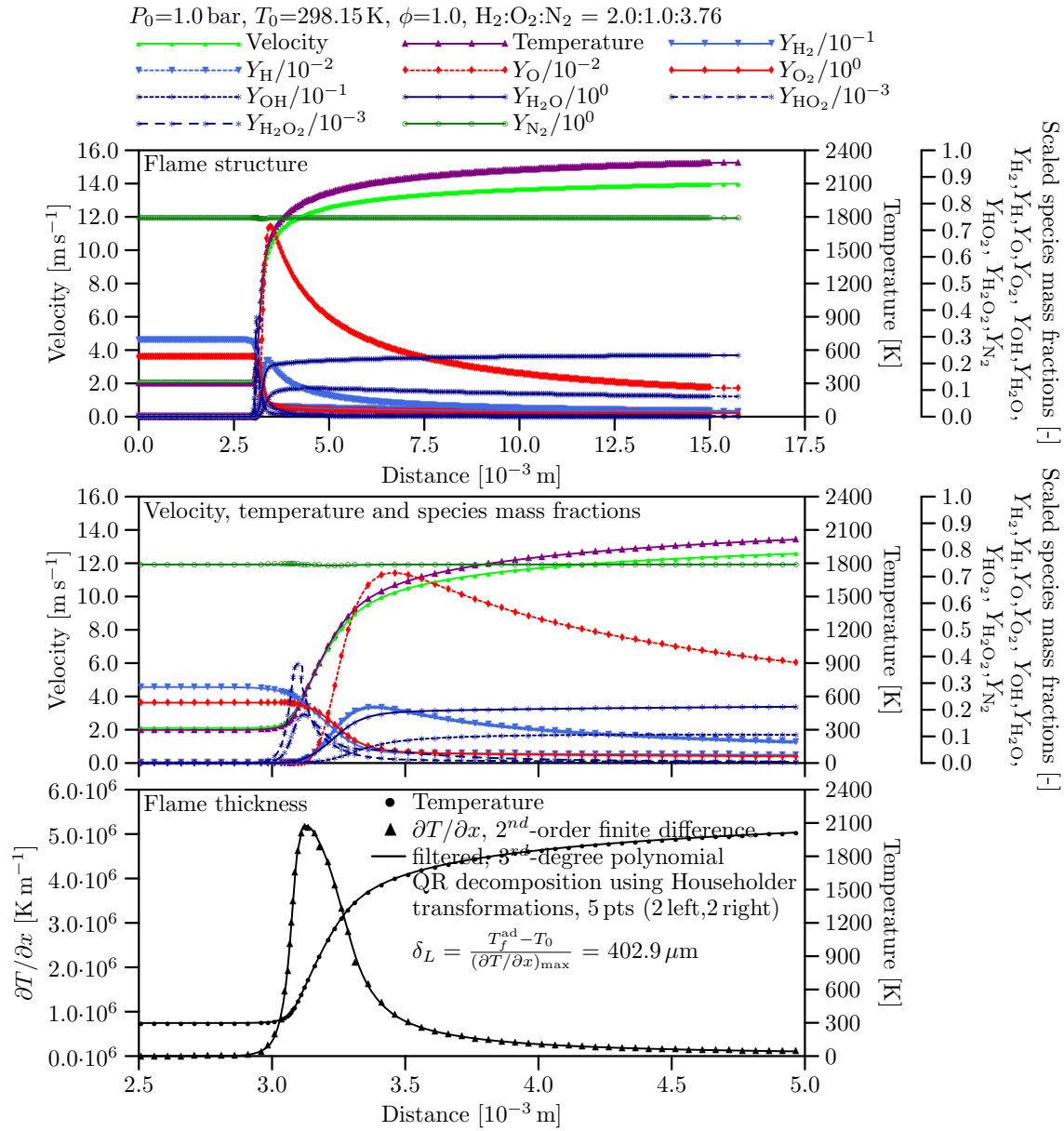


Figure 26: Numerically resolved flame structure by solving governing equations with a detailed kinetic scheme.

Reaction mechanism due to [Miller J.A., Mitchell R.E., Smooke M.D., and Kee R.J. Toward a comprehensive chemical kinetic mechanism for the oxidation of acetylene: comparison of model predictions with results from flame and shock tube experiments. In Proceedings of the Nineteenth Symposium (International) on Combustion, pages 181–196, Pittsburgh, 1982. The Combustion Institute] for the hydrogen-air reaction. The reaction rate coefficients are in the form  $k_f = AT^\beta \exp(-E_a/RT)$ . Units are in moles, cubic centimeters, seconds, Kelvins and calories.

	Reaction	A	$\beta$	$E_a$
1	$\text{H}_2 + \text{O}_2 \rightleftharpoons 2\text{OH}$	$1.70 \cdot 10^{13}$	0.0	47780.
2	$\text{OH} + \text{H}_2 \rightleftharpoons \text{H}_2\text{O} + \text{H}$	$1.17 \cdot 10^9$	1.3	3626.
3	$\text{H} + \text{O}_2 \rightleftharpoons \text{OH} + \text{O}$	$5.13 \cdot 10^{16}$	-0.816	16507.
4	$\text{O} + \text{H}_2 \rightleftharpoons \text{OH} + \text{H}$	$1.80 \cdot 10^{10}$	1.0	8826.
5	$\text{H} + \text{O}_2 + \text{M} \rightleftharpoons \text{HO}_2 + \text{M}^a$	$2.10 \cdot 10^{18}$	-1.0	0.
6	$\text{H} + \text{O}_2 + \text{O}_2 \rightleftharpoons \text{HO}_2 + \text{O}_2$	$6.70 \cdot 10^{19}$	-1.42	0.
7	$\text{H} + \text{O}_2 + \text{N}_2 \rightleftharpoons \text{HO}_2 + \text{N}_2$	$6.70 \cdot 10^{19}$	-1.42	0.
8	$\text{OH} + \text{HO}_2 \rightleftharpoons \text{H}_2\text{O} + \text{O}_2$	$5.00 \cdot 10^{13}$	0.0	1000.
9	$\text{H} + \text{HO}_2 \rightleftharpoons 2\text{OH}$	$2.50 \cdot 10^{14}$	0.0	1900.
10	$\text{O} + \text{HO}_2 \rightleftharpoons \text{O}_2 + \text{OH}$	$4.80 \cdot 10^{13}$	0.0	1000.
11	$2\text{OH} \rightleftharpoons \text{O} + \text{H}_2\text{O}$	$6.00 \cdot 10^8$	1.3	0.
12	$\text{H}_2 + \text{M} \rightleftharpoons \text{H} + \text{H} + \text{M}^b$	$2.23 \cdot 10^{12}$	0.5	92600.
13	$\text{O}_2 + \text{M} \rightleftharpoons \text{O} + \text{O} + \text{M}$	$1.85 \cdot 10^{11}$	0.5	95560.
14	$\text{H} + \text{OH} + \text{M} \rightleftharpoons \text{H}_2\text{O} + \text{M}^c$	$7.50 \cdot 10^{23}$	-2.6	0.
15	$\text{H} + \text{HO}_2 \rightleftharpoons \text{H}_2 + \text{O}_2$	$2.50 \cdot 10^{13}$	0.0	700.
16	$\text{HO}_2 + \text{HO}_2 \rightleftharpoons \text{H}_2\text{O}_2 + \text{O}_2$	$2.00 \cdot 10^{12}$	0.0	0.
17	$\text{H}_2\text{O}_2 + \text{M} \rightleftharpoons \text{OH} + \text{OH} + \text{M}$	$1.30 \cdot 10^{17}$	0.0	45500.
18	$\text{H}_2\text{O}_2 + \text{H} \rightleftharpoons \text{HO}_2 + \text{H}_2$	$1.60 \cdot 10^{12}$	0.0	3800.
19	$\text{H}_2\text{O}_2 + \text{OH} \rightleftharpoons \text{H}_2\text{O} + \text{HO}_2$	$1.00 \cdot 10^{13}$	0.0	1800.

<sup>a</sup> Third body efficiencies:  $k_5(\text{H}_2\text{O}) = 21 k_5(\text{Ar})$ ,  $k_5(\text{H}_2) = 3.3 k_5(\text{Ar})$ .

<sup>b</sup> Third body efficiencies:  $k_{12}(\text{H}_2\text{O}) = 6 k_{12}(\text{Ar})$ ,  $k_{12}(\text{H}) = 2 k_{12}(\text{Ar})$ ,  $k_{12}(\text{H}_2) = 3 k_{12}(\text{Ar})$ .

<sup>c</sup> Third body efficiency:  $k_{14}(\text{H}_2\text{O}) = 20 k_{14}(\text{Ar})$ .

## Governing equations compressible reacting flow:

$$\frac{\partial \rho}{\partial t} + \nabla \cdot (\rho \mathbf{v}) = 0 \quad (41)$$

$$\frac{\partial (\rho \mathbf{v})}{\partial t} + \nabla \cdot (\rho \mathbf{v} \mathbf{v}) = -\nabla p + \nabla \cdot \boldsymbol{\tau} + \sum_{i=1}^N \rho Y_i \mathbf{f}_i \quad (42)$$

$$\frac{\partial (\rho Y_i)}{\partial t} + \nabla \cdot (\rho \mathbf{v} Y_i) = -\nabla \cdot [\rho Y_i \mathbf{V}_i] + \dot{w}_i \quad (43)$$

$$\begin{aligned} \frac{\partial (\rho h)}{\partial t} + \nabla \cdot (\rho \mathbf{v} h) &= \frac{\partial p}{\partial t} + \mathbf{v} \cdot \nabla p + \boldsymbol{\tau} : \nabla \mathbf{v} - \nabla \cdot [\lambda \nabla T] + \nabla \cdot \mathbf{q} \\ &+ \nabla \cdot \left[ \sum_{i=1}^N \rho Y_i h_i \mathbf{V}_i + RT \sum_{i=1}^N \sum_{j=1}^N \left( \frac{X_j \alpha_i}{\mathcal{M}_i \mathcal{D}_{ij}} \right) (\mathbf{V}_i - \mathbf{V}_j) \right] + \sum_{i=1}^N \rho Y_i \mathbf{f}_i \cdot \mathbf{V}_i \end{aligned} \quad (44)$$

$$\frac{p}{\rho} = \frac{\gamma - 1}{\gamma} \sum_{i=1}^N Y_i \left[ h_{f_i}^\circ + \int_{T^\circ}^T C_{P_i}(T) dT \right] \quad (45)$$

where  $\boldsymbol{\tau} = \mu \left[ \nabla \mathbf{v} + (\nabla \mathbf{v})^\dagger \right] + \left( \kappa - \frac{2}{3} \mu \right) [\nabla \cdot \mathbf{v}] \mathbf{I}$  (46)

and  $\mathbf{q} = \epsilon \sigma T^4$  (47)

**THE QUESTION**

Compute the overpressure of the vapour cloud explosion of the hemispherical hydrogen-air cloud in Figure 16 at stand-off distances of 35m and 80m. Use equation (27) with the values for  $C$  and  $\chi$  obtained under g) for the flame speed. Apply the methodology given by [Tang M.J. and Baker Q.A. A new set of blast curves from vapor cloud explosion. Process Safety Progress, 18:235-240, 1999] to calculate the overpressure at stand-off distances of 35m and 80m. Compare your flame trajectory and overpressure with the data given in Figure 18.

- The methodology by [Tang M.J. and Baker Q.A. A new set of blast curves from vapor cloud explosion. Process Safety Progress, 18:235-240, 1999] rests on the so-called Sach scaling law.
- The Sach scaling law states that the pressure and impulse generated by an explosion can be rescaled in such a manner that they become unique functions of a appropriately rescaled distance from the origin of the explosion.
- These unique functions form a set of blast curves when the scaled pressure  $\bar{p}$  and the scaled specific impulse  $\bar{i}$  are expressed as a function of an energy-scaled distance,  $\bar{R}$ . These scalings are as follows:

$$\bar{p} = \frac{p - p_0}{p_0} (\text{scaled pressure}), \quad \bar{i} = \frac{ic_0}{E^{1/3} p_0^{2/3}} (\text{scaled impulse}), \quad \bar{R} = \frac{Rp_0^{1/3}}{E^{1/3}} (\text{scaled distance}) \quad (48)$$

- For each value of the flame Mach number,  $Ma_f$ , there exists a unique curve.

Question 3.h

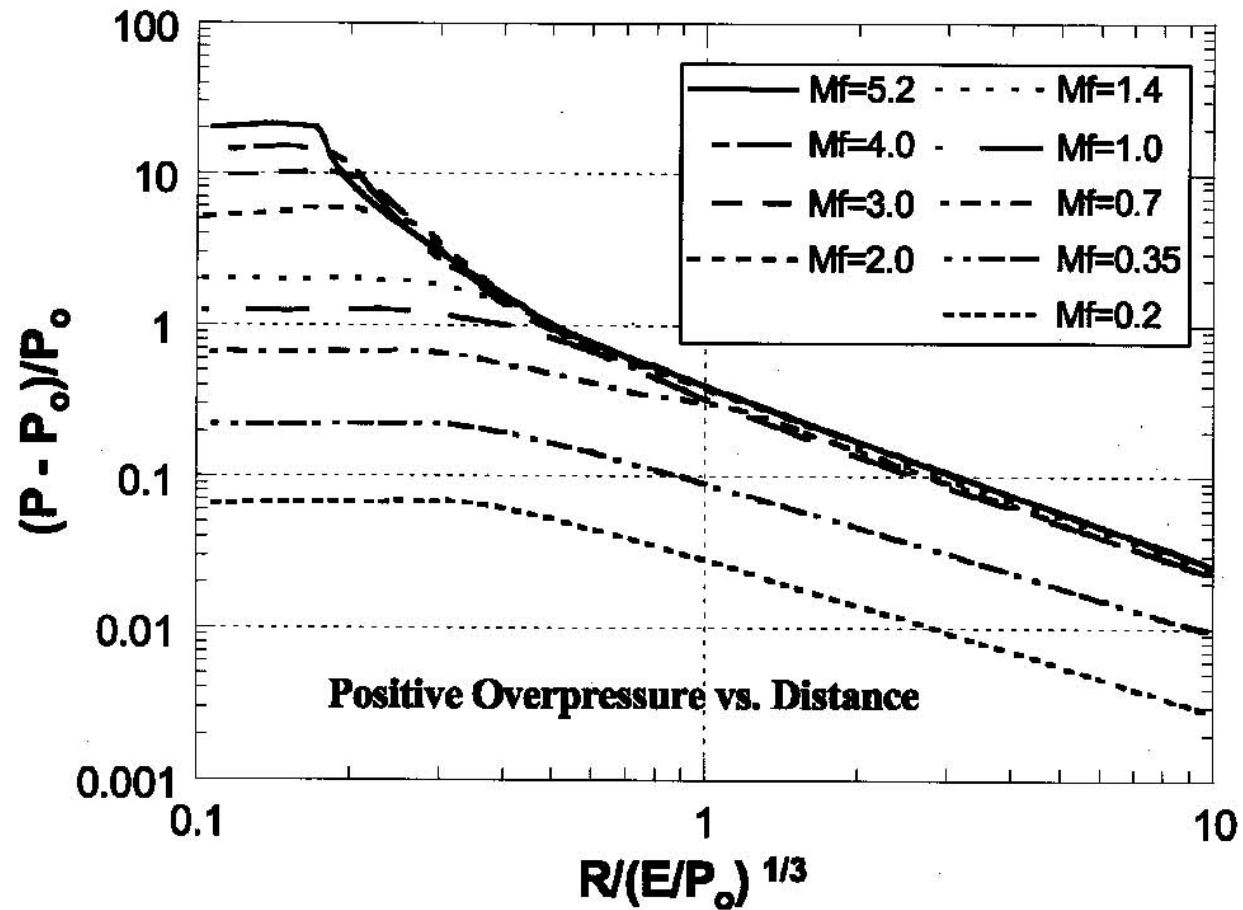


Figure 27: Blast curves for the scaling of explosions.

From: Tang M.J. and Baker Q.A. A new set of blast curves from vapor cloud explosion. Process Safety Progress, 18:235-240, 1999.

### Calculation of the flame Mach number

In Question 3.g) we determined the constants  $C$  and  $\chi$  by integrating equation (27)

$$R_f = \left(\frac{2}{3}\right)^{3/2} C^{3/2} S_{uL}^2 \chi^{-1/2} t^{3/2} = \beta S_{uL}^2 t^{3/2} \quad \text{with} \quad \beta = \left(\frac{2}{3}\right)^{3/2} C^{3/2} \chi^{-1/2} \quad (49)$$

and we found that  $\beta=28.301$  when  $S_{uL} = 2.1 \text{ m s}^{-1}$ .

To find the flame Mach number, equation (50) can be differentiated to give

$$S_f = \frac{dR_f}{dt} = \beta S_{uL}^2 t^{3/2} = \frac{3}{2} \beta S_{uL}^2 t^{1/2} \quad (50)$$

From Figure 19 it is seen that the flame speed attains its maximum value at  $t = 0.32 \text{ s}$  so that equation (50) gives  $S_f=105.9 \text{ m s}^{-1}$ . With the sonic velocity of the ambient air being  $c=343.2 \text{ m s}^{-1}$ , the flame Mach number becomes  $\text{Ma}_f = S_f/c = 0.31$ .

### Calculation of the energy scaled stand-off distance

To calculate the energy scaled stand-off distance we need to know (i) how much energy is released by the combustion of hydrogen, and, (ii) how much hydrogen is contained by the combustible gas cloud.

The combustion energy released by hydrogen is  $140 \text{ MJ kg}^{-1}$ .

The volume of the combustible cloud is  $\frac{4}{3}\pi R^3=4188.8 \text{ m}^3$  with 29.7% of it being hydrogen; that amounts

to 1244.07 m<sup>3</sup> hydrogen and hence 102.1 kg of hydrogen. So the total energy release is  $E=14294$  MJ.

According to equation (48) the energy scaled distance becomes

$$\bar{R} = \frac{Rp_0^{1/3}}{E^{1/3}} = 0.67 \quad (R=35 \text{ m}) \quad \text{and} \quad \bar{R} = \frac{Rp_0^{1/3}}{E^{1/3}} = 1.53 \quad (R=80 \text{ m}) \quad (51)$$

### **Application of the blast curve to predict over-pressures**

Then, from Figure 27, using the curve  $Ma_f = 0.35$  it is seen that

$$\bar{p} = \frac{p - p_0}{p_0} = 0.102 \quad (R=35 \text{ m}) \quad \text{and} \quad \bar{p} = \frac{p - p_0}{p_0} = 0.02 \quad (R=80 \text{ m}) \quad (52)$$

Hence,  $p= 0.102$  bar = 10.2 kPa at  $R= 35$  m and  $p= 0.02$  bar = 2 kPa at  $R= 35$  m. A comparison with the experimental and simulated over-pressures in Figure 18 shows that the blast curve over-predicts by a factor  $> 2$  at  $R= 35$  m. At  $R= 80$  m the blast curve prediction is in agreement with the experimental and simulated over-pressures.

**THE QUESTION**

Explain how the pressure profiles in Figure 5 can be used to assess the potential of an explosion to cause mechanical damage.

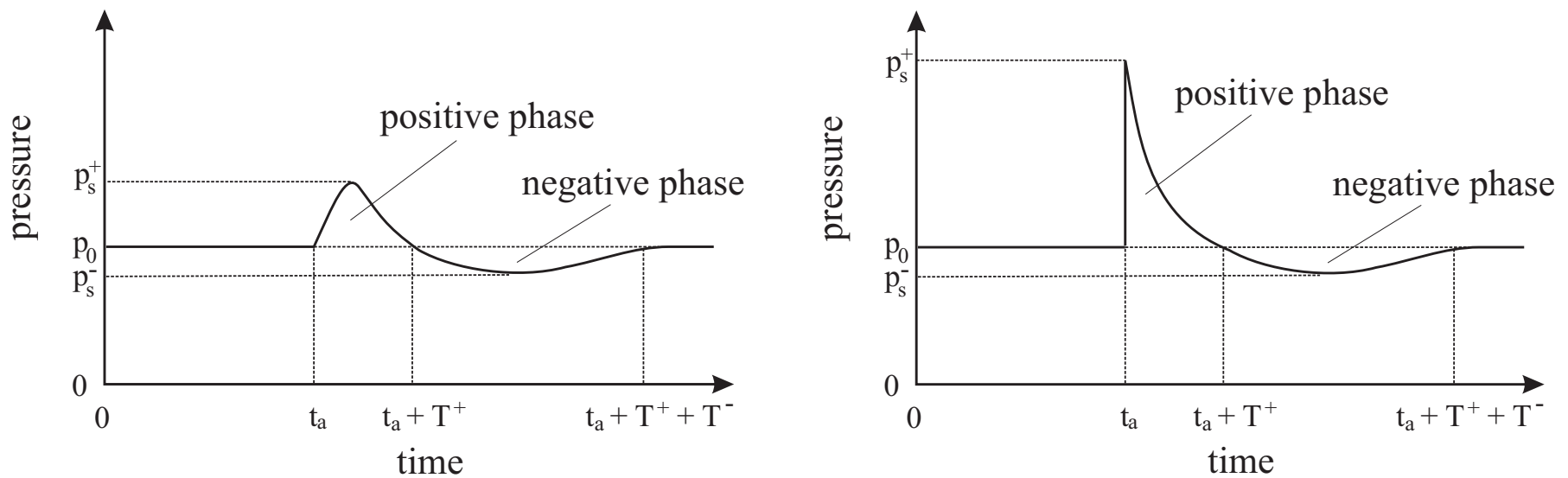


Figure 28: Blast wave structure. Left: pressure-time trace when the flame speed is less than the sonic velocity of the ambient air. Right: pressure-time trace when the flame speed is equal to or greater than the sonic velocity of the ambient air.

### Question 3.i

Blast wave properties are expressed in terms of (i) the blast wave amplitude, (ii) the blast wave duration, and, (iii) the blast wave specific impulse. These quantities are illustrated by Figure 28. Prior to wave front arrival, the pressure is equal to the ambient pressure,  $p_0$ . At arrival time  $t_a$ , the pressure rises rapidly (when the flame speed is equal to or greater than the sonic velocity of the ambient air then this pressure rise is a discontinuity) to a peak value equal to  $p_s^+ + p_0$  (i.e. the sum of the side on pressure and the ambient pressure). After this the pressure drops back to the ambient pressure in a time span equal to  $T^+$  (the positive phase duration), followed by a partial vacuum whose amplitude equals  $p_s^-$  and which lasts for a period  $T^-$  (the negative phase duration) until the pressure resumes the ambient value again. The potential of a blast wave to cause mechanical damage is usually expressed in terms of the amplitude of the positive phase,  $p_s^+$ , the amplitude of the negative phase,  $p_s^-$ , and the specific impulse (that is the total impulse per unit area). For the latter purpose, positive and negative specific impulses are defined as

$$i_s^+ = \int_{t_a}^{t_a+T^+} [p(t) - p_0] dt \quad (\text{positive impulse}) \quad (53)$$

$$i_s^- = \int_{t_a+T^+}^{t_a+T^++T^-} [p(t) - p_0] dt \quad (\text{negative impulse}) \quad (54)$$

### Question 3.j

Pressure amplitudes and specific impulses can be used in conjunction with Pressure-Impulse (P-I) diagrams, or in probit functions to estimate the degree of damage to structures. Peak values of overpressure can be translated in to levels of structural damage: e.g. light damage < 3.5 kpa, moderate damage > 17 kpa, severe damage > 35 kpa, total destruction > 83 kpa, etc.

There are also correlations to assess potential damage using pressure amplitudes and specific impulses. For example:

$$(p_s^+ - p_{\text{crit}})(i_s^+ - i_{\text{crit}}) \geq k \quad (55)$$

where  $p_{\text{crit}}$ ,  $i_{\text{crit}}$  and  $k$  are parameters characterising the type of damage (see Table 1).

Table 1: Parameters for damage criteria to be used in equation 55. From: Dorofeev S.B. A flame speed correlation for unconfined gaseous explosions. Process Safety Progress, 26(2):140-149, 2007.

Damage description	$p_{\text{crit}}$ (Pa)	$i_{\text{crit}}$ (Pa s)	$k$ (Pa <sup>2</sup> s)
Total destruction of buildings	70100	770	866100
Threshold for partial destruction 50-75% of walls destroyed	34500	520	541000
Threshold for serious structural damage; some load bearing members fall	14600	300	119200
Border of minor structural damage	3600	100	8950

### Question 3.i

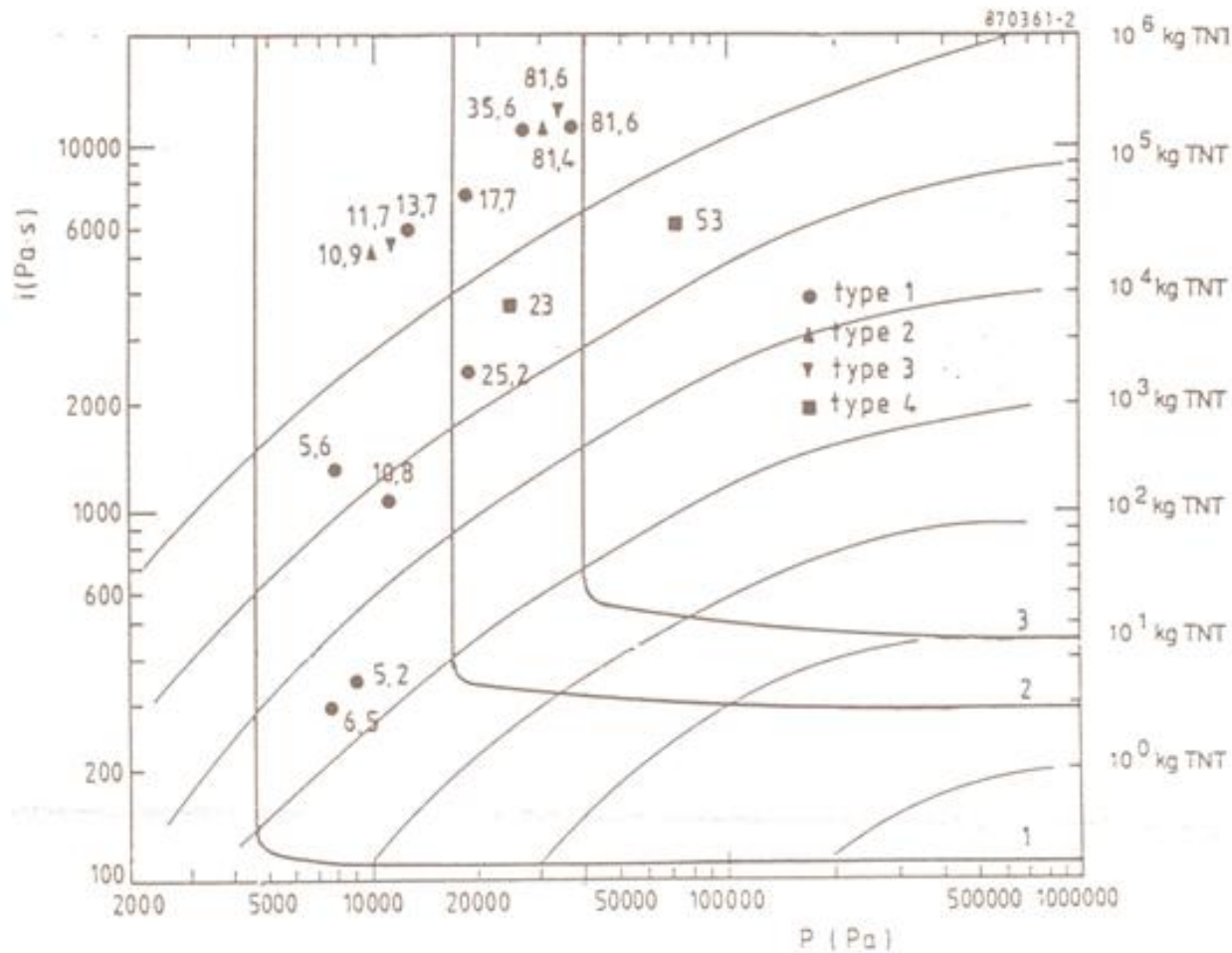


Figure 29: Pressure-impulse diagram. From: Baker W.E., Cox P.A., Westine P.S., Kulesz J.J., and Strehlow R.A. Explosion Hazards and Evaluation, volume 5 of Fundamental studies in engineering. Elsevier Scientific Publishing Company, New York, 1983.

## Question 3.j

### THE QUESTION

Refer to [Ngo T., Mendis P., Gupta A., and Ramsay J. Blast loading and blast effects on structures - An overview. *Electronic Journal of Structural Engineering*, 7:76-91, 2007. Special Issue: Loading on Structures]. Explain the Single Degree of Freedom (SDOF) model and describe how it is applied to assess the response of a structure to a blast load. In your answer, address the idealisation of the waveform, the equation of motion for the SDOF, the inclusion of the structural mass and resistance in the equation of motion, and how the solution of this equation of motion can be used to assess structural response to blast waves.

---

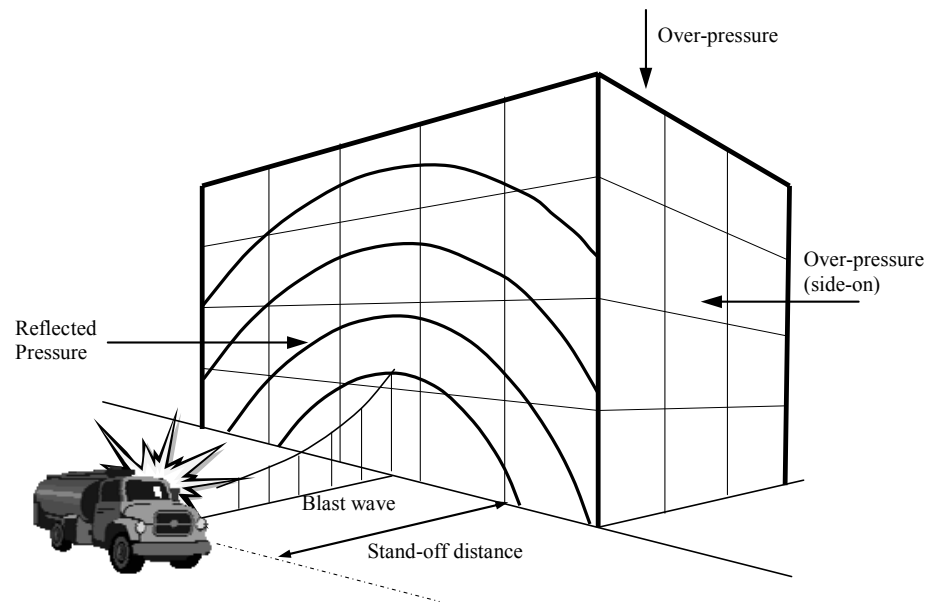


Figure 30: Example of a blast-structure interaction . From: Ngo T., Mendis P., Gupta A., and Ramsay J. Blast loading and blast effects on structures - An overview. *Electronic Journal of Structural Engineering*, 7:76-91, 2007. Special Issue: Loading on Structures

### Question 3.j

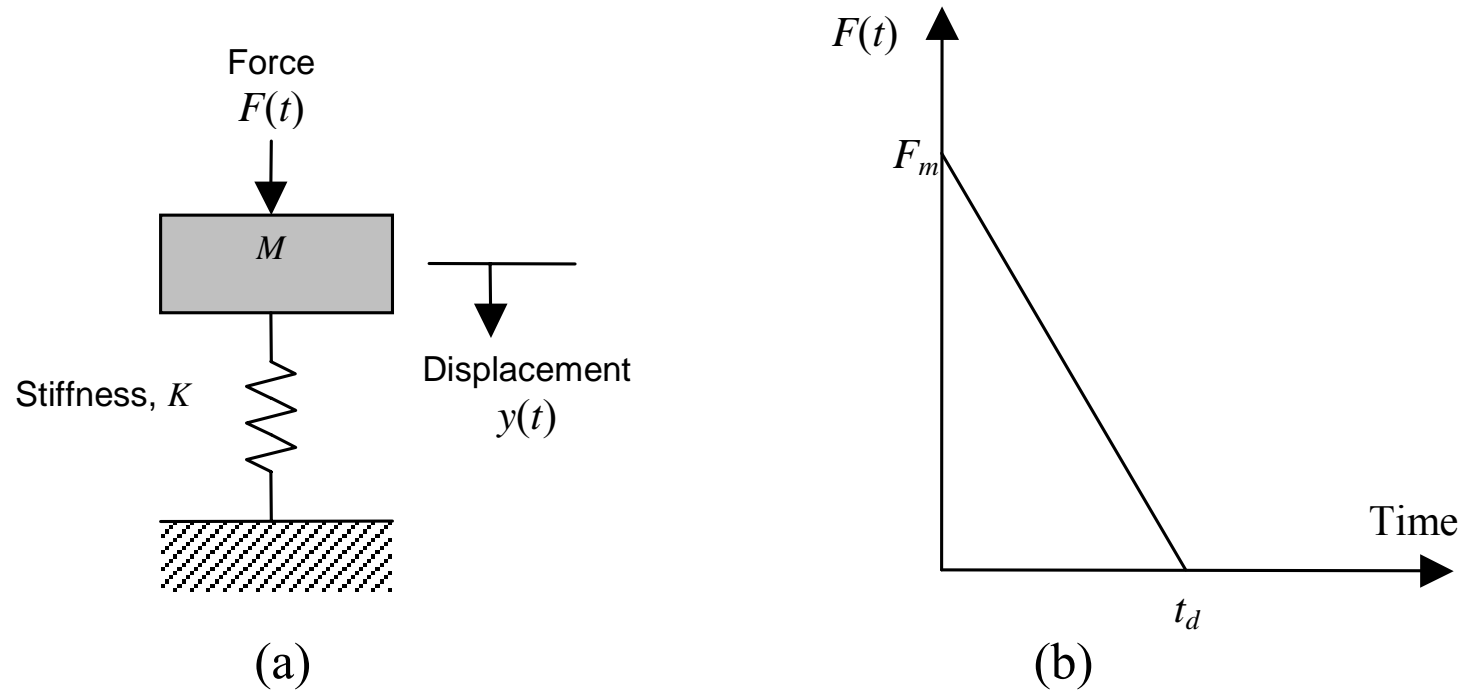


Figure 31: (a) Single degree of freedom model (SDOF). (b) Idealised blast curve (positive phase).  
From: Ngo T., Mendis P., Gupta A., and Ramsay J. Blast loading and blast effects on structures - An overview. *Electronic Journal of Structural Engineering*, 7:76-91, 2007. Special Issue: Loading on Structures

### Question 3.j

**Single Degree of Freedom Model (SDOF):** the actual structure is represented by an equivalent system consisting of one concentrated mass,  $M$  and one weightless spring representing the resistance,  $K$ , of the structure against deformation.

The response of the structure can then be described by an equation of motion of the form

$$M \frac{d^2 y}{dt^2} + Ky = F(t) \quad (56)$$

where  $M$  is the mass of the structure,  $K$  the stiffness of the structure, and,  $F(t)$  the time-dependent load by the blast wave. The blast load can be idealized as a triangular pulse with an amplitude  $F_m$  and a positive phase duration  $t_d$  (see Figure 31) so that the forcing function becomes

$$F(t) = \left[ 1 - \frac{t}{t_d} \right] \quad (57)$$

and hence the equation of motion becomes

$$M \frac{d^2 y}{dt^2} + Ky = \left[ 1 - \frac{t}{t_d} \right] \quad (58)$$

### Question 3.j

The equation of motion (58) can be solved for the displacement  $y$  and the the time rate of displacement  $dy/dt$  (velocity):

$$y(t) = \frac{F_m}{K} [1 - \cos(\omega t)] + \frac{F_m}{K t_d} \left[ \frac{\sin(\omega t)}{\omega} - t \right] \quad (59)$$

$$\frac{dy(t)}{dt} = \frac{F_m}{K} \left[ \omega \sin(\omega t) - \frac{1}{t_d} (\cos(\omega t) - 1) \right] \quad (60)$$

$$(61)$$

where  $\omega$  denotes the natural frequency of the structure.

The natural frequency  $\omega$  and the natural period  $T$  are defined by the mass and stiffness of the structure as:

$$\omega = \sqrt{\frac{K}{M}} \quad T = \frac{2\pi}{\omega} = 2\pi \sqrt{\frac{M}{K}} \quad (62)$$

The structural response to blast loading depends on the ratio  $t_d/T$  or  $\omega t_d$ . There are three loading regimes:

$\omega t_d < 0.4$  : impulsive loading regime

$0.4 \leq \omega t_d \leq 40$  : dynamic loading regime

$\omega t_d > 40$  : quasi-static loading regime

## Influence of the structure stiffness

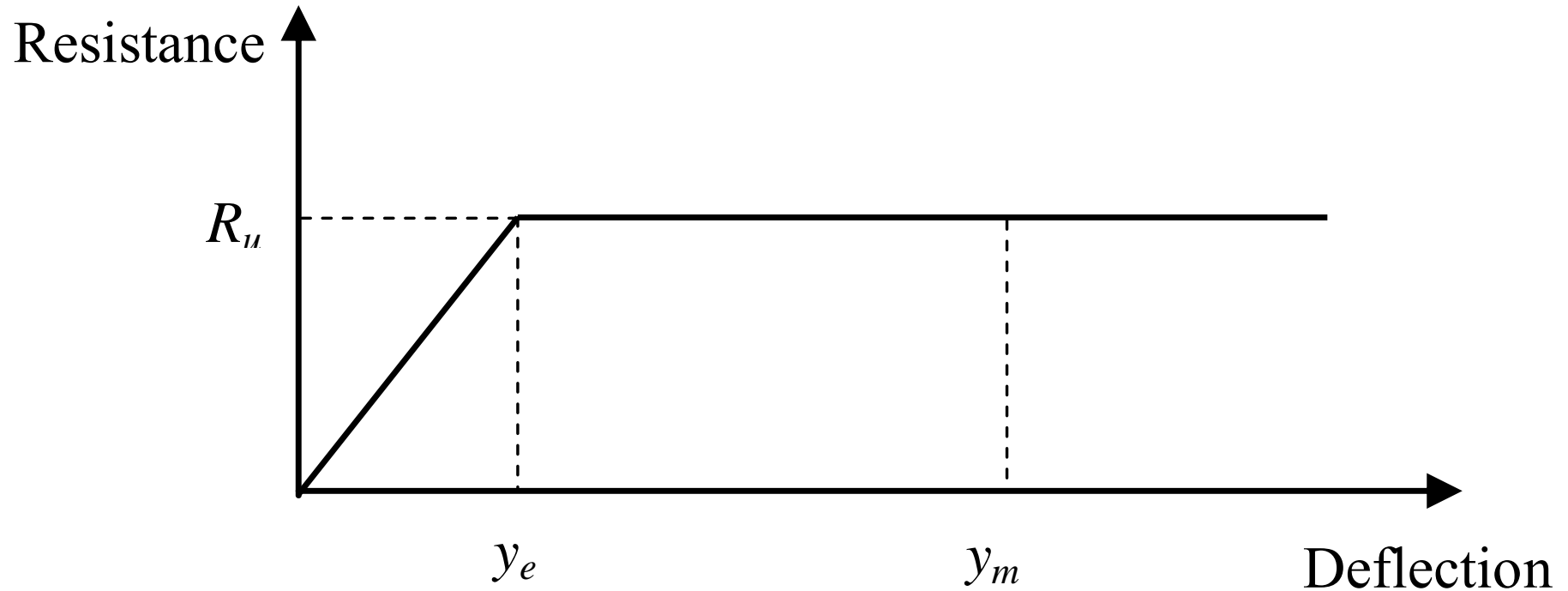


Figure 32: Example of a resistance function (elasto-plastic material;  $y_m$  = maximum deflection). From: Ngo T., Mendis P., Gupta A., and Ramsay J. Blast loading and blast effects on structures - An overview. *Electronic Journal of Structural Engineering*, 7:76-91, 2007. Special Issue: Loading on Structures

### Question 3.j

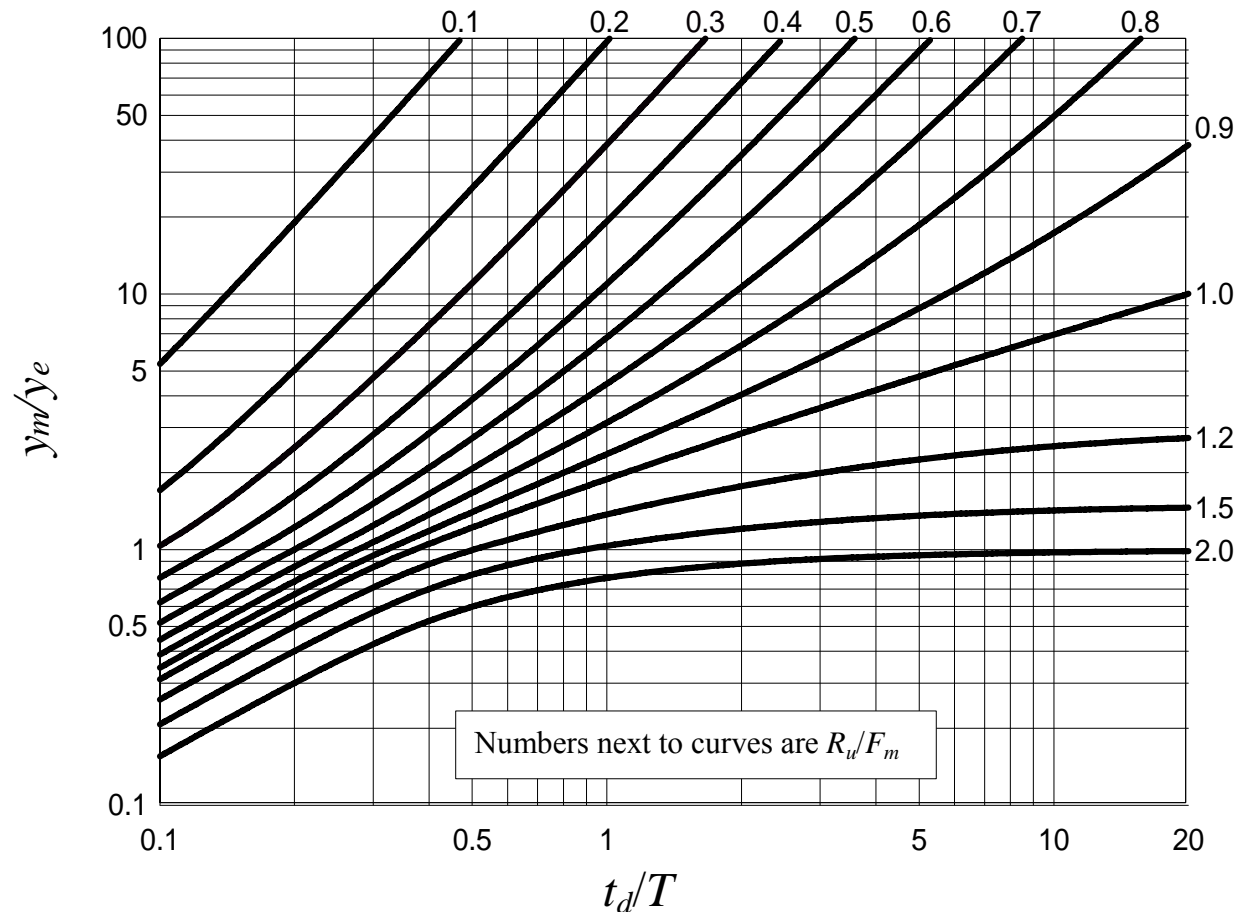


Figure 33: Response of an elasto-plastic structure to a triangular load. From: Ngo T., Mendis P., Gupta A., and Ramsay J. Blast loading and blast effects on structures - An overview. Electronic Journal of Structural Engineering, 7:76-91, 2007. Special Issue: Loading on Structures

## References

- [1] Grossel S.S. *Deflagration and detonation flame arresters*. American Institute of Chemical Engineers, Center for Chemical Process Safety, New York, 2002.
- [2] Kuo K.K. *Principles of Combustion*. John Wiley & Sons, New York, second edition, 2005.
- [3] Nettleton M.A. *Gaseous Detonations: their nature, effects and control*. Chapman and Hall, 1987.
- [4] Chapman D.L. On the rate of explosion in gases. *Physics of Fluids*, 47:90–104, 1899.
- [5] Jouguet E. On the propagation of chemical reactions in gases. *Journal de Mathematiques Pures et Appliquees*, 1:347–425, 1906.
- [6] Zeldovich Ya.B. On the theory of the propagation of detonation in gaseous systems. *Journal of Experimental and Theoretical Physics*, 10:542–568, 1940.
- [7] Neumann J. von. Theory of detonation waves. In A.H. Taub, editor, *John von Neumann, Collected Works*, volume 6 of *Theory of games, astrophysics, hydrodynamics and meteorology*. Pergamon, Oxford, 1942.
- [8] Döring W. Über den detonationvorgang in gases. *Ann. Phys. Lpz.*, 43:421–436, 1943.
- [9] Hirschfelder J.O., Curtiss C.F., and Bird R.B. *The molecular theory of gases and liquids*. John Wiley & Sons, New York, fourth edition, 1967.
- [10] Austin J.M. *The Role of Instability in Gaseous Detonation*. PhD thesis, California Institute of Technology, California, United States of America, May 2003.

- [11] Akbar R. *Mach reflection of gaseous detonations*. PhD thesis, Rensselaer Polytechnic Institute, New York, United States of America, August 1997.
- [12] Eckett C. A., Quirk J. J., and Shepherd J. E. The role of unsteadiness in direct initiation of gaseous detonations. *Journal of Fluid Mechanics*, 421:147–183, 2000.
- [13] Pintgen F., Eckett C.A., Austin J.M., and Shepherd J.E. Direct observations of reaction zone structure in propagating detonations. *Combustion and Flame*, 133:211–229, 2003.
- [14] Urtiew P.A. and Oppenheim A.K. Experimental observations of transition to detonation in explosive gas. *Philosophical Transactions of the Royal Society of London, Series A: Mathematical and Physical Sciences*, 295:13–38, 1966.
- [15] Westbrook C.K. Chemical-kinetics of hydrocarbon oxidation in gaseous detonation. *Combustion and Flame*, 46:191–216, 1982.
- [16] Shepherd J. Chemical kinetics of hydrogen-air-diluent detonations. *Progress in Aeronautics and Astronautics*, 106:263–293, 1986.
- [17] Shepherd J., Moen I.O., Murray S., and Thibault P. Analysis of the cellular structure of detonations. In *Proceedings of the Twenty-First Symposium (International) on Combustion*, pages 1649–1658, Pittsburgh, 1986. The Combustion Institute.
- [18] Lee J.H.S. Dynamic parameters of gaseous detonations. *Annual Reviews of Fluid Mechanics*, 16:311–336, 1984.

- [19] Breitung W., Chan C.K., Dorofeev S.B., Eder A., Gelfand B.E., Heitsch M., Klein R., Malliakos A., Shepherd J.E., Studer E., and Thibault P. Flame acceleration and deflagration to detonation transition in nuclear safety. State-of-the-art report by a group of experts, OECD Nuclear Energy Agency, August 2000.
- [20] Ciccarelli G. Critical tube measurements at elevated initial mixture temperatures. *Combustion Science and Technology*, 174:173–183, 2002.
- [21] Schauer F.R., Miser C.L., Tucker K.C., Bradley R.P., and Hoke J.L. Detonation initiation of hydrocarbon-air mixtures in a pulsed detonation engine. AIAA-paper 2005-1343, 2005.



## Observations of the cellular structure of fuel–air detonations

Douglas W. Stamps<sup>a,\*</sup>, Scott E. Slezak<sup>b</sup>, Sheldon R. Tieszen<sup>b</sup>

<sup>a</sup> *University of Evansville, Evansville, IN 47722, USA*

<sup>b</sup> *Sandia National Laboratories, Albuquerque, NM 87185, USA*

Received 27 July 2003; received in revised form 30 June 2005; accepted 30 June 2005

Available online 15 November 2005

### Abstract

Detonation cell widths, which provide a measure of detonability of a mixture, were measured for hydrocarbon–air and hydrogen–air–diluent mixtures. Results were obtained from a 0.43-m-diameter, 13.1-m-long heated detonation tube with an initial pressure of 101 kPa and an initial temperature between 25 and 100 °C. The cell widths of simple cyclic hydrocarbons are somewhat smaller than those of comparable straight-chain alkanes. Cyclic hydrocarbons tested generally had similar cell sizes despite differences in degree of bond saturation, bond strain energy, oxygen substitution, and chemical structure. There was a significant reduction in the cell width of octane, a straight-chain alkane, when it was mixed with small quantities of hexyl nitrate. The effect of a diluent, such as steam and carbon dioxide, on the cell width of a hydrogen–air mixture is shown over a wide range of mixture stoichiometries. The data illustrate the effects of initial temperature and pressure on the cell width when compared to previous studies. Not only is carbon dioxide more effective than steam at increasing the mixture cell width, but also its effectiveness increases relative to that of steam with increasing concentrations. The detonability limits, which are dependent on the facility geometry and type of initiator used in this study, were measured for fuel-lean and fuel-rich hydrogen–air mixtures and stoichiometric hydrogen–air mixtures diluted with steam. The detonability limits are nominally at the flammability limits for hydrogen–air mixtures. The subcellular structure within a fuel-lean hydrogen–air detonation cell was recorded using a sooted foil. The uniform fine structure of the self-sustained transverse wave and the irregular structure of the overdriven lead shock wave are shown at the triple point path that marks the boundary between detonation cells.

Published by Elsevier Inc. on behalf of The Combustion Institute.

*Keywords:* Detonation cells; Detonability limits; Subcellular structure

### 1. Introduction

The detonation cell width is associated with the ease with which a mixture can detonate. The energy required to initiate a detonation directly by a spherical initiation source is proportional to the cube of the

cell width [1]. A more likely mode of detonation initiation is through the deflagration-to-detonation transition (DDT) mechanism, since the large energies required for direct initiation of a detonation are generally not available in postulated accidents. Criteria for DDT also employ the detonation cell width [2,3].

Detonation cell width information is critical to assess the hazards associated with potential accidents in hydrocarbon processing plants, in petrochemical plants, and within nuclear power plant containments.

\* Corresponding author. Fax: +1 812 488 2780.

E-mail address: [ds38@evansville.edu](mailto:ds38@evansville.edu) (D.W. Stamps).

The production of plasticizers, elastomers, adhesives, and fertilizers often involves higher-molecular-weight hydrocarbon intermediates produced from petroleum feedstocks. A safety analysis in the hydrocarbon processing industry [4] concluded that explosions, not fire, are the primary threat to be avoided and more information on the hazards of mixtures is required to prevent accidents. Likewise, detonable concentrations of hydrogen and air may build up in postulated severe accident scenarios in light-water-reactor nuclear power plants. Steam is released into the containment as the coolant (water) is released from an accidental break in the reactor coolant system and hydrogen is released if the nuclear core is uncovered and the hot fuel cladding oxidizes. Carbon dioxide and carbon monoxide can be produced if the molten core breaches the reactor pressure vessel and spreads over the concrete in the reactor cavity of the containment. The detonability of hydrogen–air–diluent mixtures is, therefore, of significant interest for the area of nuclear reactor safety.

The susceptibility of a mixture to detonate is influenced strongly by the mixture stoichiometry and fuel structure. The mixture is most sensitive at an equivalence ratio slightly greater than stoichiometric, which is when the cell width is a minimum. The cell width increases rapidly for both fuel-lean and fuel-rich mixtures. The effect of mixture stoichiometry on hydrogen–air mixtures [5–7] and hydrocarbon–air mixtures [8–12] was determined using measurements of detonation cell width, critical tube diameters, and critical initiation energies. The effect of stoichiometry on fuel–oxygen mixtures and mixtures vitiated with nitrogen were determined using the critical initiation energy and critical tube diameter [13–17].

The ranking of relative detonation hazards [8,13], as determined by the detonation cell width or one of its equivalents, shows that all saturated alkanes have similar sensitivity regardless of molecular weight except for methane, which has a unique tetrahedral molecular structure with large C–H bond energies and a propensity to produce methyl radicals. The unsaturated alkenes are more sensitive than the alkanes. Triply bonded alkynes, like acetylene, are more sensitive than alkenes, like ethylene. Hydrogen is similar to acetylene in hazards ranking. Because of unheated facilities, early testing of most fuels was limited to low-molecular-weight compounds (four carbons or less) to maintain sufficient vapor pressure. More recent studies [18,19] used heated facilities that allow fuel–air mixtures with up to 10 carbon atoms per fuel molecule to be tested. Previous conclusions based on low-molecular-weight fuels were confirmed although the degree of sensitization due to bond unsaturation decreased with increasing molecular weight. Furthermore, it was determined that mole-

cular structure, such as a ring compound, or the addition of functional groups, such as epoxides or nitrates, can significantly increase the hazards ranking of these structures over the parent molecule. However, these studies did not determine the effect of fuel mixtures.

Mixtures become less sensitive to detonation when inert gases are added. This result is especially important in hypothetical nuclear reactor accidents where large quantities of steam may exist in the containment, from the release of coolant through a break, or carbon dioxide may exist in the lower compartments, when the molten core attacks the concrete. Dilution of a hydrogen–air mixture with an inert gas, such as steam or carbon dioxide, provides significant mitigative benefits [20,21], although the effectiveness of the diluent can be greatly diminished at elevated temperatures [22–24]. Similar effects have been observed for hydrogen–oxygen–diluent mixtures [25]. A direct comparison of the efficacy of steam and carbon dioxide for hydrogen–air mixtures at the same initial conditions has not been reported.

Cell width data are often correlated using a Zeldovich–von Neumann–Doering (ZND) model of a detonation with detailed chemical kinetics. The one-dimensional ZND model cannot describe the three-dimensional physical structure behind a detonation wave. However, Shelkin and Troshin [26] proposed that the experimentally measured detonation cell width could be correlated with the induction zone thickness. This approach has been successful in correlating the detonation cell size, critical tube diameter, and critical initiation energy for a large number of fuels with a wide range of equivalence ratios and diluents [5,10,18,20,22–24,27–35].

The ZND model assumes that a shock wave travels at the Chapman–Jouguet (CJ) velocity. The shock wave elevates the postshock gas temperature and pressure to the von Neumann state on the shock Hugoniot and initiates the chemical reaction. The reaction zone behind the shock consists of an induction zone during which the temperature and pressure are nearly constant followed by a rapid release of chemical energy as the state of the gas moves along the Rayleigh line from the von Neumann point (no reaction) to the CJ point (reaction proceeds to chemical equilibrium) on the Hugoniot curves. The release of chemical energy is governed by a set of elementary chemical reactions. A reaction mechanism proposed by Miller et al. [36] consisting of 23 elementary reactions and 11 species was used for the chemical kinetic model for hydrogen oxidation in this study. A comparably reliable chemical kinetic reaction mechanism was not available for the hydrocarbons tested in this study. The reaction zone structure is obtained by simultaneously solving the conservation equations be-

hind the shock as a function of distance. A detailed discussion of the model is given by Shepherd [27].

The present study reports experimental measurements on the effects of fuel molecular structure, functional groups, and fuel mixtures on the detonation cell widths of stoichiometric hydrocarbon–air mixtures at 1 atm initial pressure and 100 °C for common industrial hydrocarbons. The detonation cell widths of hydrogen–air mixtures at 1 atm initial pressure and 100 °C diluted with steam and carbon dioxide are reported, correlated with the ZND model, and compared directly to illustrate the efficacy of the two diluents. The detonability limits for hydrogen–air mixtures with and without dilution are also reported. The limits data are not an absolute measure of the mixture composition or stoichiometry over which detonation can occur, but are dependent on the scale and geometry of the facility and the initiator used in this study. Furthermore, the fine structure within a detonation cell has been recorded for a mixture near the detonability limits, which exhibited large cellular structure.

## 2. Experimental method

The detonation cell width data were obtained in a 0.43-m-diameter, 13.1-m-long detonation tube heated by resistive electrical heaters applied evenly along the tube's surface. A 3.66-m-long by 1.22-m-wide aluminum sheet was coated uniformly with a thin layer of soot to record the tracks of the detonation cellular structure. The sheet was rolled into a cylinder and placed in the terminal end of the tube as a liner.

The experimental procedure varied slightly depending on whether the fuel was a liquid or a gas. For liquid hydrocarbon fuels, the tube was heated to 100 °C and then evacuated. A premeasured amount of fuel was placed in a small boiler and the boiler was heated 20–40 °C above the tube temperature. The fuel vapor was introduced into the tube through a recirculation line and the pressure inside the tube was allowed to equilibrate. Heated, dry, compressed air was introduced slowly into the recirculation line and allowed to mix. For hydrogen, the tube was heated to 100 °C and then evacuated. Dry air was first introduced, then hydrogen, and finally steam or carbon dioxide depending on the experiment. The mixture was continuously circulated during the introduction of new gases. Each gas was introduced slowly over the period of time required to circulate one to two tube volumes. The final mixture was circulated two to three tube volumes to provide additional mixing.

The temperature and pressure were measured after each gas was introduced and the equivalence ratio and diluent concentrations were determined using the method of partial pressures. The uncertainty in the

equivalence ratio is less than  $\pm 4\%$ . The gas pressure was measured using a Wallace and Tiernan 0–800 mm Hg absolute gauge with an uncertainty of  $\pm 0.5$  mm Hg and the gas temperature was measured using a Chromel–Alumel (Type K) thermocouple with an uncertainty of  $\pm 1$  °C. Mixtures were initially heated to nominally 100 °C and 101 kPa.

The detonation was typically initiated using a 40-g planar charge of EL506C1 Detasheet high explosive in a “wagon wheel” arrangement, although up to 106 g of high explosive was used for mixtures that were marginally detonable. Detonation time-of-arrival was measured by up to 12 fast-response piezoelectric pressure transducers (either PCB Model 113A20 or Kistler Model 211B3) spaced approximately uniformly along the length of the tube. A constant detonation velocity along the latter 10 m of the tube verified a self-sustained wave.

The detonation cell widths,  $\lambda$ , were measured by selecting high-contrast long-running parallel lines on the sooted sheet. Two observers measured the detonation cell widths independently and the ratios of the two sets of independent measurements were used to estimate the uncertainty. Two standard deviations of the cell widths are estimated to be  $\pm 0.25\lambda$  (e.g., a 95% confidence interval).

## 3. Results and discussion

### 3.1. Hydrocarbon–air detonations

The effect of molecular structure, bond saturation, and functional groups were investigated for common industrial high-molecular-weight hydrocarbons. Table 1 lists the fuels that were tested, their chemical purity, formula, and structure, and the detonation cell widths for the stoichiometric fuel–air mixtures shown in order of increasing sensitivity to detonation. With the exception of benzene, a stable six-carbon ring, and 2,5-dihydrofuran, an unsaturated cyclic ether, all of the cyclic fuels have similar cell widths in the range of 40–50 mm, in spite of significant differences in molecular structure, strain energies in the rings, and degree of saturation. For example, quadricyclane, a saturated cyclic alkane with highly strained three-carbon rings, has the same cell width as cyclohexane, with a more stable six-carbon ring. Likewise, the saturated quadricyclane has nearly the same cell width as monounsaturated  $\alpha$ -pinene or polyunsaturated methylcyclopentadiene.

Benzene is a very stable cyclic compound. In spite of the double bonds between the carbon atoms, the detonation cell width is 126 mm. This large cell width is likely a result of the stability resonance established by the sharing of the electrons in the  $\pi$  bonds, which

Table 1

Chemical purity, formula, and structure of each hydrocarbon fuel and the detonation cell widths for stoichiometric fuel–air mixtures at 1 atm initial pressure and 100 °C initial temperature

Fuel	Purity	Formula	Structure	Cell width (mm)
Benzene	99%	C <sub>6</sub> H <sub>6</sub>	(Hexagon)	126
$\alpha$ -Methylstyrene	99%	C <sub>9</sub> H <sub>10</sub>	C <sub>6</sub> H <sub>5</sub> C(CH <sub>3</sub> )=CH <sub>2</sub> (Hexagon)	50
Decalin (decahydronaphthalene)	98%	C <sub>10</sub> H <sub>18</sub>	(Dual hexagonal ring)	49
Tetrahydrofuran	99%	C <sub>4</sub> H <sub>8</sub> O	(Pentagon)	46
<i>n</i> -Octane	99%	C <sub>8</sub> H <sub>18</sub>	(Straight-chain alkane)	42 [18]
$\alpha$ -Pinene	98%	C <sub>10</sub> H <sub>16</sub>	(Complex cyclic alkene)	42
Quadricyclane	95%	C <sub>6</sub> H <sub>8</sub>	(Highly-strained cyclic alkane)	41
Cyclohexane	99%	C <sub>6</sub> H <sub>12</sub>	(Hexagon)	41
Methylcyclopentadiene	93%	C <sub>6</sub> H <sub>8</sub>	C <sub>5</sub> H <sub>5</sub> (CH <sub>3</sub> ) (Pentagon)	40
2,5-Dihydrofuran	97%	C <sub>4</sub> H <sub>6</sub> O	(Pentagon)	21
Ethyl hexyl nitrate	97%	C <sub>8</sub> H <sub>17</sub> NO <sub>3</sub>	CH <sub>3</sub> (CH <sub>2</sub> ) <sub>3</sub> CH(C <sub>2</sub> H <sub>5</sub> )CH <sub>2</sub> ONO <sub>2</sub>	15
Hexyl nitrate	95%	C <sub>6</sub> H <sub>13</sub> NO <sub>3</sub>	CH <sub>3</sub> (CH <sub>2</sub> ) <sub>5</sub> NO <sub>3</sub>	11 [18]

Note. The 95% confidence interval on the detonation cell width ( $\lambda$ ) is  $\pm 0.25\lambda$ .

increases the difficulty in initiating the chemical reaction. The large cell width of the benzene ring can be contrasted with a cell width of 50 mm for that of  $\alpha$ -methylstyrene, which has an unsaturated hexagonal cyclic ring like that of benzene. However, unlike benzene,  $\alpha$ -methylstyrene has a methyl radical (CH<sub>3</sub>) and a methylene radical (CH<sub>2</sub>) attached to a carbon–carbon bond as shown in Table 1. Breaking bonds between these radicals and the carbon atom would be easier than breaking bonds in the benzene ring and could contribute to a smaller cell size.

Cyclohexane, with a cell size of 41 mm, has a larger cell size than cyclooctane, which has a cell size of 29 mm [18]. The more stable six-carbon ring structure of cyclohexane as compared to the eight-carbon ring structure of cyclooctane may be responsible for the larger cell size. It is interesting to note that the ratio of the detonation cell widths of hexane to cyclohexane is similar to that of octane to cyclooctane. Using cell widths of 55 and 42 mm for hexane and octane [18], respectively, the ratios of the straight-chain alkane to cyclic alkane cell widths are approximately 1.3 and 1.4 at the C<sub>6</sub> and C<sub>8</sub> levels, respectively. The sensitizing effect of the ring structure is similar on each straight-chain alkane.

The degree of bond saturation also affects the cell size. Tieszen et al. [18] showed a substantial reduction in the cell width as the degree of saturation decreased in straight-chain alkanes. A similar effect was observed in the present study in cyclic ethers. Tetrahydrofuran and 2,5-dihydrofuran have the same chemical structure except that 2,5-dihydrofuran has a double carbon bond. A cell width of 46 mm was measured for tetrahydrofuran as compared to 21 mm for 2,5-dihydrofuran.

The replacement of a single H atom by a nitrate functional group can substantially decrease the cell width. As an example, the cell width of 11 mm mea-

sured for mixed primary hexyl nitrate is five times smaller than the 55-mm cell width for hexane [18]. The cell width of 15 mm for ethyl hexyl nitrate, is slightly larger than that of mixed primary hexyl nitrate although that is consistent with earlier observations that the degree of sensitization resulting from a nitro or epoxy group decreased with increasing molecular weight [18]. The reduction in cell width comes from three factors [18]: (1) a lower bond energy between the ONO<sub>2</sub> functional group and remaining fuel radical as compared to the original C–H bond in the parent molecule, which allow the fuel to decompose rapidly, (2) the production of large quantities of alkyl radicals and ONO<sub>2</sub> groups that accelerate the overall reaction rate, and (3) a higher heat of reaction, which increases the postshock temperature and pressure.

The addition of relatively small amounts of hexyl nitrate to octane yielded a large decrease in the cell width of the mixture. For example, the cell width of a stoichiometric mixture of an octane/hexyl nitrate fuel blend and air is reduced by nearly a factor of 2, from 42 to 23 mm, when 10% hexyl nitrate is added to the fuel blend as compared to pure octane. The remainder of the octane would have to be replaced in the fuel blend, from 10 to 100% hexyl nitrate, to reduce the cell width by approximately another factor of 2, from 23 to 11 mm, as shown in Fig. 1. Another study [37] showed a linear reduction in the detonation cell width as isopropyl nitrate was added to hexane in stoichiometric fuel blend–air mixtures. However, it should be pointed out that in both studies, there was a continuous reduction in the cell width of the fuel blend–air mixture as increasing amounts of the nitrated fuel were added. Zhang et al. [37] suggested that the effect an additive has on a fuel–additive blend depends on the differences between the heats of reactions and the activation energies of the overall reactions of the additive–air mixture and the fuel–air mixture.

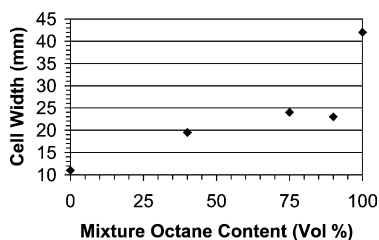


Fig. 1. The detonation cell width for overall stoichiometric mixtures of mixed primary hexyl nitrate ( $C_6H_{13}NO_3$ ) and *n*-octane ( $C_8H_{18}$ ) at 101 kPa initial pressure and 100 °C initial temperature.

### 3.2. Hydrogen–air–diluent detonations

Guirao et al. [38] and Tieszen et al. [20,39] report the effect of steam and carbon dioxide dilution on the detonation cell width of hydrogen–air mixtures using different scales of test facilities although neither of these studies provide a direct comparison of the two diluents at the same initial conditions. Both studies report variations in the detonation cell widths in hydrogen–air mixtures at an initial temperature of 25 °C and one atmosphere pressure with carbon dioxide dilution and different equivalence ratios. They also report the effect of steam dilution and equivalence ratio on the detonation cell size of hydrogen–air mixtures at 100 °C with an air density of 41.6 mol/m<sup>3</sup>, which corresponds to the density of air at 1 atm and 20 °C. The tests were conducted by heating air, initially at 20 °C and 1 atm, to 100 °C, adding hydrogen to the desired equivalence ratio, and then adding steam to the desired percentage. The final mixture temperature was constant at approximately 100 °C for all tests but the initial pressure varied from 1.46 to 2.89 atm depending on the amount of hydrogen and steam added. This testing procedure was used to study nuclear reactor safety issues and simulated the heating of air within a rigid containment while steam and hydrogen were released during a hypothetical accident. Stamps and Tieszen [22] have shown that initial temperature and pressure influence the detonation cell size. Therefore, the effect of steam and carbon dioxide dilution could not be compared directly since the tests were conducted at different temperatures and pressures.

Ciccarelli et al. [23,24] report the effect of steam dilution on the detonation cell width of hydrogen–air mixtures at elevated temperatures but did not perform any tests with carbon dioxide. The reported results are primarily for steam-diluted stoichiometric mixtures at initial pressures of 1 atm and initial temperatures up to 650 K, although a limited number of data are given for steam-diluted fuel-lean mixtures.

Detonation cell width data from the present study have been obtained at conditions different from previ-

ous studies and the tests have been designed to make a direct comparison between the effect of steam and carbon dioxide dilution. Tests were conducted with both carbon dioxide- and steam-diluted hydrogen–air mixtures at initial conditions of 100 °C and 1 atm pressure. The effect of carbon dioxide and steam dilution on the hydrogen–air detonation cell widths is shown in Figs. 2 and 3. The addition of 10 and 20% carbon dioxide to stoichiometric mixtures increased the cell width by factors of approximately 4.6 and 34 over a stoichiometric mixture with no dilution and by factors of 4 and 24 when steam was used as the diluent. Because the critical initiation energy is proportional to the cube of the cell width, this means that the addition of carbon dioxide decreases the likelihood of a directly initiated detonation by approximately factors of 100 and 40,000 over a stoichiometric hydrogen–air mixture and factors of 64 and 13,000 for steam dilution. From a comparison of the data, carbon dioxide was not only a better inhibitor of a detonation than steam, but also its effectiveness increased relative to steam with increasing concentration.

The data in Figs. 2 and 3 are qualitatively similar to those reported by Tieszen et al. [20,39], yet quantitative differences exist. Both sets of data show that the cell widths increase for off-stoichiometric hydrogen–air mixtures and for all equivalence ratios with the addition of an inert gas. However, for a given mixture composition, the present data for carbon dioxide-diluted hydrogen–air mixtures show smaller detonation cell widths than those reported by Tieszen et al. [20,39]. This is due to the higher initial temperatures used in the current study. This is consistent with the results of Stamps and Tieszen [22] and Ciccarelli et al. [23,24], which show a reduction in the detonation cell size of diluted hydrogen–air mixtures over a similar range of temperatures. Also, for a given mixture composition, the data reported by Tieszen et al. [20,39] for steam-diluted hydrogen–air mixtures show smaller detonation cell widths than the current study. This is because the tests performed by Tieszen et al. [20,39] were conducted at higher initial pressures, as discussed in Stamps and Tieszen [22].

The detonation cell widths shown in Figs. 2 and 3 are correlated with results from the ZND model. The ZND model is first used to calculate a reaction zone length. Then, the detonation cell width is predicted by multiplying the calculated reaction zone length by an empirical constant. Shepherd [27] examined the use of several different definitions of the reaction zone length to predict the detonation cell width. These definitions include the location of the maximum temperature gradient and the location where the gaseous products' velocity reached a Mach number of 0.75 and 0.9 for the ZND model and the location of

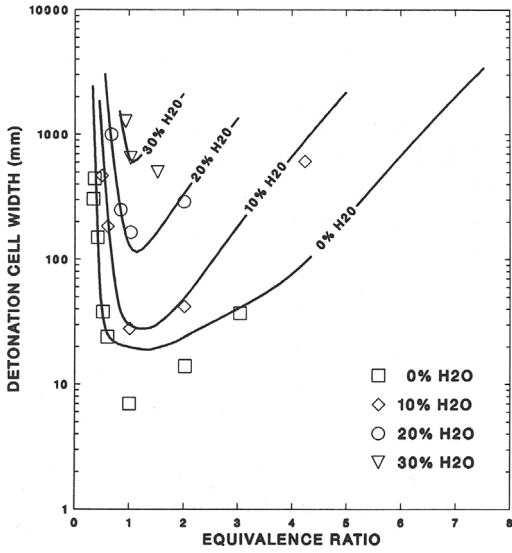


Fig. 2. The effect of inert gas dilution on the detonation cell width of hydrogen–air mixtures at 100 °C initial temperature and 101 kPa initial pressure. The 95% confidence interval on the detonation cell width ( $\lambda$ ) is  $\pm 0.25\lambda$ . Symbols represent data for steam and continuous lines represent ZND predictions.

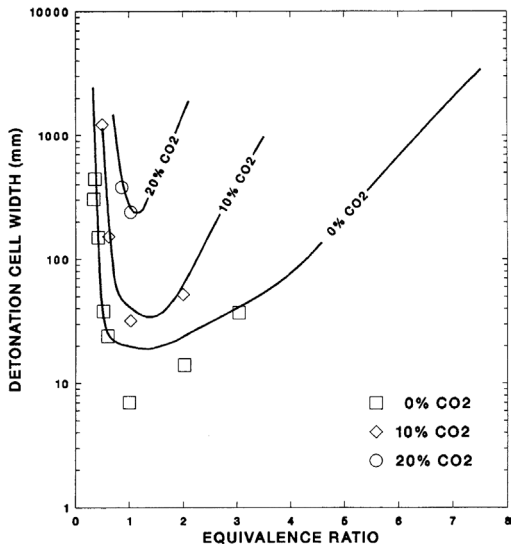


Fig. 3. The effect of inert gas dilution on the detonation cell width of hydrogen–air mixtures at 100 °C initial temperature and 101 kPa initial pressure. The 95% confidence interval on the detonation cell width ( $\lambda$ ) is  $\pm 0.25\lambda$ . Symbols represent data for carbon dioxide and continuous lines represent ZND predictions.

the maximum temperature gradient and a length related to the effective activation energy for a constant volume combustion approximation. Shepherd found that the location where the gaseous products' velocity

reached a Mach number of 0.75 was most successful in predicting the change in cell size for hydrogen–air mixtures diluted with steam and carbon dioxide at temperatures between 25 and 100 °C, which are the conditions of the mixtures tested in this study. This length scale was multiplied by a constant factor of 22 to correlate with the detonation cell width, since this method has successfully correlated previous hydrogen–air–diluent data under similar initial conditions [20]. The predicted cell widths are shown as the solid lines in Figs. 2 and 3.

### 3.3. Detonability limits of hydrogen–air–diluent mixtures

Experiments were conducted to determine the range of mixture compositions that would support detonations in this facility, since detonability limits are scale-dependent. The detonability limit is reported on a “go–no go” basis. For example, the detonability limit for a fuel-lean hydrogen–air mixture at 20 °C and 101 kPa was between 11.4 and 11.6% hydrogen. That is, a self-sustained detonation wave was observed at 11.6% hydrogen and the detonation failed at 11.4% hydrogen. The self-sustained detonations left tracks on the sooted foils while the failed detonations did not. Furthermore, since cell width data larger than the facility dimension are not independent measurements that the detonation may be marginal or failing, the experimentally measured wave velocity is reported in Table 2 and compared to the calculated Chapman–Jouguet (C–J) detonation velocity. The experimentally measured wave velocities agree within 4% at worst, and typically within less than 1%, when compared to the C–J detonation velocities for the self-sustained waves. For the failed detonations, the measured values are lower than the C–J values by an average of 26%. Table 2 summarizes the data and compares the detonability limits to the flammability limits.

Typically two flammability limits are reported for fuel-lean hydrogen–air mixtures: one each for downward and upward propagation of the flame. For example, at 20 °C and 101 kPa, the downward propagation flammability limit is 9.4% hydrogen and the upward propagation flammability limit is 4.3% hydrogen [40]. The directional difference in the fuel-lean flammability limit is because of a process called selective diffusional demixing [43]. Small hydrogen molecules easily diffuse through the air and locally enrich the fuel in the mixture near the flame, propagating upward by buoyant convection. However, at detonation time scales, selective diffusional demixing is not possible and it can be argued that the downward propagation limit is the appropriate benchmark for comparison.

Table 2

Comparison of the flammability limits and detonability limits for various hydrogen–air mixtures at an initial pressure of 1 atm

Mixture	Initial temp. (°C)	Flam. limit	Detn.	Exp. vel. (m/s)	C–J detn. vel. (m/s)	No detn.	Exp. vel. (m/s)	C–J detn. vel. (m/s)
Lean H <sub>2</sub> –air	20	9.4% H <sub>2</sub> [40]	11.6% H <sub>2</sub>	1375	1367	11.4% H <sub>2</sub>	1058	1354
Rich H <sub>2</sub> –air	20	75.0% H <sub>2</sub> [40]	74.9% H <sub>2</sub>	2316	2330	75.9% H <sub>2</sub>	1530	2333
Lean H <sub>2</sub> –air	100	8.7% H <sub>2</sub> [40]	9.4% H <sub>2</sub>	1276	1267	8.8% H <sub>2</sub>	1002	1237
Rich H <sub>2</sub> –air	100	77.4% H <sub>2</sub> [40]	76.9% H <sub>2</sub>	2337	2361	77.9% H <sub>2</sub>	1815	2365
Stoich. H <sub>2</sub> –air–H <sub>2</sub> O	100	59.4% H <sub>2</sub> O [41]	38.8% H <sub>2</sub> O	1641	1706	40.5% H <sub>2</sub> O	1114	1693
Stoich. H <sub>2</sub> –air–CO <sub>2</sub>	20	56.0% CO <sub>2</sub> [42]	24.8% CO <sub>2</sub>	1458	1518	No test	No test	No test

Note. Detonability limits were obtained in a 43-cm-diameter tube.

Table 3

Comparison of the flammability limits and detonability limits for stoichiometric hydrogen–air–diluent mixtures at an initial pressure of 1 atm

Mixture	Init temp. (°C)	Diluent	Detn. limit (% diluent)	Flam. limit (% diluent)	Detn. limit (% flam. limit)	C <sub>p</sub> (kJ/kmol K)
H <sub>2</sub> –air	20	H <sub>2</sub>	64.4	64.5	99.8	30.0
H <sub>2</sub> –air	100	H <sub>2</sub>	67.2	67.9	99.0	30.2
H <sub>2</sub> –air	20	Air	60.6	68.2	89.0	33.0
H <sub>2</sub> –air	100	Air	68.1	70.6	96.4	32.8
H <sub>2</sub> –air–H <sub>2</sub> O	100	H <sub>2</sub> O	38.8	59.4	65.3	44.2
H <sub>2</sub> –air–CO <sub>2</sub>	20	CO <sub>2</sub>	24.8	56.0	44.3	56.8

Note. The fuel-lean and fuel-rich mixtures in Table 2 are viewed alternatively as stoichiometric mixtures diluted with excess air and hydrogen, respectively.

To compare the effect of the diluent on the detonability limits, the fuel-lean and fuel-rich mixtures shown in Table 2 can be viewed alternatively as stoichiometric hydrogen–air mixtures diluted with excess air and hydrogen, respectively. For example, a fuel-lean mixture with an equivalence ratio  $\phi = 0.314$ , or 11.6% H<sub>2</sub>, has the same composition as a stoichiometric H<sub>2</sub>–air mixture with 60.6% excess air. The conversion was done for both the detonability and flammability limits shown in Table 3. For the sake of comparison, the “go” detonability limits were taken as mixtures that supported a detonation even though the actual limits lie within the “go–no go” ranges. The ratio of the diluent concentration at the detonability limit to the diluent concentration at the flammability limit is a measure of how close the detonability limit is to the flammability limit.

The data show that the detonability limits are nominally at the flammability limits for some hydrogen–air mixtures. For example, the detonability and flammability limits are nearly the same for hydrogen–air mixtures diluted with hydrogen (fuel-rich mixtures) and very close for air dilution (fuel-lean mixtures). Similar results have been reported in hydrogen–oxygen–helium mixtures tested in a 15-cm-diameter tube, where detonability and flammability limits nearly coincided. A detonation was observed in a stoichiometric hydrogen–oxygen–helium mixture at 9.4% hydrogen at the ambient conditions of 22 °C

and 101 kPa [25], while the flammability limit for a stoichiometric hydrogen–oxygen–helium mixture under similar initial conditions is 9% for both upward and downward propagation of the flame [41].

The heat capacity of the diluent has an influence on how close the detonability limits are to the flammability limits for a given apparatus. The addition of the diluents in Table 2 decreases the postshock temperature, which reduces the reaction rates and results in larger reaction-zone lengths and detonation cell sizes. The effect of the diluent increases as the specific heat of the diluent increases. Triatomic gases, such as CO<sub>2</sub> and H<sub>2</sub>O, have larger specific heats than diatomic gases, such as H<sub>2</sub>, O<sub>2</sub>, or N<sub>2</sub>, which have larger values than monatomic gases, such as He. Ultimately, the detonation limits for a fixed tube diameter, such as those in the current study, occur at lower diluent concentrations as the specific heat of the diluent increases. This effect can be seen in Table 3, which shows that the detonability limits are progressively farther from the flammability limits for diluents with greater specific heats. The specific heats are reported at a temperature that is the average of the initial temperature and the C–J detonation temperature. This temperature was chosen because the energy absorbed by the diluent can be approximated by the average specific heat times the temperature difference between the detonation and initial temperatures. Of course chemical factors, such as the diluent’s ability

to participate in or enhance some reaction rates, may also affect the cell size and ultimately the detonation limits within a given tube diameter. However, Shepherd [27] showed that the primary effect is the thermal effect for hydrogen–air–diluent detonations shown in Table 3.

Larger-diameter tubes allow a wider range of mixture compositions to detonate. For example, the range of detonable mixture compositions was found to lie between 20.3 and 57% hydrogen in a 1-cm-diameter tube [44] as compared to the wider range 11.6–74.9% hydrogen in the current 43-cm-diameter tube for hydrogen–air mixtures at ambient temperature and pressure. Because the scale of the facility influences detonability limits, this means that the intrinsic detonability limit for steam-diluted and carbon dioxide-diluted mixtures may ultimately be higher than the reported values of 38.8 and 24.8%, respectively, perhaps reaching the flammability limits of 59.4 and 56%, respectively, if the results from the hydrogen-lean and hydrogen-rich mixtures shown in Table 3 hold for the higher heat capacity diluents.

### 3.4. Subcellular structure of a detonation

The subcellular structure of a detonation cell became evident for hydrogen–air mixtures near the detonability limits because of the large size of the cells associated with these mixtures. For example, the cell width was 1320 mm for a hydrogen–air mixture at 100 °C and 101 kPa with 10.4% hydrogen. The velocity of this self-sustained detonation wave was measured at 1383 m/s compared to a calculated C–J detonation velocity of 1317 m/s. An idealized schematic of a cell from this test is shown in Fig. 4a. The structure of the detonation wave is superimposed at one location. The photograph in Fig. 4b is an enlargement of a region depicted by the rectangle in Fig. 4a along the path of the triple point. The track angle between the tube axis and the path of the triple point is 45° at the location of the subcellular structure shown in Fig. 4b. The average detonation velocity and the track angle are all that are required to calculate completely the shock structure using the technique of Huang et al. [45].

Oppenheim [46] describes how Mitrofanov, Subbotin, and Topchyan deduced the structure of a detonation wave, which was obtained independently by Schott [47]. As illustrated in Fig. 4a, the leading edge of a detonation wave is composed of an oblique shock FA and an overdriven wave AE. Because of the velocity of the oblique shock FA, the temperature of the gas behind the wave is insufficient for fast ignition and the reaction front separates from the shock. A self-sustained transverse wave BC propagates into the gas compressed by the oblique shock FA and the reaction

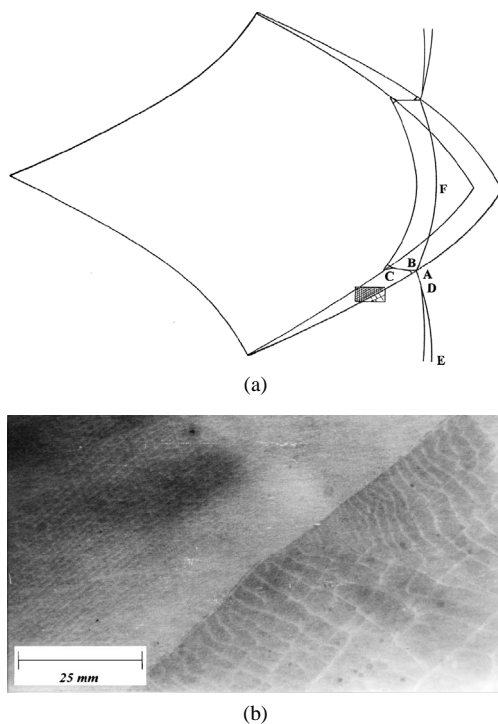


Fig. 4. The subcellular structure of a hydrogen–air detonation at 100 °C and 101 kPa with 10.4% hydrogen: (a) idealized schematic of the detonation cells with a detonation wave superimposed and (b) photograph of the rectangular region depicted in part (a).

is rapid behind the second compression. The expansion of the products of the transverse wave distorts the primary wave to create the overdriven wave AE. The gases react rapidly behind the overdriven wave AD but the reaction eventually separates from the wave DE as the effects of the gas expansion from the transverse wave disappear.

Two types of subcellular structure were recorded. The fine structures in the photograph to the left of the path of the triple point are tracings left in the wake of the transverse wave BC depicted in Fig. 4a. The uniformity of the fine structure is a consequence of the self-sustained nature of the transverse wave. The subcellular structure is small (approximately three orders of magnitude smaller than the cell width) since the gas is precompressed to high densities by the oblique lead shock FA. The average spacing between the lines parallel to the triple point path is 1.4 mm. The subcellular structures to the right of the triple point path are tracings in the wake of the overdriven lead shock wave AE. The increase in the size of the subcellular structure normal to the triple point path shown in Fig. 4b is a consequence of the loss of strength in the lead shock from point A to E in Fig. 4a. The subcellular structure in Fig. 4b provides a quantitative experimental

basis for assessing the physical and chemical models and computational schemes in numerical simulations of detonations.

#### 4. Conclusions

The detonability of stoichiometric hydrocarbon–air mixtures has been studied experimentally with emphasis on high-molecular-weight fuels, which have particular importance for the transportation and chemical process industries. For example, among the fuels tested,  $\alpha$ -pinene is a main constituent in turpentine, benzene is a natural fuel constituent, methylcyclopentadiene is an unleaded gasoline additive, and hexyl nitrate and ethyl hexyl nitrate are used as diesel additives. The detonation cell widths were measured primarily for stoichiometric cyclic and unsaturated hydrocarbons in air at 100 °C and 1 atm initial temperature and pressure. The detonability of hydrogen–air mixtures was also studied with emphasis on the effects of diluents, like steam and carbon dioxide. The detonation cell widths of hydrogen–air–diluent mixtures at 100 °C and 1 atm initial temperature and pressure were measured for a wide range of mixture stoichiometries. The detonability limits were measured and the fine subcellular structure of the detonation was recorded.

The detonability of the cyclic hydrocarbon fuels tested is similar except for benzene, a very stable six-carbon ring, and 2,5-dihydrofuran, an unsaturated cyclic ether. The detonation cell widths of most cyclic hydrocarbon fuels are within the range of 40–50 mm, despite differences in their chemical structure, the strain energies in their rings, or the degree of saturation. This finding has important implications for the petrochemical industry, where it was noted that there was a statistical correlation between cyclic or unsaturated fuels and the occurrence of blast [48].

Molecular structure, bond saturation, and functional groups can increase the detonability of a hydrocarbon fuel. For example, a cyclic fuel is more detonable than the corresponding straight-chain alkane at the same carbon level, an unsaturated cyclic ether is more sensitive than a saturated cyclic ether, and the substitution of a nitrate functional group is more detonable than the parent alkane.

The addition of a small amount of hexyl nitrate to octane substantially increases octane's susceptibility to detonate. Further addition of the nitrated fuel continues to increase the detonability of the alkane fuel but to a lesser extent.

The addition of a diluent, such as steam and carbon dioxide, decreases the detonability of hydrogen–air mixtures at all mixture stoichiometries. For equal concentrations, carbon dioxide is not only a better

inhibitor of a detonation than steam, but its effectiveness increases relative to steam with increasing concentrations. These results may be important with respect to accident mitigation strategies in hypothetical nuclear power plant accidents.

Detonability and flammability limits of hydrogen–air–diluent mixtures can be nearly identical, depending on the diluent and size of the test apparatus. Test results show the detonability limits coincided with the flammability limits for hydrogen–oxygen mixtures diluted with monatomic helium [25] and hydrogen–air mixtures diluted with diatomic hydrogen. The limits were also close for mixtures diluted with air. The discrepancy between flammability and detonability limits was greatest for hydrogen–air mixtures diluted with the triatomic gases steam and carbon dioxide, although the two limits may be closer at larger geometric scales, since detonability limits widen with increasing scale. This result may have important consequences for severe accident analyses at nuclear reactor scales, which can be an order of magnitude larger than the present experiments.

The uniform fine structure of the self-sustained transverse wave and the irregular structure of the overdriven lead shock are shown together along the path of the triple point as part of the subcellular structure of a detonation wave. Recent numerical computations of detonations with a detailed chemical reaction mechanism investigated the structure and energy release of the triple point region and transverse wave [49]. The present measurements can ultimately provide an experimental basis for assessing the physical and chemical models and computational schemes in detailed numerical simulations of detonations.

#### Acknowledgments

The authors thank the late W.B. Benedick for valuable technical discussions and assistance in obtaining the data. We thank C.J. Daniel, B. Heideman, M. Naro, and J.L. Mulder for their assistance in obtaining the data. The authors also thank Ray Lutgring for his useful discussions on hydrocarbon chemistry. This work was funded by the U.S. Nuclear Regulatory Commission and a joint U.S. DOE/DOD project. The work was performed at Sandia National Laboratories, which is operated for the U.S. Department of Energy under Contract DE-AC04-76DP00789.

#### References

- [1] J.H.S. Lee, *Annu. Rev. Fluid Mech.* 16 (1984) 311–336.
- [2] S.B. Dorofeev, V.P. Sidorov, A.E. Dvoishnikov, W. Breitung, *Combust. Flame* 104 (1996) 95–110.

- [3] O. Peraldi, R. Knystautas, J.H. Lee, *Proc. Combust. Inst.* 21 (1986) 1629–1637.
- [4] G.P. Nordstrom, in: C.H. Vervalin (Ed.), *Fire Protection Manual for Hydrocarbon Processing Plants*, vol. 1, third ed., Gulf Publishing Co., Houston, TX, 1985, pp. 2–8.
- [5] R. Atkinson, D.C. Bull, P.J. Shuff, *Combust. Flame* 39 (1980) 287–300.
- [6] C.M. Guirao, R. Knystautas, J.H. Lee, W. Benedick, M. Berman, *Proc. Combust. Inst.* 19 (1982) 583–590.
- [7] W.B. Benedick, C.M. Guirao, R. Knystautas, J.H. Lee, *Prog. Astronaut. Aeronaut.* 106 (1986) 181–202.
- [8] D.C. Bull, *Trans. Inst. Chem. Eng.* 57 (1979) 219–227.
- [9] D.C. Bull, J.E. Elsworth, G. Hooper, *Combust. Flame* 34 (1979) 327–330.
- [10] D.C. Bull, J.E. Elsworth, P.J. Shuff, E. Metcalfe, *Combust. Flame* 45 (1982) 7–22.
- [11] I.O. Moen, J.W. Funk, S.A. Ward, G.M. Rude, P.A. Thibault, *Prog. Astronaut. Aeronaut.* 94 (1984) 55–79.
- [12] I.O. Moen, S.B. Murray, D. Bjerkevedt, A. Rinnan, R. Knystautas, J.H. Lee, *Proc. Combust. Inst.* 19 (1982) 635–644.
- [13] H. Matsui, J.H. Lee, *Proc. Combust. Inst.* 17 (1978) 1269–1280.
- [14] I.O. Moen, M. Donato, R. Knystautas, J.H. Lee, *Proc. Combust. Inst.* 18 (1981) 1615–1622.
- [15] R. Knystautas, J.H. Lee, C.M. Guirao, *Combust. Flame* 48 (1982) 63–83.
- [16] A.A. Borisov, S.V. Khomik, V.N. Mikhalkin, *AIAA Prog. Astronaut. Aeronaut.* 133 (1990) 118–132.
- [17] F. Rashidi, H.J. Michels, *Combust. Flame* 91 (1992) 373–381.
- [18] S.R. Tieszen, D.W. Stamps, C.K. Westbrook, W.J. Pitz, *Combust. Flame* 84 (1991) 376–390.
- [19] Y. Lizhong, W. Qingan, F. Weicheng, L. Ronghai, *Combust. Flame* 120 (2000) 242–244.
- [20] S.R. Tieszen, M.P. Sherman, W.B. Benedick, J.E. Shepherd, R. Knystautas, J.H.S. Lee, *AIAA Prog. Astronaut. Aeronaut.* 106 (1986) 205–219.
- [21] A.Y. Kusharin, G.L. Agafonov, O.E. Popov, B.E. Gelfand, *Combust. Sci. Technol.* 135 (1998) 85–98.
- [22] D.W. Stamps, S.R. Tieszen, *Combust. Flame* 83 (1991) 353–364.
- [23] G. Ciccarelli, T. Ginsberg, J. Boccio, C. Economos, K. Sato, M. Kinoshita, *Combust. Flame* 99 (1994) 212–220.
- [24] G. Ciccarelli, T.G. Ginsberg, J.L. Boccio, *Combust. Sci. Technol.* 128 (1997) 181–196.
- [25] R.K. Kumar, *Combust. Flame* 80 (1990) 157–169.
- [26] K.I. Shelkin, Ya.K. Troshin, *Gasdynamics of Combustion*, Mono Book Corp., Baltimore, 1965.
- [27] J.E. Shepherd, *AIAA Prog. Astronaut. Aeronaut.* 106 (1986) 263–293.
- [28] C.K. Westbrook, P.A. Urtiew, *Proc. Combust. Inst.* 19 (1982) 615–623.
- [29] C.K. Westbrook, *Combust. Flame* 46 (1982) 191–210.
- [30] C.K. Westbrook, *Combust. Sci. Technol.* 29 (1982) 67–81.
- [31] C.K. Westbrook, *Proc. Combust. Inst.* 19 (1982) 127.
- [32] C.K. Westbrook, F.L. Dryer, *Prog. Energy Combust. Sci.* 10 (1984) 1.
- [33] C.K. Westbrook, W.J. Pitz, P.A. Urtiew, *AIAA Prog. Astronaut. Aeronaut.* 94 (1984) 151.
- [34] H.D. Beeson, R.D. McClenagan, C.V. Bishop, F.J. Benz, W.J. Pitz, C.K. Westbrook, J.H.S. Lee, in: *Twelfth ICDERS Meeting*, Ann Arbor, MI, 1989.
- [35] M. Plaster, R.D. McClenagan, C.V. Bishop, F.J. Benz, J.E. Shepherd, J.H.S. Lee, *AIAA Prog. Astronaut. Aeronaut.* 133 (1990) 37–55.
- [36] J.A. Miller, R.E. Mitchell, M.D. Smooke, R.J. Kee, *Proc. Combust. Inst.* 19 (1982) 181–196.
- [37] F. Zhang, R. Akbar, P.A. Thibault, S.B. Murray, *Shock Waves* 10 (2001) 457–466.
- [38] C.M. Guirao, R. Knystautas, J.H. Lee, *A Summary of Hydrogen–Air Detonation Experiments*, NUREG/CR-4961, SAND87-7128, May 1989.
- [39] S.R. Tieszen, M.P. Sherman, W.B. Benedick, M. Berman, *Detonability of H<sub>2</sub>–Air–Diluent Mixtures*, NUREG/CR-4905, SAND85-1263, June 1987.
- [40] D.W. Stamps, M. Berman, *Nucl. Sci. Eng.* 109 (1991) 39–48.
- [41] R.K. Kumar, *J. Fire Sci.* 3 (1985) 245–262.
- [42] H.F. Coward, G.W. Jones, *Bulletin* 503, Bureau of Mines, 1952.
- [43] M. Hertzberg, *Prog. Energy Combust.* 15 (1989) 203–239.
- [44] D. Pawel, H. Vastako, H. Wagner, AFOSR 69-2095 TR, *Institute für Physikalische Chemie*, Universität Göttingen, 1969.
- [45] Z.W. Huang, M.H. Lefebvre, P.J. Van Tiggelen, *Shock Waves* 10 (2000) 119–125.
- [46] A.K. Oppenheim, *Astronaut. Acta* 11 (6) (1965) 391–400.
- [47] G.L. Schott, *Phys. Fluids* 8 (5) (1965) 850–856.
- [48] K. Guban, *Unconfined Vapor Cloud Explosions*, The Institute of Chemical Engineers, London, 1979, in association with George Godwin Ltd.
- [49] E. Oran, J. Weber Jr., E. Stefaniew, M. Lefebvre, J. Anderson Jr., *Combust. Flame* 113 (1998) 147–163.

# Blast Loading and Blast Effects on Structures – An Overview

T. Ngo, P. Mendis, A. Gupta & J. Ramsay  
*The University of Melbourne, Australia*

**ABSTRACT:** The use of vehicle bombs to attack city centers has been a feature of campaigns by terrorist organizations around the world. A bomb explosion within or immediately nearby a building can cause catastrophic damage on the building's external and internal structural frames, collapsing of walls, blowing out of large expanses of windows, and shutting down of critical life-safety systems. Loss of life and injuries to occupants can result from many causes, including direct blast-effects, structural collapse, debris impact, fire, and smoke. The indirect effects can combine to inhibit or prevent timely evacuation, thereby contributing to additional casualties. In addition, major catastrophes resulting from gas-chemical explosions result in large dynamic loads, greater than the original design loads, of many structures. Due to the threat from such extreme loading conditions, efforts have been made during the past three decades to develop methods of structural analysis and design to resist blast loads. The analysis and design of structures subjected to blast loads require a detailed understanding of blast phenomena and the dynamic response of various structural elements. This paper presents a comprehensive overview of the effects of explosion on structures. An explanation of the nature of explosions and the mechanism of blast waves in free air is given. This paper also introduces different methods to estimate blast loads and structural response.

## 1 EXPLOSIONS AND BLAST PHENOMENON

An explosion is defined as a large-scale, rapid and sudden release of energy. Explosions can be categorized on the basis of their nature as physical, nuclear or chemical events. In physical explosions, energy may be released from the catastrophic failure of a cylinder of compressed gas, volcanic eruptions or even mixing of two liquids at different temperatures. In a nuclear explosion, energy is released from the formation of different atomic nuclei by the redistribution of the protons and neutrons within the interacting nuclei, whereas the rapid oxidation of fuel elements (carbon and hydrogen atoms) is the main source of energy in the case of chemical explosions.

Explosive materials can be classified according to their physical state as solids, liquids or gases. Solid explosives are mainly high explosives for which blast effects are best known. They can also be classified on the basis of their sensitivity to ignition as secondary or primary explosive. The latter is one that can be easily detonated by simple ignition from a spark, flame or impact. Materials such as mercury fulminate and lead azide are primary explosives. Secondary explosives when detonated create blast (shock) waves which can result in widespread damage to the surroundings. Examples include trinitrotoluene (TNT) and ANFO.

The detonation of a condensed high explosive generates hot gases under pressure up to 300 kilo bar and a temperature of about 3000-4000°C. The hot gas expands forcing out the volume it occupies. As a consequence, a layer of compressed air (blast wave) forms in front of this gas volume containing most of the energy released by the explosion. Blast wave instantaneously increases to a value of pressure above the ambient atmospheric pressure. This is referred to as the side-on overpressure that decays as the shock wave expands outward from the explosion source. After a short time, the pressure behind the front may drop below the ambient pressure (Figure 1). During such a negative phase, a partial vacuum is created and air is sucked in. This is also accompanied by high suction winds that carry the debris for long distances away from the explosion source.

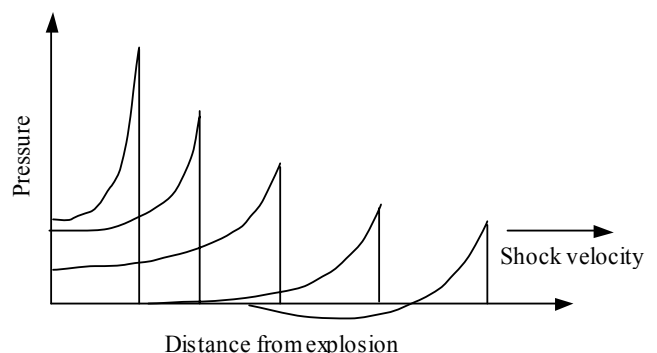


Figure 1: Blast wave propagation

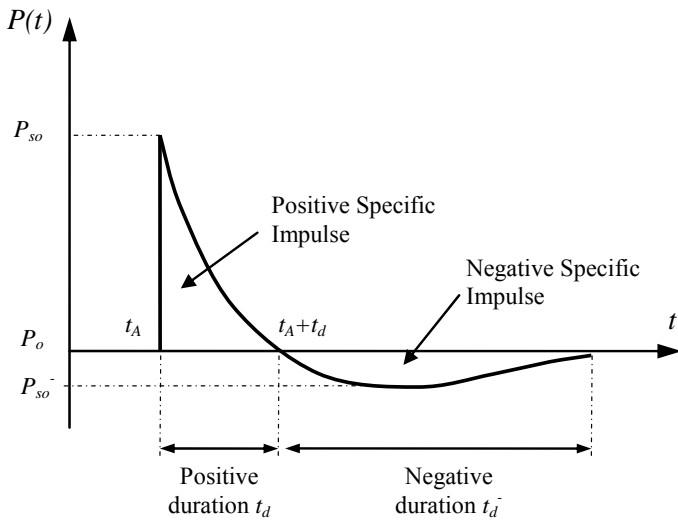


Figure 2: Blast wave pressure – Time history

## 2 EXPLOSIVE AIR BLAST LOADING

The threat for a conventional bomb is defined by two equally important elements, the bomb size, or charge weight  $W$ , and the standoff distance  $R$  between the blast source and the target (Figure 3). For example, the blast occurred at the basement of World Trade Centre in 1993 has the charge weight of 816.5 kg TNT. The Oklahoma bomb in 1995 has a charge weight of 1814 kg at a stand off of 4.5m (Longinow, 1996). As terrorist attacks may range from the small letter bomb to the gigantic truck bomb as experienced in Oklahoma City, the mechanics of a conventional explosion and their effects on a target must be addressed.

The observed characteristics of air blast waves are found to be affected by the physical properties of the explosion source. Figure 2 shows a typical blast pressure profile. At the arrival time  $t_A$ , following the explosion, pressure at that position suddenly increases to a peak value of overpressure,  $P_{so}$ , over the ambient pressure,  $P_o$ . The pressure then decays to ambient level at time  $t_d$ , then decays further to an under pressure  $P_{so-}$  (creating a partial vacuum) before eventually returning to ambient conditions at time  $t_d + t_d^-$ . The quantity  $P_{so}$  is usually referred to as the peak side-on overpressure, incident peak overpressure or merely peak overpressure (TM 5-1300, 1990).

The incident peak over pressures  $P_{so}$  are amplified by a reflection factor as the shock wave encounters an object or structure in its path. Except for specific focusing of high intensity shock waves at near  $45^\circ$  incidence, these reflection factors are typically greatest for normal incidence (a surface adjacent and perpendicular to the source) and diminish with the angle of obliquity or angular position relative to the

source. Reflection factors depend on the intensity of the shock wave, and for large explosives at normal incidence these reflection factors may enhance the incident pressures by as much as an order of magnitude.

Throughout the pressure-time profile, two main phases can be observed; portion above ambient is called positive phase of duration  $t_d$ , while that below ambient is called negative phase of duration,  $t_d^-$ . The negative phase is of a longer duration and a lower intensity than the positive duration. As the stand-off distance increases, the duration of the positive-phase blast wave increases resulting in a lower-amplitude, longer-duration shock pulse. Charges situated extremely close to a target structure impose a highly impulsive, high intensity pressure load over a localized region of the structure; charges situated further away produce a lower-intensity, longer-duration uniform pressure distribution over the entire structure. Eventually, the entire structure is engulfed in the shock wave, with reflection and diffraction effects creating focusing and shadow zones in a complex pattern around the structure. During the negative phase, the weakened structure may be subjected to impact by debris that may cause additional damage.

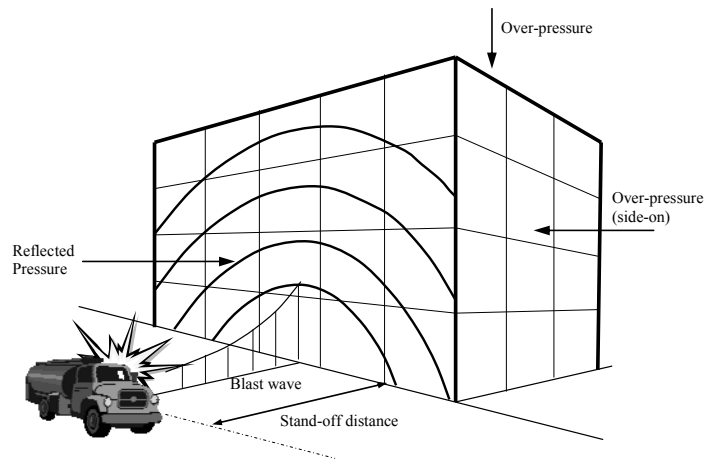


Figure 3: Blast loads on a building

If the exterior building walls are capable of resisting the blast load, the shock front penetrates through window and door openings, subjecting the floors, ceilings, walls, contents, and people to sudden pressures and fragments from shattered windows, doors, etc. Building components not capable of resisting the blast wave will fracture and be further fragmented and moved by the dynamic pressure that immediately follows the shock front. Building contents and people will be displaced and tumbled in the direction of blast wave propagation. In this manner the blast will propagate through the building.

## 2.1 Blast Wave Scaling Laws

All blast parameters are primarily dependent on the amount of energy released by a detonation in the form of a blast wave and the distance from the explosion. A universal normalized description of the blast effects can be given by scaling distance relative to  $(E/P_o)^{1/3}$  and scaling pressure relative to  $P_o$ , where  $E$  is the energy release (kJ) and  $P_o$  the ambient pressure (typically 100 kN/m<sup>2</sup>). For convenience, however, it is general practice to express the basic explosive input or charge weight  $W$  as an equivalent mass of TNT. Results are then given as a function of the dimensional distance parameter (scaled distance)  $Z = R/W^{1/3}$ , where  $R$  is the actual effective distance from the explosion.  $W$  is generally expressed in kilograms. Scaling laws provide parametric correlations between a particular explosion and a standard charge of the same substance.

## 2.2 Prediction of Blast Pressure

Blast wave parameters for conventional high explosive materials have been the focus of a number of studies during the 1950's and 1960's. Estimations of peak overpressure due to spherical blast based on scaled distance  $Z = R/W^{1/3}$  were introduced by Brode (1955) as:

$$P_{so} = \frac{6.7}{Z^3} + 1 \text{ bar } (P_{so} > 10 \text{ bar})$$

$$P_{so} = \frac{0.975}{Z} + \frac{1.455}{Z^2} + \frac{5.85}{Z^3} - 0.019 \text{ bar} \quad (1)$$

$$(0.1 \text{ bar} < P_{so} < 10 \text{ bar})$$

Newmark and Hansen (1961) introduced a relationship to calculate the maximum blast overpressure,  $P_{so}$ , in bars, for a high explosive charge detonates at the ground surface as:

$$P_{so} = 6784 \frac{W}{R^3} + 93 \left( \frac{W}{R^3} \right)^{\frac{1}{2}} \quad (2)$$

Another expression of the peak overpressure in kPa is introduced by Mills (1987), in which  $W$  is expressed as the equivalent charge weight in kilograms of TNT, and  $Z$  is the scaled distance:

$$P_{so} = \frac{1772}{Z^3} - \frac{114}{Z^2} + \frac{108}{Z} \quad (3)$$

As the blast wave propagates through the atmosphere, the air behind the shock front is moving outward at lower velocity. The velocity of the air particles, and hence the wind pressure, depends on the peak overpressure of the blast wave. This later velocity of the air is associated with the dynamic pressure,  $q(t)$ . The maximum value,  $q_s$ , say, is given by

$$q_s = 5p_{so}^2 / 2(p_{so} + 7p_o) \quad (4)$$

If the blast wave encounters an obstacle perpendicular to the direction of propagation, reflection increases the overpressure to a maximum reflected pressure  $P_r$  as:

$$P_r = 2P_{so} \left\{ \frac{7P_o + 4P_{so}}{7P_o + P_{so}} \right\} \quad (5)$$

A full discussion and extensive charts for predicting blast pressures and blast durations are given by Mays and Smith (1995) and TM5-1300 (1990). Some representative numerical values of peak reflected overpressure are given in Table 1.

Table 1. Peak reflected overpressures  $P_r$  (in MPa) with different  $W$ - $R$  combinations

$R \backslash W$	100 kg TNT	500 kg TNT	1000 kg TNT	2000 kg TNT
1m	165.8	354.5	464.5	602.9
2.5m	34.2	89.4	130.8	188.4
5m	6.65	24.8	39.5	60.19
10m	0.85	4.25	8.15	14.7
15m	0.27	1.25	2.53	5.01
20m	0.14	0.54	1.06	2.13
25m	0.09	0.29	0.55	1.08
30m	0.06	0.19	0.33	0.63

For design purposes, reflected overpressure can be idealized by an equivalent triangular pulse of maximum peak pressure  $P_r$  and time duration  $t_d$ , which yields the reflected impulse  $i_r$

$$i_r = \frac{1}{2} P_r t_d \quad (6)$$

Duration  $t_d$  is related directly to the time taken for the overpressure to be dissipated. Overpressure arising from wave reflection dissipates as the perturbation propagates to the edges of the obstacle at a velocity related to the speed of sound ( $U_s$ ) in the compressed and heated air behind the wave front. Denoting the maximum distance from an edge as  $S$  (for example, the lesser of the height or half the width of a conventional building), the additional pressure due to reflection is considered to reduce from  $P_r - P_{so}$  to zero in time  $3S/U_s$ . Conservatively,  $U_s$  can be taken as the normal speed of sound, which is about 340 m/s, and the additional impulse to the structure evaluated on the assumption of a linear decay.

After the blast wave has passed the rear corner of a prismatic obstacle, the pressure similarly propagates on to the rear face; linear build-up over duration  $5S/U_s$  has been suggested. For skeletal structures the effective duration of the net overpressure load is thus small, and the drag loading

based on the dynamic pressure is then likely to be dominant. Conventional wind-loading pressure coefficients may be used, with the conservative assumption of instantaneous build-up when the wave passes the plane of the relevant face of the building, the loads on the front and rear faces being numerically cumulative for the overall load effect on the structure. Various formulations have been put forward for the rate of decay of the dynamic pressure loading; a parabolic decay (i.e. corresponding to a linear decay of equivalent wind velocity) over a time equal to the total duration of positive overpressure is a practical approximation.

### 3 GAS EXPLOSION LOADING AND EFFECT OF INTERNAL EXPLOSIONS

In the circumstances of progressive build-up of fuel in a low-turbulence environment, typical of domestic gas explosions, flame propagation on ignition is slow and the resulting pressure pulse is correspondingly extended. The specific energy of combustion of a hydrocarbon fuel is very high (46000 kJ/kg for propane, compared to 4520 kJ/kg for TNT) but widely differing effects are possible according to the conditions at ignition.

Internal explosions likely produce complex pressure loading profiles as a result of the resulting two loading phases. The first results from the blast overpressure reflection and, due to the confinement provided by the structure, re-reflection will occur. Depending on the degree of confinement of the structure, the confined effects of the resulting pressures may cause different degrees of damage to the structure. On the basis of the confinement effect, target structures can be described as either vented or un-vented. The latter must be stronger to resist a specific explosion yield than a vented structure where some of the explosion energy would be dissipated by breaking of window glass or fragile partitions.

Venting following the failure of windows (at typically 7 kN/m<sup>2</sup>) generally greatly reduces the peak values of internal pressures. Study of this problem at the Building Research Establishment (Ellis and Crowhurst, 1991) showed that an explosion fuelled by a 200 ml aerosol canister in a typical domestic room produced a peak pressure of 9 kN/m<sup>2</sup> with a pulse duration over 0.1s. This is long by comparison with the natural frequency of wall panels in conventional building construction and a quasi-static design pressure is commonly advocated. Much higher pressures with a shorter time-scale are generated in turbulent conditions. Suitable conditions arise in buildings in multi-room explo-

sions on passage of the blast through doorways, but can also be created by obstacles closer to the release of the gas. They may be presumed to occur on release of gas by failure of industrial pressure vessels or pipelines.

### 4 STRUCTURAL RESPONSE TO BLAST LOADING

Complexity in analyzing the dynamic response of blast-loaded structures involves the effect of high strain rates, the non-linear inelastic material behavior, the uncertainties of blast load calculations and the time-dependent deformations. Therefore, to simplify the analysis, a number of assumptions related to the response of structures and the loads has been proposed and widely accepted. To establish the principles of this analysis, the structure is idealized as a single degree of freedom (SDOF) system and the link between the positive duration of the blast load and the natural period of vibration of the structure is established. This leads to blast load idealization and simplifies the classification of the blast loading regimes.

#### 4.1 Elastic SDOF Systems

The simplest discretization of transient problems is by means of the SDOF approach. The actual structure can be replaced by an equivalent system of one concentrated mass and one weightless spring representing the resistance of the structure against deformation. Such an idealized system is illustrated in Figure 4. The structural mass,  $M$ , is under the effect of an external force,  $F(t)$ , and the structural resistance,  $R$ , is expressed in terms of the vertical displacement,  $y$ , and the spring constant,  $K$ .

The blast load can also be idealized as a triangular pulse having a peak force  $F_m$  and positive phase duration  $t_d$  (see Figure 4). The forcing function is given as

$$F(t) = F_m \left( 1 - \frac{t}{t_d} \right) \quad (7)$$

The blast impulse is approximated as the area under the force-time curve, and is given by

$$I = \frac{1}{2} F_m t_d \quad (8)$$

The equation of motion of the un-damped elastic SDOF system for a time ranging from 0 to the positive phase duration,  $t_d$ , is given by Biggs (1964) as

$$M\ddot{y} + Ky = F_m \left( 1 - \frac{t}{t_d} \right) \quad (9)$$

The general solution can be expressed as:

$$y(t) = \frac{F_m}{K}(1 - \cos \omega t) + \frac{F_m}{K t_d} \left( \frac{\sin \omega t}{\omega} - t \right) \quad (10)$$

Displacement

$$\dot{y}(t) = \frac{dy}{dt} = \frac{F_m}{K} \left[ \omega \sin \omega t + \frac{1}{t_d} (\cos \omega t - 1) \right]$$

Velocity

in which  $\omega$  is the natural circular frequency of vibration of the structure and  $T$  is the natural period of vibration of the structure which is given by equation 11.

$$\omega = \frac{2\pi}{T} = \sqrt{\frac{K}{M}} \quad (11)$$

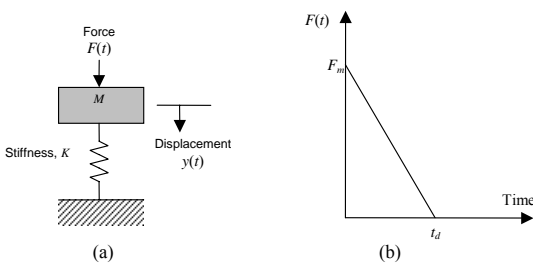


Figure 4: (a) SDOF system and (b) blast loading

The maximum response is defined by the maximum dynamic deflection  $y_m$  which occurs at time  $t_m$ . The maximum dynamic deflection  $y_m$  can be evaluated by setting  $dy/dt$  in Equation 10 equal to zero, i.e. when the structural velocity is zero. The dynamic load factor, DLF, is defined as the ratio of the maximum dynamic deflection  $y_m$  to the static deflection  $y_{st}$  which would have resulted from the static application of the peak load  $F_m$ , which is shown as follows:

$$DLF = \frac{y_{max}}{y_{st}} = \frac{y_{max}}{F_m/K} = \psi(\omega t_d) = \Psi\left(\frac{t_d}{T}\right) \quad (12)$$

The structural response to blast loading is significantly influenced by the ratio  $t_d/T$  or  $\omega t_d$  ( $t_d/T = \omega t_d / 2\pi$ ). Three loading regimes are categorized as follows:

- $\omega t_d < 0.4$  : impulsive loading regime.
- $\omega t_d < 0.4$  : quasi-static loading regime.
- $0.4 < \omega t_d < 40$  : dynamic loading regime.

#### 4.2 Elasto-Plastic SDOF Systems

Structural elements are expected to undergo large inelastic deformation under blast load or high velocity impact. Exact analysis of dynamic response is then only possible by step-by-step nu-

merical solution requiring a nonlinear dynamic finite-element software. However, the degree of uncertainty in both the determination of the loading and the interpretation of acceptability of the resulting deformation is such that solution of a postulated equivalent ideal elasto-plastic SDOF system (Biggs, 1964) is commonly used. Interpretation is based on the required ductility factor  $\mu = y_m/y_e$  (Figure 5).

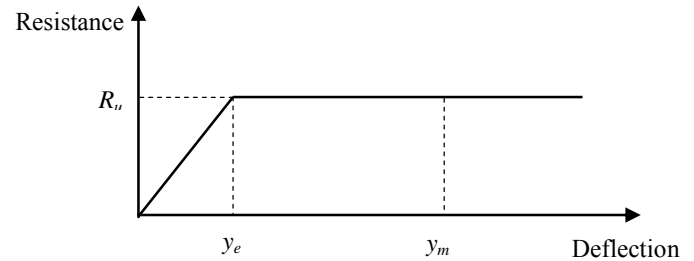


Figure 5: Simplified resistance function of an elasto-plastic SDOF system

For example, a uniform simply supported beam has first mode shape  $\phi(x) = \sin \pi x/L$  and the equivalent mass  $M = (1/2)mL$ , where  $L$  is the span of the beam and  $m$  is mass per unit length. The equivalent force corresponding to a uniformly distributed load of intensity  $p$  is  $F = (2/\pi)pL$ . The response of the ideal bilinear elasto-plastic system can be evaluated in closed form for the triangular load pulse comprising rapid rise and linear decay, with maximum value  $F_m$  and duration  $t_d$ . The result for the maximum displacement is generally presented in chart form (TM 5-1300), as a family of curves for selected values of  $R_u/F_m$  showing the required ductility  $\mu$  as a function of  $t_d/T$ , in which  $R_u$  is the structural resistance of the beam and  $T$  is the natural period (Figure 6).

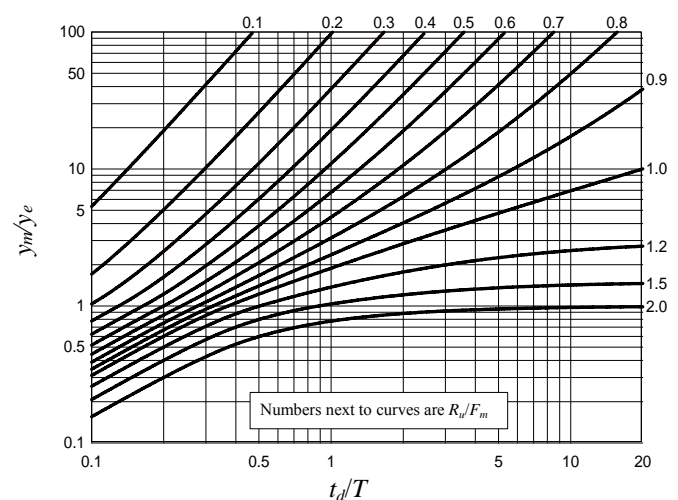


Figure 6: Maximum response of elasto-plastic SDF system to a triangular load.

## 5 MATERIAL BEHAVIORS AT HIGH STRAIN-RATE

Blast loads typically produce very high strain rates in the range of  $10^2 - 10^4 \text{ s}^{-1}$ . This high straining (loading) rate would alter the dynamic mechanical properties of target structures and, accordingly, the expected damage mechanisms for various structural elements. For reinforced concrete structures subjected to blast effects the strength of concrete and steel reinforcing bars can increase significantly due to strain rate effects. Figure 7 shows the approximate ranges of the expected strain rates for different loading conditions. It can be seen that ordinary static strain rate is located in the range :  $10^{-6} - 10^{-5} \text{ s}^{-1}$ , while blast pressures normally yield loads associated with strain rates in the range :  $10^2 - 10^4 \text{ s}^{-1}$ .

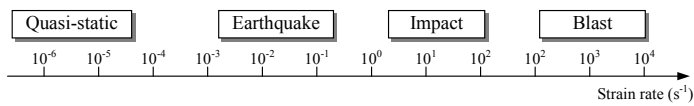


Figure 7: Strain rates associated with different types of loading

### 5.1 Dynamic Properties of Concrete under High-Strain Rates

The mechanical properties of concrete under dynamic loading conditions can be quite different from that under static loading. While the dynamic stiffness does not vary a great deal from the static stiffness, the stresses that are sustained for a certain period of time under dynamic conditions may gain values that are remarkably higher than the static compressive strength (Figure 8). Strength magnification factors as high as 4 in compression and up to 6 in tension for strain rates in the range :  $10^2 - 10^3 / \text{sec}$  have been reported (Grote et al., 2001).

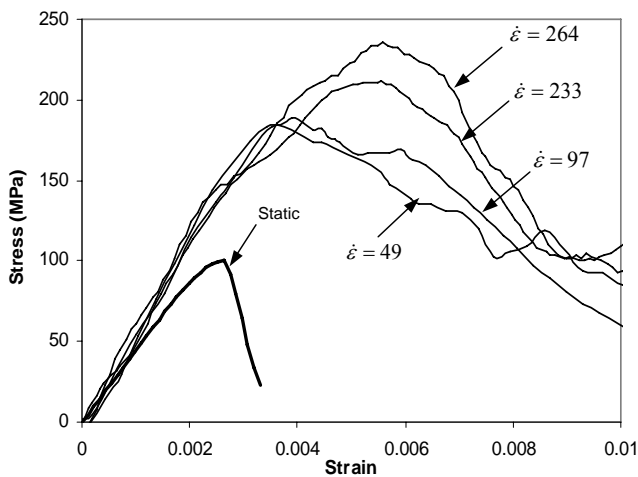


Figure 8: Stress-strain curves of concrete at different strain-rates (Ngo et al., 2004a)

For the increase in peak compressive stress ( $f'_c$ ), a dynamic increase factor (DIF) is introduced in the

CEB-FIP (1990) model (Figure 9) for strain-rate enhancement of concrete as follows:

$$DIF = \left( \frac{\dot{\epsilon}}{\dot{\epsilon}_s} \right)^{1.026\alpha} \quad \text{for } \dot{\epsilon} \leq 30 \text{ s}^{-1} \quad (13)$$

$$DIF = \gamma \left( \frac{\dot{\epsilon}}{\dot{\epsilon}_s} \right)^{1/3} \quad \text{for } \dot{\epsilon} > 30 \text{ s}^{-1} \quad (14)$$

where:

- $\dot{\epsilon}$  = strain rate
- $\dot{\epsilon}_s$  =  $30 \times 10^{-6} \text{ s}^{-1}$  (quasi-static strain rate)
- $\log \gamma = 6.156 \alpha - 2$
- $\alpha = 1 / (5 + 9 f'_c / f_{co})$
- $f_{co} = 10 \text{ MPa} = 1450 \text{ psi}$

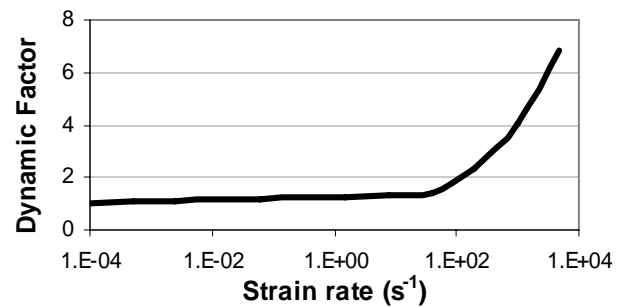


Figure 9: Dynamic Increase Factor for peak stress of concrete

### 5.2 Dynamic Properties of Reinforcing Steel under High-Strain Rates

Due to the isotropic properties of metallic materials, their elastic and inelastic response to dynamic loading can easily be monitored and assessed. Norris et al. (1959) tested steel with two different static yield strength of 330 and 278 MPa under tension at strain rates ranging from  $10^{-5}$  to  $0.1 \text{ s}^{-1}$ . Strength increase of 9 - 21% and 10 - 23 % were observed for the two steel types, respectively. Dowling and Harding (1967) conducted tensile experiments using the tensile version of Split Hopkinson's Pressure Bar (SHPB) on mild steel using strain rates varying between  $10^{-3} \text{ s}^{-1}$  and  $2000 \text{ s}^{-1}$ . It was concluded from this test series that materials of body-centered cubic (BCC) structure (such as mild steel) showed the greatest strain rate sensitivity. It has been found that the lower yield strength of mild steel can almost be doubled; the ultimate tensile strength can be increased by about 50%; and the upper yield strength can be considerably higher. In contrast, the ultimate tensile strain decreases with increasing strain rate.

Malvar (1998) also studied strength enhancement of steel reinforcing bars under the effect of high strain rates. This was described in terms of the dynamic increase factor (DIF), which can be evaluated for different steel grades and for yield stresses,  $f_y$ , ranging from 290 to 710 MPa as represented by equation 15.

$$DIF = \left( \frac{\dot{\epsilon}}{10^{-4}} \right)^\alpha \quad (15)$$

where for calculating yield stress  $\alpha = \alpha_{fy}$ ,

$$\alpha_{fy} = 0.074 - 0.04(f_y / 414) \quad (16)$$

for ultimate stress calculation  $\alpha = \alpha_{fu}$

$$\alpha_{fu} = 0.019 - 0.009(f_y / 414) \quad (17)$$

## 6 FAILURE MODES OF BLAST-LOADED STRUCTURES

Blast loading effects on structural members may produce both local and global responses associated with different failure modes. The type of structural response depends mainly on the loading rate, the orientation of the target with respect to the direction of the blast wave propagation and boundary conditions. The general failure modes associated with blast loading can be flexure, direct shear or punching shear. Local responses are characterized by localized bleaching and spalling, and generally result from the close-in effects of explosions, while global responses are typically manifested as flexural failure.

### 6.1 Global Structural Behavior

The global response of structural elements is generally a consequence of transverse (out-of-plane) loads with long exposure time (quasi-static loading), and is usually associated with global membrane (bending) and shear responses. Therefore, the global response of above-ground reinforced concrete structures subjected to blast loading is referred to as membrane/bending failure.

The second global failure mode to be considered is shear failure. It has been found that under the effect of both static and dynamic loading, four types of shear failure can be identified: diagonal tension, diagonal compression, punching shear, and direct (dynamic) shear (Woodson, 1993). The first two types are common in reinforced concrete elements under static loading while punching shear is associated with local shear failure, the familiar example of this is column punching through a flat slab. These shear response mechanisms have relatively minor structural effect in case of blast loading and can be neglected. The fourth type of shear failure is direct (dynamic) shear. This failure mode is primarily associated with transient short duration dynamic loads that result from blast effects, and it depends mainly on the intensity of the pressure waves. The associ-

ated shear force is many times higher than the shear force associated with flexural failure modes. The high shear stresses may lead to direct global shear failure and it may occur very early (within a few milliseconds of shock wave arrival to the frontal surface of the structure) which can be prior to any occurrence of significant bending deformations.

### 6.2 Localized Structural Behavior

The close-in effect of explosion may cause localized shear or flexural failure in the closest structural elements. This depends mainly on the distance between the source of the explosion and the target, and the relative strength/ductility of the structural elements. The localized shear failure takes place in the form of localized punching and spalling, which produces low and high-speed fragments. The punching effect is frequently referred to as bleaching, which is well known in high velocity impact applications and the case of explosions close to the surface of structural members. Bleaching failures are typically accompanied by spalling and scabbing of concrete covers as well as fragments and debris (Figure 10).



Figure 10: Breaching failure due to a close-in explosion of 6000kg TNT equivalent

### 6.3 Pressure-Impulse (P-I) Diagrams

The pressure-impulse (*P-I*) diagram is an easy way to mathematically relate a specific damage level to a combination of blast pressures and impulses imposed on a particular structural element. An example of a *P-I* diagram is shown in Figure 11 to show levels of damage of a structural member. Region (I) corresponds to severe structural damage and region (II) refers to no or minor damage. There are other *P-I* diagrams that concern with human response to blast in which case there are three categories of blast-induced injury, namely : primary, secondary, and tertiary injury (Baker et al., 1983).

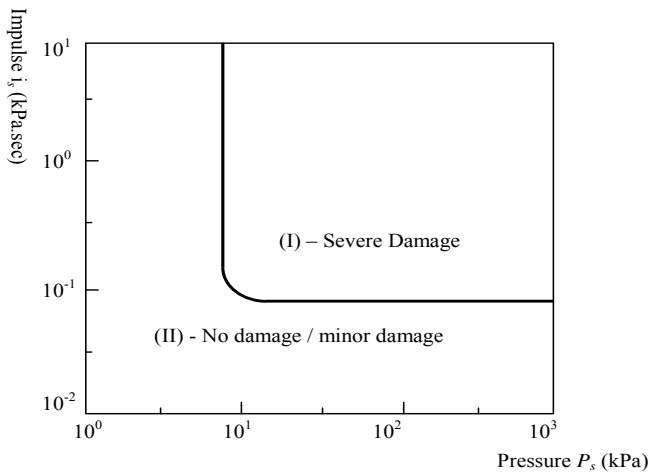


Figure 11: Typical pressure-impulse ( $P$ - $I$ ) diagram

## 7 BLAST WAVE-STRUCTURE INTERACTION

The structural behavior of an object or structure exposed to such blast wave may be analyzed by dealing with two main issues. Firstly, blast-loading effects, i.e., forces that are resulted directly from the action of the blast pressure; secondly, the structural response, or the expected damage criteria associated with such loading effects. It is important to consider the interaction of the blast waves with the target structures. This might be quite complicated in the case of complex structural configurations. However, it is possible to consider some equivalent simplified geometry. Accordingly, in analyzing the dynamic response to blast loading, two types of target structures can be considered: diffraction-type and drag-type structures. As these names imply, the former would be affected mainly by diffraction (engulfing) loading and the latter by drag loading. It should be emphasized that actual buildings will respond to both types of loading and the distinction is made primarily to simplify the analysis. The structural response will depend upon the size, shape and weight of the target, how firmly it is attached to the ground, and also on the existence of openings in each face of the structure.

Above ground or shallow-buried structures can be subjected to ground shock resulting from the detonation of explosive charges that are on/or close to ground surface. The energy imparted to the ground by the explosion is the main source of ground shock. A part of this energy is directly transmitted through the ground as directly-induced ground shock, while part is transmitted through the air as air-induced ground shock. Air-induced ground shock results when the air-blast wave compresses the ground surface and sends a stress pulse into the ground underlayers. Generally, motion due to air-induced ground is maximum at the ground surface and attenuates

with depth (TM 5-1300, 1990). The direct shock results from the direct transmission of explosive energy through the ground. For a point of interest on the ground surface, the net experienced ground shock results from a combination of both the air-induced and direct shocks.

### 7.1 Loads from Air-induced Ground Shock

To overcome complications of predicting actual ground motion, one-dimensional wave propagation theory has been employed to quantify the maximum displacement, velocity and acceleration in terms of the already known blast wave parameters (TM 5-1300). The maximum vertical velocity at the ground surface,  $V_v$ , is expressed in terms of the peak incident overpressure,  $P_{so}$ , as:

$$V_v = \frac{P_{so}}{\rho C_p} \quad (18)$$

where  $\rho$  and  $C_p$  are, respectively, the mass density and the wave seismic velocity in the soil.

By integrating the vertical velocity in Equation 18 with time, the maximum vertical displacement at the ground surface,  $D_v$ , can be obtained as:

$$D_v = \frac{i_s}{1000\rho C_p} \quad (19)$$

Accounting for the depth of soil layers, an empirical formula is given by (TM 5-1300) to estimate the vertical displacement in meters so that

$$D_v = 0.09W^{\frac{1}{6}}(H/50)^{0.6}(P_{so})^{\frac{2}{3}} \quad (20)$$

where  $W$  is the explosion yield in  $10^9$  kg, and  $H$  is the depth of the soil layer in meters.

### 7.2 Loads from Direct Ground Shock

As a result of the direct transmission of the explosion energy, the ground surface experiences vertical and horizontal motions. Some empirical equations were derived (TM 5-1300) to predict the direct-induced ground motions in three different ground media; dry soil, saturated soil and rock media. The peak vertical displacement in m/s at the ground surface for rock,  $D_{V_{rock}}$  and dry soil,  $D_{V_{soil}}$  are given as

$$D_{V_{rock}} = \frac{0.25R^{\frac{1}{3}}W^{\frac{1}{3}}}{Z^{\frac{1}{3}}} \quad (21)$$

$$D_{V_{soil}} = \frac{0.17R^{\frac{1}{3}}W^{\frac{1}{3}}}{Z^{2.3}} \quad (22)$$

The maximum vertical acceleration,  $A_v$ , in  $m/s^2$  for all ground media is given by

$$A_v = \frac{1000}{W^{\frac{1}{8}} Z^2} \quad (23)$$

## 8 TECHNICAL DESIGN MANUALS FOR BLAST-RESISTANT DESIGN

This section summarizes applicable military design manuals and computational approaches to predicting blast loads and the responses of structural systems. Although the majority of these design guidelines were focused on military applications these knowledge are relevant for civil design practice.

**Structures to Resist the Effects of Accidental Explosions, TM 5-1300 (U.S. Departments of the Army, Navy, and Air Force, 1990).** This manual appears to be the most widely used publication by both military and civilian organizations for designing structures to prevent the propagation of explosion and to provide protection for personnel and valuable equipment. It includes step-by-step analysis and design procedures, including information on such items as (1) blast, fragment, and shock-loading; (2) principles of dynamic analysis; (3) reinforced and structural steel design; and (4) a number of special design considerations, including information on tolerances and fragility, as well as shock isolation. Guidance is provided for selection and design of security windows, doors, utility openings, and other components that must resist blast and forced-entry effects.

**A Manual for the Prediction of Blast and Fragment Loadings on Structures, DOE/TIC-11268 (U.S. Department of Energy, 1992).** This manual provides guidance to the designers of facilities subject to accidental explosions and aids in the assessment of the explosion-resistant capabilities of existing buildings.

**Protective Construction Design Manual, ESL-TR-87-57 (Air Force Engineering and Services Center, 1989).** This manual provides procedures for the analysis and design of protective structures exposed to the effects of conventional (non-nuclear) weapons and is intended for use by engineers with basic knowledge of weapons effects, structural dynamics, and hardened protective structures.

**Fundamentals of Protective Design for Conventional Weapons, TM 5-855-1 (U.S. Department of the Army, 1986).** This manual provides procedures for the design and analysis of protective

structures subjected to the effects of conventional weapons. It is intended for use by engineers involved in designing hardened facilities.

**The Design and Analysis of Hardened Structures to Conventional Weapons Effects (DAHS CWE, 1998).** This new Joint Services manual, written by a team of more than 200 experts in conventional weapons and protective structures engineering, supersedes U.S. Department of the Army TM 5-855-1, Fundamentals of Protective Design for Conventional Weapons (1986), and Air Force Engineering and Services Centre ESL-TR-87-57, Protective Construction Design Manual (1989).

**Structural Design for Physical Security—State of the Practice Report (ASCE, 1995).** This report is intended to be a comprehensive guide for civilian designers and planners who wish to incorporate physical security considerations into their designs or building retrofit efforts.

## 9 COMPUTER PROGRAMS FOR BLAST AND SHOCK EFFECTS

Computational methods in the area of blast-effects mitigation are generally divided into those used for prediction of blast loads on the structure and those for calculation of structural response to the loads. Computational programs for blast prediction and structural response use both first-principle and semi-empirical methods. Programs using the first-principle method can be categorized into uncouple and couple analyses. The uncouple analysis calculates blast loads as if the structure (and its components) were rigid and then applying these loads to a responding model of the structure. The shortcoming of this procedure is that when the blast field is obtained with a rigid model of the structure, the loads on the structure are often over-predicted, particularly if significant motion or failure of the structure occurs during the loading period.

For a coupled analysis, the blast simulation module is linked with the structural response module. In this type of analysis the CFD (computational fluid mechanics) model for blast-load prediction is solved simultaneously with the CSM (computational solid mechanics) model for structural response. By accounting for the motion of the structure while the blast calculation proceeds, the pressures that arise due to motion and failure of the structure can be predicted more accurately. Examples of this type of computer codes are AUTODYN, DYNA3D, LS-DYNA and ABAQUS. Table 2 summarizes a listing of computer programs that are currently being used to model blast-effects on structures.

Table 2. Examples of computer programs used to simulate blast effects and structural response

Name	Purpose and type of analysis	Author/Vendor
BLASTX	Blast prediction, CFD code	SAIC
CTH	Blast prediction, CFD code	Sandia National Laboratories
FEFLO	Blast prediction, CFD code	SAIC
FOIL	Blast prediction, CFD code	Applied Research Associates, Waterways Experiment Station
SHARC	Blast prediction, CFD code	Applied Research Associates, Inc.
DYNA3D	Structural response + CFD (Couple analysis)	Lawrence Livermore National Laboratory (LLNL)
ALE3D	Coupled analysis	Lawrence Livermore National Laboratory (LLNL)
LS-DYNA	Structural response + CFD (Couple analysis)	Livermore Software Technology Corporation (LSTC)
Air3D	Blast prediction, CFD code	Royal Military of Science College, Cranfield University
CONWEP	Blast prediction (empirical)	US Army Waterways Experiment Station
AUTO-DYN	Structural response + CFD (Couple analysis)	Century Dynamics
ABAQUS	Structural response + CFD (Couple analysis)	ABAQUS Inc.

Prediction of the blast-induced pressure field on a structure and its response involves highly nonlinear behavior. Computational methods for blast-response prediction must therefore be validated by comparing calculations to experiments. Considerable skill is required to evaluate the output of the computer code, both as to its correctness and its appropriateness to the situation modeled; without such judgment, it is possible through a combination of modeling errors and poor interpretation to obtain erroneous or meaningless results. Therefore, successful computational modeling of specific blast scenarios by engineers unfamiliar with these programs is difficult, if not impossible.

### 10 CASE STUDY – RC COLUMN SUBJECTED TO BLAST LOADING

A ground floor column (6.4m high) of a multi-storey building (modified from a typical building designed in Australia) was analysed in this case study (see Fig. 12).

The parameters considered were the concrete strength (40MPa for NSC column and 80 MPa for

HSC column) and spacing of ligatures (400mm for ordinary detailing-OMRF and 100mm for special seismic detailing-SMRF). It has been found that with increasing concrete compressive strength, the column size can be effectively reduced. In this case the column size was reduced from 500 x 900 mm for the NSC column down to 350 x 750 for the HSC column (Table 2) while the axial load capacities of the two columns are still the same.

The blast load was calculated based on data from the Oklahoma bombing report (ASCE 1996) with a stand off distance of 11.2m. The simplified triangle shape of the blast load profile was used (see Fig. 13). The duration of the positive phase of the blast is 1.3 milliseconds.

The 3D model of the column (see Fig. 14) was analysed using the nonlinear explicit code LS-Dyna 3D (2002) which takes into account both material nonlinearity and geometric nonlinearity. The strain-rate-dependent constitutive model proposed in the previous section was adopted. The effects of the blast loading were modelled in the dynamic analysis to obtain the deflection time history of the column.

Table 3. Concrete grades and member sizes

Column	Sizes	$f'_c$ (MPa)	Ligature Spacing
NSC	500x900	40	400mm and 100mm
HSC	350x750	80	400mm and 100mm

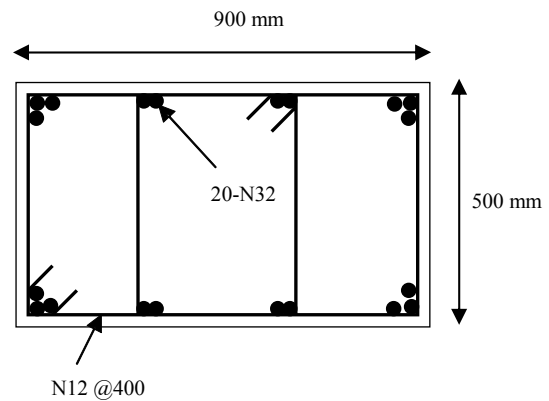


Figure 12. Cross section of the NSC column – Ordinary detailing (400 mm ligature spacing).

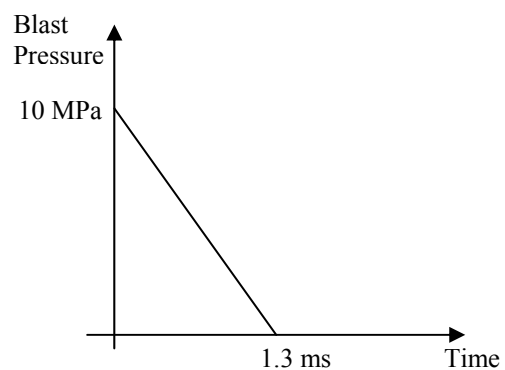


Figure 13. Blast loading

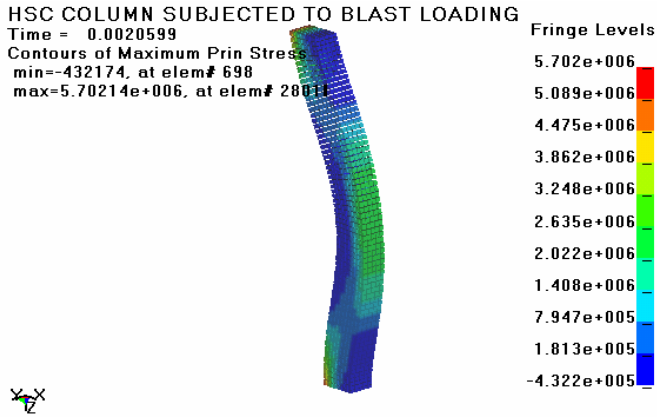


Figure 14. 3D model of the column using Explicit code LS-Dyna

The lateral deflection at mid point versus time history of two columns made of NSC and HSC are shown in Figs. 15 and 16. The graphs clearly show the lateral resistance of the columns. It can be seen that under this close-range bomb blast both columns failed in shear. However, the 80MPa columns with reduced cross section have a higher lateral deflection, which shows a better energy absorption capacity compared to that of the 40 MPa columns (see Fig. 17 and Table 4).

It can be seen from Figs. 15 and 16 that the effect of shear reinforcement is also significant. The ultimate lateral displacements at failure increase from 45mm (400 mm ligature spacing) to 63mm (100mm ligature spacing) for the HSC column. Those values for the NSC column are 20mm and 32mm, respectively.

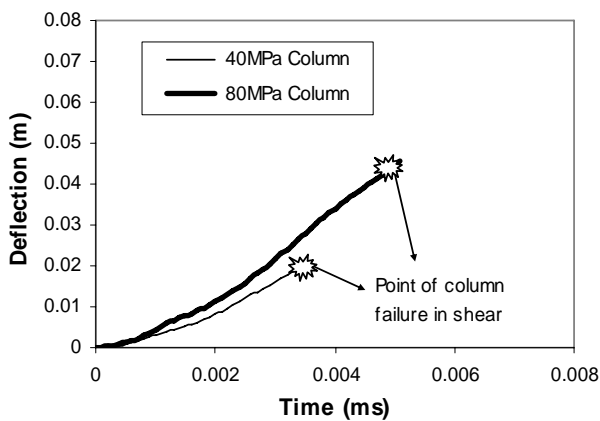


Figure 15. Lateral Deflection -Time history at mid point of column with 400mm ligature spacing (OMRF).

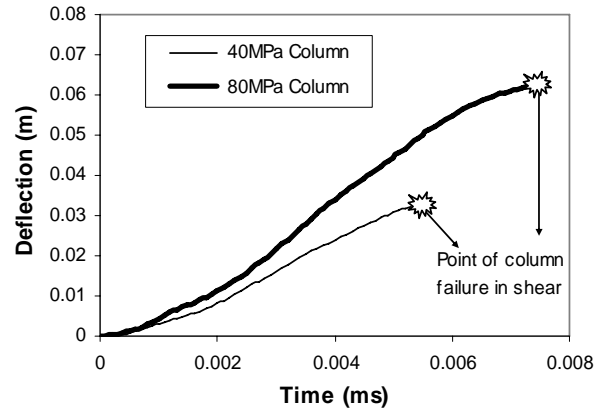


Figure 16. Lateral Deflection -Time history at mid point of column with 100mm ligature spacing (SMRF).

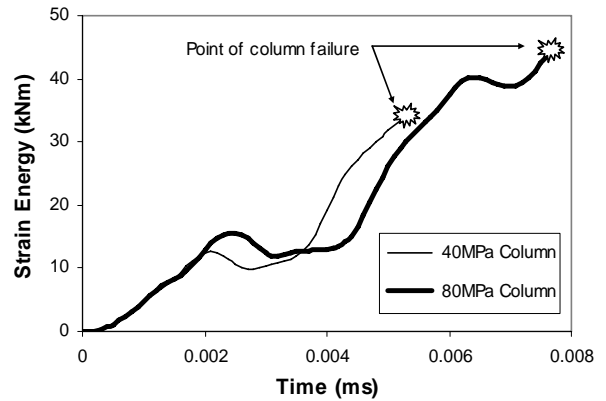


Figure 17. Comparison of energy absorption capacities (100mm ligature spacing).

Table 4. Energy absorptions at failure of HSC and NSC columns

Column	400mm spacing	100mm spacing
NSC	12.0 kNm	33.9 kNm
HSC	27.6 kNm	43.5 kNm

### 10.1 Effect of strain-rate on ductility

It is evident that increasing the rate of loading will result in increases in strength and stiffness of concrete, yield strength of steel and load-carrying capacity of reinforced concrete flexural members. A parametric study has been carried out to investigate the effects of high strain-rate on the ductility of reinforced concrete members, and on their flexural and shear capacities. The proposed strain-rate dependent model for concrete is adopted in this study. As shown in Fig. 18 the flexural capacity and the ductility of a reinforced concrete column were significantly increased due to the increase in yield strength of steel and compressive strength of concrete at high strain rate. The shear capacity of the column was calculated using the Modified Compression Field theory (Vecchio and Collins, 1986).

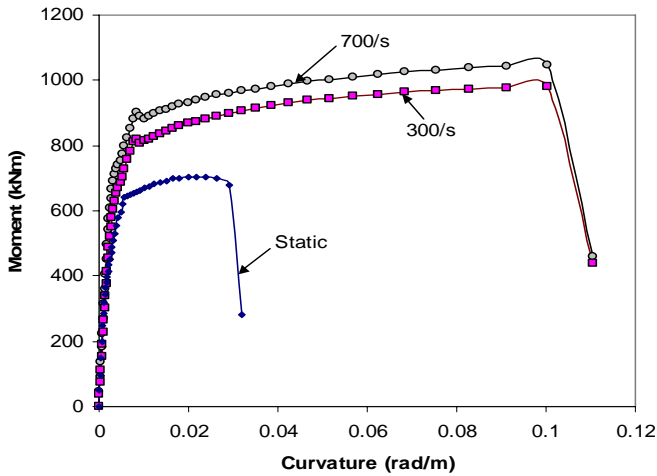


Figure 18.  $M-\phi$  curves of a cross-section of a column at different strain rates

Fig. 19 shows the increased ratio of flexural capacity ( $M_{u,dyn}/M_{u,stat}$ ) and shear capacity ( $V_{u,dyn}/V_{u,stat}$ ) at high strain rate compared to those capacities under static loading. It can be observed from Fig. 19 that the increase in flexural strength was greater than that of shear strength. Thus, the increase in the material strengths under dynamic conditions may lead to a shift from a ductile flexural failure to a brittle shear failure mode.

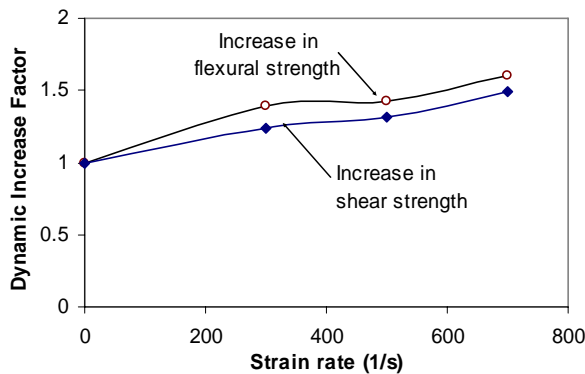


Figure 19. DIFs for flexural strength and shear strength of a column at different strain rates

## 11 CASE STUDY - PROGRESSIVE COLLAPSE ANALYSIS

Design recommendations on progressive collapse analysis have been introduced in British Standards since 1968, after the collapse of 22-storey Ronan Point apartment building. In recognition of this issue, a number of European countries, USA and Canada have incorporated progressive collapse provisions in their building codes. The American National Standards Institute (ANSI) Standard A58.1-1982, "Minimum Design Loads for Buildings and other Structures" recommends the alternative path method, in which the local failure is allowed to occur but an alternative path must be provided around the failed structural elements.

A 52 storey building (modified from a typical tall building designed in Australia) was analyzed in this study. The plan view and structural configuration of

the building are shown in Fig. 20. The typical story height is 3.85m. Perimeter columns are spaced at typical 8.4m centers and are connected by spandrel beams to support the facade. The lateral loads are resisted by 6 core boxes located at the centre of the structural plan. The building is designed to resist lateral loads due to wind and seismic ground motion specified by Australian Loading Standards AS1170.2 and AS1170.4. The slab, columns and core walls are all cast-in-place concrete. The lateral load resistance system (LLRS) of the building relies mainly on the lateral load capacity of the core walls which account for about 80% of the overall capacity.

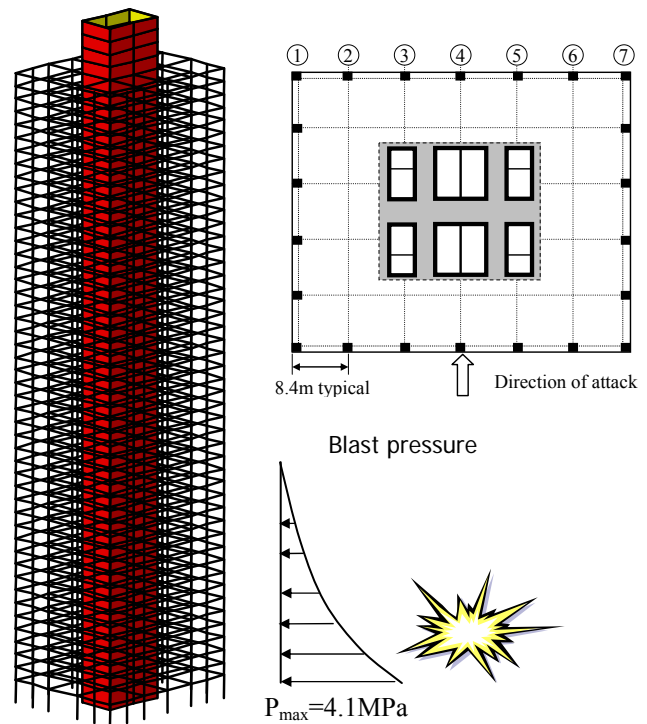


Fig. 20 Structural configuration

In this study which is based on the local damage assessment due to bomb blast at ground level, progressive collapse analyses was performed on the example building. The structural stability and integrity of the building were assessed by considering the effects of the failure of some perimeter columns, spandrel beams and floor slabs due to blast overpressure or aircraft impact. The main purpose of the analysis is to check if failure of any primary structural member will cause progressive collapse propagating beyond one story level above or below the affected member vertically, or to the next vertical structural member.

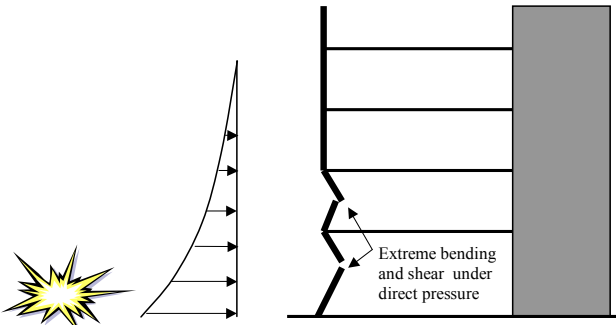


Fig. 21 Direct column loading (Blast pressure)

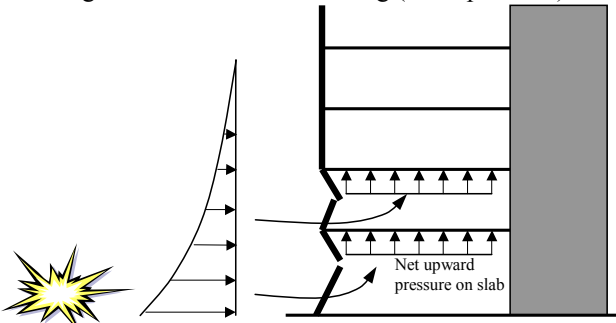


Fig. 22 Uplifting of floor slabs (Blast pressure)

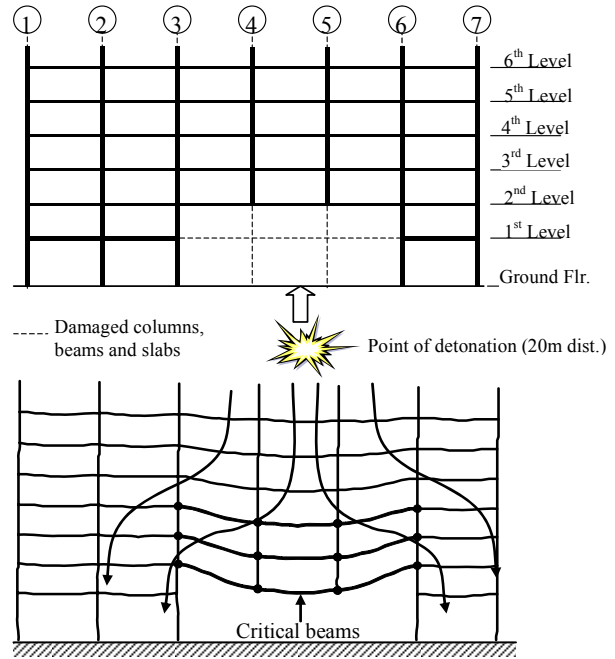


Fig. 23 Progressive collapse analysis of perimeter frame (damaged by blast load)

Figs. 21 & 22 show the effect of direct blast pressure on perimeter columns, beams and floor slabs. The concrete slabs in this example building are 125mm thick supported by prestressed wide band beams. The portion of floor slabs in close proximity to the blast were directly hit by the blast overpressure. The normal glazing façade offers insignificant resistance to the blast wave so after the failure of glazing, the blast fills the structural bay above and below each floor slab. The pressure below the slab is greater than the pressure above and causes the net upward load on each slab (Fig. 22).

To detect local damage, the blast analysis was carried out for perimeter columns, beams and floor slabs based on the actual blast pressures on each element. Results plotted in Fig. 23 show column lines 4, 5 of the ground and 1st levels failed due to the direct impact of the blast wave. Slabs and beams from column line 3 to 6 also collapsed. Member assessment was carried out using program RESPONSE (2001) based on the Modified Compression Field theory and LSDYNA (see section 10). More details are given elsewhere (Mendis & Ngo, 2002). The calculation also showed that if the columns were detailed using requirements for special moment resisting frames (SMRS) as given in ACI-318 Section 21, the shear capacity and the ductility would be improved significantly, thus improving the blast and impact resistance of the member. The damaged model of perimeter frame, in which failed elements were removed (Fig. 23), was analyzed to check if progressive collapse would propagate beyond one story level above or below.

As seen from Figs. 23, the alternative load paths go through columns surrounding the damaged area where the vertical loads are transferred. Beams and floor slabs above that area become critical due to the loss of the supporting columns. The overall stability of the structure will rely on continuity and ductility of these elements to redistribute forces within the structure. The falling debris of the collapsed members also imposes severe loading on the floors below. It is essential to check whether that overload can be carried without causing further collapse.

Parametric studies were also undertaken to investigate the impact resistance of the floor slab, assuming a floor above had collapsed onto it. The collapsing floor was treated as falling debris, i.e. the energy applied to the floor below was the weight of the collapsing floor multiplied by the height through which it fell. To obtain an estimate of the impact load-bearing capacity of the floor slab, the structure was analyzed using program LSDYNA. In addition to material and geometric nonlinearities, the analyses considered membrane action, inertia effects, and other influencing factors. The results show that the ultimate capacity of the floor slab is approximately 16.5kPa which is 2.75 times the total floor load (dead load plus 0.4 live load). Therefore in this case study if more than two floor collapsed, the falling debris of the collapsed members may impose an overload for the floor below and trigger a progressive collapse of the example building.

## 12 BLAST EFFECTS ON BUILDING'S FAÇADE

When a terrorist bomb explodes in an urban area, air blast pressure typically fractures lightweight façades

such as windows, causing catastrophic results. As a consequence of façade failure, the blast enters buildings, causing relatively superficial structural damage, but great disruption to the working environment and the mechanical and electrical services. Falling window glass shards cause injuries in addition to those resulting from blast pressure. Office fixtures and fittings are destroyed, and suspended ceiling and partitions are disturbed. Broken glass is projected everywhere, with particularly severe consequences for air conditioning systems.

Past events have shown that even relatively small explosions can cause significant window glass breakage, requiring as a minimum, window glass replacement and significant cleanup. Ideally, properly designed blast-resistant glazing should minimise, if not eliminate, flying and falling glass shards in any explosion. In addition, under air blast pressure loading, properly designed blast-resistant glazing should maintain closure of its fenestration, reducing cleanup costs and reducing pressure-related injuries. Even with blast-resistant glazing, air blast pressure will fracture windows, necessitating replacement. However, blast-resistant glazing should remain in its openings and reduce the urgency for immediate replacement.

Advanced computer codes such as CFD have been used to simulate the blast effects in the urban environment (Figs. 23, 24). A typical tall building subjected to a bomb blast detonated at different stand-off distances from the ground level was analysed in this study. The peak overpressure is 4.1MPa at the ground level and reduces rapidly up the height of the building. The average duration of loading was adopted as 15 milliseconds. Façade damage at different levels was assessed based on the blast pressure distribution and also using other in-house programs.

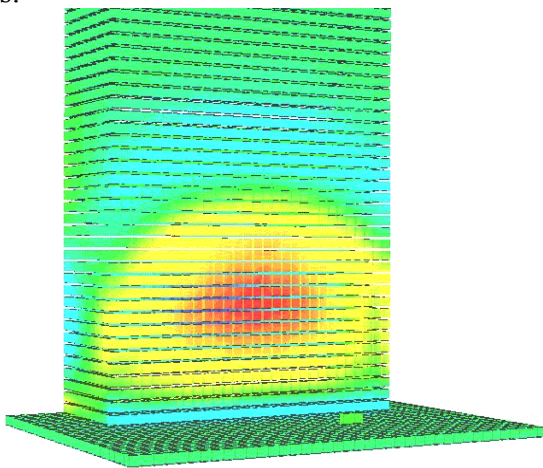


Fig. 24 CFD modelling of blast pressure on building structures (Mendis & Ngo, 2002)

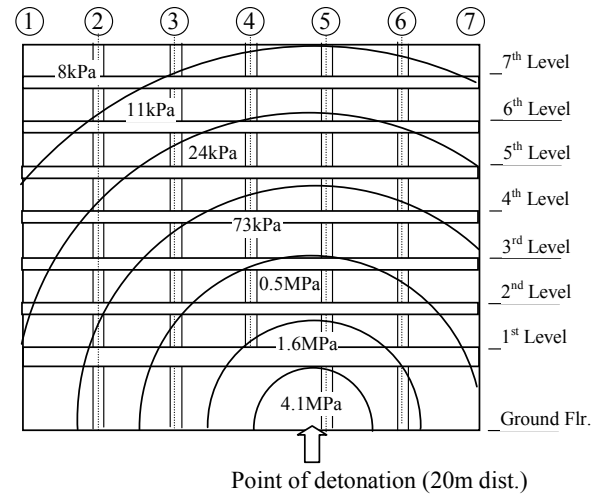


Fig. 25 Distribution of blast pressure on building façade (Mendis & Ngo, 2002)

There are only few guidelines developed to design blast-resistant façades. One of those is TM 5-1300, Structures to Resist the Effects of Accidental Explosions. In Section 6 of TM 5-1300, guidance is provided for the design, evaluation, and certification of windows to safely survive a prescribed blast environment described by a triangular-shaped pressure-time curve (Fig. 25). Window designs using monolithic (un-laminated) thermally tempered glass based on these guidelines can be expected to provide a probability of failure equivalent to that provided by current safety standards for safely resisting wind loads.

An example of a glazing system is illustrated in Fig. 25. The glazing is a rectangular, fully thermally tempered glazing panel having a long dimension,  $a$ ; a short dimension,  $b$ ; and thickness,  $t$ . The glass pane is simply supported along all four edges, with no in-plane and rotational restraints at the edges. The bending stiffness of the supporting elements of the panel is assumed to be an order of magnitude higher than that of the glass pane. Recent static and blast load tests indicate for a case in which the supporting frame deflects by up to 1/264 of the span distance, the glass pane resistance will not be significantly different to the ideal conditions of infinitely rigid supports.

The blast pressure loading is described by a peak triangular-shaped pressure-time curve as shown in Fig. 25. The blast pressure rises instantaneously to a peak blast pressure,  $B$ , and then decays linearly with a blast pressure duration,  $T$ . The pressure is uniformly distributed over the surface of the pane and applied normal to the pane.

The resistance function,  $r(X)$  (static uniform load,  $r$  as a function of centre deflection,  $X$ ) for the plate accounts for both bending and membrane stresses. The effects of membrane stresses produce a nonlinear stiffness of the resistance-deflection function (Fig. 25). The design deflection,  $X_u$  is defined as the

centre deflection where the maximum principle tensile stress at any point in the glass first reaches the design stress,  $f_u$ . Typically, as the deflection of the plate exceeds a third of its thickness, the points of maximum stress will migrate from the centre and towards the corners of the plate.

The model, illustrated in Fig. 25 uses a single-degree-of-freedom system to simulate the dynamic response of the plate. The model calculates the peak blast pressures required to exceed the prescribed probability of failure. The model assumes that failure occurs when the maximum deflection exceeds ten times the glazing thickness. More details of dynamic analysis of the glazing system can be found in TM5-1300.

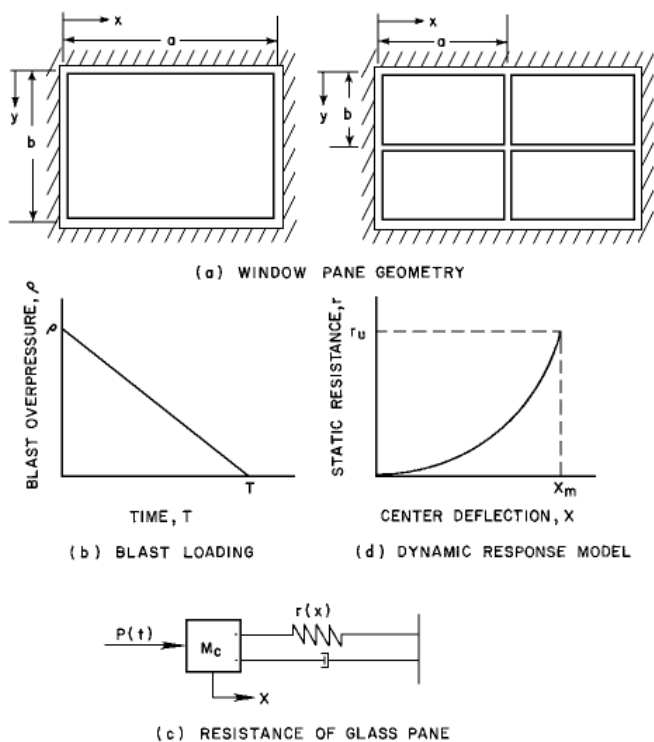


Figure 26 – Blast analysis for a glazing system

### Design Charts

In TM5-1300, guidelines are also provided in the form of load criteria for the design of both the glass panes and framing system for the window. The criteria account for both the bending and membrane stresses and their effect on maximum principle stresses and the nonlinear behaviour of glass panes. The criteria cover a broad range of design parameters for rectangular-shaped glass panes. Design charts (see Fig. 26 as an example) are presented for monolithic thermally tempered glazing with blast overpressure capacity up to 690 KPa, an aspect ratio of  $1.00 \leq a/b \leq 4.00$ , pane area  $0.1 \leq ab \leq 2.3 \text{ m}^2$ , and nominal glass thickness  $6\text{mm} \leq t \leq 20\text{mm}$ . An alternative method for blast capacity evaluation by

calculation is also provided in TM5-1300. This can be used to evaluate the blast capacity of glass when interpolation between charts is unadvisable, when design parameters are outside the limits of the chart.

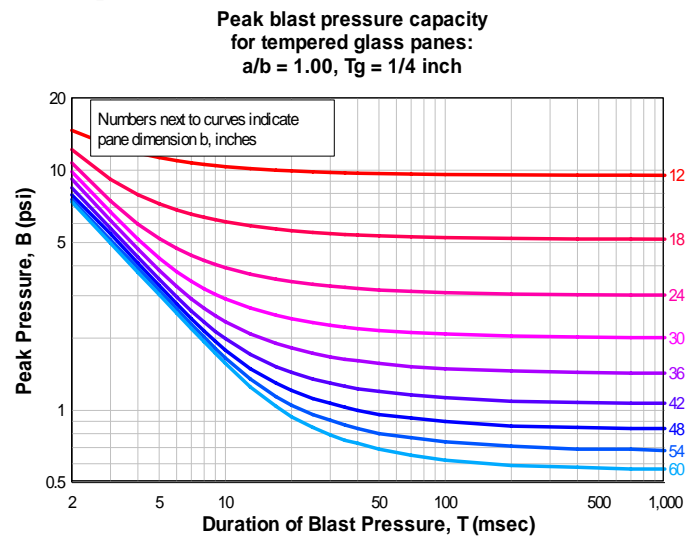


Figure 27 - A design chart for tempered glass panel (TM5-1300)

### 13 CONCLUSIONS

For high-risks facilities such as public and commercial tall buildings, design considerations against extreme events (bomb blast, high velocity impact) is very important. It is recommended that guidelines on abnormal load cases and provisions on progressive collapse prevention should be included in the current Building Regulations and Design Standards. Requirements on ductility levels also help improve the building performance under severe load conditions.

### 14 REFERENCES

1. Baker, W.E., Cox, P.A., Westine, P.S., Kulesz, J.J. and Strehlow, R.A., *Explosion hazards and evaluation*, Elsevier Scientific Publishing Company, New York, 1983.
2. Biggs, J.M, *Introduction to Structural Dynamics*, McGraw-Hill, New York, 1964.
3. Brode, H.L., "Numerical solution of spherical blast waves", *Journal of Applied Physics*, American Institute of Physics, New York, 1955.
4. Comité Euro-International du Béton, *CEB-FIP Model Code 1990*, Redwood Books, Trowbridge, Wiltshire, UK, 1990.
5. DAHS CWE, *Technical Manual - Design and Analysis of Hardened Structures to Conventional Weapons Effects*, U.S. Army Corps of Engineers (CEMP-ET), Washington DC, September, 1998.
6. DOE/TIC-11268. *A Manual for the Prediction of Blast and Fragment Loadings on Structures*, U.S. Department of Energy, Washington DC, 1992.
7. Dowling, A.R. and Harding, J., "Tensile properties of mild steel under high strain rates", *Proceedings of the 1<sup>st</sup> HERF Conf.*, University of Denver, Colorado, 1967.

8. Ellis, B.R. and Crowhurst, D., "The response of several LPS maisonettes to small gas explosions". *IStructE/BRE Seminar: Structural design for Hazardous Loads: The Role of Physical Tests*, Construction Press, New York, 1991.
9. ESL-TR-87-57, *Protective Construction Design Manual*, U.S. Air Force Engineering and Services Center, Tyndall Air Force Base, Florida, 1989.
10. Grote, D., Park, S., and Zhou, M., "Dynamic behaviour of concrete at high strain rates and pressures", *Journal of Impact Engineering*, Vol. 25, Pergamon Press, New York, pp. 869-886, 2001.
11. Longinow A, and Mniszewski KR., "Protecting buildings against vehicle bomb attacks", *Practice Periodical on Structural Design and Construction*, ASCE, New York, pp. 51-54, 1996.
12. LS-DYNA Version 960. 2002. Livermore Software Technology Corporation.
13. Malvar L.J., "Review of Static and Dynamic Properties of Steel Reinforcing Bars", *ACI Materials Journal*, 95(5), ACI, Detroit, Michigan, pp. 609-616, 1998.
14. Mendis, P.A., and Ngo, T. "Assessment of tall buildings under blast loading and aircraft impact", *Toward a better Built Environment, Innovation, Sustainability and Information Technology*, International Association of Bridge and Structural Engineering, Australia, pp. 375-376, 2002.
15. Mills, C.A., "The design of concrete structure to resist explosions and weapon effects," *Proceedings of the 1<sup>st</sup> Int. Conference on concrete for hazard protections*, Edinburgh, UK, pp. 61-73, 1987.
16. Milne-Thompson, L.M., *Theoretical Hydrodynamics*, McMillan, New York, 1968.
17. Newmark, N.M. and Hansen, R.J., "Design of blast resistant structures," *Shock and Vibration Handbook*, Vol. 3, Eds. Harris and Crede. McGraw-Hill, New York, USA. 1961.
18. Ngo, T., Mendis, P., & Itoh, A., "Modelling reinforced concrete structures subjected to impulsive loading using the Modified Continuum Lattice Model", *Proc. of 18th Australasian Conference on the Mechanics of Structures and Materials*, Perth, Australia. 2004b.
19. Ngo, T., Mendis, P., Hongwei, M. & Mak, S., "High strain rate behaviour of concrete cylinders subjected to uniaxial compressive impact loading", *Proc. of 18th Australasian Conference on the Mechanics of Structures and Materials*, Perth, Australia. 2004a.
20. Norris, G.H., Hansen, R.J., Holly, M.J., Biggs, J.M., Namyet, S. and Minami, J.K., *Structural design for dynamic loads*, McGraw-Hill, New York, USA. 1959.
21. TM 5-1300, *The Design of Structures to Resist the Effects of Accidental Explosions*, Technical Manual, US Department of the Army, Navy, and Air Force, Washington DC, 1990.
22. TM 5-855-1, *Fundamentals of Protective Design for Conventional Weapons*, U.S. Department of the Army, Washington DC, 1986.
23. Vecchio, F.J., & Collins, M.P. 1986. The Modified Compression Field Theory for Reinforced Concrete Elements Subjected to Shear, *ACI Structural Journal*, V83, 2, pp. 219-231.

# Evaluation of safety distances related to unconfined hydrogen explosions

S.B. Dorofeev\*

*FM Global, 1151 Boston-Providence Turnpike, Norwood, MA 02062, USA*

Available online 18 May 2007

## Abstract

A simple approximate method for evaluation of blast effects and safety distances for unconfined hydrogen explosions is presented. The method includes models for flame speeds, hydrogen dispersion, blast parameters, and blast damage criteria. An example of the application of this methodology for hydrogen releases in three hypothetical obstructed areas with different levels of congestion is presented. The severity of the blast effect of unconfined hydrogen explosions is shown to depend strongly on the level of congestion for relatively small releases. Extremely large releases of hydrogen are predicted to be less sensitive to the congestion level.

© 2007 International Association for Hydrogen Energy. Published by Elsevier Ltd. All rights reserved.

*Keywords:* Hydrogen explosions; Blast effects; Safety distances

## 1. Introduction

Hydrogen releases that can be expected in various accidents can result in formation of combustible mixtures of hydrogen with air. It has been shown by many investigators that weak ignition in these mixtures can easily result in efficient flame acceleration (FA), development of fast combustion regimes, and, under certain conditions, in the transition from deflagration to detonation. Pressure effects associated with fast combustion regimes can be very severe. This suggests that it is important to pay a special attention to explosion effects related to potential hydrogen releases.

It is generally agreed that hydrogen releases in confined and semi-confined geometries (tunnels, parking, garages, etc.) represent a significant safety problem, because of the principal possibility of hydrogen accumulation, and because of the promoting role of confinement for FA and pressure build-up. Unconfined hydrogen explosions can also represent a significant safety concern in situations where hydrogen releases take place in obstructed areas (refuelling stations, hydrogen production units, etc.). In these cases, relatively fast dilution of hydrogen–air mixtures at open air and inefficiency of FA without confinement can principally reduce possible consequences

of the explosions. On the other hand, these effects can be easily overbalanced by relatively large quantities of hydrogen released.

Potential consequences of unconfined hydrogen explosions are the factors that should determine safety distances for various units of hydrogen infrastructure, which deal with significant quantities of hydrogen. The major consequences of unconfined explosions are connected with blast effects, thermal effects and effects of explosion-generated fragments. Although thermal and fragment effects may be of considerable importance in some cases, the blast effects of explosions are usually of the prime interest for determination of the safety distances. This may be especially important for hydrogen because of potentially severe blast effects. Unconfined hydrogen explosions and their blast effects are the focus of the present study.

A detailed analysis of the blast effects of accidental explosions of hydrogen should generally include studies of hydrogen release and dispersion; an analysis of flame propagation, pressure build-up and blast generation in complex three-dimensional (3D) geometry; a study of the blast wave propagation and its effect on the surrounding objects. Because of the nature of the problems involved, this would generally require an application of 3D computational fluid dynamics simulations, which would be difficult or impossible to apply for all variety of the cases/applications. A simple approximate analytical tool should be useful in most cases. It can be also applied as

\* Tel.: +1 781 255 4920; fax: +1 781 255 4024.

E-mail address: [sergey.dorofeev@fmglobal.com](mailto:sergey.dorofeev@fmglobal.com).

a screening tool to select the cases where the detailed analysis may be necessary.

The objective of this study is to develop a simple approximate method for evaluation of blast effects and safety distances for unconfined hydrogen explosions. The proposed method includes:

- (i) a model for evaluation of hydrogen flame speeds in obstructed areas;
- (ii) a model for properties of “worst case” hydrogen distribution;
- (iii) a model for blast parameters;
- (iv) a set of blast damage criteria.

The following presentation includes a description of the method and an example of its application for hydrogen releases in three hypothetical obstructed areas with different levels of congestion.

## 2. Methodology

### 2.1. Evaluation of flame speeds in obstructed areas

It is well known (see, e.g., [1,2]) that the amplitude of the pressure waves generated by gaseous explosions essentially depends on the maximum flame speed achieved during the combustion process. It is therefore important to have a reliable estimate for the flame speed as a function of the propagation distance and obstacle geometry.

In the following model an initially spherical flame is considered, which propagates from an ignition source through an obstructed area. The flame speed relative to a fixed observer at a distance  $R$  from ignition,  $V_f$ , depends on the burning velocity (generally turbulent),  $S_T$ , flame area,  $A_f$ , and on the ratio of densities between the reactants and products,  $\sigma$ :

$$V_f = \sigma S_T \frac{A_f}{A_R}, \quad (1)$$

where  $A_R = 4\pi R^2$  is the area of the spherical flame at  $R$ .

The flame speed increases due to the increase of the flame area (flame folding) in an obstacle field and due to the increase of the turbulent burning rate during flame propagation. The latter effect should also describe the increase of the flame speed with distance in a system without obstacles.

The flame folding effect can be approximately described applying simple geometrical considerations as it was suggested in [3,4]. If one considers a uniform obstacle field with distance between obstacles,  $x$ , and their characteristic size,  $y$ , the following assumptions can be made. The flame is considered to be folded due to interactions of the flame with obstacles and forms a flame brush. Each obstacle inside the brush contributes the value of  $4xy$  to the total flame surface. Up to a certain distance from the ignition point,  $R_0$ , the flame brush width is equal to the flame of radius  $R$ . This yields:

$$\frac{A_f}{A_R} = 1 + \frac{4}{3} \frac{yR}{x^2}. \quad (2)$$

Flame propagation at  $R > R_0$  results in a situation where the flame brush width is smaller than the flame radius  $R$ . The width of the brush can be estimated as  $\sigma x$  because the flame tips extend with velocity  $\sigma S_T$  in the direction of the flame propagation and disappear at the rear of the brush, because of burning with the velocity  $S_T$  in the perpendicular direction. Thus at some  $R \gg R_0$ , one should expect:

$$\frac{A_f}{A_R} = 1 + \frac{4\sigma y}{x}. \quad (3)$$

If one assumes that Eq. (2) is valid for  $R = R_0 = \sigma x$ , Eq. (3) is valid at  $R = n\sigma x$ , where  $n \gg 1$ , and that the increase in the flame area with distance can be described with a power law:

$$\frac{A_f}{A_R} = 1 + AR^\alpha, \quad (4)$$

then the parameters of Eq. (4) can be expressed as

$$A = \frac{4}{3} \frac{\sigma y}{x(\sigma x)^\alpha}, \quad (5)$$

$$\alpha = \log_n 3. \quad (6)$$

The exponent  $\alpha$  may be considered as an unknown parameter of the order of 0.5 (for example,  $\alpha \approx 0.48$  for  $n = 10$ ) and Eq. (1) becomes:

$$V_f = \sigma S_T \left( 1 + \frac{4}{3} \frac{\sigma y}{x} \frac{R^\alpha}{(\sigma x)^\alpha} \right). \quad (7)$$

The effect of turbulence can be accounted for by applying Bradley correlation [5] for turbulent burning velocity,  $S_T$ :

$$\frac{S_T}{S_L} = a \left( \frac{u'}{S_T} \right)^{1/2} \left( \frac{L_T}{\delta} \right)^{1/6}, \quad (8)$$

where  $u'$  is turbulent fluctuation velocity;  $S_L$  is the laminar burning velocity;  $L_T$  is the integral length scale of turbulence;  $\delta = \nu/S_L$  is the laminar flame thickness;  $\nu$  is the viscous diffusivity; and  $a$  is a coefficient. The turbulent fluctuation velocity,  $u'$ , can be considered as a small portion of the flow speed,  $V$ , ahead of the flame:

$$u' = bV = bV_f \frac{\sigma - 1}{\sigma}, \quad (9)$$

where  $b$  is a coefficient of the order of  $10^{-2}$ . Eqs. (7)–(9) yield:

$$V_f = a^2 b \sigma (\sigma - 1) S_L \left( 1 + \frac{4}{3} \frac{\sigma y}{x} \frac{R^\alpha}{(\sigma x)^\alpha} \right)^2 \left( \frac{L_T}{\delta} \right)^{1/3}. \quad (10)$$

Eq. (10) gives an approximate description of the flame speed as a function of distance in an area with or without obstacles. It is seen that a significant increase of the flame speed with distance can be only expected in a system with obstacles,  $y \neq 0$ . In this case the contribution of parameter  $(L_T/\delta)$  is relatively weak. In the case of no obstacles,  $y = 0$ , the only estimate for  $L_T$  is a fraction of the flame radius, and the flame speed increases as  $R^{1/3}$ , which should be considered as a reasonable outcome for spherical flames without obstacles. Mixture properties are

accounted for in Eq. (10) through the values of the laminar burning velocity,  $S_L$ , and expansion ratio,  $\sigma$ .

An application of the correlation (10) for the flame speed requires determination of two unknown parameters  $a^2b$  and  $\alpha$ . For the purposes of the present analysis, these parameters were evaluated using experimental data on the flame speeds as a function of distance inside obstacle arrays [4,6] and data on flames with no obstacles [7,8]. Data for relatively high reactive fuels, including hydrogen, ethylene and propylene were selected for a wide range of distances and flame speeds (see Fig. 1). Possible values for the parameters  $a^2b$  and  $\alpha$  were determined by fitting experimental data with the function given by Eq. (10). An example of the result of the fitting procedure is presented in Fig. 2.

The model for the flame speed presented here appeared to be in a good agreement with the results of large-scale experimental data [9], presented recently in [10]. The flame speeds of about 40 and 80 m/s are reported in [10] for unconfined deflagrations in 29.7 vol% of hydrogen in air at distances of 3 and 14 m from ignition correspondingly. Eq. (10) gives 50 and 84 m/s for these distances (3 and 14 m), which is in agreement with

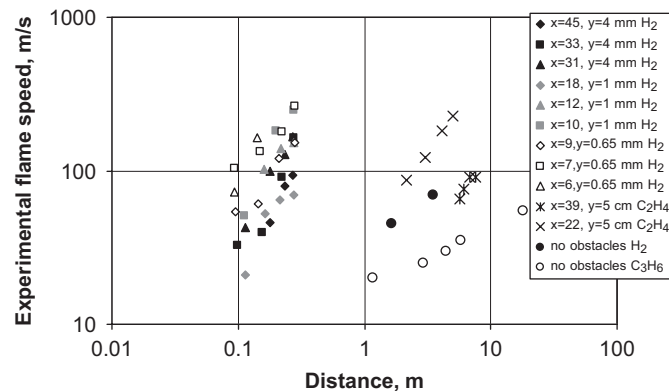


Fig. 1. Range of experimental data on flame speed versus distance used in flame speed correlation.

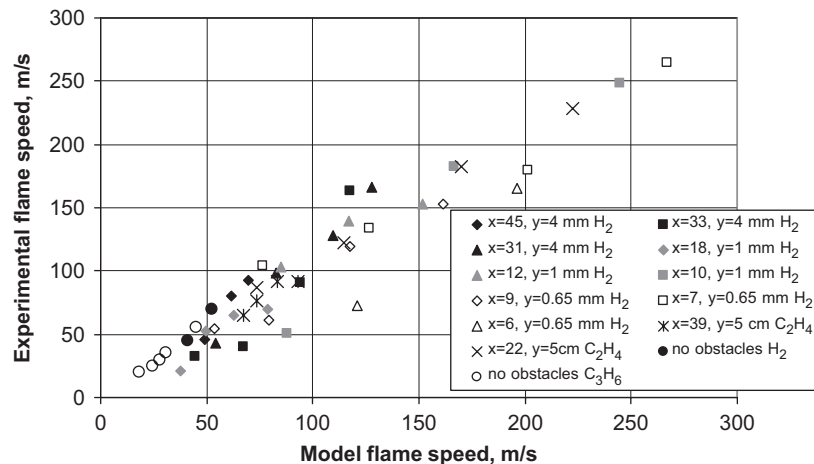


Fig. 2. Comparison of flame speed correlation ( $a^2b = 8.5e - 3$ ,  $\alpha = 0.63$ ) with experimental data.

the experimental data within the limits of accuracy of the model.

## 2.2. Hydrogen dispersion

The amplitudes of the pressure waves generated by hydrogen explosions are expected to depend on the dispersion of hydrogen in air and resulting hydrogen concentration distribution. The pressure waves generally become stronger with increase of the total energy of combustion. The blast effect also becomes more severe with the increase of the flame speed.

The focus of this section is to determine the conservative case of hydrogen dispersion for fast or nearly instantaneous releases of hydrogen. We do not consider relatively slow hydrogen releases here as they are not capable of creating a combustible mixture under unconfined conditions. Neither the assumption that all the released hydrogen forms a stoichiometric mixture with air is regarded here as a credible conservative, or “worst case” as this is considered here to be practically impossible under conditions of an unconfined accidental release of hydrogen.

There is clearly a variety of release scenarios, which can affect the resulting hydrogen dispersion. Instead of considering specific scenarios here, a simple general model will be analysed. This approximate general model assumes that the released hydrogen forms a cloud with a non-uniform hydrogen concentration. The form of the cloud is assumed to be semi-spherical, for simplicity. Hydrogen concentration is considered to reach the maximum in the centre of the semi-sphere and decreases linearly with radius. Linear decrease of the concentration with radius is chosen for simplicity as well.

The postulated properties of the hydrogen distribution are used here only for the purpose to limit the number of parameters that determine average cloud properties, and, thus, to be able to select the “worst case”. With the above assumptions, properties of hydrogen cloud are fully defined by two parameters: the maximum hydrogen concentration,  $C_{max}$ , in the cloud centre, and the total hydrogen mass in the cloud,  $m$ . As soon as the “worst case” is selected, only the average cloud properties

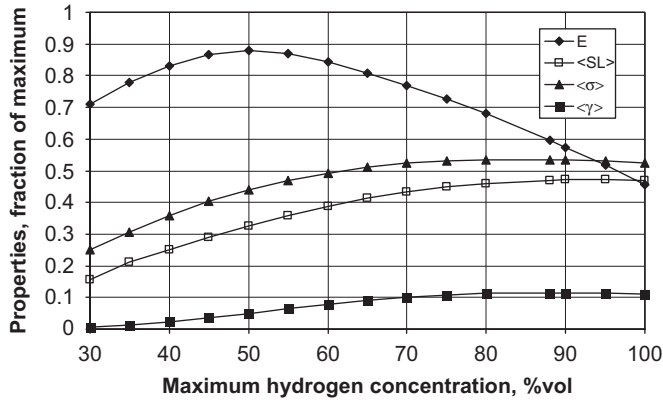


Fig. 3. Average properties of hydrogen clouds,  $E$ ,  $\langle S_L \rangle$ ,  $\langle \sigma \rangle$ , and  $\langle \gamma \rangle$  presented as fractions of their maximum achievable values versus maximum hydrogen concentration in the clouds.

are used to evaluate the explosion effect, making the assumed details of the distribution relatively unimportant.

One can define the following parameters of hydrogen distribution, which affect the severity of the blast effect. These are the total combustion energy released,  $E$ ; average laminar flame speed,  $\langle S_L \rangle$ ; average expansion ratio,  $\langle \sigma \rangle$ ; and average value of parameter  $\gamma = \sigma(\sigma - 1)S_L$ ,  $\langle \gamma \rangle$ , which defines the flame speed according to Eq. (10). A comparison of these parameters calculated as functions of the maximum hydrogen concentrations,  $C_{\max}$ , for the same total hydrogen mass is presented in Fig. 3.

The average values of the parameters were defined using integration over the volume of the flammable cloud,  $W$ . This is illustrated by the following equation for  $\langle S_L \rangle$ :

$$\langle S_L \rangle = \frac{1}{W} \int_W S_L(C) \cdot 2\pi r^2 dr, \quad (11)$$

where  $C = C(r)$  is the hydrogen concentration,  $r$  the radius from cloud centre.

Fig. 3 shows that the total energy reaches maximum at  $C_{\max} \approx 50\%$  vol, while the value of  $\langle \gamma \rangle$  at  $C_{\max} \approx 88\%$  vol. It is reasonable to assume that the “worst case” is close to the case where  $\langle \gamma \rangle$  reaches maximum ( $C_{\max} \approx 88\%$  vol), because the variation of  $E$  is relatively small compared to that of  $\langle \gamma \rangle$ . Also, the blast effect can be shown (see Section 2.3) to be determined by  $\langle \gamma \rangle^2$  and  $E^{1/3}$  as parameters. The average properties of this “worst case” are given by  $\langle S_L \rangle = 1.4$  m/s;  $\langle \sigma \rangle = 3.75$ ; and explosion energy,  $E$ , is 0.6 of the total chemical energy of hydrogen in the cloud.

The estimated value for the energy,  $E$ , does not mean that the explosion effect would be equivalent to that of an ideal (TNT) explosion with the energy of 60% of the total chemical energy of hydrogen released. This would be extremely conservative assumption. We should emphasise that in the model presented here the explosion effect is a function of the flame speed, which is proportional to the parameter  $\gamma$ , which, in its turn, is estimated to be only of about 0.1 of its maximum value for our “worst case”.

### 2.3. Blast parameters

Calculations of blast parameters are based on the methodology presented in [2]. Maximum blast overpressure,  $P$ , and positive impulse,  $I$ , are calculated as a function of distance,  $R$ , from the blast epicentre using dimensionless Sach’s variables for distance,  $R^*$ , overpressure,  $P^*$  and impulse,  $I^*$ :

$$R^* = \frac{Rp_0^{1/3}}{E^{1/3}}, \quad (12)$$

$$P^* = P/p_0, \quad (13)$$

$$I^* = \frac{Ic_0}{E^{1/3}p_0^{2/3}}, \quad (14)$$

where  $p_0$  and  $c_0$  are pressure and sound speed in the surrounding air.

According to [2], dimensionless overpressure and impulse are considered to be functions of dimensionless distance and the flame speed,  $V_f$ :

$$P^* = \min(P_1^*, P_2^*), \quad (15)$$

$$I^* = \min(I_1^*, I_2^*), \quad (16)$$

$$P_1^* = 0.34/(R^*)^{4/3} + 0.062/(R^*)^2 + 0.0033/(R^*)^3, \quad (17)$$

$$I_1^* = 0.0353/(R^*)^{0.968}, \quad (18)$$

$$P_2^* = \frac{V_f^2}{c_0^2} \frac{\sigma - 1}{\sigma} (0.83/R^* - 0.14/(R^*)^2), \quad (19)$$

$$I_2^* = \frac{V_f}{c_0} \frac{\sigma - 1}{\sigma} \left( 1 - 0.4 \frac{V_f}{c_0} \frac{\sigma - 1}{\sigma} \right) (0.06/R^* + 0.04/(R^*)^2 - 0.0025/(R^*)^3). \quad (20)$$

Eqs. (17)–(20) are presented with coefficients applicable for air explosions. These equations can be applied for ground explosions as well by doubling the value of the explosion energy in Eqs. (12) and (14).

For the purposes of the present analysis, the above description of the air blast parameters can be applied for the range of dimensionless distances  $0.33 < R^* < 3.77$ , and for visible flame speeds  $V_f \leq 500$  m/s. For higher flame speeds, transition to detonation might be possible in principle. Description of the critical conditions for transition to detonation is beyond the scope of the present model. It is worthwhile to note, however, that the blast effects from detonations and from fast flames with flame speeds of more than 500 m/s relative to a fixed observer are similar in the far field, where  $P^* < 1$ . For this reason, formulas for gas detonations, Eqs. (17) and (18), may be used directly for flame speeds exceeding 500 m/s.

Although experimental data for hydrogen were not used in [2] to derive the above descriptions for blast parameters, it is worthwhile to compare the maximum overpressures generated by spherical flames without obstacles with prediction of the present model. Experimental data of Fraunhofer ICT [9], which were recently released in [10] may be used for this purpose. The ICT experiments were made with stoichiometric hydrogen–air

Table 1  
Parameters of  $(P, I)$  diagrams for selected levels of damages

Damage description	$P_a$ (Pa)	$I_a$ (Pa s)	$k$ (Pa <sup>2</sup> s)
Total destruction of buildings	70 100	770	866 100
Threshold for partial destruction; 50–75% of walls destroyed	34 500	520	541 000
Threshold for serious structural damage; some load bearing members fall	14 600	300	119 200
Border of minor structural damage	3600	100	8950

mixtures in a hemi-spherical plastic envelope with radius of 10 m, which was cut before ignition. The maximum flame speed of 80 m/s was reported. The maximum overpressure recorded in the air blast wave was about 6 kPa. According to Eq. (10), the maximum flame speed is estimated to be 73 m/s and the maximum overpressure given by Eq. (11) is 5.1 kPa, which is in good agreement with the experimental data.

#### 2.4. Blast damage criteria

An assessment of damage potential is made here using pressure–impulse  $(P, I)$  damage criteria:

$$(I - I_a)(P - P_a) \geq k, \quad (21)$$

where  $I_a$ ,  $P_a$ , and  $k$  are parameters characterising levels of equal damage. The values of parameters  $I_a$ ,  $P_a$ , and  $k$  characterising different levels of damages from an air blast are collected in Table 1 [1,11]. As suggested in [11] these  $(P, I)$  diagrams are applicable for houses, and light-frame industrial buildings (factories, main offices, and main engineering workshops). These diagrams form the basis for evaluation of safety distances adopted in the UK.

### 3. Results and discussion

The methodology described in the previous section is applied here to calculate standoff distances from the blast epicentre at selected levels of damages. The main variable in the calculations is the total mass of hydrogen released. The methodology is applied to three hypothetical cases of obstacles surrounding the release location:

- High congestion*: Characteristic distance between obstacles,  $x = 0.2$  m; characteristic size of obstacles,  $y = 0.1$  m. This situation may be typical for a unit with multiple tubes and pipelines.
- Medium congestion*: Characteristic distance between obstacles,  $x = 1$  m; characteristic size of obstacles,  $y = 0.5$  m. This situation may be typical for a technological unit surrounded by other units/boxes.
- Low congestion*: Characteristic distance between obstacles,  $x = 4$  m; characteristic size of obstacles,  $y = 2$  m. This situation may be typical for a large technological unit surrounded by other large units (e.g., refueling station)

Fig. 4 shows the maximum flame speed in the hemispherical cloud as a function of the total mass of hydrogen released.

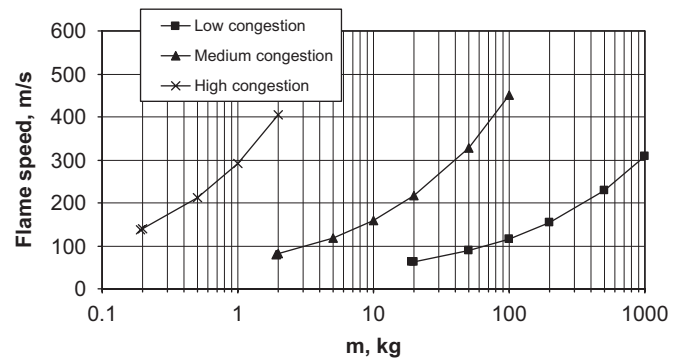


Fig. 4. Flame speed in hydrogen cloud as a function of total mass of hydrogen released.

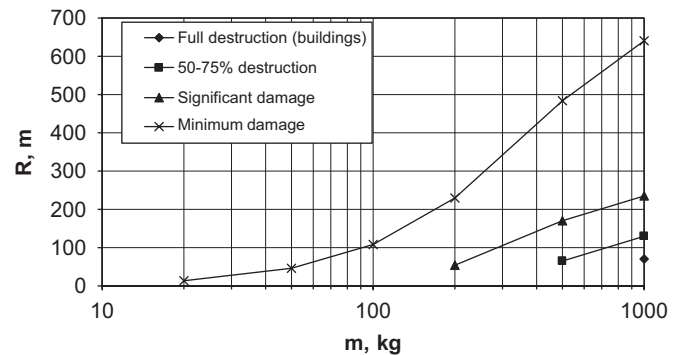


Fig. 5. Radii from blast epicentre to locations with selected levels of building damages versus total mass of hydrogen released for low congestion.

It is seen that the obstacle geometry affects significantly the maximum flame speed. It would be necessary, e.g., to release 1, 40, and 1000 kg of H<sub>2</sub> in high, medium, and low congestion correspondingly to achieve the flame speed of 300 m/s.

Radii from the blast epicentre to locations where selected levels of building damages can be observed versus total mass of hydrogen released for the three levels of congestion are presented in Figs. 5–7. It is seen that a release of 10 kg of hydrogen, e.g., would not result in building damages for the case of the low congestion. The same release in the medium congestion case would result in building damages at distances of up to 40 m. In the case of the high congestion the same release would be very severe, potentially resulting in building damages at distances of up to 70 m.

The minimum building damage criterion may be used as an option for defining safety distances. It should be noted that this

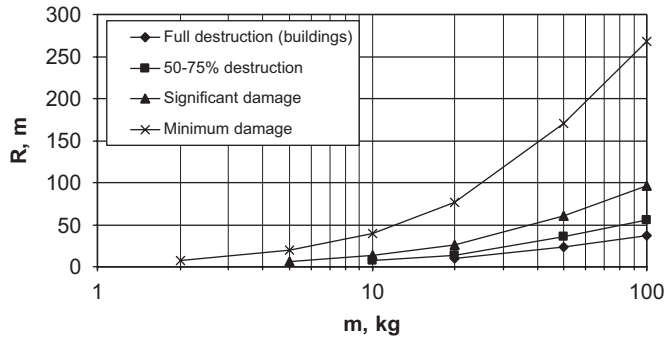


Fig. 6. Radii from blast epicentre to locations with selected levels of building damages versus total mass of hydrogen released for medium congestion.

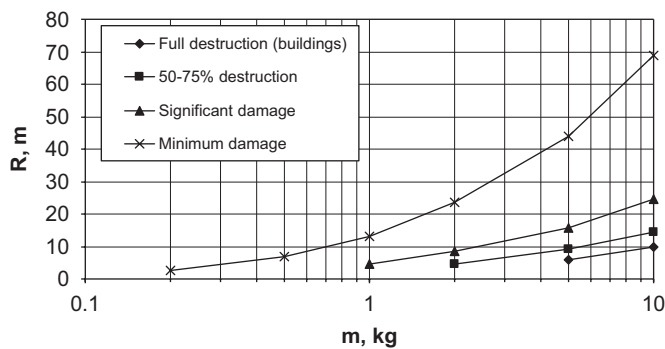


Fig. 7. Radii from blast epicentre to locations with selected levels of building damages versus total mass of hydrogen released for high congestion.

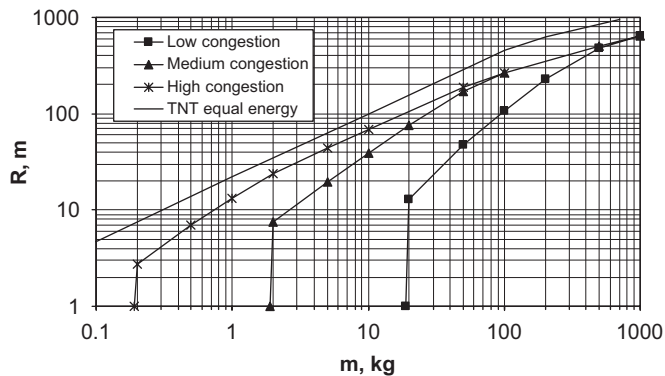


Fig. 8. Safety distances (defined by minimum damage for buildings) versus total mass of hydrogen released for three selected levels of congestion.

is not the only choice and different criteria defining safety distances may be selected. This may depend on the type of the technological unit, the type of surrounding, and/or on the applicable standards and regulations. The choice of the minimum building damage may be reasonable in many practical cases, however, it is used here as an illustration.

Fig. 8 shows the safety distances (defined by the minimum damage for buildings) versus total mass of hydrogen released for the selected levels of congestion. It is seen that there are certain threshold values of the mass of hydrogen released for

each level of congestion that may be considered as potentially damaging. These threshold values may be used as the target values to be achieved by safety systems designed to limit the release amount. It is seen also that for very large quantities of hydrogen released, the level of congestion becomes unimportant. Releases of about 1000 kg of hydrogen would certainly be very dangerous for any obstacle geometries.

Fig. 8 also shows the curve for an ideal explosion (TNT explosion is used as an ideal source) with the energy equal to the total chemical energy of hydrogen released. This curve gives the upper bound for the safety distances based on the total energy content. It is seen that the methodology presented here suggests the safety distances that are significantly smaller than the absolute maximum values. The difference is up to an order of magnitude for the masses of hydrogen released above the threshold values for each level of congestion.

If one defines an explosion yield as a fraction of the energy of TNT-explosion that produces the same damage at a specified distance, such an energy yield for unconfined hydrogen explosions considered here varies from about 2% to 50% depending on the congestion level and mass of hydrogen released (for the masses of hydrogen released above the threshold values). This suggests that the methodology presented here is able to give more accurate estimates for safety distances compared to those based on the average explosion yield, or “TNT-equivalency” values.

It should be noted here that the data presented in Fig. 8 are calculated for the purpose to illustrate the methodology proposed. They cannot be used directly as safety distances for a particular hydrogen application. Each application would require a set of calculations to be performed with account for specific density of congestion and damage criteria to be used in the definition of the safety distances.

It should be also noted that the total mass of hydrogen released is not the same as the total mass of hydrogen stored on the site. Most of applications include special safety measures designed to limit the amount of hydrogen released. It is important to mention once again here that the model for hydrogen dispersion and the respective “worst case” scenario is applicable to nearly instantaneous releases of hydrogen. It is very probable that relatively weak hydrogen releases would not be capable of creating the combustible mixture under unconfined conditions.

#### 4. Conclusions

A simple approximate method for evaluation of blast effects and safety distances for unconfined hydrogen explosions has been presented. The proposed method includes: (i) a model for evaluation of the flame speeds depending on the cloud size, composition, and obstacle geometry; (ii) a model for average parameters of “worst case” hydrogen distribution for cases of relatively fast hydrogen releases; (iii) a model for evaluation of air blast parameters; and (iv) a selection of blast damage criteria.

This set of models may be used as a simple approximate analytical tool for evaluation of the blast effects and safety

distances for unconfined hydrogen explosions. It can be also applied as a screening tool to select the cases where a detailed analysis may be necessary.

In accordance with available observations the method predicts that the blast effect of unconfined hydrogen explosions strongly depends on the level of congestion.

It was shown that certain threshold values of the mass of hydrogen released may be defined as potentially damaging. This minimum of the mass of hydrogen released varies by several orders of magnitude depending on the level of congestion. It was also shown that large hydrogen releases, of the order of 1000 kg, and more, become less sensitive to the obstacle geometry and can be dangerous for any level of congestion.

## References

- [1] Baker WE, Cox PA, Westine PS, Kulesz JJ, Strehlow RA. Explosion hazards and evaluation. Oxford, New York: Elsevier, Amsterdam; 1983.
- [2] Dorofeev SB. Blast effect of confined and unconfined explosions shock waves. In: Sturtevant B, Shepherd J, Hornung H, editors. Proceedings of the 20th ISSW, vol. 1. Singapore: Scientific Publishing Co.; 1996. p. 77–86.
- [3] Vesper A, Breitung W, Dorofeev SB. Run-up distances to supersonic flames in obstacle-laden tubes. *J Phys IV France* 2002;12(7):333–40.
- [4] Grune J, Vesper A, Stern G, Breitung W, Dorofeev S. Acceleration of unconfined flames in congested areas. Proceedings of 19th International colloquium on the dynamics of explosions and reactive systems (ICDERS), Hakone, Japan, July 27–August 1, 2003.
- [5] Bradley D, Lau KC, Lawes M. Flame stretch rate as a determinant of turbulent burning velocity. *Proc R Soc London A* 1992;338:359–87.
- [6] Pierorazio AP, Thomas JK, Baker QA, Ketchum DE. An update to the Baker–Strehlow–Tang vapor cloud explosion prediction methodology flame speed table. *Process Saf Prog* 2005;24(1):59–65.
- [7] Groethe M, Colton J, Choba S, Sato Y. Hydrogen deflagrations at large scale. Proceedings of the world hydrogen energy conference, Japan; 2004.
- [8] Geisbrecht H, Hess K, Leuckel W, Maurer B. Analysis of explosion hazards on spontaneous release of inflammable gases into the atmosphere. *Ger Chem Eng* 1981;4:305–14.
- [9] Schneider H, Pfortner H. PNP-Sicherheitssofortprogramm, Prozeßgasfreisetzung-Explosion in der Gasfabrik und Auswirkungen von Druckwellen auf das Containment. Dezember 1983, Fraunhofer-ICT internal report.
- [10] Molkov VV, Makarov DV, Schneider H. Hydrogen-air deflagrations in open atmosphere: large eddy simulation analysis of experimental data. Proceedings of first international conference on hydrogen safety, Pisa, September 8–10, 2005.
- [11] Jarrett DE. Derivation of British explosive safety distances. *Ann New York Acad Sci* 1968;152:18–35 [Article 1].

# Comparison of blast curves from vapor cloud explosions

M.J. Tang, Q.A. Baker \*

*Wilfred Baker Engineering, Inc., 8700 Crownhill, Suite 310, San Antonio, TX 78209, USA*

## Abstract

Several sets of blast curves are frequently used in the prediction of blast effects from vapor cloud explosions. However, they have not been validated by experiments since systematic experimental data have only become available in recent years. The aim of this paper is to present a comparison between the calculated blast curves and available experimental data. Also presented is a comparison between several blast curves. The comparison showed that for detonations and subsonic flames, the blast curves produced by one-dimensional numerical calculations are generally in agreement with experimental data. However, there is great difference between the measured and calculated overpressures for supersonic deflagrations. The experimental overpressures fall well below the calculated values and decay much faster. The discrepancy is more pronounced for less reactive mixtures. It can be concluded from the comparison that the prediction using one-dimensional numerical calculations is conservative and may be overly conservative for supersonic deflagrations. © 2000 Published by Elsevier Science Ltd. All rights reserved.

*Keywords:* Blast curves; Vapor cloud explosions

## 1. Introduction

Although detailed numerical simulations of fuel vapor/air combustion and the resulting blast wave propagation are being developed, there still is a great need for simple approaches which can be used on a routine basis to predict blast effects from vapor cloud explosions (VCEs). Several sets of blast curves were developed by different groups of researchers. Among them, Baker–Strehlow (Strehlow, Luckritz, Adamczyk & Shimp, 1979) and TNO (Van den Berg, 1985) blast curves are most frequently used and well accepted in safe sitting and other applications. Nevertheless, these blast curves have not been validated by experiments since systematic experimental data have only become available in recent years. Due to the efforts of investigators in many countries during the last two decades, knowledge of blast effects generated by VCEs has greatly improved. Therefore, the aim of this paper is to present a comparison between the calculated blast curves and available experimental data. Also presented is a comparison between several numerical results. In order to make a comparison,

TNO's blast curves, which are for hemispherical gas charges exploding on the ground, were converted to the blast curves for spherical, free air explosions.

The primary source of experimental data for VCE detonations is the publication by Brossard, Hendrickx, Garnier, Lannoy & Perrot (1984). The results from three different sets of experiments, which covered a volume range from  $5.2 \times 10^{-4} \text{ m}^3$  up to  $1.45 \times 10^4 \text{ m}^3$ , were summarized. Since the effect of ground reflection was carefully minimized as stated in their paper, Brossard et al.'s experimental data were directly used as free air explosions. However, the dimensional parameters employed by Brossard et al. were converted to Sach's scaling in order to make a comparison. The comparison on blast overpressure and positive impulse is presented in this paper while comparisons of other blast wave properties, such as negative overpressure, negative impulse, durations of positive and negative phases were presented in a previous paper (Tang & Baker, 1998).

Also presented in the comparison for VCE detonations is the empirical equations which were summarized by Dorofeev (1995) from spherical explosions in free air and expressed in Sach's scaling. Only overpressure and positive impulse data are available from Dorofeev's empirical equations.

The experimental data used in the comparison for supersonic and subsonic deflagrations were taken from

\* Corresponding author. Tel.: +1-210-824-5960; fax: +1-210-824-5964.

*E-mail address:* qbaker@wbeng.com (Q.A. Baker).

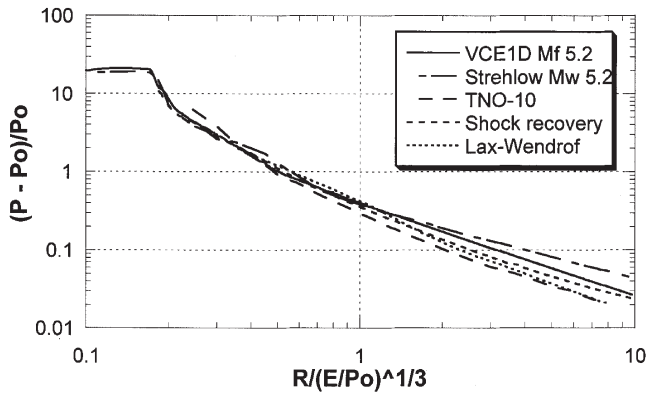


Fig. 1. Blast overpressure by various numerical techniques for vapor cloud detonations.

the EMERGE (Extended Modeling and Experimental Research into Gas Explosions) report (Mercox, Popat & Linga, 1997). The overpressures measured at four stand-off distances were also converted to Sach's scaling. Unfortunately, only overpressure data were available from the EMERGE report.

**2. Vapor cloud detonations—comparison with experimental data**

The comparison of the blast overpressures for the detonation case by using different numerical schemes is presented in Fig. 1. A discussion on several numerical schemes was presented in a previous paper (Tang, Cao & Baker, 1996). It can be seen in Fig. 1 that the Baker–Strehlow curve decays too slowly in the far field and departs significantly from the other curves. The modified Baker–Strehlow curve, which is named the Baker–Strehlow–Tang curve in order to distinguish it from the original Baker–Strehlow curve, is close to the other curves but still conservative in maintaining the slowest blast wave decay.

Comparisons of several blast curves with experimental data are presented in Figs. 2 and 3 for overpres-

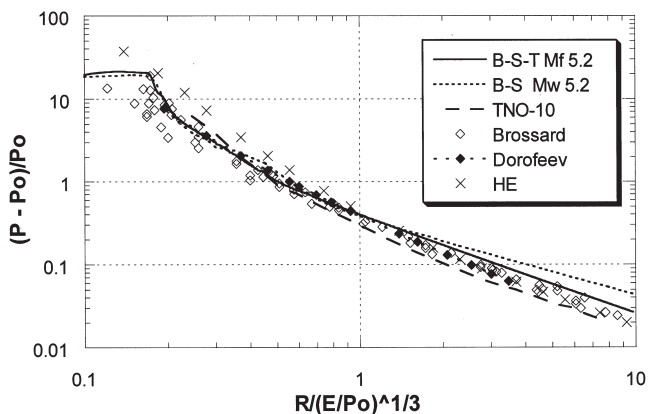


Fig. 2. Overpressure versus distance curves for vapor cloud detonations.

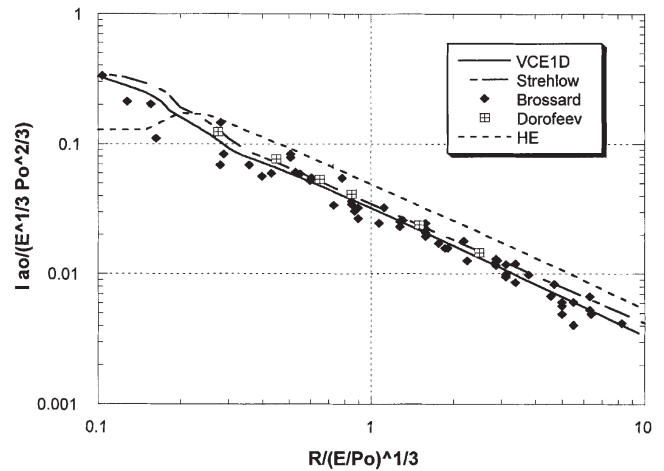


Fig. 3. Positive impulse versus distance curves for vapor cloud detonations.

sure and positive impulse versus distances, respectively. (In Figs. 1–3 the Baker–Strehlow–Tang curve is presented by a solid line). In these figures the scaled overpressure, impulse, and distance are given by the following expressions:

$$\bar{P} = \frac{p - p_0}{p_0}$$

$$\bar{i} = \frac{i a_0}{E^{1/3} p_0^{2/3}}$$

$$\bar{R} = \frac{R}{(E/p_0)^{1/3}}$$

where  $p_0$  is atmospheric pressure,  $a_0$  is the acoustic velocity at ambient conditions,  $p$  is the absolute peak pressure,  $R$  is stand-off distance,  $E$  is the energy release from the explosion source, and  $i$  is specific impulse.

The source energy in distance scaling for TNO blast curve was doubled in order to compare with free air explosions. Published experimental data were compiled and, where necessary, scaled or converted to Sach's scaling for a free air blast. Dorofeev's empirical equations are as follows:

$$\bar{P} = \frac{0.34}{\bar{R}^{4/3}} + \frac{0.062}{\bar{R}^2} + \frac{0.033}{\bar{R}^3}$$

$$\bar{i} = \frac{0.0353}{\bar{R}^{0.968}}$$

for  $0.21 < \bar{R} < 3.77$

It is shown in Fig. 2 for blast overpressure that the original Baker–Strehlow curve decays too slowly at  $\bar{R} > 2$ ; consequently, blast pressures are over-predicted in the far field. TNO's overpressures are considerably above all VCE data at close-in distances but decay faster and fall below experimental data at larger  $\bar{R}$ . The Baker–

Strehlow–Tang curve is in good agreement with experimental data over the entire range of standoffs and still conservative in the far field as shown in Fig. 2. Overpressures produced by high explosives are much higher at close-in distances as would be expected. The decay rate of the HE curve is considerably faster than for a VCE, causing the curves to cross at  $\bar{R} \cong 1.5$ . In the far field, the HE curve provides good approximation for VCE blast effects.

As shown in Fig. 3 for the positive impulse versus distance, the positive impulse predicted by the original Baker–Strehlow curve is slightly higher but still in the band of the empirical data and the Baker–Strehlow–Tang curve is in good agreement with Brossard's and Dorofeev's data. The positive impulses produced by high explosives are in general higher except very close-in to the explosion. At  $\bar{R}$  less than about 0.3, the HE curve is much lower than those produced by vapor cloud explosions. This may be attributed to the much longer time duration of vapor cloud explosions.

Comparisons of other blast wave properties, such as negative maximum overpressure, negative impulse, durations of positive and negative phases with experimental data, were presented in a previous paper (Tang & Baker, 1998). Unfortunately, only Brossard's data are available for these parameters. Good agreement is shown between the calculation and experiments except for negative time duration, for which the experimental data are quite scattered.

The good agreement between numerical calculations and experimental measurements is expected for detonation cases. In detonation experiments, strong ignition at the cloud center was applied which resulted in the detonation of the whole cloud. In the numerical models, constant flame propagation at the maximum flame speed is assumed which provides good simulation of the detonation experiments.

### 3. Fast deflagration of vapor clouds—comparison with experimental data

Although the detonation mode of combustion, which produces the most severe damage, is extremely unlikely to occur, fast deflagrations of the cloud may result from flame acceleration under confined and congested conditions in industrial environments. As the result of the MERGE (Modeling and Experimental Research into Gas Explosions) and EMERGE (Extended Modeling and Experimental Research into Gas Explosions) program, systematic experimental study was carried out for vapor clouds under various confined and congested conditions. The aim of this paper is not to study the effects of confinement and congestion on blast parameters but rather to study the blast decay from vapor clouds with various flame speeds.

A comparison was made between the experimental data and the Baker–Strehlow–Tang blast curve. Overpressures from vapor cloud explosions measured at four stand-off distances were converted to Sach's scaling. The source energies were calculated from obstructed regions in the cloud and a factor of 2 was included to account for ground reflection. Several types of combustible mixtures were tested in the EMERGE experiments. The symbols M and P denote stoichiometric mixtures of methane/air and propane/air; M+ and P+ denote stoichiometric mixtures of methane and propane with 22.5% oxygen enriched air; M++ and P++ denote stoichiometric mixtures of methane and propane with 24% oxygen enriched air, respectively. Heat of combustion for each type of mixture was calculated according to the stoichiometry and oxygen concentration in air. This resulted in slight differences in scaled distances.

The details of obstacle configuration, which is the dominant factor in flame acceleration, and other experimental details are neglected and only the maximum of flame speed and the pressure achieved in the cloud are presented as the variables since the flame acceleration process is not of concern in this paper. Obstacle configurations and other experimental details can be found from the EMERGE report since the same test number is used in the figures (the letters, S (small) and M (medium) are added to the test number to illustrate the test scale).

The location of the largest distance from the ignition point where flame speed and pressure remain at their maximum values does influence the blast decay curve. Unfortunately, the location at which pressure began to decay was not provided in the EMERGE report. It is assumed for this paper that the maximum was at the cloud edge before expansion.

The blast curves for various flame speeds in the supersonic regime merge into a single one outside the cloud in energy scaled coordinates, as presented by the authors in a previous paper (Tang & Baker, 1998). Only inside the cloud does the overpressure and impulse vary with flame speed. Comparison of Baker–Strehlow–Tang blast curves with EMERGE data for supersonic flames is presented in Figs. 4 and 5 for the medium and small scale tests since overpressure outside the cloud was not obtained in large scale tests.

Blast curves corresponding to flame Mach numbers 1 and 2 are presented in the comparison since the measured maximum overpressures were in the range between flame Mach numbers 1 and 2.

The decay of the experimental blast curves is much faster than the calculations, as shown in Figs. 4 and 5. This may be explained by the fact that the constant flame speed at the maximum value was used in the calculations whereas in the experiments a large portion of the cloud burned at very low burning velocities before the flame accelerated to the maximum speed. Therefore, the fraction of the source energy which is released at sufficiently

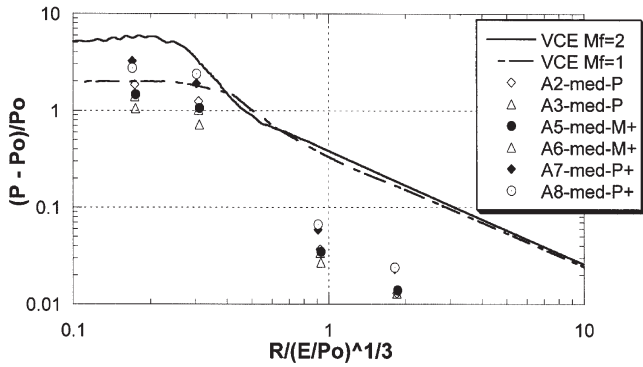


Fig. 4. Baker–Strehlow–Tang Curves and EMERGE medium scale supersonic flames.

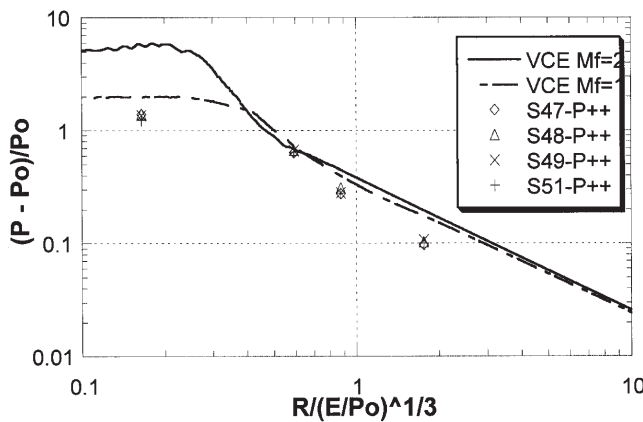


Fig. 5. Baker–Strehlow–Tang curves and EMERGE small scale supersonic flames.

high rate to support the shock wave is much less in the experiments than in the calculations.

Comparing Figs. 4 and 5, it can be seen that the decay of the experimental blast curves from medium scale tests is much faster than that from the small scale tests. This may be attributed to the fact that more reactive mixtures were used in the small scale tests in order to achieve high flame speed in a much shorter propagation distance. The fast flame acceleration in small scale tests also indicated that the fraction of the source energy which is effective in supporting the shock waves is relatively greater than in medium scale tests where the mixture reactivity is relatively lower.

#### 4. Subsonic deflagration of vapor clouds—comparison with experimental data

Unlike the blast curves from supersonic flames, the speed of flame propagation has a significant influence on blast parameters both inside and outside the source volume for subsonic flames. Here, the terminology “supersonic” and “subsonic” are with respect to the ambient sound velocity. Comparison of the calculated and the

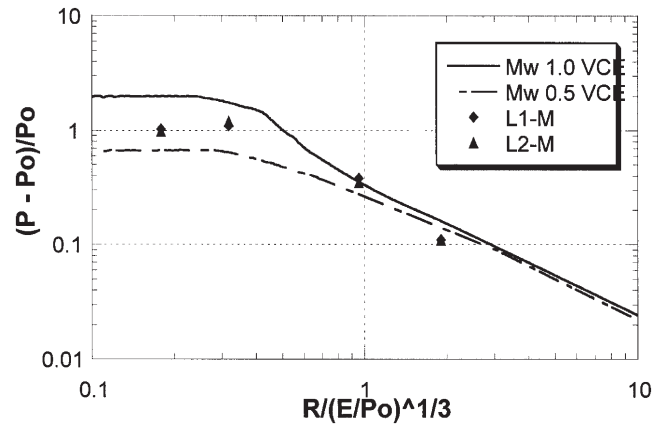


Fig. 6. Baker–Strehlow–Tang curves and EMERGE large scale subsonic flames.

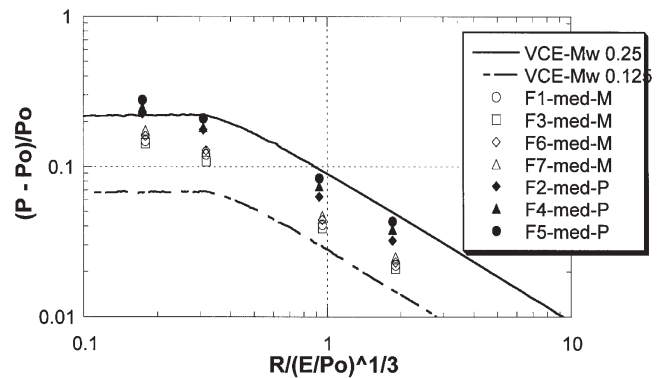


Fig. 7. Baker–Strehlow–Tang curves and EMERGE medium scale subsonic flames.

measured overpressures in large scale and medium scale experiments are presented in Figs. 6 and 7.

Only two test runs were conducted in the large scale experiments for a methane/air mixture and the maximum flame speeds achieved in the cloud were between flame Mach number of 0.7 to 0.8. The maximum overpressures were about 1 bar. The blast decay of these two runs is shown in Fig. 6 which is comparable with the Baker–Strehlow–Tang blast curves of Mw between 0.5 and 1.0; however, the experimental blast data decay faster. Unfortunately, there are not enough experimental data to draw any conclusions. In two other large scale runs using a more reactive mixture, propane/air, higher flame speeds and overpressures were measured inside the cloud. The flame Mach number was about 1.3 and overpressures were about 3 bar. The data of overpressure at locations outside the cloud were not available.

The maximum flame speeds and overpressures obtained in the cloud in medium scale experiments are much lower than those measured in large scale experiments. Flame Mach numbers were between 0.25 and 0.4 and the maximum overpressures were about 0.15 to 0.3 bar. The decay of the blast waves obtained in medium

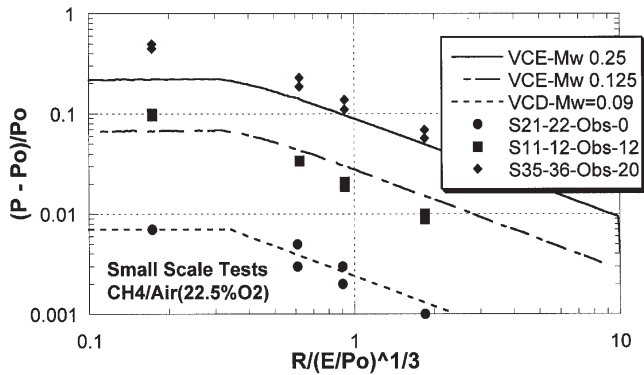


Fig. 8. Baker–Strehlow–Tang curves and EMERGE small scale subsonic flames.

scale experiments is shown in Fig. 7, which is comparable with the Baker–Strehlow–Tang blast curves of Mw between 0.125 and 0.25.

The experimental blast curves for individual runs and the calculated curves are nearly parallel. This indicates that they follow the same decay laws. The explanation is that in this regime the disturbance is weak and the blast waves are close to sound waves. It is also shown in Fig. 7 that overpressures are higher at all distances for the propane/air mixture.

In order to present more experimental data in Figs. 8–10, each symbol represents several test runs under the same experimental conditions. The effects of the number of obstacles and mixture reactivity are clearly shown in these figures. However, the focus of this paper is on the blast decay outside the cloud. As can be seen in these figures, the experimental blast curves agree well with the calculated ones in the subsonic regime. This may be explained by the fact that the blast waves generated by slow deflagrations are not much stronger than a sound wave so that they follow the same decay law.

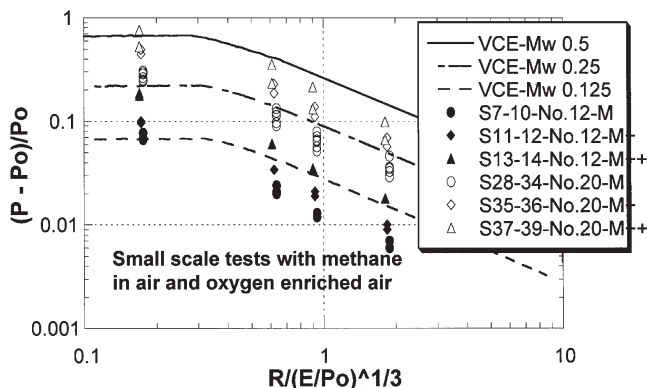


Fig. 9. Baker–Strehlow–Tang curves and EMERGE medium scale subsonic flames (methane).

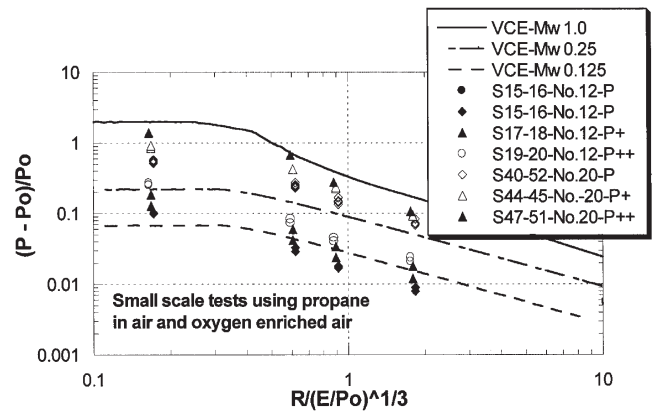


Fig. 10. Baker–Strehlow–Tang curves and EMERGE medium scale subsonic flames (propane).

## 5. Conclusions and discussions

The following conclusions were drawn as a result of the comparisons presented between numerical calculations and experimental data.

1. For vapor cloud detonations, the blast curves produced by one-dimensional numerical calculations are generally in agreement with experimental data. This is due to the fact that a constant flame speed at the maximum value is assumed in the calculations, which is consistent with the detonation experiments.
2. Among various numerical methods, the Baker–Strehlow–Tang blast curves were found to be in good agreement with available experimental data. It appears that the original Baker–Strehlow curves decay too slowly with distance, particularly for the overpressure curve, resulting in over-prediction in the far field. Conversely, TNO's overpressures were too high at close-in distances and lower than experimental data at far distances.
3. An overall conclusion could not be developed for the comparison between calculated blast curves and experimental data for vapor cloud deflagrations due to the complication of VCE deflagrations. In order to draw meaningful conclusions, the comparison was made for supersonic and subsonic deflagrations, respectively.
4. For supersonic deflagrations, the calculated blast curves for various flame speeds merge with the detonation curve once outside the cloud. The EMERGE experimental overpressures fall well below the calculated values and decay much faster. This may be explained by the difference in flame propagation. A constant flame speed is assumed for the whole cloud in numerical calculations, whereas in experiments the maximum flame speed was only achieved after flame acceleration. In other words, a large fraction of the

cloud was burned at much lower rate which is not sufficient to support the shock wave.

5. The discrepancy between the measured and calculated overpressures is more pronounced for less reactive mixtures. This may be due to the longer distance required for flame acceleration with less reactive mixtures, causing a larger percentage of the cloud to burn at a low rate.
6. For subsonic flames, the flame speed plays a dominant role in determining blast effects both inside and outside the cloud. In the subsonic regime, experimental and calculated blast waves agree well because both follow the decay law of a sound wave.
7. An overall conclusion is that the prediction using one-dimensional numerical calculations with a constant flame speed is conservative for compact clouds (dimensional effects for elongated clouds will be discussed in another paper), and may be overly conservative for supersonic deflagrations.
8. The conclusions on vapor cloud deflagrations are based on the comparison between experimental data and blast curves on overpressures only because impulse data are not available.

## References

- Brossard, J., Hendrickx, S., Garnier, J. L., Lannoy, A., & Perrot, J. L. (1984). Air blast from unconfined gaseous detonations. In *Proceedings of the 9th International Colloquium on Dynamics of Explosion and Reactive Systems*. The American Institute of Aeronautics and Astronautics.
- Dorofeev, S. B. (1995). Blast effects of confined and unconfined explosions. In *Proceedings of the 20th International Symposium on Shock Waves*.
- Mercx, W.P.M., Popat, N.R., & Linga, H. (1997). Experiments to investigate the influence of an initial turbulence field on the explosion process. Final Summary Report for EMERGE.
- Strehlow, R. A., Luckritz, R. T., Adamczyk, A. A., & Shimp, S. A. (1979). The blast wave generated by spherical flames. *Combustion and Flame*, 35, 297–310.
- Tang, M. J., Cao, C. Y., & Baker, Q. A. (1996). Blast effects from vapor cloud explosions. In *International Loss Prevention Symposium, Bergen, Norway, June 1996*.
- Tang, M. J., & Baker, Q. A. (1998). Predicting blast effects from fast flames. In *32th Loss Prevention Symposium*. AIChE.
- Van den Berg, A. C. (1985). The multi-energy method—a framework for vapor cloud explosion blast prediction. *Journal of Hazard Materials*, 12, 1–10.

# LES modelling of an unconfined large-scale hydrogen–air deflagration\*

Vladimir Molkov<sup>1,3</sup>, Dmitriy Makarov<sup>1</sup> and Helmut Schneider<sup>2</sup>

<sup>1</sup> FireSERT Institute, University of Ulster, Newtownabbey, Co. Antrim BT37 0QB, UK

<sup>2</sup> Fraunhofer Institute on Chemical Technology, Joseph-von-Fraunhoferstr. 7, 76327 Pfingsttal, Germany

E-mail: [v.molkov@ulster.ac.uk](mailto:v.molkov@ulster.ac.uk)

Received 16 February 2006, in final form 28 July 2006

Published 29 September 2006

Online at [stacks.iop.org/JPhysD/39/4366](http://stacks.iop.org/JPhysD/39/4366)

## Abstract

This paper describes the large eddy simulation modelling of unconfined large-scale explosions. The simulations are compared with the largest hydrogen–air deflagration experiment in a 20 m diameter hemispherical polyethylene shell in the open. Two combustion sub-models, one developed on the basis of the renormalization group (RNG) theory and another derived from the fractal theory, were applied. Both sub-models include a sub-grid scale model of the turbulence generated by flame front itself based on Karlovitz's theory and the observation by Gostintsev *et al* on a critical distance for transition from laminar to self-similar flame propagation regime. The RNG sub-model employs Yakhot's formula for turbulent premixed flame propagation velocity. The best fit flame propagation dynamics is obtained for the fractal sub-model with a fractal dimension  $D = 2.22$ . The fractal sub-model reproduces the experimentally observed flame acceleration during the whole duration of explosion, accurately simulating the negative phase of the pressure wave but overestimating by 50% the positive phase amplitude. The RNG sub-model is closer to the experiment in predicting the positive phase but under-predicts by 30% the negative phase amplitude. Both sub-models simulate experimental flame propagation up to 20 m and pressure dynamics up to 80 m with reasonable accuracy.

(Some figures in this article are in colour only in the electronic version)

## Nomenclature

$A$	Flame area, m <sup>2</sup>	$E_{\text{ign}}$	Ignition energy, J
$CFL$	Courant–Friedrichs–Lewy number	$g$	Gravitational acceleration, m s <sup>-2</sup>
$C$	Hydrogen concentration in a mixture, % by volume	$H(x)$	Heaviside function
$c$	Progress variable (normalised product mass fraction)	$H_c$	Heat of combustion, J kg <sup>-1</sup>
$c_p$	Specific heat capacity of mixture at constant pressure, $c_p = \sum_m c_{p_m} Y_m$	$h$	Enthalpy, J kg <sup>-1</sup> , $h = \int_{298.15}^T c_p dT$
$D$	Fractal dimension	$M$	Molecular mass, kg kmole <sup>-1</sup> , $M = \sum_m V_m M_m$
$E$	Total energy, J kg <sup>-1</sup> $E = h - p/\rho + u^2/2$	$m_0$	Temperature index in dependence of burning velocity on temperature
$E_{\text{act}}$	Activation energy, J mol <sup>-1</sup>	$n_0$	Baric index in dependence of burning velocity on pressure
$E_i$	Expansion coefficient, $E_i = \rho_u/\rho_b$	$Pr$	Prandtl number, $Pr = \mu c_p/k$ , where $k$ is thermal conductivity W/m/K
		$p$	Pressure, Pa
		$R$	Radius, m
		$R_0$	Characteristic radius for onset of fractal, self-similar regime of the turbulent flame front propagation, m

\* This paper was presented at the Second International Symposium on Nonequilibrium Processes, Combustion, and Atmospheric Phenomena (Dagomys, Sochi, Russia, 3–7 October 2005).

<sup>3</sup> Author to whom any correspondence should be addressed.

$R_{\text{sph}}$	Initial radius of the hydrogen–air cloud (radius of polyethylene balloon), m
$R_{\text{univ}}$	Universal gas constant, $8314.4 \text{ J K}^{-1} \text{ kmol}^{-1}$
$S_c$	Source term in conservation equation for progress variable, $\text{kg m}^{-3} \text{ s}^{-1}$
$S_E$	Source term in energy conservation equation, $\text{J m}^{-3} \text{ s}^{-1}$ , $S_E = S_c H_c$
$\tilde{S}_{ij}$	Rate of strain tensor, $\text{s}^{-1}$
$Sc$	Schmidt number, $Sc = \mu/\rho D$ , where $D$ is the diffusion coefficient, $\text{m}^2 \text{ s}^{-1}$
$S_t$	Turbulent burning velocity, $\text{m s}^{-1}$
$S_{u0}$	Laminar burning velocity at initial conditions, $\text{m s}^{-1}$
$S_u$	Laminar burning velocity, $\text{m s}^{-1}$
$T$	Temperature, K
$t$	Time, s
$u_{i,j,k}$	Velocity components, $\text{m s}^{-1}$
$u'$	Root-mean square of SGS velocity component, $\text{m s}^{-1}$
$V$	Volume, $\text{m}^3$
$x_{i,j,k}$	Spatial coordinates, m
$Y$	Mass fraction

### Greek

$\Delta p_F$	Peak overpressure associated with flame propagation through pressure transducer location, kPa
$\Delta_{\text{CV}}$	Control volume characteristic size, m
$\Delta t$	Time step, s
$\lambda_o$	Outer cut-off of the fractal structure, m
$\lambda_i$	Inner cut-off of the fractal structure, m
$\varepsilon$	Overall thermokinetic index, $\varepsilon = m_0 + n_0 - m_0/\gamma_u$
$\gamma$	Specific heat ratio
$\mu$	Dynamic viscosity, Pa s
$\rho$	Density, $\text{kg m}^{-3}$ , $\rho = (pM)/(R_{\text{univ}}T)$
$\Xi_{\text{SGS}}$	SGS flame front wrinkling factor
$\Xi_{\text{MAX}}$	Maximum SGS flame front wrinkling factor due to turbulence generated by the flame front itself

### Subscripts and superscripts

$a$	Air
$b$	Burned mixture
$c$	Source term in progress variable equation
$E$	Source term in energy conservation equation
eff	Effective value
$f$	Fuel
hsph	Hemispherical
$\text{H}_2$	Hydrogen
$i, j, k$	Spatial coordinate indexes
$m$	$m$ -th component of gas mixture
MAX	Maximum
SGS	Sub-grid scale
Stoich	Stoichiometric
$t$	Turbulent
$u$	Unburned mixture
0	Initial conditions

### Bars

$\bar{\quad}$	LES filtered quantity
$\tilde{\quad}$	LES mass-weighted filtered quantity

## 1. Introduction

The use of hydrogen as an energy carrier and its wide introduction into the market throughout the world, especially transportation and storage, raises many questions if compromising safety is to be avoided. Explosion of hydrogen–air mixtures in the open atmosphere is one of the likely scenarios. Analysis of unscheduled releases, followed by disastrous explosions, can be performed through examination of on-site blast data, infrasound and ionosphere effects and their numerical simulations. But first the physics of the process should be understood and computational fluid dynamics models need be developed and validated against large-scale experiments to provide predictive tools for hydrogen safety engineering. Ten years ago predictive modelling of turbulent deflagration was not possible [1]. In this paper we demonstrate the capability of the large eddy simulation (LES) model developed from the first principles to simulate dynamics of the largest unconfined hydrogen–air deflagration ever performed [2].

The emphasis in combustion research for energy applications differs from that in accidental combustion research, i.e. fire and explosion safety research. Significant flow turbulence, high flame strain rates and relatively small scales of inhomogeneous regions are characteristic for most combustion devices. These features can differ significantly from those in large-scale unwanted combustion. The initial flame propagation after accidental ignition usually takes place in a quiescent or moderately agitated mixture in a quasi-laminar mode. While the combustion community is mainly focused on the aspects of flame behaviour to increase the efficiency of combustion devices, explosion safety researchers are focused on combustion mitigation through a proper prediction of flow, pressure and temperature dynamics during unwanted flame propagation in complex geometries under various conditions, usually attributed to essentially larger scale experiments. Conventional models, used to design combustion devices, may not be appropriate to analyse large-scale explosions as the regularities and physical phenomena for freely propagating accidental flames are different from those for stabilized flames, e.g. burner flames. In particular larger scale and/or low stretch rate are typical for large-scale unconfined explosions [3].

LES technique is promising for deflagration simulation as it avoids time averaging and allows better prediction of highly non-isotropic turbulent flows and large-scale flame flow interaction at the resolved level [4, 5]. In most approaches to LES of premixed combustion there is a numerical requirement for a minimum number of computational grid points within the simulated flame front thickness, normally 4–5 points [4], independent of the mesh size. Unstructured grids are recommended for LES in complex geometries [6]. For tetrahedral unstructured grids 4–5 points through the numerical flame front thickness can be ‘collected’ at a distance equal to 2–3 edges of tetrahedral control volume (CV). It means that LES can resolve elements of a flame front structure with a size larger than about 4–6 edges of the tetrahedron of the applied mesh, and smaller sub-grid structures can be only modelled.

There are different views on the possibility of the deflagration to detonation transition (DDT) in fuel–air mixtures initiated by a weak source such as a spark. Literature

**Table 1.** Experimental conditions and results for different tests [2].

Test No.	$C$ , % vol.	$T_i$ , K	$p_i$ , kPa	$E_{ign}$ , J	$V$ , m <sup>3</sup>	Hemisphere diameter, m	Maximum flame speed, m s <sup>-1</sup>
GHT 23	29.1	282	98.1	10	7.5	3.06	43
GHT 26	29.2	281	99.1	1000	7.5	3.06	43
GHT 39	29.4	279	98.5	1000	50	5.76	50
GHT 40 <sup>a</sup>	29.5	279	98.5	150	50	5.76	54
GHT 11	31.0	281	100.7	314	262	10.0	60
GHT 13	25.9	283	100.9	314	262	10.0	48
GHT 34 <sup>a</sup>	29.7	283	98.9	150	2094	20.0	84

<sup>a</sup> Experiments with rhombus-shaped wire net over the hemispherical balloon.

review [7] indicates that there is no reliable data on DDT in unconfined clouds of combustible gases. Theoretical considerations [8] admit DDT of free spherical premixed combustion due to flame front instabilities and acceleration. Hydrogen–air deflagrations in unconfined conditions (rubber balloons) were studied experimentally in Russia in 1983 [9]. A spark with energy of 1 J was used to ignite a mixture in the centre of a balloon with a volume of 35 or 86 m<sup>3</sup> (diameter about 4 m and 5.5 m, respectively). Experiments in a 4 m diameter balloon demonstrated that flame front acceleration at the initial stage of combustion ceased and the flame propagated with a practically constant velocity of 38 m s<sup>-1</sup> (35% by volume of hydrogen). In a 5.5 m diameter balloon test the flame propagation velocity was continuously increasing to 105 m s<sup>-1</sup> for the mixture with the same concentration of hydrogen. The authors [9] concluded that the maximum velocity is increasing with diameter of an initial cloud, and for volume larger than 500 m<sup>3</sup> (diameter larger than 10 m), DDT is possible. In the same year experimental studies with hemispherical volumes of up to 2094 m<sup>3</sup> were performed in Germany [2, 10, 11]. Tests were conducted with ignition sources of energy within the range from 10 to 1000 J in near stoichiometric hydrogen–air clouds with diameter of hemisphere up to 20 m, but no DDT was registered.

The characteristics of blast waves, from unconfined deflagrations, are determined by gaseous cloud combustion and differ from that of high explosives. For example, in the near-field the overpressure from the positive phase of gaseous explosion is much less compared with that from high explosives, while the duration of the phase is greater. In the far-field, pressure waves from deflagrations decay more slowly with distance from a source of initiation and cannot be described by means of the TNT-equivalence concept [12, 13]. The TNT-equivalence concept is inadequate to describe the large amplitude of the negative phase of gaseous explosions [13], which is larger than the positive phase amplitude for deflagrations [12].

In 1999 Bradley suggested that in the case of large-scale explosion flames ‘the fractal analyses is probably valid because of the large length-scales and small flame stretch rates, unlike turbulent flames in many engineering applications where the flame stretch rate usually reduces the burning rate’ [3]. This is in line with the analysis of 20 unconfined explosions carried out earlier by Gostintsev *et al* [14]. They described the behaviour of spherical turbulent premixed flames propagation as a self-similar process in which a total flame front surface area grows  $R^{1/3}$  times faster (theoretical fractal dimension  $D = 2.33$ ) than the surface of a sphere with the same radius.

According to the fractal theory a ratio of the turbulent flame front area  $A_t$  to the area of the smooth laminar spherical flame  $A_{u0}$  is equal to  $A_t/A_{u0} = S_t/S_u = (\lambda_i/\lambda_0)^{(2-D)}$  [15], where  $S_u$  is laminar and  $S_t$  is turbulent burning velocities, respectively. Bearing in mind, that for freely propagating flames, the outer cut-off  $\lambda_0$  is growing proportionally to the flame front radius  $R$  and the inner cut-off  $\lambda_i$  is a constant, the turbulent burning velocity  $S_t$  is a function of the average flame front radius  $R$ :  $S_t/S_{t0} = (R/R_0)^{(D-2)}$ , where  $S_{t0}$  is the burning velocity at radius  $R_0$ . It was reported [14] that for stoichiometric hydrogen–air mixtures a self-similar regime of flame propagation is established at a critical radius of 1.0–1.2 m. Different values have been proposed for the fractal dimension,  $D$ . Gouldin [15] used  $D = 2.37$  adopted from [16]. A wide range of experimental values of fractal dimension  $D = 2.11–2.36$  was cited for premixed combustion by Gulder in 1990 [17]. In 1999 [3] Bradley suggested a theoretical value  $D = 2.33$  for freely propagating flames. Gostintsev *et al* [18] demonstrated in 1999 that for self-similar freely propagating flames the fractal dimension is within the range  $D = 2.2–2.33$ . In 2000 Gulder reported, for turbulent premixed combustion in Bunsen-type burners, the fractal dimension within the range  $D = 2.14–2.24$  [19].

This study is devoted to LES modelling and validation of the model, with two combustion sub-models, one based on the renormalization group (RNG) theory and another on the fractal theory, against the largest ever performed experiment on stoichiometric hydrogen–air deflagration in the open atmosphere GHT 34 [2]. In this paper simulation results are compared against experimental data on flame propagation, flame shape and overpressure transients at different distances from ignition source. The value of fractal dimension for use in LES of large-scale explosions is determined. More information relevant to this study could be found in [20–33].

## 2. Largest hydrogen–air deflagration test in atmosphere

A series of experiments with near stoichiometric hydrogen–air deflagrations, in unconfined hemispherical volumes, was performed in 1983 by the Fraunhofer Institute for Propellants and Explosives [2]. The experimental conditions and main results are presented in table 1. The principal aim of these experiments was to investigate the dependence of flame propagation velocity on the cloud size. Mixtures were ignited on the ground level inside the shell made of thin polyethylene (PE) film to exclude the effect of reflected pressure waves.

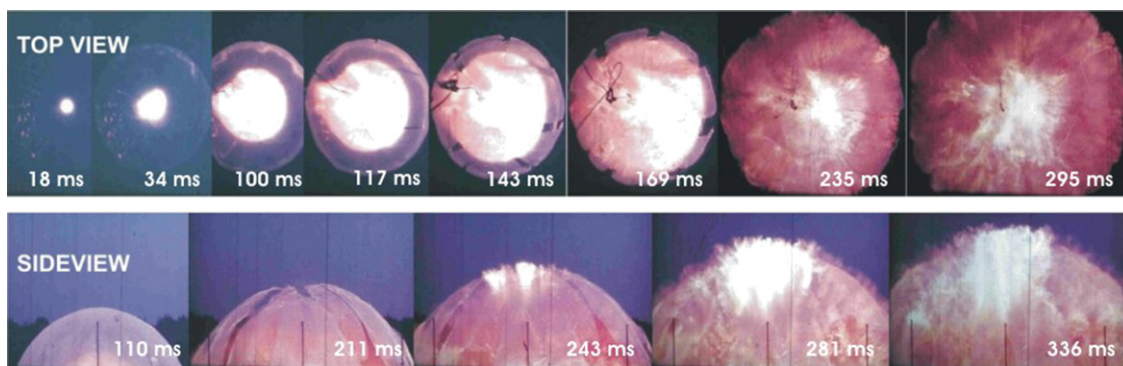


**Figure 1.** Snapshots of test GHT 34 in a 20 m diameter hemisphere.

Burnout of the cloud occurs approximately at two initial diameters corresponding to the cubic root of the products expansion coefficient. After burnout the peak overpressure decays with distance from the initiation point. The duration of the positive and the negative phases is independent of the distance for any given size of balloon. The amplitude of negative pressure peak was usually somewhat larger than that of the positive pressure phase and the negative phase being of shorter duration. For spherical sonic waves the authors [2] cited a theoretical result obtained by Landau that at any distance the integral of overpressure in time should be equal to zero. This theoretical result complies with experimental records of the outward propagating pressure wave outside the combustion area (see pressure transients at 35 and 80 m below). Processing of visual images of the flame propagation yielded a continuous increase in flame propagation velocity up to a maximum value, which was reached at a distance between the initial radius of the cloud  $R_{\text{hsph}}$  and  $1.5 R_{\text{hsph}}$ . For initially quiescent stoichiometric hydrogen–air mixture this upper limit was estimated as  $125 \text{ m s}^{-1}$  with a peak overpressure 13 kPa assuming the validity of the authors' approach [2] based on simple turbulent combustion models of Damkohler and Karlovitz. The experimental results indicate that the flame propagation velocity approaches an upper limit with an increase in the cloud size.

In test GHT 34, with hydrogen–air mixture 29.7% by volume in a 20 m diameter hemisphere, the maximum flame propagation velocity was  $84 \text{ m s}^{-1}$  with the initial burning velocity estimated by authors [2] as  $2.39 \text{ m s}^{-1}$  (the expansion coefficient of combustion products was calculated as 7.26 with a density of combustible mixture  $0.8775 \text{ kg m}^{-3}$  and a speed of sound  $397.3 \text{ m s}^{-1}$ ). Errors in velocity measurements were assessed as +5% without taking into account certain asymmetries in flame propagation. In the  $2094 \text{ m}^3$  hemisphere experiment, GHT 34, a rhombus-shaped wire net was laid over the hemispherical balloon which was fastened to the ground at 16 points to compensate the buoyancy force. In order to make the hydrogen–air flame visible in daylight finely ground NaCl powder was dispersed inside the balloon at the end of the filling process to produce a yellow-coloured flame. Generally 10 to 12 piezo-resistive Kistler pressure sensors (100 kPa range, natural frequency 14 kHz) were used. These were mounted in a steel case having a mass of 20 kg in a way that their pressure-sensitive surfaces were fitted flush with the surface of the ground and covered with a 2 mm thick layer of silicone

grease on the membrane to avoid the influence of temperature and heat radiation. In addition a sensor, located at a 5 m distance from the ignition source, was protected by means of a laminated plastic plate screwed to the steel casing and having an opening of 4 mm diameter in the middle. For the GHT 34 test an additional pressure sensor was installed at right angles to the axis with main sensors and mounted on a vertical timber wall  $1 \times 1 \text{ m}^2$  (head-on measurement). The explosion pressure was measured at distances 2.0, 3.5, 5.0, 6.5, 8.0, 18, 25, 35, 60 and 80 m from the initiation point. The mixture was ignited by pyrotechnical charges with total ignition energy 150 J. The pressure transients of sensors inside the combustion products did not return to zero after the negative pressure phase, except for the sensor installed at 5 m. This can be attributed to the fact that the transducers were thermalized to high temperatures during the explosion. Since they did not remain at the temperature at which they were calibrated, they were no longer calibrated and did not return to the baseline. This is an indication that the protective measures taken by the experimenters to insulate these transducers were insufficient for this large test.

Experimental results for flame propagation and pressure dynamics for test GHT 34 are presented in figures 4 and 6 and discussed further in the paper. The flame propagated in an almost hemispherical form. The balloon shell first stretched slightly outwards until it burst when the flame had reached about half of the original radius of the balloon  $0.5R_0$  (figure 1).

The explosion overpressure of about 6 kPa was practically the same within the cloud distances in GHT 34 test. A sharp overpressure peak  $\Delta p_F$  of about 10 kPa in the pressure transients followed flame propagation. This peak occurs when the flame passes the sensor on the ground. The cause for the occurrence of this peak is not clear, but is probably associated with the mounting of the PE foil in the sensor housing.

### 3. The LES model description

#### 3.1. Governing equations

The main governing equations of the LES model were described elsewhere [34–36]. The equations were obtained by the filtering (filter size is CV size) of three-dimensional conservation equations for mass, momentum, energy, progress

variable and air concentration for compressible Newtonian fluid:

$$\frac{\partial \bar{\rho}}{\partial t} + \frac{\partial}{\partial x_j} (\bar{\rho} \tilde{u}_j) = 0, \quad (1)$$

$$\begin{aligned} \frac{\partial \bar{\rho} \tilde{u}_i}{\partial t} + \frac{\partial}{\partial x_j} (\bar{\rho} \tilde{u}_j \tilde{u}_i) &= -\frac{\partial \bar{p}}{\partial x_i} + \frac{\partial}{\partial x_j} \\ &\times \left( \mu_{\text{eff}} \left( \frac{\partial \tilde{u}_i}{\partial x_j} + \frac{\partial \tilde{u}_j}{\partial x_i} - \frac{2}{3} \frac{\partial \tilde{u}_k}{\partial x_k} \delta_{ij} \right) \right) + \bar{\rho} g_i, \end{aligned} \quad (2)$$

$$\begin{aligned} \frac{\partial}{\partial t} (\bar{\rho} \tilde{E}) + \frac{\partial}{\partial x_j} (\tilde{u}_j (\bar{\rho} \tilde{E} + \bar{p})) \\ &= \frac{\partial}{\partial x_j} \left( \frac{\mu_{\text{eff}} c_p}{Pr_{\text{eff}}} \frac{\partial \tilde{T}}{\partial x_j} - \sum_m \tilde{h}_m \left( -\frac{\mu_{\text{eff}}}{Sc_{\text{eff}}} \frac{\partial \tilde{Y}_m}{\partial x_j} \right) \right) \\ &+ \tilde{u}_i \mu_{\text{eff}} \left( \frac{\partial \tilde{u}_i}{\partial x_j} + \frac{\partial \tilde{u}_j}{\partial x_i} - \frac{2}{3} \frac{\partial \tilde{u}_k}{\partial x_k} \delta_{ij} \right) + \tilde{S}_E, \end{aligned} \quad (3)$$

$$\frac{\partial}{\partial t} (\bar{\rho} \tilde{c}) + \frac{\partial}{\partial x_j} (\bar{\rho} \tilde{u}_j \tilde{c}) = \frac{\partial}{\partial x_j} \left( \frac{\mu_{\text{eff}}}{Sc_{\text{eff}}} \frac{\partial \tilde{c}}{\partial x_j} \right) + \tilde{S}_c, \quad (4)$$

$$\frac{\partial}{\partial t} (\bar{\rho} \tilde{Y}_a) + \frac{\partial}{\partial x_j} (\bar{\rho} \tilde{u}_j \tilde{Y}_a) = \frac{\partial}{\partial x_j} \left( \frac{\mu_{\text{eff}}}{Sc_{\text{eff}}} \frac{\partial \tilde{Y}_a}{\partial x_j} \right) - \frac{Y_a}{Y_f + Y_a} \tilde{S}_c. \quad (5)$$

The model is of the numerical type, as defined by Pope for a case of equivalence between filter and cell size, and does not include an ‘artificial, i.e. non-physical, parameter  $\Delta$ ’ [37] applied in some LES models in a source term of the progress variable equation.

The RNG turbulence model by Yakhot *et al* [38] was employed to model sub-grid scale (SGS) turbulence. In this model the effective viscosity is equal to  $\mu_{\text{eff}} = \mu [1 + H(\mu_s^2 \mu_{\text{eff}} / \mu^3 - 100)]^{1/3}$ , where  $\mu_s = \bar{\rho} (0.157 V_{CV}^{1/3})^2 \sqrt{2 \tilde{S}_{ij} \tilde{S}_{ij}}$ ,  $H(x)$  is the Heaviside function and the rate of strain tensor is  $\tilde{S}_{ij} = 1/2((\partial \tilde{u}_i / \partial x_j) + (\partial \tilde{u}_j / \partial x_i))$ . The RNG model is similar to the Smagorinsky’s model [39], but does not contain adjustable or ad hoc parameters and is capable to describe transitional and laminar flow regimes: in the laminar flow the Heaviside function argument is negative and the effective viscosity recovers molecular viscosity,  $\mu_{\text{eff}} = \mu$ . In present simulations the values of molecular Prandtl and Schmidt numbers were chosen equal to those characteristic for air:  $Pr = 0.7$ ,  $Sc = 0.7$ . The effective Prandtl number was calculated according to the RNG theory [38] for non-reactive flows and was equal to the effective Schmidt number:

$$\left| \frac{1/Pr_{\text{eff}} - 1.3929}{1/Pr - 1.3929} \right|^{0.6321} \left| \frac{1/Pr_{\text{eff}} + 2.3929}{1/Pr + 2.3929} \right|^{0.3679} = \frac{\mu}{\mu_{\text{eff}}}.$$

The conservation equation for air concentration (5) is introduced into the model to account for dilution of initial stoichiometric hydrogen–air cloud with ambient air.

### 3.2. The combustion model

The combustion model is based on the equation for the progress variable (4) and the gradient method. The source term in the energy equation (3) is a heat release rate due to combustion,  $S_E = H_c \cdot S_c$ . The mass burning rate is modelled similar to [34–36] using the gradient method  $\tilde{S}_c = \rho_u \cdot S_t \cdot |\nabla \tilde{c}|$ . The gradient method allows decoupling between the physical requirement to keep the turbulent mass burning rate equal to  $\rho_u S_t$  and a numerical requirement for a simulated flame front to occupy 4–5 CVs, when the gradient method is applied, independent of a mesh size and a scale of a problem. However, the integral of the source term throughout a numerical flame front thickness always gives a physically correct value for the mass burning rate per unit area, i.e.  $\rho_u S_t$ , independent of the numerical flame front thickness. As a result, simulations (flame propagation and pressure dynamics) will not be affected noticeably, regardless of the fact that the structure and size of a numerical flame front are not actual characteristics of the prototype. Furthermore, by tackling real problems with a scale of tens and hundreds of metres, there is no chance of resolving a whole structure of real turbulent flame front, where the turbulence generated by the flame front itself plays a role at scales comparable to the thickness of real flamelets of the order of millimetre. Nevertheless, the giving up of a fine flame front structure resolution allows one to reproduce reasonably hydrodynamics of flows ahead and behind the numerical flame front, overall flame propagation and explosion pressure dynamics because energy release in a flame front is kept physically correct.

The following general form for dependence of burning velocity on hydrogen concentration,  $Y_{H_2}$ , temperature,  $T$ , and pressure,  $p$ , is a general feature of the model (in the approximation of adiabatic compression/expansion  $\varepsilon = m_0 + n_0 - m_0/\gamma_u$ ):

$$\begin{aligned} S_u(Y_{H_2}, T, p) &= S_{u0}(Y_{H_2}) \cdot \left( \frac{T}{T_{u0}} \right)^{m_0(Y_{H_2})} \left( \frac{p}{p_0} \right)^{n_0(Y_{H_2})} \\ &= S_{u0}(Y_{H_2}) \cdot (p/p_0)^{\varepsilon(Y_{H_2})}. \end{aligned} \quad (6)$$

This equation is a convenient and widely used approximation of the theoretical formula for burning velocity  $S_u \propto k \cdot p^{n_0} \cdot \exp(-E_{\text{act}}/2R_{\text{univ}}T_b)$ , where  $k$  is the pre-exponential factor, in a comparatively narrow range of temperatures between the temperature of combustion products at initial conditions,  $T_{bi}$ , and at the end of combustion,  $T_{be}$ . It was demonstrated that an error of the approximation does not exceed 15% [40].

The dependence of burning velocity on hydrogen concentration was accounted for by using a linear function  $f(Y_{H_2})$ , equal to 1 in the stoichiometric mixture (29.7% by volume of hydrogen) and 0 at the lower flammability limit (4% by volume of hydrogen):  $S_{u0}(Y_{H_2}) = S_{u0}^{\text{Stoich}} \cdot f(Y_{H_2})$ .

Two combustion sub-models applied in this study, i.e. the RNG combustion sub-model and the fractal combustion sub-model, are described below. For both models a common component, giving some augmentation to flame propagation velocity in simulations, is partially resolved flame front wrinkling due to hydrodynamic instability. The initial value of global (stretched) laminar burning velocity  $S_{u0} = 1.91 \text{ m s}^{-1}$ , obtained by Lamoureux *et al* [41] through direct registration of flame propagation by a schlieren system and a high speed camera system, was applied in this study in equation (6) for 29.7% hydrogen–air mixture.

**3.2.1. RNG combustion sub-model.** The first model applied to model turbulent burning velocity  $S_t$  is based on the RNG premixed turbulent combustion model [42] and the theoretical analysis of self-turbulized flames by Karlovitz *et al* [43].

Based on the analysis by Karlovitz *et al* [43] the maximum value of the flame wrinkling factor due to the turbulence generated by flame front itself can be estimated as  $\Xi_{\text{MAX}} = (E_i - 1)/\sqrt{3}$ . For stoichiometric hydrogen–air mixture it gives the value  $\Xi_{\text{MAX}} = 3.6$ . The following dependence of the SGS flame wrinkling factor on flame front radius was assumed in this study to model a smooth increase in flame front surface area during transition from laminar to fully developed turbulent flame:

$$\Xi_{\text{SGS}}(R) = 1 + (\Xi_{\text{MAX}} - 1)(1 - \exp(-R/R_0)), \quad (7)$$

where  $R_0$  is a characteristic radius at which transition to the self-turbulized regime takes place. Gostintsev *et al* [14] reported previously that the characteristic radius for the onset of a self-similar regime of flame propagation for stoichiometric hydrogen–air mixture is  $R_0 = 1.0 - 1.2$  m and the value  $R_0 = 1.2$  m was adopted here.

The joint effect of ‘large-scale’ flow turbulence and SGS ‘small-scale’ turbulence generated by the flame front itself on the turbulent burning velocity was accounted for through the implementation of Yakhot’s formula for premixed turbulent combustion, based on the RNG analysis [42], into the LES model in the following form:

$$S_t = [S_u \cdot \Xi_{\text{SGS}}(R)] \cdot \exp(u'/S_t)^2. \quad (8)$$

The difference with the original Yakhot’s formula is the use of SGS turbulent burning velocity  $[S_u \cdot \Xi_{\text{SGS}}(R)]$  in our study instead of laminar burning velocity  $S_u$ . This is to account for a physical phenomenon of turbulence generated by flame front itself, acting at SGS, in the LES model.

**3.2.2. Fractal combustion sub-model.** The second combustion sub-model, applied to simulate the open atmosphere hydrogen–air explosion, is based on the fractal analysis of the freely propagating premixed flames and was described previously [44]. Following the conclusions of the fractal theory the burning velocity is modelled as

$$S_t = S_t^{R_0} \cdot f(Y_{\text{H}_2}) \cdot (R/R_0)^{D-2}, \quad (9)$$

where  $S_t^{R_0}$  is the burning velocity at radius  $R_0$  of the onset of self-similar (fractal) regime of flame propagation and  $D$  is a fractal dimension. The theoretical value  $D = 2.33$  corresponds to the upper limit of the experimentally observed range  $D = 2.20-2.33$  reported by Gostintsev *et al* [28] for freely propagating flames in the open atmosphere.

Self-similar (fractal) regime of flame propagation takes place at flame radii above critical  $R > R_0$ . Hence, the fractal combustion sub-model can be applied only after that. The simulations of the transitional stage of the deflagration (flame radius  $R < R_0$ ) were performed by the RNG sub-model. The value of burning velocity, extracted from the RNG sub-model at  $R = R_0$  for implementation in formula (9) of the fractal sub-model, was calculated as  $S_t^{R_0} = 6.44$  m s<sup>-1</sup> by the following procedure. The location of a simulated flame front, at any moment of time, was determined by the averaging of coordinates of all CVs with values of the progress variable within the range  $c = 0.01-0.99$ . At the moment when the

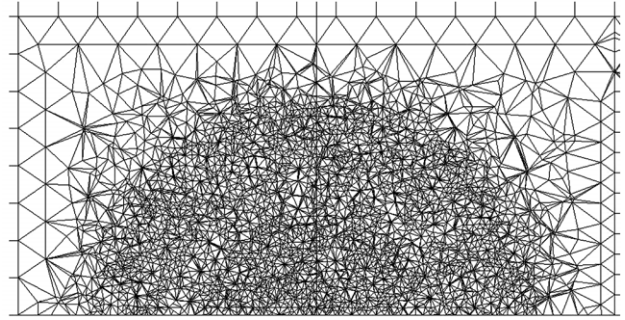


**Figure 2.** Cross section of the central part of the calculation domain.

radius of the flame front became equal to  $R_0$  a total mass burning rate in the flame front was calculated. Then, to obtain the sought burning velocity, the mass burning rate was divided by the product of a combustible mixture density and the area of the hemisphere with radius  $R_0$ . The obtained value  $S_t^{R_0} = 6.44$  m s<sup>-1</sup> is  $\Xi = 6.44/1.91 = 3.37$  larger compared with the laminar burning velocity for the hydrogen–air mixture 29.7% by volume. This augmentation of burning velocity is due to the effects of turbulence generated by flame front itself and flow turbulence. The augmentation of burning velocity for radii  $R > R_0$  was calculated in the fractal sub-model by equation (9) in place of equations (7) and (8) in the RNG sub-model.

### 3.3. Numerical details

**3.3.1. Initial and boundary conditions.** Initial temperature and initial pressure were equal to 283 K and 98.9 kPa, respectively, as in the experiment. Mixture was quiescent at ignition,  $u = 0$ . The progress variable was equal to  $c = 0$  all over the domain. Air concentration was equal to  $Y_a = 0.9713$  within the hydrogen–air cloud ( $R \leq R_{\text{hsph}}$ ) and  $Y_a = 1.0$  beyond it ( $R > R_{\text{hsph}}$ ).

The no-slip impermeable adiabatic boundary condition was used on the ground. Non-reflecting boundary conditions were used on the boundaries representing the far-field in the atmosphere.

Ignition was modelled by the increase in the progress variable from  $c = 0$  to  $c = 1$  in one CV during the period  $t = 22$  ms calculated as a time of flame propagation through spherical CV equal by volume to the ignition tetrahedral CV. The value  $c = 1$  was kept in the ignition CV until the moment 29 ms. No adjustment of simulation results in time was required with this procedure.

**3.3.2. Calculation domain.** The calculation domain with sides  $L \times W \times H = 200 \times 200 \times 100$  m was created to simulate both the flame front and the pressure wave propagation. The characteristic size of the tetrahedral CVs in the flame propagation area ( $R \leq 22$  m) was about 1 m and the characteristic size of the hexahedral CVs in the rest of the domain ( $R \geq 30$  m) was 4 m. The transitional area ( $22 < R < 30$  m) was meshed using a tetrahedral mesh with the CV size changing from 1 to 4 m. The total number of CVs was 294296. The cross section of the central part of the calculation domain ( $0 < R < 30$  m) is shown in figure 2.

The grid sensitivity analysis was conducted for the RNG combustion sub-model, as a part of a standard benchmark

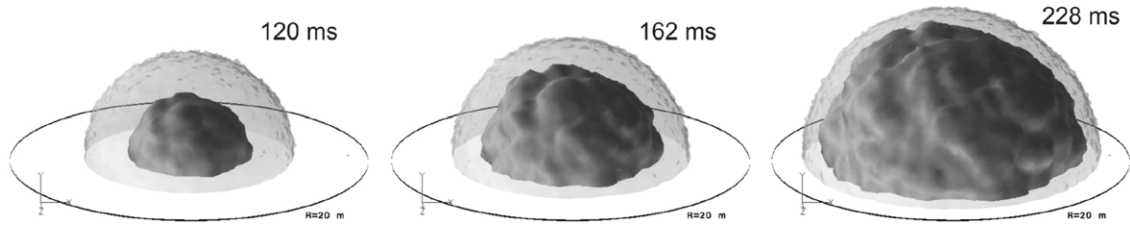


**Figure 3.** Snapshots of numerical simulation of flame front propagation in test GHT 34 (dark grey—flame front iso-surface  $c = 0.5$ , light grey—unburnt hydrogen–air mixture).

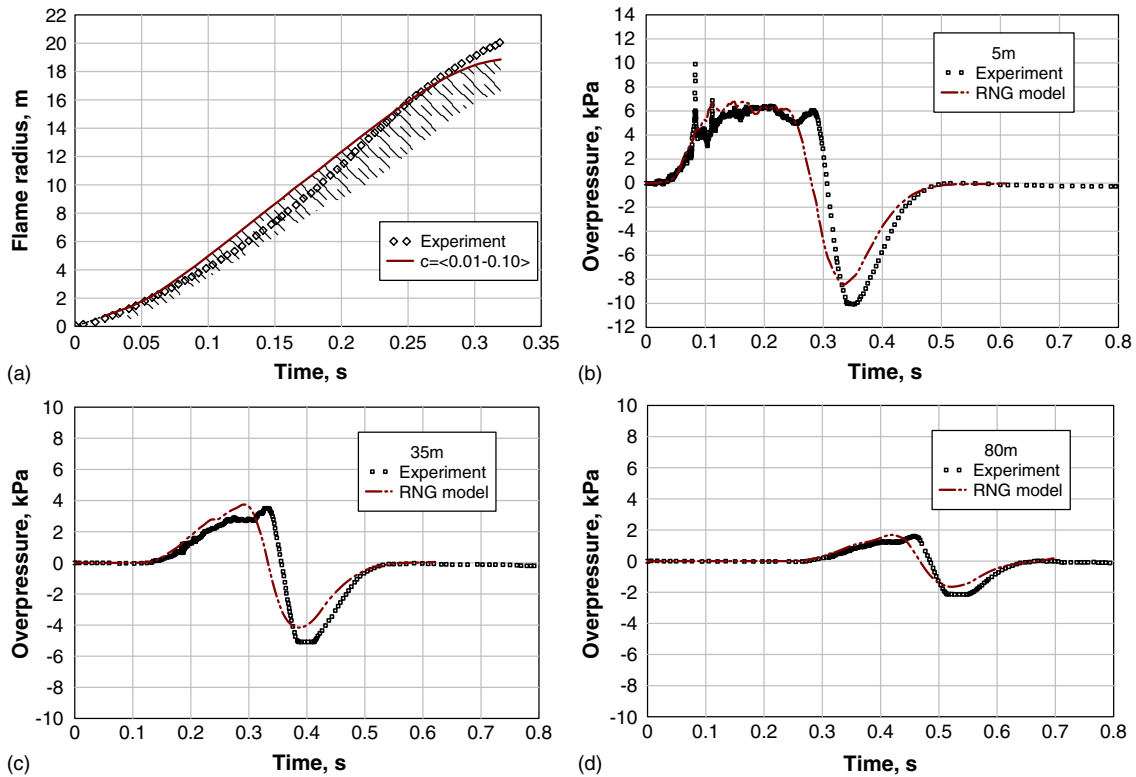


**Figure 4.** Comparison between experiment and simulations by the RNG combustion sub-model: (a) flame front propagation dynamics: solid line—leading flame edge (averaging through CVs with the progress variable within the range 0.01–0.10), hatched area—numerical flame front thickness; (b)–(d) pressure dynamics at  $R = 5$  m,  $R = 35$  m and  $R = 80$  m, respectively.

exercise in the framework of activities of the European Network of Excellence HySafe [45]. Two similar grids with a characteristic CV size in the area of flame propagation 1.0 m and 0.5 m, respectively, were used. The difference in the flame front propagation dynamics, i.e. the growth of the flame front radius in time, was about 5%. This difference is due to better resolution of the flame front wrinkling by the hydrodynamic instability for a finer grid, which provides a larger mass burning rate and, thus, faster flame propagation.

**3.3.3. CFD solver and numerical scheme.** The FLUENT 6.2.16 solver was employed as a platform for the realization of the LES model. The double precision parallel version of solver was used with explicit linearization of the governing equations. The second order upwind scheme was used for convection terms and the central difference scheme for diffusion terms. The 4-stage Runge–Kutta scheme was applied for time stepping. The Courant–Friedrichs–Lewy number was equal to  $CFL = 0.8$  to ensure stability. Simulation of real time of deflagration and pressure wave propagation up to 0.63 s

takes about 6 days on a workstation IBM630 (12GB RAM, 2CPUx1.2GHz Power 4, 1CPU SPECfp=961).

## 4. Simulation results

### 4.1. Flame shape

The simulated flame front propagation for experiment GHT 34 is shown in figure 3. Distinctive large-scale wrinkling of the flame front by the hydrodynamic instability can be seen. The cascade of characteristic wrinkles above a LES filter size, i.e. a cell size in the numerical LES approach, of 1 m is close in size to the experimentally observed [2] wrinkles as presented in our paper [46], where the simulated flame front profiles are compared against experimental data.

### 4.2. Flame front propagation and pressure dynamics

Figures 4–6 show a comparison between the experimental results of test GHT 34 and the numerical simulations for the two applied combustion sub-models.

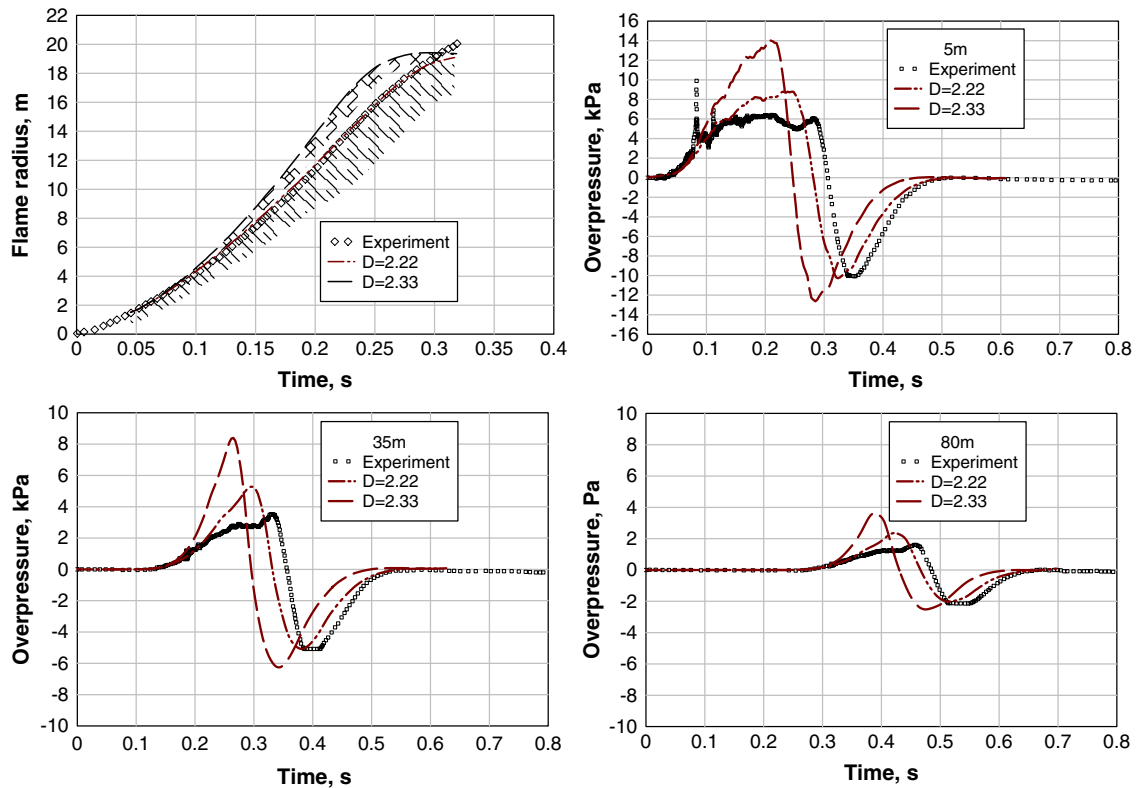


**Figure 5.** Comparison between experiment and simulations by the fractal combustion sub-model with fractal dimensions  $D = 2.22$  and  $2.33$ : (a) flame front propagation dynamics: lines—leading flame edge (averaging through CVs with the progress variable within the range 0.01–0.10), hatched area—numerical flame front thickness (only partially reproduced for  $D = 2.33$ ); (b)–(d) pressure dynamics at  $R = 5$  m,  $R = 35$  m and  $R = 80$  m, respectively.

Experimental data on flame propagation dynamics are represented in figures 4 and 5 as a change in the time position of a leading flame front edge. The thickness of a simulated flame front is shown in figure 4(a) by the hatched area with the leading flame edge depicted by a solid line. At final stages of deflagration the thickness of the numerical flame front is about 4 m which is close to experimental observations [46].

Both combustion sub-models reproduce the deceleration of flame at the final stage of the explosion, when the initial hydrogen–air mixture is diluted by atmospheric air that leads to a decrease in the burning rate (figure 5(a)). The deceleration of the numerical flame front is more pronounced compared with the experiment. This could be attributed to noticeably large cell sizes used in the simulations in the areas of mixture non-uniformity. Performing simulation on an adaptive grid in the area of large hydrogen concentration gradients could improve predictive capability of the model at final stages of deflagration. Some insignificant change in rear flame front edge dynamics can be seen in figure 4(a) at radius 10 m. This is apparently due to the numerical grid structure as the grid was generated having a sphere at radius 10 m in the calculation domain to separate the combustible mixture area from the ambient air area.

For the RNG combustion sub-model the maximum deviation of the simulated from the experimental leading flame front edge does not exceed 1 m. With this obviously good correlation between LES and experiment, the acceleration of the real flame front is reproduced only in the initial stage of the deflagration. At later stages simulations give practically constant flame propagation velocity (figure 4(a)).

The simulated pressure dynamics (figures 4(b)–(d)) is close to experimental pressure transients at locations of properly functioning transducers at 5, 35 and 80 m. Both positive and negative phases of the pressure wave are reproduced by the numerical experiment, including arrival time, duration and decay of the pressure wave with distance. The amplitude of the positive phase of the pressure wave is reproduced in simulations exactly with a bit faster arrival time in a far-field. However, amplitude of the negative phase is up to 30% less than in experiment. The simulated rear front of the positive phase overpressure wave passes ahead of the experimental one due to significantly stronger deceleration of the flame front in simulation at the end of the deflagration compared with experiment.

Simulation results of the flame front propagation for two fractal dimensions, i.e.  $D = 2.33$  and  $D = 2.22$ , are presented in figure 5(a). As expected the fractal sub-model simulations reproduce the monotonic increase in flame propagation velocity similarly to the experimental study [2]. Overpressure dynamics for both fractal dimensions are shown in figures 5(b)–(d). The simulation with theoretical fractal dimension  $D = 2.33$  obviously over-predicts both flame propagation and overpressure dynamics. During numerical experiments it was found that a best fit value for the flame propagation dynamics for the fractal sub-model is  $D = 2.22$ , which is within the range  $D = 2.20$ – $2.33$  reported by Gostintsev *et al* [14]. One of the reasons for the optimum fractal dimension to be below the theoretical value is partial resolution of the flame wrinkling structure by LES. Indeed, it

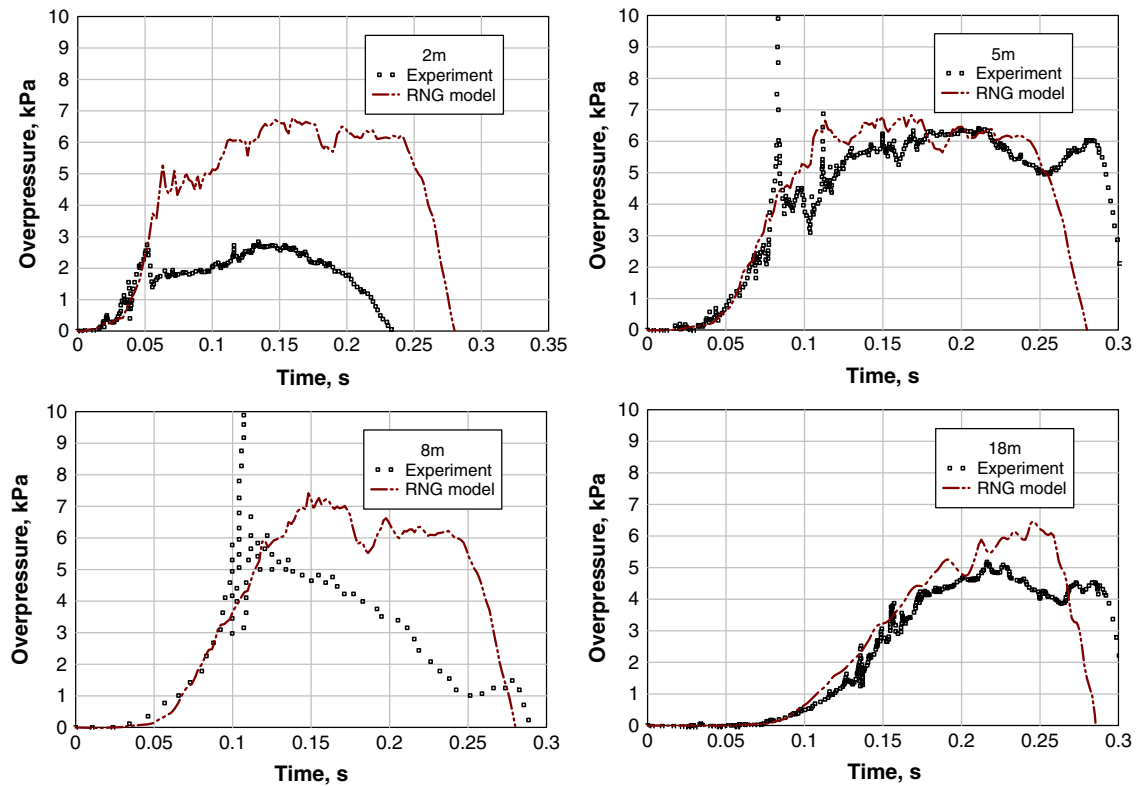


**Figure 6.** Comparison between experiment and simulation by the RNG combustion sub-model for pressure transients at the positive phase of the explosion pressure wave at locations 2 (a), 5 (b), 8 (c) and 18 m (d) from the ignition source.

was reported previously that for spherical flames the resolved fractal dimension is within the range 2.02–2.15 [34]. Along with good agreement in the prediction of the amplitude of the negative phase of the pressure wave the fractal sub-model over-predicts the amplitude of the positive phase by up to 50%. The reason for over-prediction of the positive pressure peak by the fractal model is not clear. This could be due to the effect of the PE balloon on the pressure wave. Indeed, segments of a balloon could ‘consume’ part of the energy in the pressure wave in the test. The effect of PE balloon segments is weakened at later stages and as a result the negative phase amplitude could be less affected.

The positive phase of the pressure wave at transducer locations inside the combustion zone, i.e. 2, 5, 8 and 18 m, is shown in figure 6. Transducers located at 2, 8 and 18 m from the ignition source were affected by the combustion products as their pressure transients did not return back to atmospheric pressure after the explosion. Still, pressure readings from these transducers may be used for explosion analysis until the time of flame arrival. A distinctive overpressure peak  $\Delta p_F$  of about 10 kPa in the pressure transients followed flame propagation (see figures 6(b) and (c)). The simulations reproduced an overpressure peak at the moment when the flame front arrived at the location of a sensor. Experimental pressure peak appears somewhat earlier compared with simulation results. It is in agreement with experimental data [2] where it was reported that the flame proliferates along the pressure measurement axis much more rapidly than in other directions. The fact of higher  $\Delta p_F$  at 5 and 8 m transducers could be explained by the intensification of combustion after the balloon shell had burst when the flame reached about half of the original radius of the

balloon  $0.5R_0$  (see figure 1). This is in line with results on easy DDT in hydrogen–air mixtures during venting of deflagration.

## 5. Conclusions

The LES model of large-scale accidental combustion is advanced further and applied to simulate the dynamics of the largest unconfined hydrogen–air deflagration ever performed. Two combustion sub-models were applied to analyse experimental data, one derived from the RNG theory and another from the fractal theory. Both sub-models include a SGS model of a transition from laminar to self-similar turbulent regime of flame propagation, which is based on a theoretical consideration by Karlovitz *et al* of the maximum turbulence generated by flame front itself and the results by Gostintsev *et al* on a critical radius of 1.0–1.2 m for the transition for stoichiometric hydrogen–air mixture.

Both combustion sub-models were applied in the calculation domain  $200 \times 200 \times 100$  m on an unstructured tetrahedral grid with a moderate number of CVs less than 300 000. Grid sensitivity analysis demonstrated that the LES model predictions vary to less than 5% for two unstructured tetrahedral grids with a difference in the characteristic cell size of 2.

Formation and decay of the pressure wave are reproduced in simulations, including the experimental observation that a negative phase has a shorter duration and a higher amplitude compared with a positive phase.

There is a more pronounced deceleration of simulated flame front at the end of deflagration compared with

experiment. It is thought to be due to insufficient resolution of the grid and affects slightly the duration of the positive phase of the pressure wave. Simulations on the adaptive grid in the area of hydrogen concentration gradients would better reproduce experimental data.

In the RNG combustion sub-model the effect of flow turbulence on the turbulent burning velocity is taken into account by the implementation of Yakhot's formula for turbulent premixed flame propagation velocity, which does not include either adjustable parameters or empirical coefficients. The RNG sub-model simulations reproduce initial flame acceleration and after that give practically constant flame front propagation velocity. The RNG sub-model is closer to experimental results in prediction of the positive phase but under-predicts by up to 30% the negative phase amplitude.

The fractal combustion sub-model gives a best fit to experimental flame propagation dynamics with a fractal dimension  $D = 2.22$ , which is within the range 2.20–2.33 reported by Gostintsev *et al* for large-scale unconfined explosions. Simulation with  $D = 2.22$  reproduces accurately the experimentally observed flame front acceleration during the whole process of deflagration, the negative phase of the explosion pressure wave and overestimates by up to 50% the positive phase. Higher pressure peak of the positive phase in simulation compared with experiment could be attributed to the effect of the PE balloon. Simulations with theoretical value  $D = 2.33$  apparently over-predicts both flame propagation and pressure dynamics.

Numerical simulations partially resolve flame front wrinkling due to hydrodynamic instability. This contributes by a factor of the order of 1.1 to the flame propagation velocity. The flow turbulence in the RNG sub-model contributes by an additional factor of the order of 1.15 to the burning velocity. Fractals increase the flame surface area in the fractal sub-model by a factor of the order of  $(R/1.2)^{0.22}$  depending on the flame front radius, e.g. 1.74 for a radius  $R = 15$  m. The turbulence generated by flame front itself is the main contribution to the augmentation of the turbulent burning velocity and equals to 3.6 for stoichiometric hydrogen–air mixture.

Both sub-models reproduce experimental flame front propagation dynamics up to 40 m diameter and pressure dynamics up to 80 m, i.e. at scales characteristic for hydrogen safety engineering problems. The agreement between numerical simulations and experimental data demonstrates the merits of the developed LES model for large-scale accidental premixed combustion.

## Acknowledgments

Authors acknowledge the support of this work by their institutions and by the Commission of the European Union (Contract No 502630 HySafe 'Safety of Hydrogen as an Energy Carrier', [www.hysafe.org](http://www.hysafe.org)).

## References

- [1] Dorofeev S B 1995 Blast effects of confined and unconfined explosions *Proc. 20th Symp. (Int.) on Shock Waves (Pasadena, CA, USA, July 1995)* pp 77–86
- [2] Fraunhofer-institut für treib- und explosivstoffe 1983. ICT-Projektforchung 1983. Forschungsprogramm "Prozeßgasfreisetzung—Explosion in der Gasfabrik und Auswirkungen von Druckwellen auf das Containment". Ballonversuche zur Untersuchung der Deflagration von Wasserstoff/Luft-Gemischen (Abschlußbericht). Projektleiter: H.Pförtner, Bearbeiter: H.Schneider, Dezember 1983
- [3] Bradley D 1999 *Phil. Trans. R. Soc. Lond. A* 3567–81
- [4] Hawkes E R and Cant R S 2001 Implication of a flame surface density approach to large eddy simulation of premixed turbulent combustion *Combust. Flame* **126** 1617–29
- [5] Poinso T and Veynante D 2001 *Theoretical and Numerical Combustion* (Edwards: Philadelphia)
- [6] Kaufmann A, Nicoud F and Poinso T 2002 Flow forcing techniques for numerical simulation of combustion instabilities *Combust. Flame* **131** 371–85
- [7] Strehlow R A and Baker W E 1976 The characterization and evaluation of accidental explosions *Prog. Energy Combust. Sci.* **2** 27–60
- [8] Zeldovich Ya B, Barenblatt G I, Librovich V B and Makhviladze G M 1980 *Mathematical Theory of Combustion and Explosion* (Moscow: Nauka)
- [9] Makeev V I, Gostintsev Yu A, Strogonov V V, Bokhon Yu A, Chrnushkin Yu N and Kulikov V N 1983 Combustion and detonation of hydrogen–air mixtures in free spaces *Combust., Explosion Shock Waves* **19** 16–18
- [10] Pförtner H 1985 The effects of gas explosions in free and partially confined fuel/air mixtures *Propellants, Explosives, Pyrotech.* **10** 151–5
- [11] Becker Th and Ebert F 1985 Vergleich zwischen experiment und theorie der explosion grosser, freier Gaswolken *Chem. Ing. Tech.* **57** 42–5
- [12] Gorev V A 1982 Comparison of the air explosion waves from different sources *Combust., Explosion Shock Waves* **8** 77
- [13] Bystrov S A and Gorev V A 1982 Interaction of explosion waves from a spherical deflagration with an obstacle *Combust., Explosion Shock Waves* **20** 113–6
- [14] Dorofeev S B, Sidorov V P and Dvoinishnikov A E 1995 Blast parameters from unconfined gaseous detonations *Proc. 20th Symp. (Int.) on Shock Waves (Pasadena, CA, USA, July 1995)* pp 673–8
- [15] Gostintsev Yu A, Istratov A G and Shulenin Yu V 1988 Self-similar propagation of a free turbulent flame in mixed gas mixtures *Combust., Explosion Shock Waves* **24** 63–70
- [16] Gouldin F C 1987 *Combust. Flame* **68** 249–66
- [17] Abdel-Gayed R G, Al-Khishali K J and Bradley D 1984 *Proc. R. Soc. Lond. A* 391 393–414
- [18] Gulder O L 1990 Turbulent premixed combustion modelling using fractal geometry *Proc. Comb. Inst.* **23** 835
- [19] Gostintsev Yu A, Istratov A G, Kidin N I and Fortov V E 1999 *High Temp. Thermophys.* (Teplofizika Vysokih Temperatur) **37** 633–7 (in Russian)
- [20] Gulder O L *et al* 2000 Flame front surface characteristics in turbulent premixed propane/air combustion *Combust. Flame* **120** 407–16
- [21] Lee J H S 1977 Initiation of gaseous detonation *Ann. Rev. Phys. Chem.* **28** 75–104
- [22] Bull D C and Martin J A 1977 Explosion of unconfined clouds of natural gas *American Gas Association, Transmission Conf. (Missouri, USA 16–18 May)(AGA Operating Section Proc.)* Paper 77-T-40
- [23] Lee J H S and Moen I O 1980 The mechanism of transition from deflagration to detonation in vapor cloud explosions *Prog. Energy Combust. Sci.* **6** 359–89
- [24] Moen I O, Lee J H S, Hjertager B H, Fuhre K and Eckhoff R K 1982 Pressure development due to turbulent flame propagation in large-scale methane-air explosions *Combust. Flame* **47** 31–52
- [25] Pfortner H 1983 Flame acceleration and pressure build up in free and partially confined hydrogen-air clouds

- 9th Colloquium on the Dynamics of Explosions and Reactive Systems* (Poitiers, France: ICDEERS)
- [25] Pfortner H 1985 The effects of gas explosions in free and partially confined fuel/air mixtures *Propellants, Explosives, Pyrotech.* **10** 151–5
- [26] Pikaar M J 1985 Unconfined vapour cloud dispersion and combustion: an overview of theory and experiments *Chem. Eng. Res. Des.* **63** 75–81
- [27] Berman M 1986 Critical review of recent large-scale experiments on hydrogen–air detonations *Nucl. Sci. Eng.* **93** 321–47
- [28] Moen I O, Bjerketvedt D, Jenssen A and Thibault P A 1985 Transition to detonation in a large fuel–air cloud *Combust. Flame* **61** 285–91
- [29] Leyer J C, Desbordes D, Saint-Cloud J P and Lannoy A 1993 Unconfined deflagrative explosion without turbulence: experiment and model *J. Hazard. Mater.* **34** 123–50
- [30] Moen I O 1993 Transition to detonation in fuel–air explosive clouds *J. Hazard. Mater.* **33** 159–92
- [31] Dorofeev S B, Sidorov V P and Dvoinishnikov A E 1996 Deflagration to detonation transition in large confined volume of lean–hydrogen–air mixtures *Combust. Flame* **104** 95–110
- [32] Khokhlov A M, Oran E S, Wheeler J C 1997 A theory of deflagration-to-detonation transition in unconfined flames *Combust. Flame* **108** 503–17
- [33] Kelly T J, Pierorazio A J, Goodrich M L, Kolbe M, Baker Q A and Ketchum D E 2003 Deflagration to detonation transition in unconfined vapor cloud explosions *18th Annual Int. Conf. - Managing Chemical Reactivity Hazards and High Energy Release Events, (Scottsdale (AZ), 23–25 September 2003)* (New York: Center for Chemical Process Safety) pp 155–68
- [34] Molkov V, Makarov D and Grigorash A 2004 Cellular structure of explosion flames: modelling and large eddy simulation *Combust. Sci. Tech.* **176** 851–85
- [35] Makarov D and Molkov V 2004 Large eddy simulation of gaseous explosion dynamics in an unvented vessel *Combust., Explosion Shock Waves* **40** 136–44
- [36] Molkov V and Makarov D 2004 Large eddy simulation of hydrogen–air explosion at elevated temperature *Adv. Chem. Phys.* **23** 25–36
- [37] Pope S B 2004 Ten questions concerning the large-eddy simulation of turbulent flows *New J. Phys.* **6** 1–24
- [38] Yakhot V and Orszag S 1986 Renormalization group analysis of turbulence: I. Basic theory *J. Sci. Comput.* **1** 3–51
- [39] Smagorinsky J 1963 General circulation experiments with the primitive equations: I. The basic experiment *Mon. Weather Rev.* **91** 99–164
- [40] Babkin V S, Viun A V and Kozachenko L S 1966 The investigation of pressure dependence of burning velocity by the constant volume bomb method *Combust., Explosion Shock Waves* **2** 52–60
- [41] Lamoureux N, Djebaili-Chaumeix N and Paillard C E 2002 Laminar flame velocity determination for H<sub>2</sub>–air–steam mixtures using the spherical bomb method *J. Phys. IV (France)* **12** Pr7-445–7-458
- [42] Yakhot V 1988 Propagation velocity of premixed turbulent flames *Combust. Sci. Technol.* **60** 191–214
- [43] Karlovitz B, Denniston D W Jr and Wells F E 1951 Investigation of turbulent flames *J. Chem. Phys.* **19** 541–7
- [44] Makarov D, Molkov V and Gostintsev Yu 2006 Comparison between RNG and fractal combustion models for LES of unconfined explosions *Combust. Sci. Technol.* at press
- [45] [www.hysafe.org](http://www.hysafe.org)
- [46] Molkov V V, Makarov D V, Schneider H 2006 Hydrogen-air deflagrations in open atmosphere: large eddy simulation analysis of experimental data *Int. J. Hydrog. Energy* submitted

# A New Set of Blast Curves from Vapor Cloud Explosion

M.J. Tang and Q.A. Baker

Wilfred Baker Engineering, Inc., 8700 Crownhill, Suite 310, San Antonio, Texas 78209

*Past accidents have demonstrated that vapor cloud explosions (VCEs) are the most severe threat to refining and petrochemical industries. In order to estimate the air blast parameters at any given distance from a possible explosion source, a variety of prediction methods have been developed. A brief description of these prediction methods is first presented. Then, the focus of this paper is on an engineering method based on blast curves, which is the most frequently used prediction method.*

*Knowledge of blast effects from vapor cloud explosions has greatly improved due to the efforts of investigators in many countries during the last three decades; however, blast curves have not been reexamined. One of the aims of this paper is to present a new set of blast curves which have been validated with available experimental results and analytical solutions. Another aim is to present a comprehensive set of blast curves including blast parameters for both positive and negative phases.*

*The new blast curves, which are a modification of the Baker-Strehlow curves, improve the prediction for detonations and supersonic deflagrations as well as for subsonic flames. By changing the slope of the blast pressure versus distance curve, the overly conservative blast pressure predictions by the previous Baker-Strehlow curves at large standoff distances for detonations and supersonic deflagrations are reduced. By clarifying the labeling of the flame Mach number for each blast curve, the overly conservative pressure and impulse predictions for subsonic flames are also avoided.*

*The new blast curves have been validated against VCE experiments including detonations, fast deflagrations, and slow deflagrations. Particular attention was given to large scale deflagration experiments, which became available only recently. Good agreement is shown between the new blast curves and the experimental blast data for vapor cloud detonations and subsonic deflagrations. For supersonic deflagrations, the blast curve predictions are overly conservative in that blast pressure decays more rapidly with distance in experiments than the calculated curves.*

## INTRODUCTION

Since the Flixborough disaster, which occurred in June, 1974, it has been realized that the most severe threat to chemical and petrochemical industries is the

hazard of vapor cloud explosions, which have been the predominant causes of the largest losses in these industries [1]. Unfortunately, these types of devastating accidents still occur. The focus of this paper is on the prediction of blast effects from vapor cloud explosions because the air blast parameters at any given distance from a possible explosion source must be estimated in order to evaluate the risk associated with a given installation or activity. Furthermore, with proper safety guidelines, appropriate structural design and safe distancing considerations, blast hazards from vapor cloud explosions may be reduced to acceptable levels.

## VAPOR CLOUD EXPLOSION BLAST PREDICTION METHODS

Blast prediction methods for vapor cloud explosions (VCEs) may be grouped into three types of categories according to their nature and complexity.

### TNT Equivalence Method

It had been common practice for many years to compare the air blast effects of a VCE with the blast from a TNT charge. The available combustion energy in the vapor cloud is converted into an equivalent charge weight of TNT. This approach was attractive since the blast effects of TNT as a function of distance from the explosion source are well known. However, case studies revealed that there is almost no correlation between the amount of fuel involved in a VCE and the total quantity of fuel released and/or the yield. Reported yield factors generally range from 0.1 to 10% with the majority less than 1 to 2% according to accident investigations; a limited number of higher yield values have been reported. Various institutions have recommended markedly different of yield factor [2] values. A portion of this spread in yield factor values is due to uncertainties in the amount of fuel released. In addition, some investigators have developed yield factors based on the total amount of fuel released, whereas others have used only that in the flammable range or even a portion of the flammable range (i.e. that assumed to be capable of supporting an explosion). However, a significant portion of the spread in yield factor values is due to differences in the vapor cloud combustion mode. The major drawback of the TNT equivalence method is that the

blast yield is only associated with the amount of fuel involved and not the combustion mode.

It is now well understood that blast effects from vapor cloud explosions are determined not only by the amount of fuel burned, but more importantly by the combustion mode of the cloud. A wide spectrum of flame speeds may result from flame acceleration under various confinement and congestion conditions in industrial environments. In energy scaled coordinates, the TNT blast represents a single curve, whereas the blast waves generated by vapor cloud explosions are represented by a family of curves corresponding to various cloud combustion modes. Furthermore, there are dramatic differences between explosions involving vapor clouds and high explosives at close distances; for the same amount of energy, the high explosive blast overpressure is much higher and the blast impulse is much lower than that from a VCE [3].

Since control rooms and other blast resistant structures on plant sites are usually located close to potential explosions, we strongly recommend that the TNT equivalence method not be used for close-in VCEs blast load predictions. However, the TNT equivalence method is reasonable for far-field predictions of VCE overpressure except for very low flame speeds. Impulses from TNT blast curves are generally over-predicted in the far field.

#### Methods Based on Blast Curves

The use of a gas charge explosion to replace the TNT charge detonation has greatly improved the accuracy of VCE blast predictions. One-dimensional numerical studies of gas charge explosions were carried out by several groups of researchers using different numerical techniques, which resulted in several sets of blast curves. Among these, the most frequently used and widely accepted are the Baker-Strehlow [4] blast curves for spherical free air explosions and TNO [5] blast curves for hemispherical explosions.

The Baker-Strehlow curves provide positive pressure and impulse as a function of distance. The pressure, impulse and distance are non-dimensionalized using Sach's scaling law as follows:

$$\bar{P} = \frac{p - p_0}{p_0} \quad \bar{i} = \frac{ia_0}{E_t^{1/3} p_0^{2/3}} \quad \bar{R} = \frac{R}{(E_t / p_0)^{1/3}}$$

Where  $p_0$  is atmospheric pressure;  
 $a_0$  is acoustic velocity at ambient conditions;  
 $p$  is absolute peak pressure;  
 $R$  is stand-off distance;  
 $E_t$  is total energy release from the explosion source;  
 $i$  is specific impulse.

Both overpressure and impulse versus distance relations are presented as a families of curves, with the flame speed differentiating the curves within each family. In the non-dimensional form, flame speed is the only factor to determine the blast pressure and impulse at a given distance. A vapor cloud detonation is, of course, the worst case and produces the most

severe blast effects.

The TNO curves consist of positive pressure and time duration as functions of distance. The parameters were also non-dimensionalized using Sach's scaling law with pressure and distance as defined above, and the positive phase duration as follows:

$$\bar{P} = \frac{p - p_0}{p_0} \quad \bar{R} = \frac{R}{(E_t / p_0)^{1/3}} \quad \bar{t}_+ = \frac{t_+ a_0}{(E_t / p_0)^{1/3}}$$

where  $t_+$  is the time duration of the positive phase. Each curve in the TNO blast curve set is labeled by the initial explosion strength, ranging from 1 to 10, with 10 representing the worst case of a vapor cloud detonation.

In both Baker-Strehlow and TNO methods, the source energy is defined by a stoichiometric fuel/air mixture located within the confined and/or congested region. The flame speed or initial explosion strength is determined by empirical approaches based on the degree of confinement and obstruction within the source region as well as the distance available for flame acceleration [6-7]. As discussed above, one-dimensional numerical curves based on gas charges provide a better representation of VCE blast parameters than the TNT equivalence method. However, the one-dimensional curves are idealized symmetric representations that cannot describe the impact of non-symmetric vapor cloud shape, the location of turbulence generating obstacles, or the ignition location. Nevertheless, by simplifying real world scenarios, blast curve methods are still most frequently used as the engineering tool.

#### The Detailed Numerical Simulations

The application of three-dimensional numerical simulation based on computational fluid dynamics (CFD) to model vapor cloud explosions has developed rapidly during recent years. This approach has the potential of providing higher accuracy and directly addressing the details of real world scenarios without drastic simplifications; as a result, the empirical determination of the flame speed can be avoided. However, there are still significant difficulties in establishing combustion models capable of accurately representing the flame and flow field turbulence interactions in order to correctly simulate the flame acceleration process.

As a result of several intensive research programs, CFD codes are being developed and improved. However, the accuracy of a CFD simulation is limited by the accuracy of the numerical method and the underlying physical sub-models. Experimental validation is critical because the model employed to simulate the positive feedback loop for turbulent combustion rely to a great extent on empirical coefficients. Therefore, the application of any computer code for the detailed numerical VCE modeling should be limited to the type of problems for which the code has been validated by experiments. Also, a number of variables, such as grid and time resolution, have significant effects on the results, hence a high level of user expertise is required. It should also be noted that this type of sim-

ulation may also require a significant amount of time to setup and execute: this is particularly relevant where a number of scenarios must be investigated.

#### IMPROVEMENTS TO THE BAKER-STREHLOW BLAST CURVES

As discussed above, although detailed numerical methods are being developed, there is still a great need for less complex approaches which can be used on a routine basis to predict VCE blast effects for a large number of scenarios. The type of detailed information required for CFD modeling may not be available. Furthermore, the requisite experimental validation is not available for many cases. Moreover, blast curve methods are comparatively cost effective and easy to use. Therefore, concurrent with promoting the development of sophisticated CFD numerical simulations, efforts have been undertaken by WBE to improve the one-dimensional blast curves.

Two basic improvements have been made to the Baker-Strehlow blast curves. The first is a change in the slope of blast pressure decay curve that resulted in a considerable reduction of the predicted blast pressure at large standoff distances for supersonic flames. The other is a clarification in the labeling of the individual blast curves that resulted in a nearly two-fold decrease of blast pressure and impulse at all distances for subsonic flames. Here, the terms "supersonic" and "subsonic" refer to the flame Mach numbers with respect to the ambient sound velocity.

The comparison of the blast curves obtained by several numerical methods showed that the Baker-Strehlow supersonic curves decay too slowly in the far field and depart significantly from the other curves [8-9] in this range. Actually, the numerical calculation associated with the original Baker-Strehlow curve was only carried out to scaled distance of about two and was extrapolated to ten. The TNO curves give higher blast pressures at close distances, but decay more rapidly to provide the lowest blast pressures at medium and far distances.

The new blast curves were obtained by optimizing the numerical calculations. They are denoted as the Baker-Strehlow-Tang blast curves in order to distinguish them from the previous Baker-Strehlow curves. The Baker-Strehlow-Tang curves are similar to other numerical results, but still conservative in that a comparatively slow blast wave decay is maintained.

The other improvement in the Baker-Strehlow-Tang curves relative to the Baker-Strehlow curves is the labeling of each blast curve. The previous Baker-Strehlow curves were labeled by  $M_w$ , which refers to the velocity of heat addition in the numerical calculations in a Lagrangian coordinate system. However, the flame speed,  $M_f$ , measured in experiments is the velocity relative to a fixed observer (i.e., the velocity in an Eulerian coordinate system). As a consequence, a misuse of the blast curve often occurs due to the misinterpretation of the flame Mach numbers. Nearly twice of the blast overpressure is predicted when an empirical flame speed is used to select the blast curves for subsonic flames labeled according to  $M_w$ .

The blast curves obtained by one-dimensional

numerical calculations, such as the Baker-Strehlow and TNO curves, were published in 1970's and have since been frequently used in a variety of plant safety applications. However, since systematic experimental data became available only in recently years, they have not been validated by experiments. As part of this work, the Baker-Strehlow-Tang curves were validated by experiments. The validation was carried out in three different combustion mode regimes: vapor cloud detonation, supersonic deflagration and subsonic deflagration. The primary sources of experimental data for VCE detonation are the publications by Brossard et al. [10] and the empirical equations summarized by Dorofeev [11]. The experimental data used in the comparison for supersonic and subsonic vapor cloud deflagrations were taken from the MERGE (Modeling and Experimental Research into Gas Explosions) [12] and EMERGE (Extended Modeling and Experimental Research into Gas Explosions) [13] summary reports. The validation comparisons were presented in previous papers [9, 14] and are omitted here for the sake of brevity.

#### RELATIONSHIP BETWEEN FLAME VELOCITIES

The following relationship between  $M_{su}$  and  $M_f$  is derived from the mass conservation for low flame velocities:

$$M_f = (\rho_u / \rho_b) M_{su}$$

where  $M_f$  is apparent flame Mach number relative to a fixed observer (flame speed)

$M_{su}$  is flame Mach number relative to the moving gas ahead of the flame (burning velocity);

$\rho_b$  and  $\rho_u$  are gas densities behind (burnt) and ahead of the flame (unburnt), respectively;

The Mach number,  $M_w$ , refers to the Lagrangian velocity of the heat addition in numerical calculations and a correction factor to relate  $M_w$  and  $M_{su}$  was derived by Strehlow and Luckritz [4] is given below:

$$M_{su} = (\rho_b / \rho_u)^{2/3} M_w \quad (1)$$

Thus, the relation between  $M_w$  and  $M_f$  is:

$$M_f = (\rho_u / \rho_b)^{1/3} M_w \quad (2)$$

The above relations are invalid when  $M_f$  approaches unity. For supersonic flames,  $M_f = M_w$ . For near sonic flames, the relationship between  $M_f$  and  $M_w$  was established by using the approximate equation for the apparent flame Mach number and the overpressure at the flame front. Assuming an expansion ratio,  $\rho_b / \rho_u$  of 7 for stoichiometric mixtures of commonly used hydrocarbon - air mixtures and a specific heat ratio of 1.4 (ambient air), this equation can be written as:

$$\frac{p_{max} - p_0}{p_0} = 2.4 \frac{M_f^2}{1 + M_f} \quad (3)$$

where  $p_{max}$  is the maximum pressure at the flame front. Although the above equation was derived from acoustic theory [15], comparison with experimental measurements shows that it is valid for a wide range of flame speeds [16]. The procedure employed was to determine the maximum overpressure for a range of  $M_w$  values of by numerical calculations. Then,  $M_f$  was calculated for a given  $p_{max}$  using equation (3). The previous Baker-Strehlow curves were labeled by  $M_w$  while the new Baker-Strehlow-Tang curves are labeled by  $M_f$ . Table 1 presents the relationships among  $M_w$ ,  $M_f$  and the scaled value of  $p_{max}$ .

TABLE 1.  $M_f$  and  $M_w$  Relations

$M_w$	$M_f$	$P_{max}$
0.037	0.07	0.010
0.074	0.12	0.028
0.125	0.19	0.070
0.250	0.35	0.218
0.500	0.70	0.680
0.750	1.00	1.240
1.000	1.40	2.000

PRESENTATION OF THE BAKER-STREHLOW-TANG CURVES

The families of blast curves for the positive and negative overpressure, positive and negative impulse, arrival time of the shock front and the maximum particle velocity versus distance for a spectrum of flame Mach numbers are presented in Figures 1 - 6. The blast curves for negative phase parameters are included in this presentation due to the importance of negative phase blast loading on structure response. A brief discussion of the blast curves characteristics in different flame speed regimes is presented in the following sections:

Detonation and Fast Deflagrations

As can be seen from Figures 1 and 2, the overpressure versus distance curves merge into a single curve

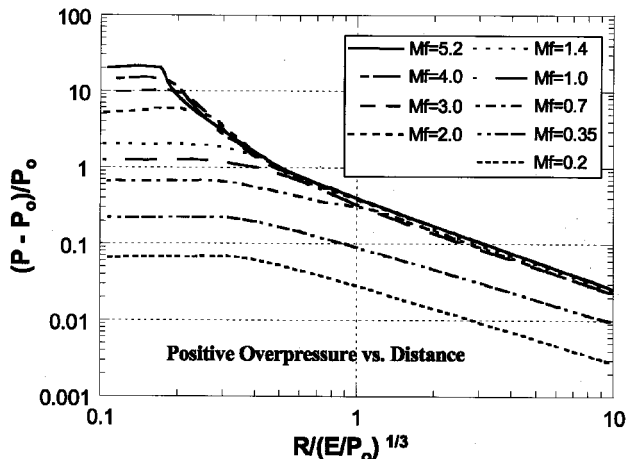


FIGURE 1. Positive Overpressure vs. Distance for Various Flame Speeds

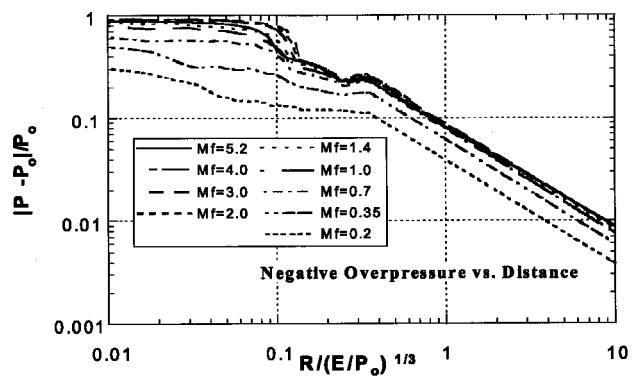


FIGURE 2. Negative Overpressure vs. Distance for Various Flame Speeds

for various flame speeds in the supersonic regime for locations outside the vapor cloud. The overpressures inside the vapor cloud are nearly uniform and the pressure increases with the flame speed for positive overpressure. As can be seen by comparing Figures 1 and 2 the negative overpressure (absolute value) never exceeds the positive overpressure for supersonic flames. This generalization does not hold true for subsonic flames.

The impulse versus distance curves for the supersonic regime also merge outside the cloud, as shown in Figures 3 and 4. The highest flame speed (detona-

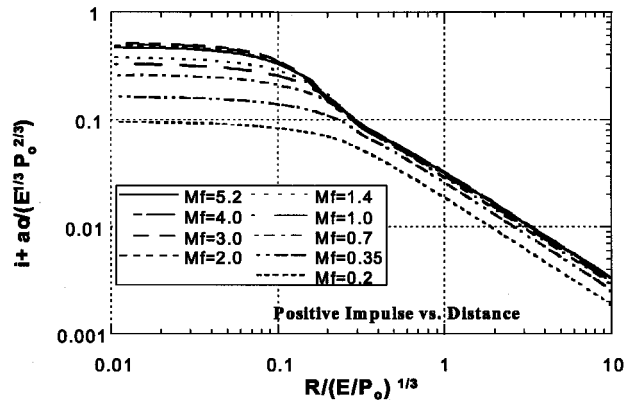


FIGURE 3. Positive Impulse vs. Distance for Various Flame Speeds

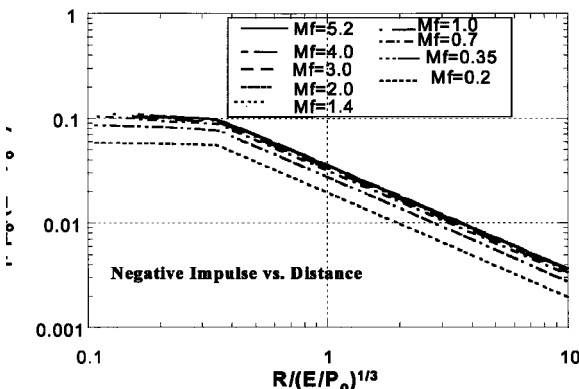


FIGURE 4. Negative Impulse vs. Distance for Various Flame Speeds

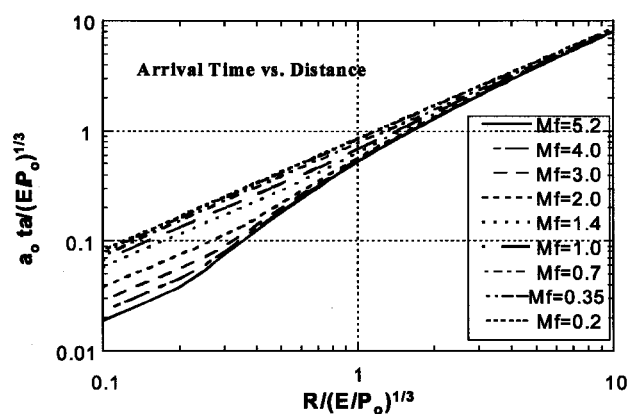


FIGURE 5. Arrival Time vs. Distance for Various Flame Speeds

tion with  $M_f = 5.2$ ) generated the lowest positive impulse inside the cloud. The negative impulse versus distance curves for various flame speeds in the supersonic regime merge at all distances. The magnitude of the negative impulse is comparable with that of the positive impulse for locations outside the combustion zone (about  $R/(EP_0)^{1/3} > 0.4$ ).

Good agreement between numerical calculations and experimental measurements was achieved for the detonation mode [9,14], as expected. In the detonation experiments, a strong ignition at the cloud center was applied which resulted in a detonation involving the entire cloud. In the numerical calculations, constant flame propagation at the maximum flame speed is assumed, which provides a good simulation of the detonation experiments.

Although the detonation combustion mode, which produces the most severe damage, is extremely unlikely to occur, fast deflagrations of the cloud can result from flame acceleration under confined and congested conditions in industrial environments. A comparison was made between the EMERGE experimental data and the Baker-Strehlow-Tang blast pressures in the supersonic deflagration regime [14]. The decay of the experimental blast pressures is much faster than the calculations in this regime. This may be

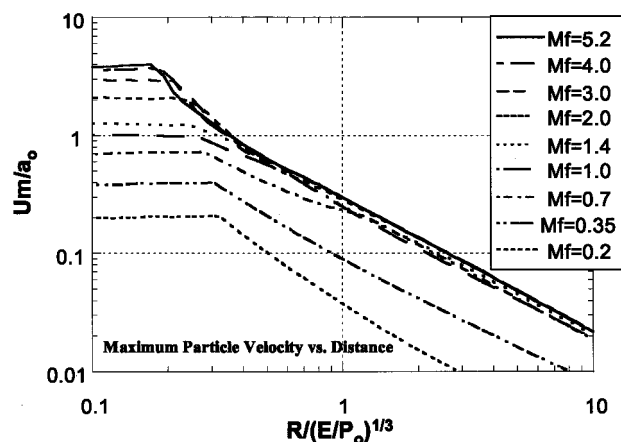


FIGURE 6. Maximum Particle Velocity vs. Distance for Various Flame Speeds

explained by the fact that a constant flame speed at the maximum value was used in the calculations, whereas in the experiments a large portion of the cloud burned at very low velocities before the flame accelerated to the maximum speed. Therefore, the fraction of the source energy released at a rate sufficiently high to support the shock wave is much less in the experiments than in the calculations. This argument is supported by the fact that the deviation of experimental data from the calculated blast curve is more pronounced for less reactive mixtures, for which flame acceleration is slower than with more reactive fuels.

### Sonic Deflagrations

For a VCE with a flame Mach number close to unity, the overpressure curves merge into a single curve outside the vapor cloud, the magnitude of which is only marginally below the supersonic curve (see Figure 1). This can be explained by the shock formation due to a piston moving at subsonic speed. In fact, the blast waves produced by sonic flames have the features of a shock wave that decays faster than the acoustic waves generated by subsonic flames. The comparison of the blast curves with experimental data in the sonic regime is similar to that in supersonic regime. The decay of the experimental pressures is also much faster than the calculations in this regime.

### Subsonic Deflagrations

Unlike the blast waves generated by supersonic and sonic flames the pressure versus distance curves produced by slow subsonic flames do not merge. The flame propagation speed has a significant influence on the blast parameters both inside and outside the source volume. The fact that the blast curves for various flame speeds are nearly parallel indicates that the blast waves produced by slow subsonic flames ( $M_f$  less than 0.7 or  $M_w$  less than 0.5) follow the acoustic decay law and the decay rate is not influenced by the flame speed.

Good agreement was found between the numerical results, analytical solution by acoustic theory, and experimental data in the subsonic regime. According to the acoustic solution, the overpressure is inversely proportional to the distance. Thus, the inverse-radius law, can be used to extend the blast curves to far distances.

### CONCLUSIONS

A newly developed set of VCE blast curves provides an improved representation of blast parameters in both the positive and negative phases. Labeling of the curves has been modified to allow direct use of empirical flame speed data to select a blast curve. Validation against VCE experiments has shown good agreement in the supersonic and subsonic regimes, and conservative predictions in the sonic deflagration regime.

## LITERATURE CITED

1. **Lenoir, E.M. and J.A. Davenport**, "A Survey of Vapor Cloud Explosions-Second Update", *26th Loss Prevention Symposium*, AIChE, 1992
2. "Guidelines For Evaluating The Characteristics Of Vapor Cloud Explosions, Flash Fires, And BLAVES", *Center For Chemical Process Safety*, AIChE, 1994
3. **Baker, Q.A. and W.E. Baker**, "Pros and Cons of TNT Equivalence for Industrial Explosion Accidents", *Proceedings of the International Conference and Workshop on Modeling and Mitigating the Consequences of Accidental Releases of Hazardous Materials*, May, 1991
4. **Strehlow, R.A. R.T. Luckritz, A.A. Adamczyk and S.A. Shimp**, "The Blast Wave Generated By Spherical Flames", *COMBUSTION AND FLAME*, 35: 297-310, 1979
5. **van den Berg, A.C.** "The Multi-Energy Method - A Framework For Vapor Cloud Explosion Blast Prediction", *J. of Hazard Materials*, 12, 1-10, 1985
6. **Baker, Q.A. M.J. Tang, E. Scheier and G.J. Silva**, "Vapor Cloud Explosion Analysis", *28th Loss Prevention Symposium*, AIChE, April, 1994
7. **Baker, Q.A. C.M. Doolittle, G.A. Fitzgerald and M.J. Tang**, "Recent Developments in the Baker-Strehlow VCE Analysis Methodology", *31th Loss Prevention Symposium*, AIChE, March, 1997
8. **Tang, M.J. and Baker, Q.A.**, "Predicting Blast Effects From Fast Flames", *32th Loss Prevention Symposium*, AIChE March 1998
9. **Tang, M.J., Cao, C.Y., and Baker, Q.A.**, "Blast Effects From Vapor Cloud Explosions", *International Loss Prevention Symposium*, Bergen, Norway, June 1996
10. **J. Brossard, S. Hendrickx, J.L. Garnier, A. Lannoy and J.L. Perrot**, "Air Blast From Unconfined Gaseous Detonations", *Proceedings of the 9th International Colloquium on Dynamics of Explosion and Reactive Systems*, *The American Institute of Aeronautics and Astronautics, Inc.*, 1984
11. **Dorofeev, S.B.** "Blast Effects Of Confined And Unconfined Explosions", *Proceedings Of The 20th International Symposium On Shock Waves*, 1995
12. **Mercx, W.P.M.**, "Modeling and Experimental Research into Gas Explosions", Overall final report of the MERGE project
13. **Mercx, W.P.M. N.R. Popat and H. Linga**, "Experiments to Investigate the Influence of an Initial Turbulence Field on the Explosion Process", *Final Summary Report for EMERGE*
14. **Tang, M. J, Baker, Q. A.**, "Comparison of Blast Curves from Vapor Cloud Explosions", *Proceedings of the International Symposium on Hazards, Prevention and Mitigation of Industrial Explosions* Schaumburg, Illinois, USA, September, 1998
15. **Taylor, G.I.**, "The air wave surrounding an expanding sphere", *Proc. Roy. Soc. London, Series A*, 186:273-292, 1946
16. **Harrison, A.J. and J.A. Eyre**, "The effect of Obstacle Arrays on the combustion of Large premixed Gas/air clouds, "Combustion Science and Technology," Vol.52. March 1987.

*This paper (29e) was presented at the 33rd Loss Prevention Symposium held during the AIChE Spring National Meeting in Houston, Texas, March 14-18, 1999*

# A Flame Speed Correlation for Unconfined Gaseous Explosions

**Sergey B. Dorofeev**

FM Global, Norwood, MA 02062; serгей.dorofeev@fmglobal.com (for correspondence)

Published online 15 November 2006 in Wiley InterScience (www.interscience.wiley.com). DOI 10.1002/prs.10176

*An approximate method for description of flame acceleration in congested areas filled with combustible gases is presented. The method takes into account both the flame folding arising from interactions with obstacles of the flow produced by the flame and the increase of the burning rate resulting from turbulence generated in the flow ahead of the flame. A simple analytical expression for the flame speed is suggested. Coefficients in this correlation are determined by fitting the model predictions with a set of experimental data. This correlation is then used to evaluate the maximum flame speed that may be developed in vapor cloud explosions as a function of scale and obstacle density. As an example of applications, the flame speeds are evaluated for four typical fuels: methane, propane, ethylene, and hydrogen, and for three different levels of congestion. Both ideal stoichiometric mixtures of the four fuels with air and clouds with nonuniform concentration distributions are considered. The method is shown to take appropriate account of mixture properties. In particular, the well-known difference in combustion behavior of methane, propane, ethylene, and hydrogen was well captured by the method. On the basis of the maximum flame speeds, the severity of the blast effect from unconfined gaseous explosions is evaluated. The results are compared with other methods for evaluation of the blast effect from unconfined vapor cloud explosions. © 2006 American Institute of Chemical Engineers Process Saf Prog 26: 140–149, 2007*

## 1. INTRODUCTION

It has been shown by many investigators (for example, see Strehlow *et al.* [1] and Baker *et al.* [2]) that the amplitude of the pressure waves generated by gaseous explosions essentially depends on the maximum flame speed achieved during the combustion process. There are several vapor cloud explosion (VCE) prediction methods that are essentially based on the flame speeds. The TNO multienergy method [3] provides ten numerically defined curves for both pressure and duration. The curves are evenly spaced based on maximum overpressure, with a severity number specified for each curve. The severity number depends on the maximum flame speed. The Baker–Strehlow–Tang (BST) method [4–7] uses a continuum of numerically determined pressure and impulse curves that are based on the flame speed or Mach number. The method presented in Dorofeev [8] provides analytical approximations for the pressure and impulse curves as functions of flame speeds and the mixture expansion ratio.

Applications of the VCE prediction methods mentioned above require reliable estimates for the flame speed as a function of the propagation distance and obstacle geometry. For this purpose, the BST method uses flame speed tables [4–7] based on experimental data. Applications of the TNO multienergy method rely on a correlation for flame speeds based on the specific geometrical configuration used in the project MERGE (Modeling and Experimental Research into Gas Explosions), a cooperative European project [9,10]. These two methods address geometries with relatively heavy obstructions. At the same time there are more experimental data available on flame speeds [11–16]. These data include unconfined cases without obstacles, where significant blast effects were observed [11–15].

The present study is aimed at the development and evaluation of an analytical model for the maxi-

Prepared for presentation at American Institute of Chemical Engineers 2006 Spring National Meeting, 40th Annual Loss Prevention Symposium, Orlando, FL, April 24–26, 2006  
 AIChE shall not be responsible for statements or opinions contained in articles or printed in its publications.

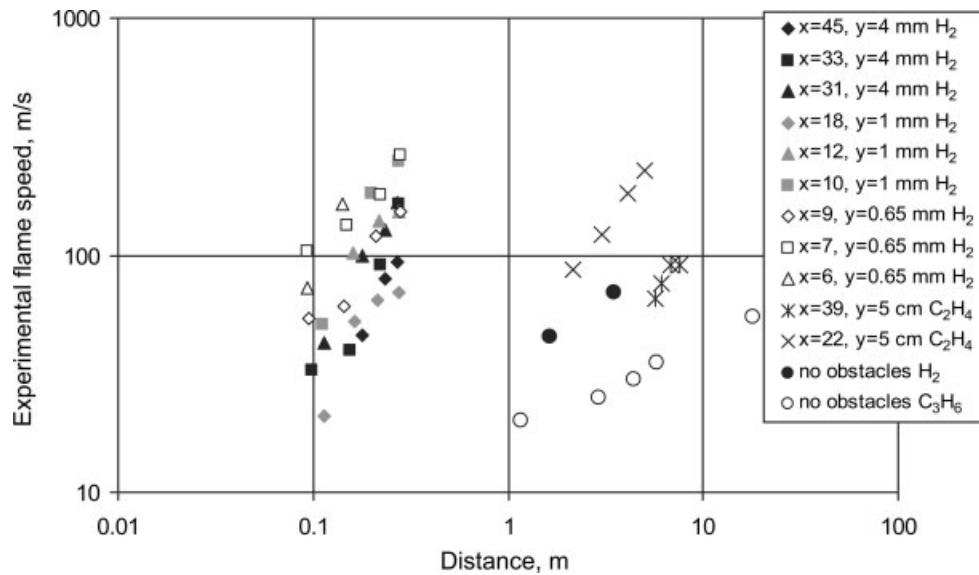


**Figure 1.** Range of experimental data on flame speed vs. distance used in flame speed correlation.

imum flame speeds for unconfined explosions in regions both with and without obstacles. The following presentation includes a description of the method, its validation, and examples of its application for simplified VCE predictions.

## 2. METHODOLOGY

### 2.1. Evaluation of Flame Speeds

In the following model, an initially spherical flame is considered, which propagates from an ignition source through an obstructed area. The flame speed  $V_f$ , relative to a fixed observer at a distance  $R$  from ignition, depends on the burning velocity (generally turbulent)  $S_T$ , the flame area  $A_f$ , and the ratio of densities between the reactants and products  $\sigma$ :

$$V_f = \sigma S_T \frac{A_f}{A_R} \quad (1)$$

where  $A_R = 4\pi R^2$  is the area of the spherical flame at  $R$ .

The flame speed increases as a result of the increase of both the flame area (flame folding) in an obstacle field and the turbulent burning rate during flame propagation. The latter effect should also describe the increase of the flame speed with distance in a system without obstacles.

The flame folding effect can be approximately described by applying simple geometrical considerations as was suggested in Grune *et al.* [16] and Vesper *et al.* [17]. If one considers a uniform obstacle field with distance between obstacles  $x$  and their characteristic size  $y$ , the following assumptions can be made:

- The flame is folded, as a result of interactions of the flame with obstacles, and forms a flame brush.
- Each obstacle inside the brush contributes the value of  $4xy$  to the total flame surface.

- The brush width is variable so that it is equal to the flame radius at small  $R$  and is close to  $\sigma x$  at large  $R$ .
- The flame area changes with  $R$  can be described by a power law.

Based on these assumptions Eq. 1 becomes

$$V_f = \sigma S_T \left[ 1 + \frac{4\sigma y}{3x} \frac{R^\alpha}{(\sigma x)^\alpha} \right] \quad (2)$$

where the exponent  $\alpha$  may be considered as an unknown parameter of the order of 0.5.

The effect of turbulence can be accounted for by applying Bradley's correlation [18] for turbulent burning velocity ( $S_T$ ):

$$\frac{S_T}{S_L} = a \left( \frac{u'}{S_L} \right)^{1/2} \left( \frac{L_T}{\delta} \right)^{1/6} \quad (3)$$

where  $u'$  is turbulent fluctuation velocity;  $S_L$  is laminar burning velocity;  $L_T$  is the integral length scale of turbulence;  $\delta = \nu/S_L$  is the laminar flame thickness, where  $\nu$  is kinematic viscosity; and  $a$  is a coefficient. The turbulent fluctuation velocity  $u'$  can be written as a fraction of the flow speed  $V$  ahead of the flame:

$$u' = bV = bV_f \frac{\sigma - 1}{\sigma} \quad (4)$$

where  $b$  is a coefficient of the order of  $10^{-2}$ . Equations 2–4 yield

$$V_f = a^2 b \sigma (\sigma - 1) S_L \left[ 1 + \frac{4\sigma y}{3x} \frac{R^\alpha}{(\sigma x)^\alpha} \right]^2 \left( \frac{L_T}{\delta} \right)^{1/3} \quad (5)$$

Equation 5 gives an approximate description of the flame speed as a function of distance in an area with or without obstacles. It is seen that a significant

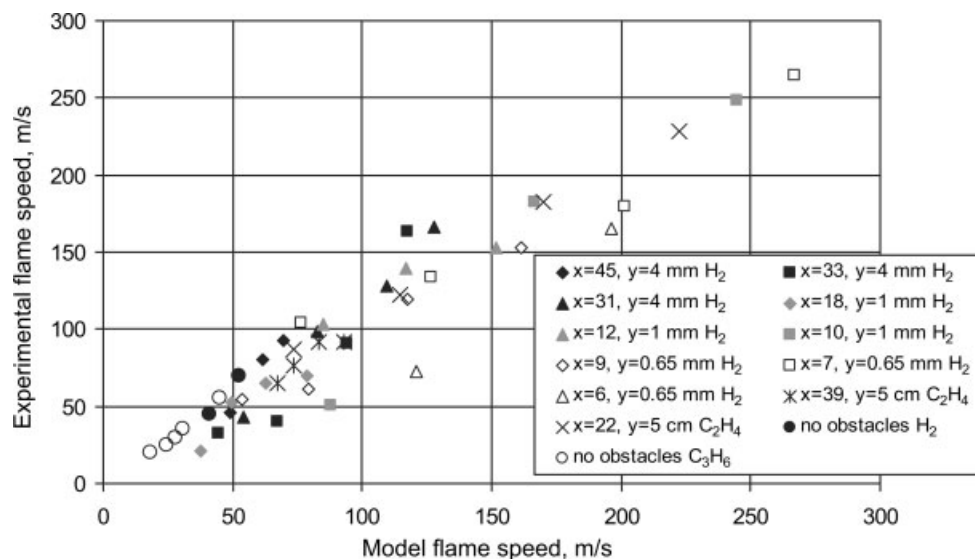


**Figure 2.** Comparison of flame speed correlation with experimental data.

increase of the flame speed with distance can be expected only in a system with obstacles,  $y \neq 0$ . In this case the contribution of parameter  $(L_T/\delta)$  is relatively weak and may be considered unimportant. In the case of no obstacles,  $y = 0$ , the only value with the dimension of length, which affects  $L_T$ , is the flame radius  $R$ . Thus,  $L_T$  may be considered to be proportional to  $R$ , and the flame speed increases as  $R^{1/3}$ , which should be regarded as a reasonable outcome for spherical flames without obstacles. Mixture properties are accounted for in Eq. 5 through the values of the laminar burning velocity  $S_L$  and expansion ratio  $\sigma$ .

An application of the correlation in Eq. 5 for the flame speed requires determination of two unknown parameters:  $a^2b$  and  $\alpha$ . These parameters were evaluated here using experimental data on the flame speeds as a function of distance inside obstacle arrays [7, 16] and data on flames with no obstacles [14, 15]. Data for relatively high reactivity fuels, including hydrogen, ethylene, and propylene were selected for a wide range of distances and flame speeds (see Figure 1). Another set of experimental data with obstacles [9, 10] and without obstacles [11, 13] is used here for model validation.

Possible values for the parameters  $a^2b$  and  $\alpha$  were determined by fitting experimental data with the function given by Eq. 5. An example of the result of the fitting procedure is presented in Figure 2.

## 2.2. Loss of Expansion

The expansion of the combustion products, which act as a piston driving the flame, is known to be extremely important for flame acceleration. It is this expansion that actually leads to the flame folding and generation of turbulence ahead of the flame. In the cases where the combustion products are enveloped within the flame and surrounded by reactants, or partially confined with rigid surfaces, full expansion is available to drive flame acceleration. In other cases,

combustion products may expand or vent directly into surrounding air. This is possible, say, in cases where vapor clouds are characterized by large aspect ratios, such as elongated clouds or thin layers of combustible vapors. In these situations full expansion is not available to contribute to flame acceleration.

To account for the loss of expansion, the reduced effective value of the expansion ratio ( $\sigma_{eff}$ ) should be used in the flame speed correlation instead of  $\sigma$ . This effective value depends on the relation between the flame area and the area through which the combustion products vent into air. It should be noted that the value of  $\sigma_{eff}$  generally varies during flame propagation. Some average value may be estimated for practical applications.

In the cases where obstacles occupy a part of a combustible cloud, open boundaries of the congested region may effectively play the same role as open mixture boundaries for loss of expansion. This is explained by the fact that the products (and expansion) are mostly generated in the congested areas.

In summary, the approach presented here suggests that a reduced effective expansion ratio should be used in the flame speed correlation to account for the loss of expansion effect. The same effect is addressed in studies reported by Baker and colleagues [4–7] using the options of 1D, 2D, and 3D expansion in the flame speed tables. It may be suggested that the latter options do not always accurately represent the situation. For example, a semispherical uniform obstacle array with central ignition allows for full expansion potential, similar to the 1D geometry. On the other hand, 1D flame propagation in an elongated cloud without any confinement represents the smallest potential for flame acceleration.

## 2.3. Blast Parameters

The model for the flame speed is developed here as part of a methodology to calculate blast effects

from VCEs. A model for evaluation of blast parameters should also be defined to provide a complete methodology. The models presented in the TNO Yellow Book [3], in works by Baker and various colleagues [4–7], and in Dorofeev [8] all give similar results for the blast overpressures and impulses as functions of distance for a given flame speed. Here, the method presented in Dorofeev [8] is adopted. This method includes simple analytical expressions for blast parameters and refers to the mixture expansion ratio, which is consistent with the flame speed correlations described in the previous section.

Maximum blast overpressure  $P$  and positive impulse  $I$  are calculated as functions of distance  $R$  from the blast epicenter using dimensionless Sach's variables for distance  $R^*$ , overpressure  $P^*$ , and impulse  $I^*$ :

$$R^* = \frac{Rp_0^{1/3}}{E^{1/3}} \quad P^* = P/p_0 \quad I^* = \frac{Ia_0}{E^{1/3}p_0^{2/3}} \quad (6)$$

where  $E$  is explosion energy and  $p_0$  and  $a_0$  are, respectively, pressure and sound speed in the surrounding air.

According to Dorofeev [8], dimensionless overpressure and impulse are considered to be functions of dimensionless distance and the flame speed  $V_f$ :

$$P^* = \min(P_1^*, P_2^*) \quad (7)$$

$$I^* = \min(I_1^*, I_2^*) \quad (8)$$

$$P_1^* = 0.34/(R^*)^{4/3} + 0.062/(R^*)^2 + 0.0033/(R^*)^3 \quad (9)$$

$$I_1^* = 0.0353/(R^*)^{0.968} \quad (10)$$

$$P_2^* = \frac{V_f^2 \sigma - 1}{c_0^2 \sigma} [0.83/R^* - 0.14/(R^*)^2] \quad (11)$$

$$I_2^* = \frac{V_f \sigma - 1}{c_0 \sigma} \left( 1 - 0.4 \frac{V_f \sigma - 1}{c_0 \sigma} \right) \times [0.06/R^* + 0.04/(R^*)^2 - 0.0025/(R^*)^3] \quad (12)$$

Equations 9–12 are presented with coefficients applicable for air explosions. These equations can be applied for ground explosions as well by doubling the value of the explosion energy in Eq. 6.

For purposes of the present analysis, the above description of the air blast parameters can be applied for the range of dimensionless distances  $0.33 < R^* < 3.77$ , and for visible flame speeds  $V_f \leq 500$  m/s. For higher flame speeds, transition to detonation might be possible in principle. Description of the critical conditions for transition to detonation is beyond the

scope of the present model. It is worthwhile to note, however, that the blast effects from detonations and from fast flames with flame speeds of  $>500$  m/s relative to a fixed observer are similar in the far field, where  $P^* < 1$ . For this reason, formulas for gas detonations (Eqs. 9 and 10) may be used directly for flame speeds exceeding 500 m/s.

### 3. EXPERIMENTAL VALIDATION

#### 3.1. Unconfined Spherical Deflagrations

An analysis of a representative set of experimental data on unconfined spherical deflagrations presented in Gostintsev *et al.* [11] included mixtures of  $C_2H_2$ ,  $H_2$ ,  $C_2H_4$ ,  $C_2H_4O$ ,  $C_3H_8$ , and  $CH_4$  with air and oxygen, and their experiments were carried out with initial mixture radii ranging from 0.3 to 10 m. These same investigators suggested that the self-similar regime of flame propagation is attributable to the hydrodynamic flame instability named after L. Landau. This led to the following expression for the flame speed ( $\sigma = 8$ ):

$$V_f = 0.4 \cdot S_L^{4/3} \chi^{-1/3} R^{1/3} \quad (13)$$

where  $\chi$  is the temperature diffusivity of the mixture and the coefficient was determined from experimental data. Using the approximate expression,  $\delta \approx \chi/S_L$ , our correlation of Eq. 5 may be rewritten as

$$V_f = 0.47 \cdot S_L^{4/3} \chi^{-1/3} R^{1/3} \quad (14)$$

It is seen that the functional dependencies of the flame speed in Eqs. 13 and 14 are the same and the coefficients are similar, which signify substantial agreement and reflect much better accuracy than that of the empirical coefficients in Eqs. 13 and 14.

It is remarkable that our approach, based on the assumption of flame self-turbulization and on the turbulent velocity correlation of Bradley [18], and the analysis [11] based on the Landau instability and fractal theory, both resulted in similar functional dependencies of the flame speed on propagation distance and on mixture properties. The coincidence of the results of these two approaches to the same phenomenon gives a strong argument for applicability of the correlation expressed in Eq. 5 for unconfined flames without obstacles.

In addition to the flame speeds, it is worthwhile comparing the maximum overpressures generated by spherical flames without obstacles with prediction of the present model. Experimental data of Fraunhofer ICT [12], which were recently released in the report by Molkov *et al.* [13], may be used for this purpose. The ICT experiments were made with stoichiometric hydrogen–air mixtures in a hemispherical plastic envelope with radius of 10 m, which was cut before ignition. The maximum flame speed of 80 m/s was reported. The maximum overpressure recorded in the air-blast wave was about 6 kPa. According to Eq. 5, the maximum flame speed is estimated to be 73 m/s

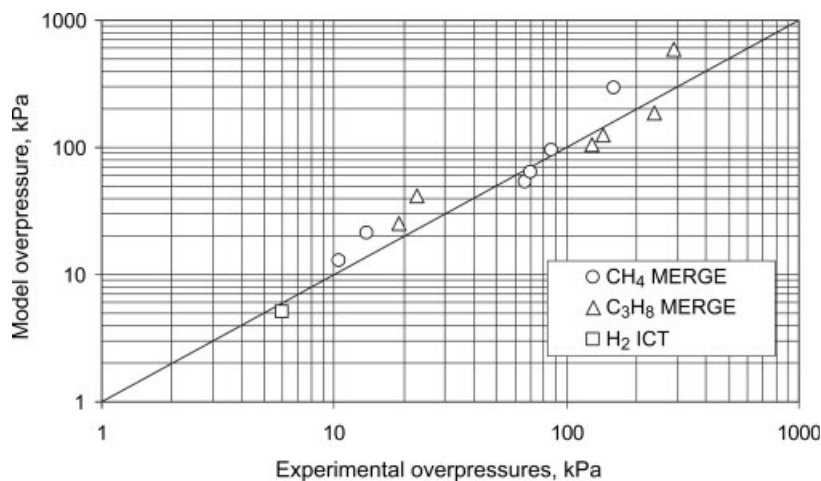


**Figure 3.** Maximum overpressures from the MERGE data and from Eqs. 1 and 5.

and the maximum overpressure given by Eq. 11 is 5.1 kPa, which is in good agreement with the experimental data.

### 3.2. Flames in Congested Areas

A substantial amount of experimental data on combustion behavior in congested area was generated through project MERGE (Modeling and Experimental Research into Gas Explosions). Here we compare the maximum overpressures reported in Mercx *et al.* [9] and Mercx and van den Berg [10] for medium- and large-scale tests with predictions of our method based on the flame speed correlation (Eq. 5). We use the data only for propane and methane with air. Methane/propane mixtures and mixtures with oxygen-enriched air are not included in the present comparison because of the uncertainties in the laminar burning velocities for these mixtures. For the MERGE geometry, the reported pitch is taken here as the characteristic distance  $x$ , and the cubic root of the volume blockage times  $x$  is used as a characteristic obstacle size  $y$  in Eq. 5.

A comparison of the maximum overpressures obtained from the MERGE data and data from the model is presented in Figure 3. Data from the unconfined ICT tests discussed in the previous section are also plotted in Figure 3. It is seen that there is good agreement of the experimental and predicted values of the maximum overpressures. The deviation is about 50% over the range from 6 to 300 kPa. Generally, this should be considered as a very good agreement for predictions of the pressure effect from gaseous explosions in congested areas. We should also note that the only parameters used to calculate model values were fundamental fuel properties, such as the laminar burning velocities and the expansion ratios.

## 4. APPLICATIONS—ASSUMPTIONS

Definitions and assumptions concerning mixture properties, levels of congestion, and damage criteria are given in this section. These definitions are

**Table 1.** Combustion properties of stoichiometric fuel–air mixtures.

Fuel	$\sigma_0^*$	$S_{L0}^*$ , (m/s)	$10^4 \delta_0^*$ , (m)	$\gamma_0^*$ , (m/s)
CH <sub>4</sub>	7.52	0.37	0.44	18.1
C <sub>3</sub> H <sub>8</sub>	7.99	0.40	0.35	22.3
C <sub>2</sub> H <sub>4</sub>	8.10	0.65	0.23	37.4
H <sub>2</sub>	6.89	2.10	0.10	85.2

\*Subscript 0 refers to stoichiometric mixture with air.

intended to be used here only for the purpose of illustrating the methodology. They are not universal and should be appropriately chosen for each specific application.

### 4.1. Fuel–Air Mixtures

The following fuels, known to behave differently in VCEs, were chosen here as typical examples:

- Methane
- Propane
- Ethylene
- Hydrogen

The fuel properties necessary for application of Eq. 1 for these four fuels are presented in Table 1. These properties are calculated for stoichiometric fuel–air mixtures. The values of the laminar burning velocities in Table 1 and thermodynamic parameters were taken from Egolfopoulos *et al.* [19], Vagelopoulos and Egolfopoulos [20], Aung *et al.* [21], and Reynolds [22]. Also given in Table 1 are the values of parameter  $\gamma$ , which defines the magnitude of the flame speed in Eq. 5:

$$\gamma = S_L \sigma (\sigma - 1) \quad (15)$$

## 4.2. Worst-Case Vapor Clouds

It is hardly possible to expect that the entire fuel mass will form a stoichiometric mixture after it is released. Such a situation is practically impossible and should be considered as overly conservative. There is clearly a variety of release scenarios that can affect the resulting composition of vapor clouds. In the present section we suggest a simple approximate method for the determination of “worst-case” compositions, based on a model for a smooth and monotonic distribution of fuel with distance in vapor clouds. The form of the cloud is assumed to be semispherical, for simplicity. Fuel concentration is considered to reach the maximum in the center of the semisphere and to decrease linearly with radius. A linear decrease of the concentration with radius is chosen for simplicity as well.

The postulated properties of the composition distributions are used here only for the purpose of limiting the number of parameters that determine average cloud properties and, thus, to be able to select the “worst case.” With the above assumptions, properties of vapor clouds are fully defined by two parameters: the maximum fuel concentration  $C_{max}$ , in the cloud center, and the total fuel mass in the cloud  $m$ . As soon as the “worst case” is selected, only the average cloud properties are used to evaluate the explosion effect, making the assumed details of the distribution relatively unimportant.

One can define the following average properties of vapor clouds that affect the severity of the blast effect. These are the ratio  $E/E_0$  of the total combustion energy in the cloud over the total energy of the released fuel; average laminar flame speed,  $\langle S_L \rangle$ ; average expansion ratio,  $\langle \sigma \rangle$ ; and average value of parameter  $\gamma$ ,  $\langle \gamma \rangle$ . The average values of the properties were defined using integration over the volume of the flammable cloud  $W$ . This is illustrated by the following equation for  $\langle S_L \rangle$ :

$$\langle S_L \rangle = \frac{1}{W} \int_W S_L(C) \cdot 2\pi r^2 dr \quad (16)$$

where  $C = C(r)$  represents fuel concentration and  $r$  is the radius from the cloud center.

With a constant mass of fuel in the cloud, the average fuel properties depend on the maximum fuel concentration  $C_{max}$ . The “worst case” is selected as the case where  $\langle \gamma \rangle$  reaches maximum. The average properties of “worst-case” vapor clouds are presented in Table 2.

Table 2 shows that only a portion of the total chemical energy is available for combustion in the “worst-case” vapor clouds. Also the average flame speed parameter  $\langle \gamma \rangle$  is an order of magnitude smaller than that for stoichiometric mixtures. It is interesting to note that  $\langle \gamma \rangle$  is further reduced for methane, making it significantly different from propane, although the laminar burning velocity and the expansion ratio of stoichiometric mixtures are both similar for methane and propane. On the contrary, ethylene comes

**Table 2.** Combustion properties of worst-case vapor clouds.

Fuel	$\langle \sigma \rangle$	$\langle S_L \rangle$ (m/s)	$E/E_0$	$\langle \gamma \rangle$ (m/s)	$\langle \gamma \rangle / \gamma_0$
CH <sub>4</sub>	3.8	0.18	0.59	1.81	0.10
C <sub>3</sub> H <sub>8</sub>	4.7	0.21	0.52	3.74	0.17
C <sub>2</sub> H <sub>4</sub>	5.5	0.42	0.25	10.5	0.28
H <sub>2</sub>	3.7	1.41	0.49	14.5	0.17

closer to hydrogen in terms of  $\langle \gamma \rangle$ , whereas the available energy appears to be relatively small. This relatively small  $E/E_0$  for ethylene is explained by the fact that the worst case is selected to have maximum average flame speed but not the maximum available energy.

These interesting observations arise from the fact that the average properties of vapor clouds depend on a number of parameters including the lower and upper flammability limits and on the dependency of the laminar burning velocity on fuel concentration. It may be suggested that  $\langle \gamma \rangle$ , or a similar parameter, may be used as the basis for classification of fuel reactivity for VCEs.

## 4.3. Geometry

For cases with obstacles, typical levels of congestion should be defined to simplify the choice of input parameters in applications. The effect of obstacles in Eq. 1 is accounted for through the parameters  $y/x$  and  $R/x$ . The first one is proportional to the square root of the blockage per plane cross section or to the cubic root of the volume blockage. The second is defined by the number of layers of obstacles in the flame path. Definitions of congestion levels based on the number of layers would mean that the same geometry would be classified differently for different cloud sizes. Definitions based on obstacle sizes and pitches are independent of the cloud size. It is suggested to use the latter option here with the following typical cases (which are similar to those used in Pierorazio *et al.* [7]):

- *Low congestion* is defined as less than 2% of volume blockage and more than 2 m between obstacles. This is represented by  $y/x = 0.25$  and  $x = 4$  m.
- *Medium congestion* is defined as between 2 and 6% of volume blockage and from 0.5 to 2 m between obstacles. This is represented by  $y/x = 0.33$  and  $x = 1$  m.
- *High congestion* is defined as more than 6% of volume blockage and less than 0.5 m between obstacles. This is represented by  $y/x = 0.5$  and  $x = 0.25$  m.

The typical levels of congestion presented above are relevant to obstructed regions with nearly uniform congestion.

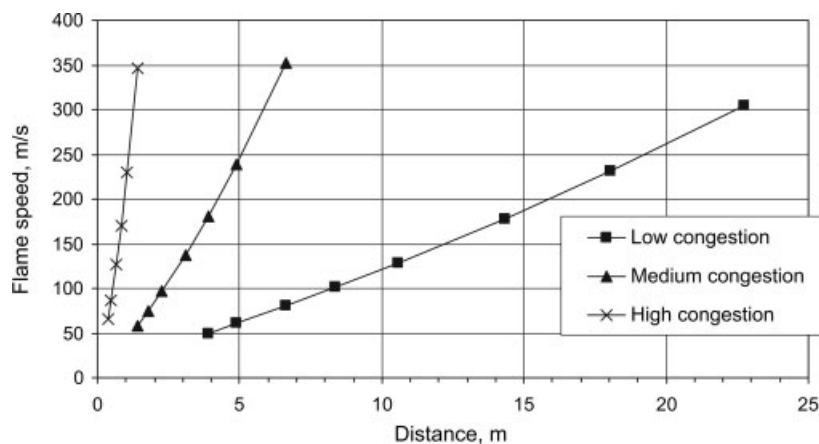


**Figure 4.** Flame speeds for stoichiometric ethylene-air mixture as a function of flame propagation distance for different levels of congestion.

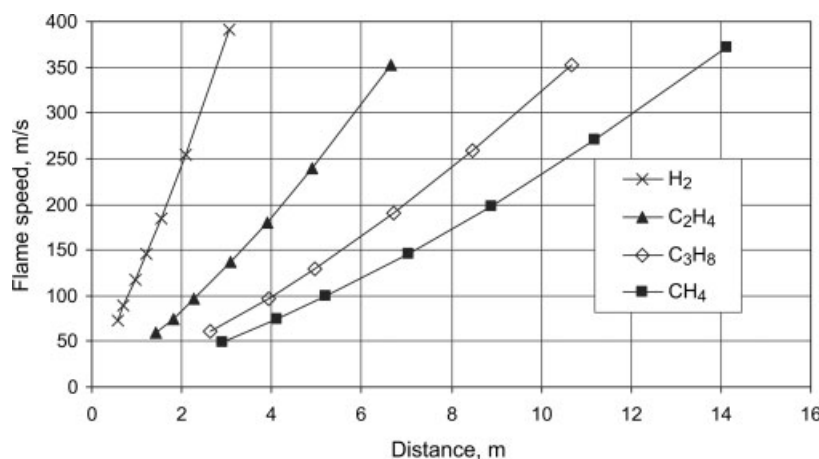


**Figure 5.** Flame speeds for stoichiometric fuel-air mixtures as a function of flame propagation distance for medium congestion.

## 5. APPLICATIONS—EXAMPLES

Examples of the results concerning maximum flame speeds in vapor clouds and pressure effects of VCEs are given in this section. These examples are intended to be used only as illustrations of the methodology. The conclusions are not universal and possible applications would require calculations to be made with assumptions appropriate for these applications.

### 5.1. Flame Speeds in Stoichiometric Mixtures

Maximum flame speeds for stoichiometric mixtures as a function of flame propagation distance for different obstacle geometries and mixtures are given here as an illustration of what can be expected in a given obstructed region with known mixture composition.

Maximum flame speeds for stoichiometric ethylene-air mixture are shown in Figure 4. It is seen that congestion significantly influences the flame speeds.

It takes about 1, 6, and 23 m for the flame to reach the speed of about 300 m/s propagating through high, medium, and low levels of congestion, respectively. Figure 5 shows maximum flame speeds for the four fuels for a medium level of congestion. It is seen that the fuel properties strongly affect the flame speeds. For the flame radius of 3 m and medium congestion, for example, flames reach speeds of about 50, 75, 130, and 400 m/s, respectively, for methane, propane, ethylene, and hydrogen mixtures with air.

It is seen that the flame speeds are not linear functions of distance in Figures 4 and 5. Tentatively, predictions of Eq. 5 (without loss of expansion) are in between the 2D and 1D cases of the BST tables [4–7], depending on the actual value of  $R$  and on the fuel chosen to represent one of the reactivity classes from the BST tables. Lower flame speeds would be estimated for cases with loss of expansion, such as the 3D cases in the BST tables.

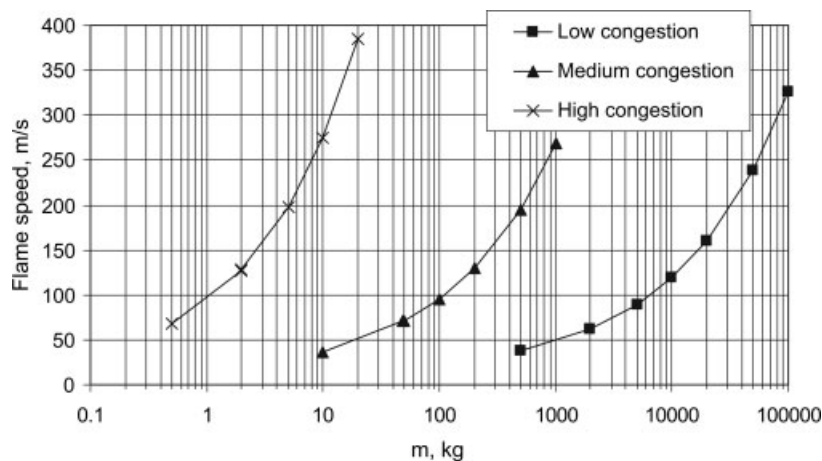


Figure 6. Flame speeds vs. fuel mass in “worst-case” ethylene cloud for different obstacle geometries.

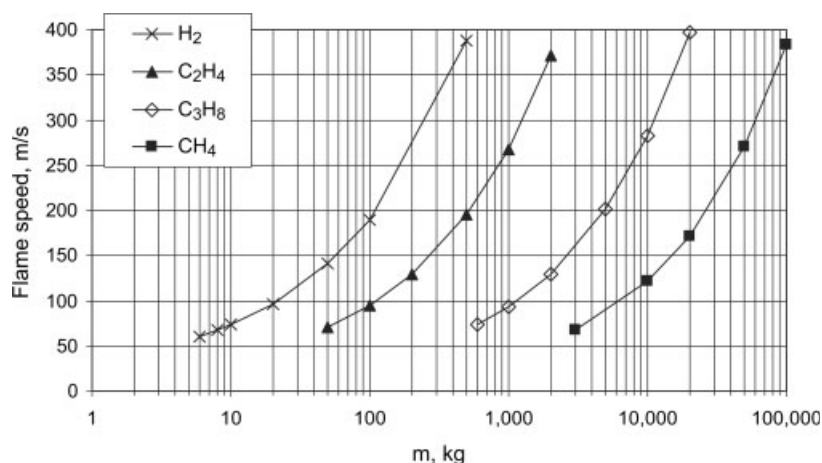


Figure 7. Flame speeds for different fuels vs. fuel mass in “worst-case” clouds for medium level of congestion.

## 5.2. Flame Speeds in Vapor Clouds

Flame speeds for the “worst-case” clouds are given here as an illustration of the maximum flame speeds in a given obstructed region with a nonuniform cloud.

Flame speeds for “worst-case” ethylene clouds as functions of fuel mass for different obstacle geometries are shown in Figure 6. It is seen that congestion significantly influences the flame speeds. It is necessary to have 1, 100, and 10,000 kg of ethylene released to be able to reach the flame speed of about 100 m/s for high, medium, and low levels of congestion, respectively.

Figure 7 shows flame speeds for the four fuels in the “worst-case” clouds in an obstructed region with a medium level of congestion. It is seen that fuel properties strongly affect the flame speeds. The minimum masses of fuel necessary to reach a given level of flame speed differ by orders of magnitude for different fuels.

## 5.3. Pressure Effects from Vapor Clouds

Pressure effects for the “worst-case” clouds are presented here as an illustration of what can be

expected from deflagrations in a given obstructed region occupied by a nonuniform cloud.

For illustration of pressure effects and damage potential from VCEs we use here the following pressure ( $P$ )–impulse ( $I$ ) damage criterion for the border of serious structural damages to buildings [3]:

$$(I - I_a)(P - P_a) \geq k \quad (17)$$

where the parameters are given by:  $I_a = 300 \text{ Pa}\cdot\text{s}$ ,  $P_a = 14,600 \text{ Pa}$  (2 psig), and  $k = 119,200 \text{ Pa}^2\cdot\text{s}$ .

Figure 8 shows distances from the explosion epicenter to locations with serious building damages for medium congestion as a function of fuel mass. Figure 9 shows the distances as a function of total released energy. The plots are presented for wide ranges of the mass of fuel released. It should be noted that all the clouds are assumed to be inside obstructed regions with the specified level of congestion. This may be difficult to occur in practice for released masses of  $>10^4 \text{ kg}$ , which correspond, for  $\text{CH}_4$ , for example, to cloud radii of  $>50 \text{ m}$ .

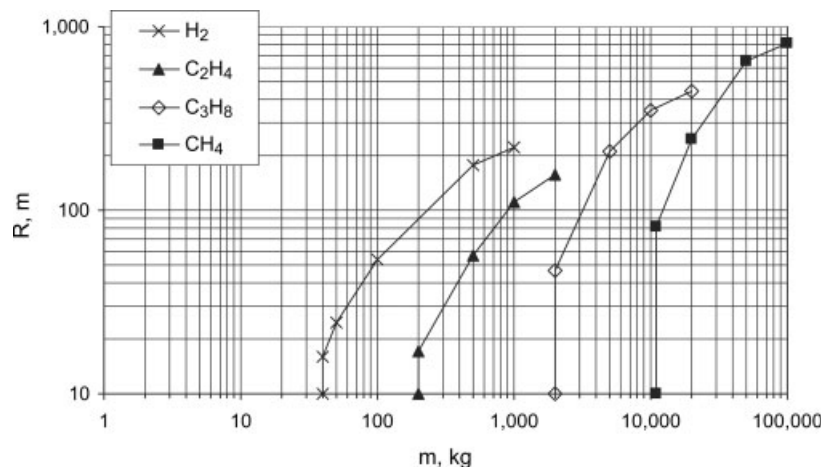


**Figure 8.** Radii from blast epicenter to locations with serious building damages vs. total mass of fuel released for medium congestion.

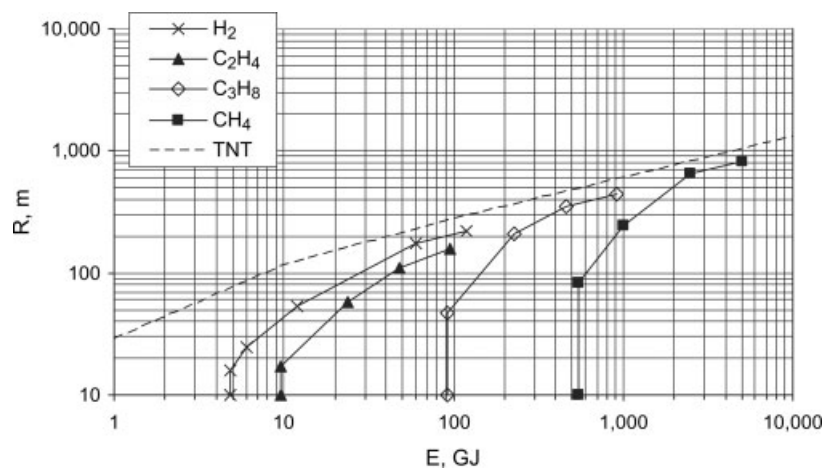


**Figure 9.** Radii from blast epicenter to locations with serious building damages vs. total energy of fuel released for medium congestion.

It is seen that there are certain threshold values of the mass (or energy) of fuel released that may be considered as potentially damaging. These threshold values depend on both the congestion level and the fuel type. For the low level of congestion the threshold masses of fuel are about 100-fold larger for all the fuels than for the medium congestion.

Figure 9 shows for comparison the radii for the serious building damages from TNT explosions with energy equal to the total fuel energy. Explosion efficiency factors of VCEs or explosion yields may be defined as the ratio of the TNT explosion energy and the fuel energy in the VCE cloud that give the same damage radius. The efficiency factors for serious building damages at  $R = 100$  m are estimated to be 0.23, 0.18, 0.05, and 0.01 for H<sub>2</sub>, C<sub>2</sub>H<sub>4</sub>, C<sub>3</sub>H<sub>8</sub>, and CH<sub>4</sub>, respectively. For  $R > 500$  m the efficiency factors become about 0.25 for all the fuels. Thus these factors depend on the release amount. This is difficult to account for within the

framework of the simplified TNT equivalency methods for VCE predictions (see, for example, the CCPS guidelines [23]).

## 6. CONCLUSIONS

An approximate correlation has been suggested for the flame speed as a function of distance and obstacle geometry. It was shown that this correlation and the predictions of blast effect based on it agree well with a representative set of experimental data for unconfined deflagrations with and without obstacles.

It was shown that the flame speed correlation supplemented with blast curves gives a simple and efficient method for VCE predictions. The method is based exclusively on the fundamental fuel properties and level of congestion. It may be applied both as a plant-specific method for separate obstructed regions and as a simplified screening tool for "worst-case" clouds and geometries.

The method was shown to give an appropriate account for mixture properties. In particular, the well-known difference in combustion behaviors of methane, propane, ethylene, and hydrogen was well captured by the method. The method was also shown to be able to predict that certain threshold amounts of fuel may be considered as potentially damaging. As a simplified tool, it was shown to reproduce accidental observations in terms of average explosion efficiency factors for various fuels.

#### LITERATURE CITED

1. R.A. Strehlow, R.T. Luckritz, A.A. Adanczyk, and S.A. Shimp, The blast wave generated by spherical flames, *Combust Flame* 35 (1979), 297–310.
2. W.E. Baker, P.A. Cox, P.S. Westine, J.J. Kulesz, and R.A. Strehlow, *Explosion hazards and evaluation*, Elsevier, Amsterdam, 1983.
3. The Netherlands Organization for Applied Scientific Research (TNO), *TNO yellow book* (1st edition), TNO, Apeldoorn, The Netherlands, 1997.
4. Q.A. Baker, M.J. Tang, E.A. Scheier, and G.J. Silva, Vapor cloud explosion analysis, *Proc 28th AIChE Annual Loss Prevention Symposium on Risk Analysis and Process Safety Management*, Atlanta, GA, 1994.
5. Q.A. Baker, C.M. Doolittle, G.A. Fitzgerald, and M.J. Tang, Recent developments in the Baker–Strehlow VCE analysis methodology, *Proc 31st AIChE Annual Loss Prevention Symposium*, Houston, TX, March 10–13, 1997.
6. M.J. Tang and Q.A. Baker, A new set of blast curves from vapor cloud explosions, *Proc 33rd AIChE Annual Loss Prevention Symposium*, Houston, TX, March 14–18, 1999.
7. A.P. Pierorazio, J.K. Thomas, Q.A. Baker, and D.E. Ketchum, An update to the Baker–Strehlow–Tang vapor cloud explosion prediction methodology flame speed table, *Process Safety Prog* 24 (2005), 59–65.
8. S.B. Dorofeev, “Blast effect of confined and unconfined explosions,” *Shock waves*, Proceedings of the 20th ISSW (Volume 1), B. Sturtevant, J. Shepherd, and H. Hornung (Editors), Scientific Publishing Co., Singapore, 1996, pp. 77–86.
9. W.P.M. Mercx, D.M. Johnston, and J. Puttock, Validation of scaling techniques for experimental vapor cloud explosion investigations, *Proc 28th AIChE Annual Loss Prevention Symposium on Risk Analysis and Process Safety Management*, Atlanta, GA, 1994.
10. W.P.M. Mercx and A.C. van den Berg, The explosion blast prediction model in the revised “Yellow Book,” *Proc 31st AIChE Annual Loss Prevention Symposium*, Houston, TX, March 10–13, 1997.
11. Yu.A. Gostintsev, A.G. Istratov, and Yu.V. Shulenin, Self-similar propagation of a free turbulent flame in mixed gas mixtures, *Fizika Goreniya i Vzryva* (Combustion, Explosion, and Shock Waves) 24 (1988), 63–70.
12. H. Schneider and H. Pfortner, PNP-Sicherheitssofortprogramm, Prozessgasfreisetzung-Explosion in der Gasfabrik und Auswirkungen von Druckwellen auf das Containment, Fraunhofer ICT internal report, December, Fraunhofer Institut Chemische Technologie, Pfinztal, Germany, 1983.
13. V.V. Molkov, D.V. Makarov, and H. Schneider, Hydrogen–air deflagrations in open atmosphere: Large eddy simulation analysis of experimental data, *Proc 1st Int Conf on Hydrogen Safety*, Pisa, Italy, September 8–10, 2005.
14. H. Geisbrecht, K. Hess, W. Leuckel, and B. Maurer, Analysis of explosion hazards on spontaneous release of inflammable gases into the atmosphere, *Ger Chem Eng* 4 (1981), 305–314.
15. M. Groethe, J. Colton, S. Choba, and Y. Sato, Hydrogen deflagrations at large scale, *Proc World Hydrogen Energy Conf*, Yokohama, Japan, 2004.
16. J. Grune, A. Vesper, G. Stern, W. Breitung, and S. Dorofeev, Acceleration of unconfined flames in congested areas, *Proc 19th Int. Colloquium on Dynamics of Explosions and Reactive Systems (ICDERS)*, Hakone, Japan, July 27–August 1, 2003.
17. A. Vesper, W. Breitung, and S.B. Dorofeev, Run-up distances to supersonic flames in obstacle-laden tubes, *J Phys IV France* 12 (2002), 333–340.
18. D. Bradley, K.C. Lau, and M. Lawes, Flame stretch rate as a determinant of turbulent burning velocity, *Proc R Soc Lond A Phys Sci A338* (1992), 359–387.
19. F.N. Egolfopoulos, D.L. Zhu, and C.K. Law, Experimental and numerical determination of laminar flame speeds: Mixtures of C<sub>2</sub>-Hydrocarbons with Oxygen and Nitrogen. *Proc Combust Inst*, 23 (1990), 471.
20. C.N. Vagelopoulos and F.N. Egolfopoulos, Direct experimental determination of laminar flame speeds. *Proc Combust Inst*, 27 (1998), 513.
21. K.T. Aung, M.I. Hassan, and G.M. Faeth, Effect of pressure and nitrogen dilution on flame/stretch interactions of laminar premixed H<sub>2</sub>/O<sub>2</sub>/N<sub>2</sub> flames, *Combust Flame* 112 (1998), 1–15.
22. W.C. Reynolds, The element potential method for chemical equilibrium analysis: Implementation in the interactive program STANJAN Version 3, Dept. of Mechanical Engineering, Stanford University, Palo Alto, CA, January 1986.
23. Center for Chemical Process Safety (CCPS), *Guidelines for evaluating the characteristics of vapor cloud explosions, flash fires, and BLEVES*, CCPS, American Institute of Chemical Engineers, New York, 1994.